



# Balkan Journal of Electrical & Computer Engineering

An International Peer Reviewed, Referred, Indexed and Open Access Journal

[www.bajece.com](http://www.bajece.com)

Vol :9  
No : 2  
Year : 2021  
ISSN : 2147 - 284X



It is abstracted and indexed in, Index Google Scholarship, the PSCR, Cross ref, DOAJ, Research Bible, Indian Open Access Journals (OAJ), Institutional Repositories (IR), J-Gate (Informatics India), Ulrich's, International Society of Universal Research in Sciences, DRJI, EyeSource, Cosmos Impact Factor, Cite Factor, SIS Scientific Indexing Service, IJIF, iijifactor. ULAKBİM-TR Dizin.

**General Publication Director & Editor-in-Chief**  
Musa Yılmaz, Batman University, Turkey.

**Vice Editor**  
Hamidreza Nazarpouya, University of California Riverside, USA

#### Scientific Committee

Abhishek Shukla (India)  
Abraham Lomi (Indonesia)  
Aleksandar Georgiev (Bulgaria)  
Arunas Lipnickas (Lithuania)  
Audrius Senulis (Lithuania)  
Belle R. Upadhyaya (USA)  
Brijender Kahanwal (India)  
Chandar Kumar Chanda (India)  
Daniela Dzhonova-Atanasova (Bulgaria)  
Deris Stiawan (Indonesia)  
Emel Onal (Turkey)  
Emine Ayaz (Turkey)  
Enver Hatimi (Kosovo)  
Ferhat Sahin (USA)  
Gursel Alici (Australia)  
Hakan Temeltaş (Turkey)  
Ibrahim Akduman (Turkey)  
Jan Izykowski (Poland)  
Javier Bilbao Landatxe (Spain)  
Jelena Dikun (Lithuania)  
Karol Kyslan (Slovakia)  
Kunihiko Nabeshima (Japan)  
Lambros Ekonomou (Greece)  
Lazhar Rahmani (Algerie)  
Marcel Istrate (Romania)  
Marija Eidukeviciute (Lithuania)  
Milena Lazarova (Bulgaria)  
Muhammad Hadi (Australia)  
Muhamed Turkanović (Slovenia)  
Mourad Houabes (Algerie)  
Murari Mohan Saha (Sweden)  
Nick Papanikolaou (Greece)  
Okay Kaynak (Turkey)  
Osman Nuri Ucan (Turkey)  
Ozgur E. Mustecaplioglu (Turkey)  
Padmanaban Sanjeevikumar (India)  
Ramazan Caglar (Turkey)  
Rumen Popov (Bulgaria)  
Tarek Bouktir (Algeria)  
Sead Berberovic (Croatia)  
Seta Bogosyan (USA)  
Savvas G. Vassiliadis (Greece)  
Suwarno (Indonesia)  
Tulay Adali (USA)  
Yogeshwarsing Calleecharan (Mauritius)  
YangQuan Chen (USA)  
Youcef Soufi (Algeria)

#### Aim & Scope

The journal publishes original papers in the extensive field of Electrical-Electronics and Computer engineering. It accepts contributions which are fundamental for the development of electrical engineering, computer engineering and its applications, including overlaps to physics. Manuscripts on both theoretical and experimental work are welcome. Review articles and letters to the editors are also included.

Application areas include (but are not limited to): Electrical & Electronics Engineering, Computer Engineering, Software Engineering, Biomedical Engineering, Electrical Power Engineering, Control Engineering, Signal and Image Processing, Communications & Networking, Sensors, Actuators, Remote Sensing, Consumer Electronics, Fiber-Optics, Radar and Sonar Systems, Artificial Intelligence and its applications, Expert Systems, Medical Imaging, Biomedical Analysis and its applications, Computer Vision, Pattern Recognition, Robotics, Industrial Automation.



ISSN: 2147- 284X  
Vol: 9  
No : 2  
Year: April 2021

#### CONTENTS

- M. Abdeh, F. Abut, F. Akay;** Autonomous Navigation in Search and Rescue Simulated Environment using Deep Reinforcement Learning, .....**92 - 98**
- T. Özmen, N. Onat;** The Effects of Magnetic Circuit Geometry and Material Properties on Surface Mounted Permanent Magnet Synchronous Generator Performance,.....**99 - 105**
- H. Sucu, T. Göktaş, M. Arkan;** Design, Simulation and Application of Buck Converter with Digital PI Controller,.....**106 - 113**
- R. Çelikel, A. Gündoğdu;** Comparison of PO and INC MPPT Methods Using FPGA In-The-Loop Under Different Radiation Conditions,.....**114 - 122**
- A. Gencer;** Comparison of T-Type Converter and NPC for the Wind Turbine Based on Doubly-Fed Induction Generator,.....**123 - 128**
- S. Yazar;** Reconstruction of the Taguchi Orthogonal Arrays with the Support Vector Machines Method,.....**129 - 137**
- B. K. Engiz, Y. A. Rajab;** Spectrum Occupancy Measurements in Cellular Frequency Band in Samsun,.....**138 - 143**
- I. Aksakalli, S. Kaçdioğlu, Y. S. Hanay;** Kidney X-ray Images Classification using Machine Learning and Deep Learning Methods,.....**144 - 151**
- E. Demir, A. Öztekin;** Automatic Positioning of Mobile Users via GSM Signal Measurements,.....**152 - 160**
- H. Eroğlu, Y. Oğuz;** Energy Efficient Driving Optimization of Electrical Vehicles Considering the Road Characteristics,.....**161 - 170**
- A. Çiçek, B. Uluğ;** First-Principles Study of Graphene-6H SiC Surface Interactions,.....**171 - 177**
- M. A. Yimer, S. Sevinç, A. R. Şişman, Ö. Aktaş, O. Yıldırım, E. Yaşar;** Monitoring the Treatments and Interventions to Intensive Care Patients: A Study for Multidimensional Evaluation of Changes in Patient Test Results with Principal Component Analysis,.....**178 - 186**
- E. Gilddoğan;** A Proposed Ensemble Model for The Prediction of Coronavirus Anxiety Scale of Migrant Workers,.....**187 - 190**
- Z. K. Küçük, N. Ekren;** Light Pollution and Smart Outdoor Lighting,.....**191 - 200**
- C. Şeker, M. T. Guner, Ş. Kuzey;** The Topologies of Multi-Input Single-Output Isolation-Free DC-DC Converter for Hybrid Power Plants,.....**201 - 206**
- A. Doğaner;** An Infodemiological Study to Estimate Risk Factors of Urinary Incontinence Using Elastic Net Regression,.....**207-211**
- G. U. Kaya, T. Ö. Onur;** Reconstruction with In-Line Digital Holography Quantitative Phase Imaging for Tissue-Mimicking Phantom Samples,.....**213-220**

**BALKAN  
JOURNAL OF  
ELECTRICAL & COMPUTER ENGINEERING**  
(An International Peer Reviewed, Indexed and Open Access Journal)

#### Contact

Batman University  
Department of Electrical-Electronics Engineering  
Bati Raman Campus Batman-Turkey

**Web:** <http://dergipark.gov.tr/bajece>  
<https://www.bajece.com>  
**e-mail:** [bajece@hotmail.com](mailto:bajece@hotmail.com)

# Autonomous Navigation in Search and Rescue Simulated Environment using Deep Reinforcement Learning

Mohammed Abdeh, Fatih Abut, M. Fatih Akay

**Abstract**— Human assisted search and rescue (SAR) robots are increasingly being used in zones of natural disasters, industrial accidents, and civil wars. Due to complex terrains, obstacles, and uncertainties in time availability, there is a need for these robots to have a certain level of autonomy to act independently for approaching certain SAR tasks. One of these tasks is autonomous navigation. Previous approaches to develop autonomous or semi-autonomous SAR navigating robots use heuristics-based methods. These algorithms, however, require environment-related prior knowledge and enough sensing capabilities, which are hard to maintain due to restrictions of size and weight in highly unstructured environments such as collapsed buildings. This study approaches the problem of autonomous navigation using a modified version of the Deep Q-Network algorithm. Unlike the classical usage of the entire game screen images to train the agent, our approach uses only the images captured by the agent's low-resolution camera to train the agent for navigating through an arena avoiding obstacles and to reach a victim. This approach is a much more relevant way of decision making in complex, uncertain contexts; since in real-world SAR scenarios, it is almost impossible to have the area's full information to be used by SAR teams. We simulated a SAR scenario, which consists of an arena full of randomly generated obstacles, a victim, and an autonomous SAR robot. The simulation results show that the agent was able to reach the victim in 56% of the evaluation episodes after 400 episodes of training.

**Index Terms**— Deep Reinforcement Learning, Autonomous Navigation, Autonomous Search and Rescue, Simulation.

**MOHAMMED ABDEH**, is with the Department of Computer Science and Engineering, Sabancı University, Istanbul, Turkey, (e-mail: [mohammadabdeh@sabanciuniv.edu](mailto:mohammadabdeh@sabanciuniv.edu))

 <https://orcid.org/0000-0002-5450-1316>

**FATIH ABUT**, is with the Department of Computer Engineering, Çukurova University, Adana, Turkey, (e-mail: [fabut@cu.edu.tr](mailto:fabut@cu.edu.tr)).

 <https://orcid.org/0000-0001-5876-4116>

**M. FATİH AKAY**, is with the Department of Computer Engineering, Çukurova University, Adana, Turkey, (e-mail: [mfakay@cu.edu.tr](mailto:mfakay@cu.edu.tr)).

 <https://orcid.org/0000-0003-0780-0679>

Manuscript received August 16, 2020; accepted Feb 05, 2021.

DOI: [10.17694/bajece.781162](https://doi.org/10.17694/bajece.781162)

## I. INTRODUCTION

EVERY YEAR, around 60.000 people die worldwide in natural disasters. The majority of the deaths are caused by building collapse in earthquakes [1]. Only a small fraction of the victims of urban disasters might survive. Consider from [2, 3] that 80% of survivors of urban disasters are surface victims, i.e., the people lying on the surface of the rubble or readily visible. However, only 20% of survivors of urban disasters come from the interior of the rubble, yet the interior is often where the majority of victims are located.

The complexity of the collapses and the need for a fast response after the disaster requires multiple tasks to be done simultaneously. One approach to solve this problem is the use of robots that have a variety of capabilities such as unmanned ground vehicles (UGVs) and unmanned aerial vehicles (UAVs) to assess human search and rescue experts. In other words, the number of human experts can be limited and does not serve the need for controlling the robots along with fulfilling the other critic tasks that require human interference and moral understanding. Hence, there is a need for supplying these robots with a certain level of autonomy to be able to navigate through a SAR area and thus provide some tasks without the need for human control. In [4], Murphy et al. describe the tasks that can be addressed. Those tasks include (a) reaching small and dangerous places (voids) that humans and dogs cannot reach, (b) exploring the interior and exterior of the hot zone and extending wireless communication ranges.

Navigation is one of the fundamental tasks of mobile robots. The algorithms used to approach this task are divided into two sets [5]:

- Greedy heuristics-based algorithms that operate using a map, which needs to be provided or extracted from the environment. After generating such a map, the central system performs the task of path planning, which is finding the optimal or suboptimal path to reach the target. Then the robots perform the navigation through the specified path. Autonomous mobile robots that use these techniques need to localize themselves within the generated map at the start of the planned trajectory, and then monitor their motion along the path using sensors (e.g., wheel

encoders and inertial sensors) which are hard to be maintained on board of a small mobile robot navigating through small voids within rubbles.

- Algorithms that operate without the use of maps (e.g., DistBug); These algorithms are often used if a path has to be traveled only once and therefore does not necessarily have to be optimal. Although the Bug family algorithms use limited sensors and computation capabilities, they tend to rely on perfect position estimations. In [6], McGuire et al. concluded that the Bug algorithms performance is sensitive to sensor-related noise, which makes them hard to implement in real-world uncertain noisy contexts.

In [7], the authors studied different search methods based on greedy heuristics, and partially observable Markov Decision Process (POMDP) to design the autonomous control of UAVs to act in search and rescue contexts. Their evaluation results showed the great potential of POMDP in SAR scenarios; they also acknowledged that using these methods requires a high computation power as the cost grows exponentially (i.e., the curse of dimensionality) and that existed algorithms were not sufficient yet to tackle real-world problems. With the rise of deep learning and the expanding computational power, researchers have been able to come up with algorithms that can be used to tackle the curse of dimensionality more efficiently and solve problems that were not intractable in the past, such as playing Atari games at a superhuman level [8] and defeating a 9-dan Go player [9].

The main purpose of this study is to approach the problem of autonomous navigation using a modified version of DQN by relying only on the agent's camera without the use of any environment-related prior knowledge or any info gathered from another source (e.g., human experts, other robots, maps). This decentralized approach using only the agent's limited vision-based capabilities is a relevant strategy in deep voids where wireless connections might be hard to maintain, and also in any other situation where no enough outside information is available in the process of decision making. The DQN algorithm modified and used in this work is a valid method of solving real-world problems that can be interpreted as a POMDP.

The rest of the paper has the following structure. Section II gives an overview of related works. Section III describes the theoretical foundations of the utilized learning algorithms. Section IV presents the simulation setup and evaluation methodology. Section V presents the results and discussion. Finally, Section VI outlines the paper along with future directions.

## II. RELATED WORKS

One of the applications of autonomous navigation is creating 3D visualizations of buildings and large-scale construction sites using scanning technologies. The scanning process has been often carried out using scanners handled by people [10] or scanners on board of vehicles controlled by people [11]. In [12], Kim et al. assisted the scanning process with UAVs that generated an initial 3D map of the area, then based on this map,

the optimal scanning locations are estimated, and the optimal navigation path is determined. After that, a robot equipped with a laser scanning system is used to follow the path and obtain high-resolution scans in the estimated locations. Although such techniques are powerful in navigating through large construction sites, they cannot be used to assess small UGVs navigating through small-scale indoor environments. These robots must perform navigation without any outside assessments due to the limitation of wireless sensing technologies.

The problem of autonomous navigation in search and rescue contexts has been approached previously using heuristics-based methods. A heuristic function ranks a set of options available at one point and decides which one to choose according to the ranking. These approaches require situation related prior knowledge and a wide range of sensing abilities. In the EU funded project ICARUS [13], several robots with different structures and capabilities have been designed to assess SAR experts. Small Unmanned Ground Vehicles (UGVs) used to navigate through narrow voids were supplemented with a very limited level of autonomy. This is caused by the use of heuristic algorithms that require a massive amount of sensors and power, which cannot be added to the vehicles due to the restrictions of size and weight in highly unstructured environments, such as collapsed buildings. A similar approach has been carried out in the SHERPA project [14] in which the goal was to develop a mix of ground and aerial robots to support SAR teams in real-world hostile environments.

DQN was implemented in [15] to support a UAV with the ability to navigate independently towards a specified goal in a simulated environment. They evaluated their work by comparing the success rate, and the average steps undertaken by the trained agent and a random decision-making agent. This research resulted in an 8% success rate for the trained agent compared to a 5% success rate for the random-action taking agent. Although the algorithm showed some success as the trained agent outperformed the random agent in terms of success rate, it is clear that it can be further developed.

This study approaches autonomous navigation using a modified version of the DQN algorithm relying only on the agent's camera. Unlike the previous methods, this approach does not require a map to be generated or any extra sensors to monitor the agent's motion. While the recent implementation of DQN in autonomous navigation [15] used the same proposed CNN, the CNN (convolutional neural network) being used in this work for training the agent to make decisions based on the captured images has been designed with simplicity in mind to suit the simulated scenario.

## III. THEORETICAL BACKGROUND

### A. Reinforcement Learning

RL is the machine learning paradigm concerned with training agents to act autonomously to reach certain goals in an environment. A typical reinforcement learning scenario consists of the following components: an agent (the decision-maker), an environment in which its state changes according to the agent's actions. As the agent explores the environment, it receives a reward for each action it makes. Hence by trial and error, it learns to maximize this reward.

Formally an RL scenario is modeled as a Markov Decision Process (MDP) which consists of a tuple  $(S, A, R, T, \gamma)$  where  $S$  is the set of states,  $A$  is the set of actions, (alternatively  $A(s)$ : the set of actions that can be taken at state  $s$ );  $R(s)$  is the reward function, it returns the immediate reward;  $T(s, a, s') \sim P(s'|s, a)$  is the probability that taking action  $a$  will change the environment state from  $s$  to  $s'$ ; and finally,  $\gamma \in [0,1]$  is the discount factor, which is how much we value future reward over the immediate one.

The main problem of an MDP is to find the optimal policy  $\pi^*$ . A policy  $\pi(s)$  is a function that specifies the action that should be taken at a certain state. Thus the optimal policy  $\pi^*$  is the policy that maximizes the expected long term reward (i.e., the reward from all states):

$$\pi^* = \operatorname{argmax}_{\pi} E[\sum_{t=0}^{\infty} \gamma^t R(s_t) | \pi]. \quad (1)$$

Partially Observable Markov Decision Process (POMDP) is a generalization of Markov Decision Process (MDP). POMDP consists of a tuple  $(S, A, O, \Omega, R, T, \gamma)$ , where  $S$  is the set of states;  $A$  is the set of actions (or alternatively  $A(s)$  is the set of actions that can be taken at state  $s$ );  $O$  is the set of observations;  $\Omega(o, s', a) \sim P(o|s', a)$  is the probability of observing  $o$  at state  $s'$  after taking action  $a$ ;  $R(s)$  is the reward function, it returns the immediate reward;  $T(s, a, s') \sim P(s'|s, a)$  is the probability that taking action  $a$  will change the environment state from  $s$  to  $s'$ ; and finally,  $\gamma \in [0,1]$  is the discount factor, which is how much we value future reward over the immediate one.

A POMDP scenario can be described as follows: at each time frame the environment is in some state  $s \in S$ , the agent takes action  $a \in A$  which changes the environment state from  $s$  to  $s'$  according to the transition probability  $T$ , after a step time, the agent receives an observation  $o$  from the environment state  $s'$ . The observation depends on the current state  $s'$  and the previous action  $a$  according to the probability  $\Omega(o, s', a)$ . The goal of the agent is to find the optimal policy  $\pi^*$  that maximizes the expected long-term reward. As the states in POMDP are not fully observable, the agents only receive partial information about the environment. This generalization is more realistic than MDP, and it can describe a variety of real-world problems. Hence it is an appropriate framework to describe the simulated scenario.

### B. Q-Learning

Reinforcement learning methods fall into two categories; the policy-based and value-based methods. The policy-based methods aim at finding the optimal policy  $\pi^*$  by starting with a parameterized policy and updating its parameters using gradient-based or gradient-free methods, on the other hand, the value-based methods use a value function that determines the expected long term reward of executing an action at a particular state, and hence providing which action to undertake. One of the most well-known value-based methods is Q-learning. It can find the optimal policy in finite stationary and fully-observable environments with discrete actions. The algorithm starts by

initializing a table called the Q-table with arbitrary Q-values. A q-value is a value that corresponds to how well an action is at a specific state. Then at each state, an action  $a$  is being selected, and its corresponding Q-value is being calculated using the Q-function:

$$Q^{new}(s, a) = Q(s, a) + \alpha [r + \gamma \max_{a'} Q(s', a') - Q(s, a)] \quad (2)$$

where  $Q(s, a)$  is the Q-value of executing an action  $a$  at state  $s$ ,  $\alpha \in (0,1]$  is the learning rate, and  $r$  is the immediate reward. Although Q-learning can find the optimal policy in small finite environments, it performs poorly on non-stationary partially observable complex environments.

### C. Deep Q-Network

With the rise of deep learning and particularly in [8], Mnih et al. introduced the Deep Q-Network algorithm (DQN), which gave birth to the field of deep reinforcement learning. DQN was the first algorithm to reach a superhuman performance in playing Atari games from pixels. Instead of using a table to track the Q-values, they used a convolutional neural network as a function approximator to predict Q-values from states. One of the problems the RL algorithms have when using artificial neural networks as function approximators is the problem of instability. The DQN algorithm uses two separate models to stabilize the learning; namely, the main model and the target model, the main model's weights get copied to the target model every  $c$  steps. The DQN also keeps a memory buffer termed Experience Reply to store the transactions. At every training step, the DQN uses the main model to predict the action to take, and then the agent executes the action and observes a new state together with the immediate reward. After adding the new transaction to the experience replay, it takes random samples from the experience replay and uses them as data to fit the main model by minimizing the mean-square error (MSE) between the main and target models. The training process is visualized in Fig. 1.

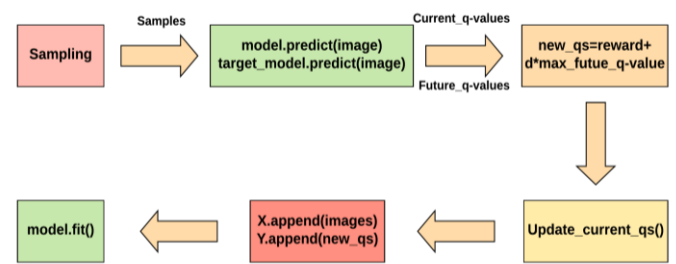


Figure 1. Visualization of one training step

### D. The $\epsilon$ -Greedy Policy

The  $\epsilon$ -greedy policy is a method used to balance the exploration and exploitation done by the agent; that is deciding at a certain point whether it should take random actions to explore unexplored space, or whether it should use the trained model's action-value estimations to predict the best action. It keeps track

of a parameter  $\epsilon$ , which represents the probability of choosing a random action. Similar to the original DQN, in this work,  $\epsilon$  starts at 1 and decreases linearly throughout the training until it reaches a fixed point.

#### IV. SIMULATION SETUP AND METHODOLOGY

The scenario was simulated using Webots [16], an open-source robot simulator widely used for educational and professional purposes. It includes a complete toolbox to design environments, robots, and simulation experiments. It can execute controllers written in compiled C/C++ and Java or interpreted python and Matlab languages. In this study, the agent controller was written in python to take advantage of the required libraries (i.e., Numby, Tensorflow, and Keras).

An e-puck robot was used for its motion simplicity. It has two motors, a left wheel motor and a right wheel one. It also has a color camera with a maximum resolution of 640x480, eight light sensors, and eight distance sensors. For this research, only the camera and the motors have been used.

At the beginning of the simulation, a square arena is created. The center of the arena is at the center of the coordination, and the objects can be placed within  $[-1, 1]$  and  $[-1, 1]$  at X and Z dimensions, respectively, whereas the Y dimension remains the same. At every episode, the agents and obstacles are placed randomly. The victim robot is randomly placed according to the uniform distribution at a position within the upper left part of the arena between  $[-1, -0.5]$  and  $[-1, -0.5]$  at X and Z dimensions, respectively. Similarly, the agent is placed randomly according to the uniform distribution at the downright part of the arena between  $[0.5, 1]$  and  $[0.5, 1]$  at X and Z dimensions, respectively. The obstacles (i.e., 20 boxes) are positioned randomly according to the normal distribution of 0 mean and standard deviation of 0.5. The objects are positioned in this manner to ensure that the obstacles will get in the agent's way. Fig. 2 shows a view of the arena at the beginning of an episode.

In this work, DQN has been modified to ensure more success in the simulated scenario. These modifications are as follows:

- The CNN that has been used in the original DQN has performed poorly on the simulated scenario. The agent at an early level of the training starts to memorize one action regardless of the image fed into the network, and hence it rarely reaches the victim robot. Instead, in this work, a simpler CNN has been used. It showed much better results. Fig. 3 shows the architecture of the modified CNN, which is used to predict the best action to be executed according to the image fed.



Figure 2. A bird view of the arena at the beginning of an episode. The trained SAR agent is at the downright, and the victim is located up at the left most of the image.

- The agent was trained for 400 training episodes executed in 8 identical parts; within each part, 50 episodes were executed. At each training part, the  $\epsilon$ -greedy policy's  $\epsilon$  starts from 1 and decays until it reaches 0.1 after 25 episodes, which is half of a training part, as illustrated in Fig. 4.
- While in the original DQN, a stack of 4 frames is being fed into the CNN as one observation, for simplicity, we use only one image. Fig. 5 shows an image captured by the agent during training.
- The use of a simple distance-dependent reward function:

$$reward = 100(last_d - current_d) \quad (3)$$

where  $last_d$  is the distance between the agent and the victim at the previous step, and  $current_d$  is the distance between the agent and the victim at the current step.

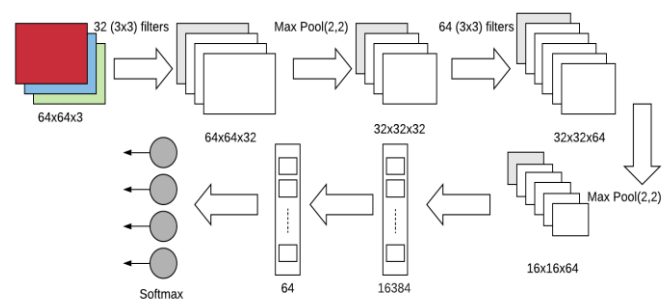


Figure 3. The architecture of the modified CNN used to train the agent to predict actions.

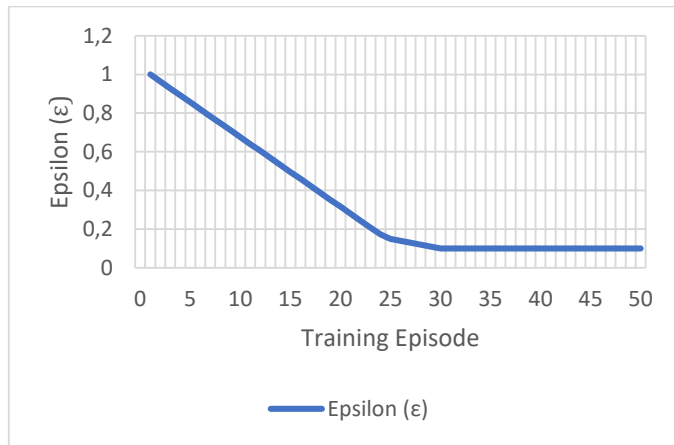


Figure 4. Linear change of  $\epsilon$  throughout a single training part



Figure 5. An image captured using the agent’s camera. Images of this type were used in training and testing.

### V. RESULTS AND DISCUSSION

Several evaluation methods were used to test the suitability of the original CNN architecture proposed in [8]. The original CNN was designed to learn generalizing the learning process over many distinct Atari games, while in our scenario, the agent has to learn to interact in one environment. In other words, due to the complexity of the model, the agent starts to memorize behaviors at a very early level, and thus at one point, it starts to take only one action regardless of the image captured. This resulted in a bad performance in terms of navigating towards the target.

Fig. 6 illustrates the number of steps taken by the agent to reach the victim in a single episode by using the original CNN. If the agent does not reach the victim during the episode, the finishing step will be equal to the maximum number of steps used (i.e., 1000). This is due to the low  $\epsilon$  value 0.1 which limits the agent exploration. The line shows that using the original approach the agent was only able to reach the victim before the episode 25 (i.e., the episode at which the randomness is minimized), which demonstrates clearly that the agent is not able to reach the victim when relying on the original complex CNN and hence performs poorly in the simulated environment.



Figure 6. The finishing steps of the agent when trained using the original CNN

Using our modified CNN proposed in the methods section, the agent showed better results when evaluated in 1000 step epochs. Fig. 7 illustrates the number of steps taken by the agent to reach the victim in a single episode by using the modified CNN. If the trained agent does not reach the victim during the episode, the finishing step will be equal to the maximum number of steps used (i.e., 1000). The line shows that using the modified approach, the agent was able to reach the victim at most of the episodes, while also reaching the victim in less number of finishing steps on average after the episode 25. This, in turn, clearly demonstrates that the agent is able to reach the victim more efficiently relying only on the trained model using the modified CNN.

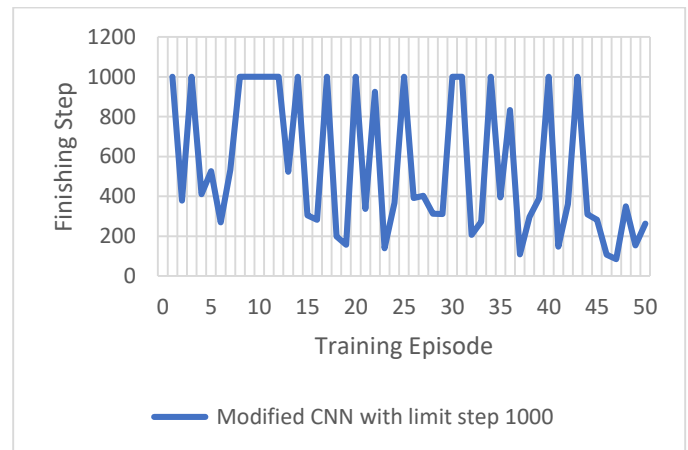


Figure 7. The finishing steps of the agent when trained using the modified CNN

The finishing step is going smaller along with the training. Since the  $\epsilon$  is decaying linearly, this shows that the agent is performing better when it predicts the actions based on the trained model. Table 1 shows the training results of the agent during the different parts of the training.

TABLE 1. THE TRAINING RESULTS OF THE AGENT DURING THE DIFFERENT PARTS OF THE TRAINING

Training Part (Episodes)	Success Rate	Minimum Steps
0 - 50	24%	42
51 - 100	40%	38
101 - 150	46%	65
151 - 200	52%	45
201 - 250	60%	50
251 - 300	50%	68
301 - 350	64%	65
351 - 400	46%	59

Note: The success rate shows the percentage of the successful episodes, in which the agent successfully reaches the victim, whereas the minimum steps show the minimum step number at which the agent reached the victim.

TABLE 2. COMPARING THE VALIDATION RESULTS OF THE AGENTS WITH PREVIOUS WORK

Study	Agent	Average Steps	Success Rate	Minimum Steps
The results of [15]'s approach	Random Agent	22.35	5%	-
	Trained Agent	258.54	8%	-
The results of this study	Random Agent	400 (the limit)	0%	400 (the limit)
	Trained Agent (400 episodes)	242.44	56%	21

Using the methods proposed above, the agent was trained on an Intel Core (TM) i5-3230M CPU. Training 400 episodes lasted appr. 21 hours and 7 minutes. The training episodes were executed in 8 parts to ensure the stability of the simulation physics engine (i.e., after training for more than 50 epochs, the physics engine starts to produce some delay and the simulation info file stored in the RAM reaches its limits).

After the training, the agent's performance was evaluated using the same evaluation method used in [15]. The trained agent's success rate and the number of steps it took to finish the simulation were calculated and compared with a fully random-action taken agent. Table 2 shows a comparison between the evaluation results of this work and the previous study.

While the random agent was not able to reach the victim even once, after 400 episodes of training, the agent was able to reach a 56% success rate in 40 evaluation episodes. That means that the e-puck robot was able to reach the victim in 56% of the evaluation episodes. Moreover, it was able to reach the victim in 21 steps at least in one episode, which is a great result giving the complexity of the environment. The poor performance of the random agent in our study shows the complexity of our simulated scenario when compared with the simulation scenario in [15]. Hence, this proves how well the trained agent performed.

Compared with the results proposed in [15], this work has reached significant improvements in terms of the difference between the results of the random agent and the trained one. This is due to the use of a simpler CNN that learns to navigate through obstacles contained in similar settings, instead of the use of the original CNN that generalize the learning over many Atari games. Another factor is the used version of the  $\epsilon$ -greedy policy; that is partitioning the training into parts with an  $\epsilon$  that starts at each part from 1 and linearly decays until it

reaches a 0.1. With this method, the agent has been able to explore the changing state of the environment across episodes more efficiently.

## VI. CONCLUSION AND FUTURE WORK

This paper presented a SAR simulation scenario, in which an autonomous e-puck robot's main goal is to explore an area full of randomly generated obstacles and yet to learn to navigate through them to reach a certain victim without any use of environment-related prior knowledge. The scenario and the environment, in general, can be used to test the suitability and the efficiency of different deep reinforcement learning methods to solve autonomous SAR problems. A modified DQN algorithm was implemented using some new approaches. These approaches include (a) the use of modified CNN instead of the original one, a distance-dependent reward function, and agent's low-resolution camera images to train the agent; (b) feeding one frame to the CNN as an observation instead of a stack of four images; and finally (c) training the agent in 8 parts; at each part, the  $\epsilon$ -greedy policy's  $\epsilon$  is decaying linearly from one until it reaches 0.1 at the middle of the training part. Using these methods, our modified DQN has shown great results compared to previous work when evaluated using the same evaluation methods and metrics, reaching a success rate of 56% at an average step of 242.

Despite the work's success, a variety of future works can be conducted to increase efficiency and real-world interpretability. The scenario can be further developed to become more realistic; e.g., by placing a variety of obstacles, increasing the number of obstacles and victims. A more complex CNN can be designed to train the agent to navigate in the developed complex scenario. The reward function can be optimized to depend on other factors, such as the distance between the agent and the nearest

obstacle. Finally, as the number of victims increases together with the complexity of the environment, using a multi-agent SAR team will be a relevant strategy. Agents should learn to cooperate as a team to approach a common goal.

#### REFERENCES

- [1] C. Kenny, *Why Do People Die In Earthquakes? The Costs, Benefits, And Institutions of Disaster Risk Reduction In Developing Countries*. Policy Research Working Paper 4823. The World Bank, 2009.
- [2] "NFPA 1670, Standard on Operations and Training for Technical Rescue Incidents - National Fire Protection Association". <https://www.nfpa.org/codes-and-standards/all-codes-and-standards/list-of-codes-and-standards/detail?code=1670&tab=nextedition> (accessed Aug. 03, 2020).
- [3] "Rescue: Technical Rescue Program Development Manual", U.S. Fire Administration and Federal Emergency Management Agency, ISBN: 1482709600.
- [4] R. R. Murphy *et al.*, "Search and Rescue Robotics," in *Springer Handbook of Robotics*, 2008, pp. 1151–1173.
- [5] T. Bräunl, "Localization and Navigation," in *Embedded Robotics*, Springer Berlin Heidelberg, 2008, pp. 241–269.
- [6] K. N. McGuire, G. C. H. E. de Croon, and K. Tuyls, "A comparative study of bug algorithms for robot navigation," *Rob. Auton. Syst.*, vol. 121, p. 103261, Nov. 2019.
- [7] S. Waharte and N. Trigoni, "Supporting search and rescue operations with UAVs," in *Proceedings - EST 2010 - 2010 International Conference on Emerging Security Technologies, ROBOSEC 2010 - Robots and Security, LAB-RS 2010 - Learning and Adaptive Behavior in Robotic Systems*, 2010, pp. 142–147.
- [8] V. Mnih *et al.*, "Human-level control through deep reinforcement learning," *Nature*, vol. 518, no. 7540, pp. 529–533, Feb. 2015.
- [9] D. Silver *et al.*, "Mastering the game of Go with deep neural networks and tree search," *Nature*, vol. 529, no. 7587, pp. 484–489, Jan. 2016.
- [10] J. Xiao, A. Owens, and A. Torralba, "SUN3D: A database of big spaces reconstructed using SfM and object labels," in *Proceedings of the IEEE International Conference on Computer Vision*, 2013, pp. 1625–1632.
- [11] I. Toschi, P. Rodríguez-González, F. Remondino, S. Minto, S. Orlandini, and A. Fuller, "Accuracy evaluation of a mobile mapping system with advanced statistical methods," in *International Archives of the Photogrammetry, Remote Sensing and Spatial Information Sciences - ISPRS Archives*, 2015, vol. 40, no. 5W4, pp. 245–253.
- [12] P. Kim, J. Park, Y. K. Cho, and J. Kang, "UAV-assisted autonomous mobile robot navigation for as-is 3D data collection and registration in cluttered environments," *Autom. Constr.*, vol. 106, p. 102918, Oct. 2019.
- [13] "ICARUS Project.", European Union's Horizon 2020 research and innovation programme, <https://icarus2020.eu/> (accessed Aug. 03, 2020).
- [14] L. Marconi *et al.*, "The SHERPA project: smart collaboration between humans and ground-aerial robots for improving rescuing activities in alpine environments," 2012.
- [15] J. G. C. Zuluaga, J. P. Leidig, C. Trefftz, and G. Wolffe, "Deep Reinforcement Learning for Autonomous Search and Rescue," in *Proceedings of the IEEE National Aerospace Electronics Conference, NAECON*, Dec. 2018, vol. 2018-July, pp. 521–524.
- [16] O. Michel, "Cyberbotics Ltd. Webots TM: Professional Mobile Robot Simulation," 2004. Accessed: Aug. 03, 2020. [Online]. Available: <http://www.cyberbotics.com>.

#### BIOGRAPHIES



Mohammad ABDEH received B.Sc. degree in Computer Engineering from Çukurova University, Turkey, in 2020. He had been awarded an undergraduate scholarship from Turkey Scholarships in 2017. He is currently a M.Sc. student and a Teaching Assistant at the Department of Computer Science and Engineering at Sabanci University, Istanbul, Turkey. His research interests include artificial intelligence, reinforcement learning, and autonomous search and rescue robotics.



Fatih ABUT received B.Sc. and M.Sc. degrees in Computer Science from Bonn-Rhein-Sieg University of Applied Sciences, Germany, in 2008 and 2010, respectively; and a Ph.D. degree in Computer Engineering in the year 2017 from Çukurova University, Adana, Turkey. He is currently an Assistant Professor in the Department of Computer Engineering at Çukurova University. His research interests include machine learning and artificial intelligence, computer and wireless communications, and IP network measurement and characterization.



Mehmet Fatih AKAY received B.Eng. and M.Eng. degrees in Electrical and Electronics Engineering from Çukurova University, Turkey, in 1999 and 2001, respectively; and a Ph.D. degree in Electrical and Computer Engineering in the year 2005 from Drexel University, Philadelphia, USA. He is currently a Professor in the Department of Computer Engineering at Çukurova University. His research interests include machine learning and artificial intelligence, simulation, and modeling of multiprocessors.

# The Effects of Magnetic Circuit Geometry and Material Properties on Surface Mounted Permanent Magnet Synchronous Generator Performance

Tuğberk Özmen and Nevzat Onat

**Abstract**—Permanent magnet synchronous generator is one of the generator types used in electrical energy production. In this study, a 1.5 kW inner rotor, surface located permanent magnet synchronous generator is used as a reference. The computer model of this generator has been prepared using Maxwell Rmxprt software. Rmxprt analysis of the generator has been performed and results were obtained for no-load and nominal load operating conditions. Parameters such as cogging torque which is an important parameter especially for permanent magnet synchronous generators used in wind turbines and efficiency were examined. The effects of changing in magnetic circuit as the permanent magnet pole arc to pole pitch ratio, magnet thickness and magnet material parameters on the generator performance were analyzed comparatively. Using the effects of these parameters, an optimization study has been carried out to increase the performance of the reference PMSG and compared with the values obtained in the initial state.

**Index Terms**—Cogging torque, efficiency, surface mounted PMSM.

## I. INTRODUCTION

PERMANENT MAGNET synchronous machines (PMSM) which have magnets in the rotor, have less copper losses, small volume and high power density, lightweight and higher efficiency compared to conventional electrical machines [1]. Thanks to their superiority, they are used in computer technologies, robotics, space technologies, electric vehicles and renewable energy systems.

Permanent magnet synchronous machines are used as generator in renewable energy conversion systems. Permanent

TUĞBERK ÖZMEN, is with Vocational School of Manisa Technical Sciences, Manisa, Turkey, (e-mail: [tugberk.ozmen@cbu.edu.tr](mailto:tugberk.ozmen@cbu.edu.tr)).

 <https://orcid.org/0000-0002-8636-6091>

NEVZAT ONAT, is with Department of Electrical and Electronics Engineering University of Manisa Celal Bayar University, Manisa, Turkey, (e-mail: [nevzat.onat@cbu.edu.tr](mailto:nevzat.onat@cbu.edu.tr)).

 <https://orcid.org/0000-0002-2244-4441>

Manuscript received October 28, 2020; accepted January 9, 2021.

DOI: [10.17694/bajece.817766](https://doi.org/10.17694/bajece.817766)

magnet synchronous generators (PMSG) which are used especially in wind turbines can be produced in different powers and designs. PMSG can be produced in different designs. In low power applications, PMSG with surface mounted magnets can be preferred due to its easy structure and reliability [2]. PMSG does not require DC supply for excitation circuit. This eliminates the need for rings and brushes. This is an important point that provides many technical and efficiency advantages. However, it is not possible to control the air gap magnetic flux in these machines. This situation creates difficulties in voltage stability control since it means that the speed and voltage output change linearly. In addition, permanent and fixed value magnetic fields can create security problems in many processes such as montage, technical work in the field, maintenance and repair. Thermal and technical problems arise in the production and physical processing of permanent magnets. The combination of the main magnetic field created by the permanent magnets on rotor and the armature reaction field causes the excessively increasing of magnetic flux density in the air gap and the saturation on the core. In these machines, the magnetic circuit must be modeled very well at the design stage and the geometries and material properties of permanent magnets which will be used in the magnetic circuit must be optimized. As mentioned above, it is not possible to change at later of parameters which are determined at the design stage. PMSGs provide significant advantages in small power applications thanks to these features, but do not offer suitable solutions for high power systems. In addition, it has some disadvantages such as high costs and having cogging torque due to its structure.

One of the torque components of PMSG is cogging torque which occurs due to the interaction between the stator slots and the permanent magnets in the rotor under no-load operation conditions. While the cogging torque can prevent rotation of wind turbines at low speeds, it also causes noise and vibration at PMSG. Therefore, studies are carried out to eliminate the cogging torque in PMSG.

Stator design improvements [3], alternative designs of surface-mounted permanent magnet motors [4] and embedded permanent magnet motors [5] are available in the literature to

reduce the cogging torque. The effects of magnet shape and geometries [6 and 7], of skewed and separated design of magnets [8], of using different magnet materials [9 and 10], of changing in magnet offset values [11] and magnet thickness [12] on machine performance have been investigated. The effects of magnet geometry on cost are also among the topics discussed in the literature [13]. The cogging torque is considered comparatively between the axial flux PMSM and the outer rotor PMSM [14] and between the PMSM and the induction motor [15]. Occurring errors during the manufacturing process in the stator slots of the machine, [16] and stator tooth geometries [17] affect the cogging torque. Designing the machine at a different ratio of poles/slots has an observable effect on the cogging torque [18]. Another issue examined in the literature is the effects of shifting magnets on the cogging torque of the change in the arc angle of the pole [19]. The shifting of the magnets and the change in the pole arc angle have effects on the cogging torque [19].

In this study, a 1500 W PMSG was used as a reference machine. The three-dimensional model of the machine was scaled and imported to the Rmxprt software. Performance of machine has been analyzed by simulating the no-load and nominal loaded operating conditions by using given label values by the manufacturer. The cogging torque and efficiency results were investigated by depending on the changes of the machine magnetic circuit. In this paper, cogging torque reducing methods has not been examined and the generator performance was examined by using only magnet structure and materials comparatively by making changes on the ratio of pole arc to pole pitch, magnet thickness and material of magnet of the reference machine.

## II. FINITE ELEMENT METHOD

To analyze a system as electromagnetically, the geometry is divided into finite number of small parts, the boundary conditions are defined and differential equations are written and then solved for each part. For the magnetostatic analysis in this study, ANSYS Maxwell 2D package program based on finite element method was used.

Maxwell's equations that describe how the electric and magnetic field behave are used in the background of ANSYS Maxwell software which is used in the analysis of electrical machines. An average magnetic flux density on the yoke of the stator was obtained as between 0.2 T and 0.9 T depending on the pole position in the magnetostatic analysis of the reference machine. Also, the magnetic flux density in the stator teeth is about 1.7 T on average.

## III. RMXPRT MODEL OF REFERENCE ELECTRICAL MACHINE

The design parameters of the PMSG used as reference in this paper are given in Table I, and the geometrical Rmxprt model of this generator is given in Fig. 1. Stator, rotor and magnet dimensions of the reference machine given in Table I are the values obtained from the measurements made with the caliper.

TABLE I  
THE DESIGN PARAMETERS OF THE PMSG

Design Parameters	Values
Nominal power	1500 W
Nominal speed	450 rpm
Number of slot	72
Number of poles	16
Stator outer diameter	221.5 mm
Rotor outer diameter	157.5 mm
Air gap distance	1 mm
Magnet material	NdFe35
Pole arc ratio	84.774 (%)
Skew ratio	1.5 mm
Magnet thickness	5.3196 mm
Offset distance	0 mm

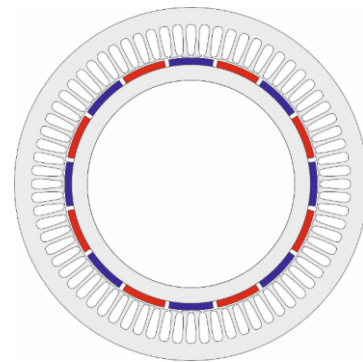


Fig.1. Slot and magnet structure of PMSG

With the Rmxprt analysis of PMSG used in this study, phase current was 12.42 A, phase voltage 40.66 V and efficiency value was obtained as 87% under nominal load operating condition. The same analysis, the stator tooth flux density was found as 1.8 T, the stator yoke flux density as 0.89 T, the air gap flux density as 0.88 T and the magnet flux density as 0.93 T under no-loaded operating conditions.

The graph of induced voltage in the stator windings for rated load of the reference PMSG is given in Figure 2. As can be seen in this figure, the voltage wave is not pure-sinusoidal shaped and the harmonic components of this voltage wave are shown in Figure 3.

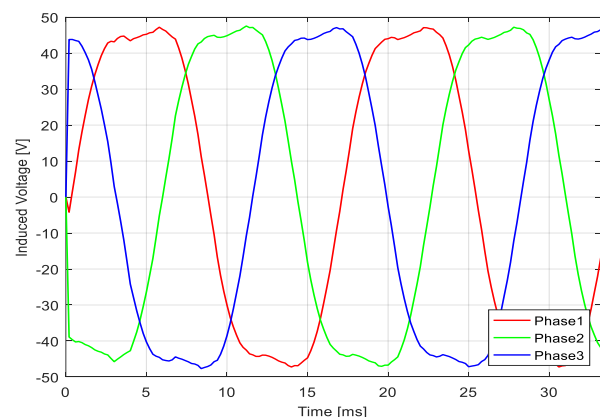


Fig.2. Induced voltage under rated-load conditions of PMSG

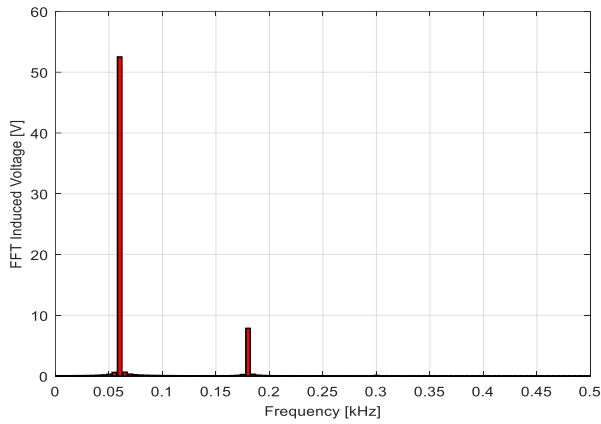


Fig.3. Harmonic spectrum of induced voltage of PMSG

IV. INVESTIGATION OF THE EFFECT OF DESIGN PARAMETERS

In this paper, the magnetic circuit geometry and material properties of the PMSG which was used as a reference, were changed and the effects on performance were examined. Analysis results given in section 3 are obtained by using magnet pole arc ratio and magnet thickness values and magnet material as given in Table I. In this section, the generator performance is comparatively examined for the values of magnet pole arc ratio between 0.80 and 0.95 and for values of magnet thickness between 5 mm and 6 mm and for using SmCo24, SmCo28 and NdFe35 as the magnet type. The effects of the change of these parameters on the cogging torque, air gap magnetic flux density and efficiency were determined. The drawing of the rotor of the reference machine used in the paper is given in Fig.4.

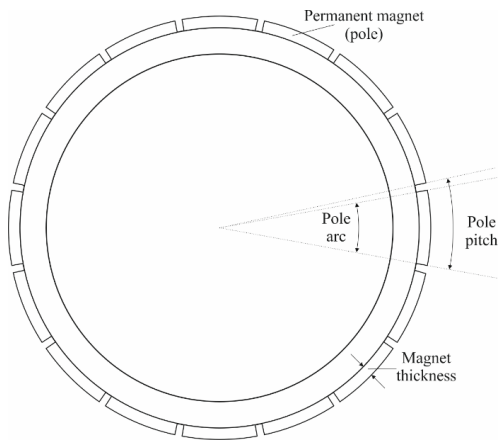


Fig.4. Detailed drawing of PMSG rotor

A. Ratio of Magnet Pole Arc to Pole Pitch

The cogging torque graph according to electrical angle obtained in the simulations made through the Rmxprt software depending on the change in the ratio of the pole arc to the pole pitch is given in Fig. 5, the air gap magnetic flux density graph is given in Fig. 6 and the numerical values found given in Table II. In the obtained results, it was observed that the increase in the ratio of pole arc to pole pitch from 80% to 95% cause an increase at the cogging torque and flux density in the

air gap. Especially for 90% and 95% values of pole arc to pole pitch ratio, increasing in the cogging torque reaches very high values. The effect of the changing in pole arc to pole pitch ratio on the air gap magnetic flux density is quite limited. On the other hand, the efficiency value decreased around to 3% for pole arc to pole pitch ratio.

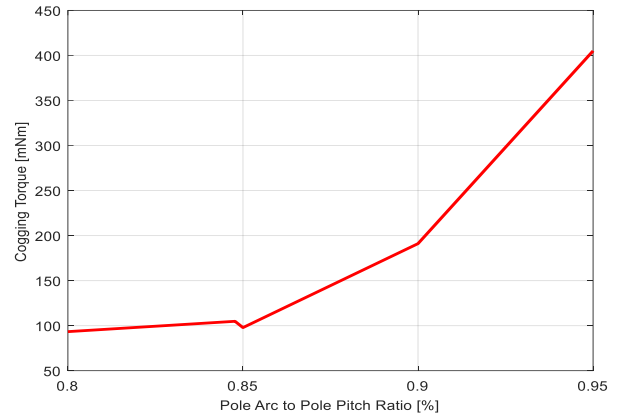


Fig.5. The effect of the change in the pole arc to pole pitch ratio on the cogging torque

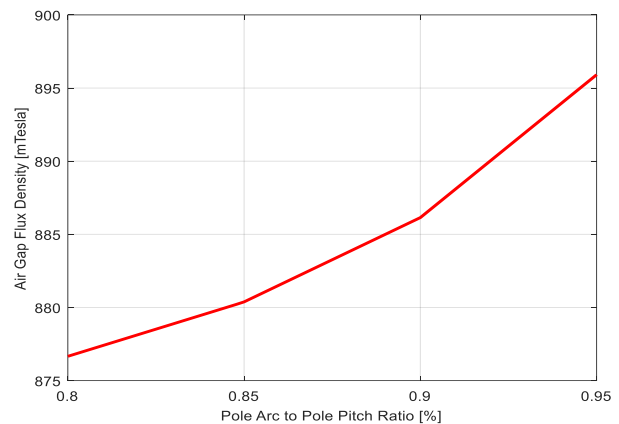


Fig.6. The effect of the change in the pole arc to pole pitch ratio on the air gap flux density

TABLE II  
THE EFFECT OF THE CHANGE IN THE POLE ARC TO POLE PITCH RATIO

Pole Arc to Pole Pitch Ratio (%)	Cogging Torque (Nm)	Air Gap Flux Density (mT)	Efficiency (%)
80,00	0,093	876,58	88,41
84,77	0,104	880,16	87,43
85,00	0,097	880,33	87,39
90,00	0,191	886,11	86,50
95,00	0,405	895,89	85,66

B. Thickness of Magnet

In the second step, the effects of the change in magnet thickness on the PMSG performance were examined by calculations made through the Rmxprt software. The obtained results are given in Fig. 7, Fig. 8 and Table III. It has been determined that when the magnet thickness is increased gradually up to a maximum of 20%, the cogging torque

decreased 6.9%. Despite this increase, the air gap flux density increased by 2,5%. Increasing in magnet thickness creates changes 1,5% in efficiency value.

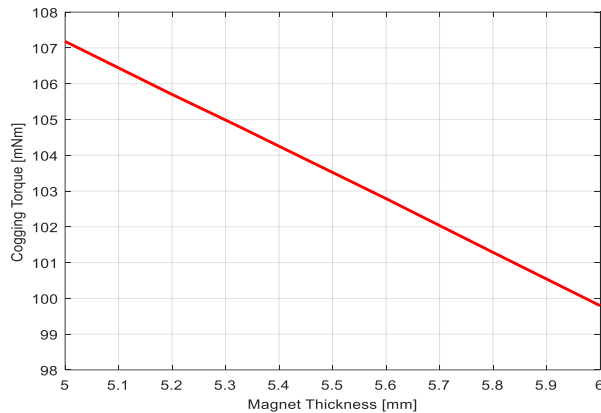


Fig.7. The effect of the change in the magnet thickness on the cogging torque

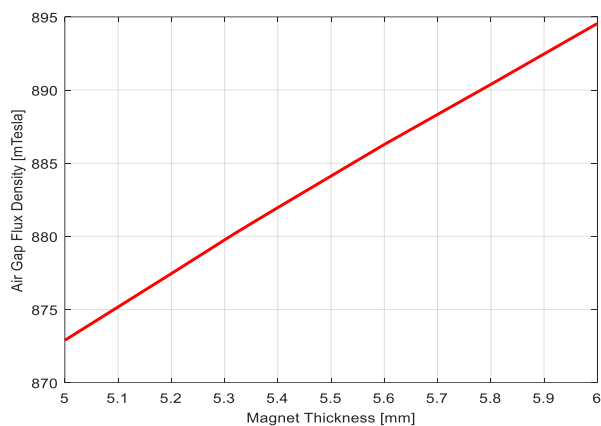


Fig.8. The effect of the change in the magnet thickness on the air gap flux density

TABLE III  
THE EFFECT OF THE CHANGE IN THE MAGNET THICKNESS

Magnet Thickness (mm)	Cogging Torque (mNm)	Air Gap Flux Density (mT)	Efficiency (%)
5,00	107,18	872,86	87,95
5,20	105,69	877,41	87,63
5,3196	104,84	880,16	87,43
5,40	104,25	881,91	87,31
5,60	102,78	886,21	86,99
5,80	101,28	890,3	86,69
6,00	99,79	894,45	86,39

### C. Magnet Material

Different materials have been using as a permanent magnet in PMSG such as AlNiCo, NdFe, Ferrit, SmCo. There are differences of these materials between the demagnetization values, coercivity force values and the maximum values of multiplication of magnetic field strength and magnetic flux density. Therefore, the application should be considered when choosing the magnet. In this paper, effects of magnet materials on cogging torque, air gap magnetic flux density and efficiency were investigated by using SmCo24, SmCo28 and

NdFe35 magnets. In this study, NdFe35 and SmCo magnets were preferred because they have superior magnetic properties compared to AlNiCo and Ferrite type magnets. Used magnets' some magnetic values get from the library of ANSYS Maxwell software are given in Table IV.

TABLE IV  
MAGNETIC PROPERTIES OF USED MAGNET MATERIALS

	NdFe35	SmCo24	SmCo28
Relative permeability	1,099	1,063	1,038
Bulk conductivity (S/m)	625.000	1.111.111	1.111.111
H magnitude (A/m)	890.000	756.000	820.000

In Fig. 9, the cogging torque curves of NdFe35, SmCo24 and SmCo28 are given together obtained from the calculations made over Rmxprt software. The air gap flux density curve obtained for these three types of magnets with the calculations is given in Fig. 10. The obtained results are given in Table V. NdFe35 provides the highest air gap flux density and the cogging torque value highest when this magnet is used. Similarly, when SmCo24 magnet is used, the cogging torque and air gap flux density values are the lowest compared to other magnet materials. From this point of view, besides some advantages of magnet materials, there are also disadvantageous parameters. In this study that three different materials discussed, changes such as 5% in efficiency, 16% in air gap flux and 34,5% in cogging torque occur. Therefore, it is important to choose the magnet material according to the functions expected from the machine.

M19-29G steel material is used as core material of the machine used as a reference in this paper. B-H curve for the material M19-29G is given in Fig. 11. This curve loses its linearity after about 1.8 T and the material will begin to saturate. It is necessary to design a magnetic circuit in which values below the saturation point will be obtained. For this reason, the flux distribution in the core material depending on the magnet material of the machine was also examined. Magnetic flux distribution graphs obtained as a result of magnetostatic analysis of the machine are given respectively in Fig.12, Fig.13 and Fig.14 for SmCo24, SmCo28 and NdFe35 magnets.

When the flux distributions of magnetostatic analysis are examined, the difference in the flux densities in the stator teeth is observed when only the magnet types are changed for the same machine geometry. For the same machine, when SmCo24 and SmCo28 type magnets are used, the pole thickness parameter should be increased to obtain higher efficiency and air gap flux. The magnetic flux density is higher when NdFe35 magnet is used. This results in an increase in efficiency and cogging torque also increases. Flux density values are below the saturation point for all three materials are used. In this respect, it can be said that the selected steel sheet model is suitable in terms of design.

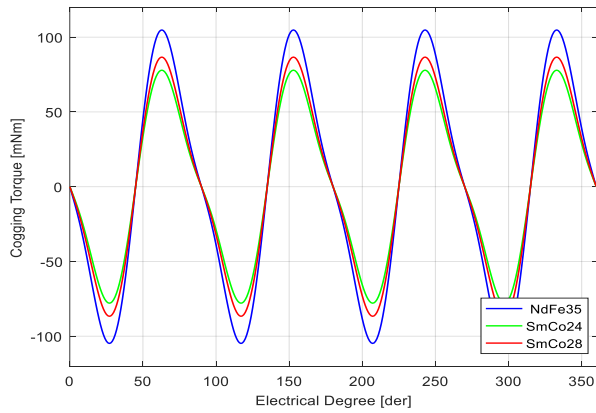


Fig.9. The effect of different magnet materials on the torque

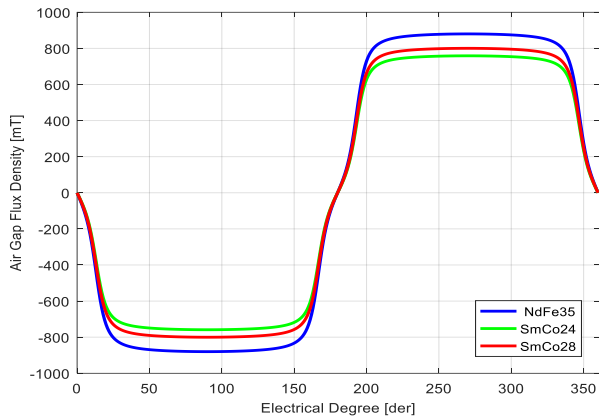


Fig 10. The effect of different magnet materials on the air gap flux density

TABLE V  
THE EFFECT OF DIFFERENT MAGNET MATERIALS

Magnet Material	Cogging Torque (mNm)	Air Gap Flux Density (mT)	Efficiency (%)
SmCo24	77,91	758,81	83,64
SmCo28	86,67	800,32	86,18
NdFe35	104,84	880,16	87,43

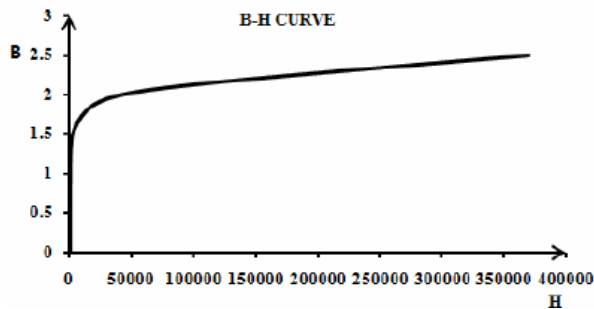


Fig 11. B-H curve of M19-29G [20]

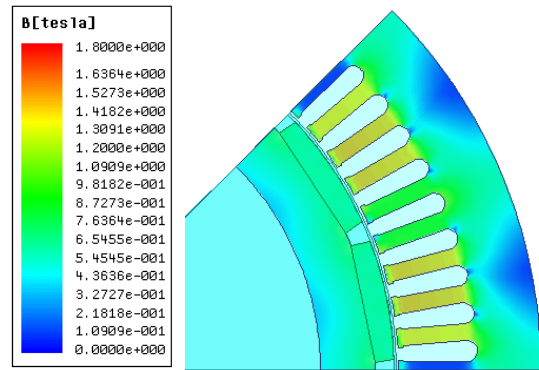


Fig.12. Flux density of magnetostatic analysis of machine when used SmCo24 magnet

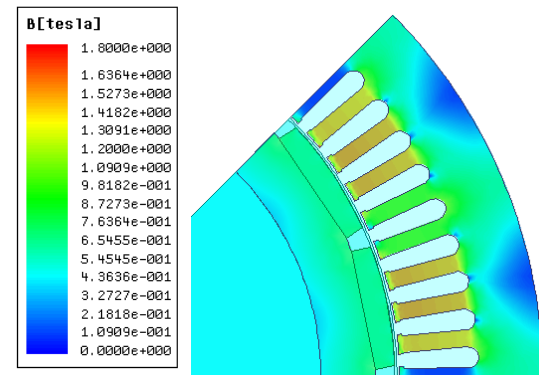


Fig.13. Flux density of magnetostatic analysis of machine when used SmCo28 magnet

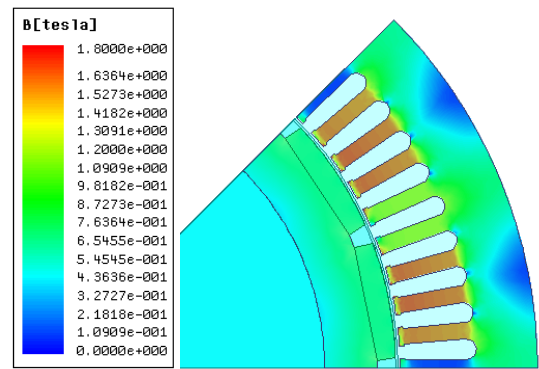


Fig.14. Flux density of magnetostatic analysis of machine when used NdFe35 magnet

In order to increase the performance of the PMSG which is used as a reference in this study, an optimization approach has been made over the examined magnetic circuit parameters. NdFe35 has been used as the magnet material and the magnet thickness has selected as 6 mm and the pole arc to pole pitch ratio has selected as 0.85. In this case, the change in the analyzed performance parameters has given in Table VI. Thanks to the improvement, the efficiency of the PMSG was increased by 1.01%, the air gap flux density was increased by 1.66% and the cogging torque was reduced by 11.59%.

TABLE VI  
EFFECTS OF REFERENCE AND OPTIMIZED KMSG

	Reference KMSG	Optimized KMSG
Cogging Torque (mNm)	104,84	92,69
Air Gap Flux Density (mT)	880,16	894,76
Efficiency (%)	87,43	88,31

## V. CONCLUSION

In this paper, the effects of some design parameters such as the ratio of pole arc to pole pitch, magnet thickness and type of magnet materials, on the cogging torque, air gap flux density and efficiency of PMSG were investigated. Using the obtained results, new values of PMSG parameters have been presented for better output performance.

When the value of pole arc ratio increased from 80% to 95%, the cogging torque increased from 0.093 Nm to 0.405 Nm. Air gap flux density value increased, and the efficiency value decreased with increasing in pole arc ratio. The increase of the pole arc ratio can be decided according to the usage purpose of the machine. In applications where high cogging torque is required, being high in this ratio may be an advantage. However, it should be taken into account that the increase in the pole arc ratio is a disadvantage in terms of energy efficiency. The increase in magnet thickness results in a decrease in the cogging torque and it caused an increase in the amount of flux in the air gap. The efficiency decreased when magnet thickness is increase. Increasing the magnet thickness does not provide an advantage in terms of general parameters. Both the cogging torque and the decrease in efficiency are remarkable in this respect. However, the effects of increasing the magnet thickness on the torque ripple may be examine in different study.

In order to examine the effects of the used magnet materials on machine performance; SmCo24, SmCo28 and NdFe35 type magnets have analyzed using on the same reference machine. In the analysis, the highest values of efficiency and air gap flux density are obtained for NdFe35 magnet, on the other hand, the cogging torque value for this magnet is obtained higher compared to other types of magnets. In the analysis, although the cogging torque value for SmCo24 magnet was low, efficiency and air gap flux density values were also obtained at the lowest value. As a result of the magnetostatic analysis, the magnetic flux density value in the stator teeth of PMSG was obtained as approximately 1.3 T when SmCo24 magnet was used, 1.5 T when SmCo28 magnet was used, and 1.8 T when NdFe35 magnet was used. With the optimization approach made on the magnetic circuit parameters, the cogging torque was reduced, the air gap flux density and efficiency values were increased. In the selection of the magnet by using the above results, the purpose of use of the PMSM and the expected performance, cost, etc. factors can be considered.

As a continuation of the study, the effects of the examined parameters on the PMSG performance will be examined and interpreted under loaded operating conditions and failure conditions and the results of the experiments to be made with the real machine model will be compared.

## REFERENCES

- [1] M. Güleç, E. Yolacan, Y. Demir, O. Ocak, M. Aydın. "Modeling based on 3D finite element analysis and experimental study of a 24-slot 8-pole axial-flux permanent-magnet synchronous motor for no cogging torque and sinusoidal back-EMF." *Turkish Journal of Electrical Engineering & Computer Sciences*, vol. 24, 1, 2016, pp 262-275.
- [2] H. Li, Z. Chen. "Design optimization and site matching of direct-drive permanent magnet wind power generator systems." *Renewable Energy*, vol. 34, 4, 2009, pp 1175-1184.
- [3] D. Uygun, Y. Çetinçeviz. "Yüzey yerleştirmeli kalıcı mıknatıslı senkron generatörlerin tutma torkunun azaltılması için stator yapılandırması." *Gazi Üniversitesi Fen Bilimleri Dergisi Part C: Tasarım ve Teknoloji*, vol. 6, 3, 2018, pp 605-620.
- [4] N. Bianchi, S. Bolognani. "Design techniques for reducing the cogging torque in surface-mounted PM motors." *IEEE Transactions on industry applications*, vol. 38, 5, 2002, pp 1259-1265.
- [5] Z. Q. Zhu, S. Ruangsinchaiwanich, N. Schofield, D. Howe. "Reduction of cogging torque in interior-magnet brushless machines." *IEEE Transactions on Magnetics*, vol. 39, 5, 2003, pp 3238-3240.
- [6] G. C. Lee, S. H. Kam, T. U. Jung. "Design on Permanent Magnet Structure of Radial Flux Permanent Magnet Generator for Cogging Torque Reduction and Low Torque Ripple." *16th European Conference on Power Electronics and Applications, Lappeenranta, Finland, 2014.*
- [7] Z. Li, J. H. Chen, C. Zhang, L. Liu, X. Wang. "Cogging Torque Reduction in External-Rotor Permanent Magnet Torque Motor Based on Different Shape of Magnet." *2017 IEEE International Conference on Cybernetics and Intelligent Systems (CIS), China, 2017.*
- [8] A. Dalcalı, E. Kurt, E. Çelik, N. Öztürk. "Cogging torque minimization using skewed and separated magnet geometries." *Politeknik Dergisi*, vol. 2, 3, 2020, pp 223-230.
- [9] A. Dalcalı, C. Ocak. "Farklı mıknatıs malzemelerinin yüzey mıknatıslı doğrudan tahrikli sabit mıknatıslı senkron motor performansına etkisi." *Journal of Awareness*, vol. 3, Special, 2018, pp 217-224.
- [10] H. Mamur. "Performance evaluation for a PMSG with interior rotor of N35 and N42 NdFeB PMS having same geometry in micro wind turbines." *International Journal of Energy Applications and Technologies*, vol. 3, 2, 2016, pp 50-54.
- [11] A. N. Patel. "Cogging Torque Minimization by Magnet Edge Inset Variation Technique in Radial Flux Surface Mounted Permanent Magnet Brushless DC (PMBLDC) Motor." *5th Nirma University International Conference on Engineering (NUiCONE), Gujarat, India, 2015.*
- [12] B. Vidhya, K. N. Srinivas. "Effect of stator permanent magnet thickness and rotor geometry modifications on the minimization of cogging torque of a flux reversal machine." *Turkish Journal of Electrical Engineering & Computer Sciences*, vol. 25, 6, 2017, pp 4907-4922.
- [13] C. Ocak. "Doğrudan tahrikli asansör sistemlerinde kullanılan sabit mıknatıslı senkron motorlarda mıknatıs geometrisinin motor performansı ve maliyeti üzerindeki etkilerinin incelenmesi." *Mühendislik Bilimleri ve Tasarım Dergisi*, vol. 7, 4, 2019, pp 825-834.
- [14] A. Aksöz, A. Saygın. "Aynı fiziksel ve elektromanyetik parametreler altında EASMSM ve ORSMSM'un vuruuntu torkuna göre karşılaştırılması." *Gazi Üniversitesi Fen Bilimleri Dergisi Part C: Tasarım ve Teknoloji*, vol. 6, 3, 2018, pp 659-667.
- [15] H. Yetiş, T. Gökaş. "Comparative design of permanent magnet synchronous motors for low-power industrial applications." *Balkan Journal of Electrical and Computer Engineering*, vol. 8, 3, 2020, pp 218-224.
- [16] E. Çetin, F. Daldaban. "Eksenel akılı motorlarda oluk açıklıklarındaki hatanın moment üzerine etkisi." *El-Cezeri Fen ve Mühendislik Dergisi*, vol. 4, 3, 2017, pp 374-381.
- [17] A. Gündoğdu, R. Çelikel, and Ş. Fidan. "Analysis and Simulation of A Three-Phase Delta Inverter for A Star-Connected RL Load." *European Journal of Technique* 10.2, 2020, 274-288.

- [18] C. Ocak. "Design and performance comparison of four-pole brushless DC motors with different pole/slot combinations." *The International Journal of Energy and Engineering Sciences*, vol. 3. 3, 2018, pp 69-78.
- [19] L. Dosiek, P. Pillay. "Cogging torque reduction in permanent magnet machines." *IEEE Transactions on industry applications*, vol. 43. 6, 2007, pp 1565-1571.
- [20] R. Jayapragash, C. Chellamuthu. "Development of analytical models for switched reluctance machine and their validation." *Journal of Electrical Engineering & Technology*, vol. 10. 3, 2015, pp 990-1001.

### BIOGRAPHIES



**TUGBERK OZMEN** graduated from department of Electrical Engineering at Istanbul Technical University, in 2015. He worked some companies in the field of renewable energies and photovoltaic power plants until 2018. He started to work in Vocational School of Manisa Technical Sciences, in 2018. His M.Sc. continues at Manisa Celal Bayar University in department of Electrical and Electronics Engineering.



**NEVZAT ONAT** graduated from department of Electrical Education at Marmara University, in 1995. He received his M.Sc. and Ph.D. degrees in Electrical Education from Marmara University, Istanbul, Turkey in 1999 and 2005 respectively. He worked at Marmara University between 1997 and 2015. He has been working at Manisa Celal Bayar University since 2015. Nevzat Onat has been the Dean of Manisa Celal Bayar University Technology Faculty since 2019. His research interests include electrical machines, protection in power systems and photovoltaic systems.

# Design, Simulation and Application of Buck Converter with Digital PI Controller

Hasan Sucu, Taner Goktas, Muslum Arkan

**Abstract**—In this paper, a dc-dc buck converter with digital PI-controlled is analyzed and designed considering all design parameters such as inductance current variation, output voltage ripple etc. The designed dc-dc buck converter provides stable output voltage against to load changes and output voltage variations. Buck converter control method relies on voltage mode controlled PWM (Pulse width Modulation) with digital PI (Proportional Integral) controller. The design criteria, operating mode selection, suitable material selection, etc. of low cost and high-performance buck converter are explained in detail. Finally, the designed converter is carried out experimentally and the experimental results shows the effectiveness of designed converter under different load profiles.

**Index Terms**—Buck Converter, PWM (Pulse Width Modulation), digital PI controller (Proportional Integral), voltage mode controller.

## I. INTRODUCTION

WITH THE widespread use of renewable energy sources, it is obvious that dc microgrid networks and smart home systems will take place more in our lives in the future. In addition, with the developments in battery technology, the number of electric vehicles and portable devices is constantly increasing. It seems that dc voltage is the trend of the future. Thus, high quality, reliable, adaptable and efficient DC voltage conversion is of great importance.

Buck converters, one of the circuits widely used for dc voltage conversion in power electronics applications, reduce the input dc voltage at the rate of duty cycle. These types of converters are widely used in motor drive applications [1], electric vehicle charging stations [2], li-ion battery supplied application [3], led lamp driver applications [4], dc micro-grid applications [5], wind energy systems [6], photovoltaic systems [7], server applications [8]. Their important advantages are that

they can be designed at high powers, be highly efficient and have a low price/performance ratio.

Buck converters generate output voltage by switching methods called pulse width modulation (PWM) and pulse frequency modulation (PFM). While frequency modulation technique is used in low load conditions under  $50mA$ , pulse width modulation technique is generally used in heavy load conditions over  $100mA$  [9-10]. In the pulse width modulation technique, the semiconductor power switch is switched in the specified duty cycle by keeping the switching frequency constant.

However, changes in input voltages and output load and nonlinear properties of circuit elements make it difficult to obtain a constant output voltage in a constant duty cycle in open loop dc to dc converters. Therefore, a feedback loop is required to achieve output voltage regulation with fast line and load transient response. Buck converters are classified into voltage mode and current mode according to the feedback control loop [11]. Compensation circuits are used because simple control loops will drive the circuit to oscillation. Compensation circuits can be implemented as analog or digital to improve the stability and transition time [12]. The digital controller has some abilities such as faster switching, easy to implementing algorithm etc. [13-14]. Digital control is applied through the Microprocessors, *FPGA* (Field Programmed Gates Array) and Custom *IC* Design.

Linear control methods such as *PI* control [15] and nonlinear control methods such as sliding mode [16] and fuzzy logic [17] are used to ensure stability in output voltage. Each of these control methods for various applications has some advantages and disadvantages in itself. Classical linear feedback is most commonly used for duty cycle control, especially the well-known *PID* control [18]. The dynamic and steady state response are effective in *PID* control method. [19]. On the other hand, linear controllers like *PI/PID* are easy to design and implement in real physical systems and a well-tuned *PI* controller in the buck converter will provide good performance [20].

In this study, the analysis, selection of design parameters, control, simulation and experimental application of a about  $10\text{ Watt}$  microcontroller based buck dc-dc converter are conducted. Dynamic performance features such as high efficiency and low output current ripple have been taken into account in the converter design. The designed converter is analyzed in *MATLAB@Simulink* environment and the compatibility of the simulation results with the design parameters are checked. Using the *Altium Designer* program,

**HASAN SUCU** is with Department of Electricity, Arapgir Vocational High School, University of Malatya Turgut Ozal, Malatya, Turkey, (e-mail: [hasan.sucu@ozal.edu.tr](mailto:hasan.sucu@ozal.edu.tr)).  <https://orcid.org/0000-0002-5061-4735>

**TANER GOKTAS** is with Department of Electrical and Electronics Engineering University of Inonu University, Malatya, Turkey (e-mail: [taner.goktas@inonu.edu.tr](mailto:taner.goktas@inonu.edu.tr)).  <https://orcid.org/0000-0002-8218-3239>

**MUSLUM ARKAN** is with Department of Electrical and Electronics Engineering University of Inonu University, Malatya, Turkey (e-mail: [muslum.arkan@inonu.edu.tr](mailto:muslum.arkan@inonu.edu.tr)).  <https://orcid.org/0000-0001-5313-2400>

Manuscript received February 21, 2021; accepted March 15, 2021.  
DOI: [10.17694/bajece.884290](https://doi.org/10.17694/bajece.884290)

the converter PCB-card design is realized. The Texas Instrument *TMS320F28379D series DSC* control card is used for digital *PI* control. The accuracy of the design criteria and simulation results are proved with the experimental results.

II. ANALYSIS OF BUCK CONVERTER AND DETERMINATION OF DESIGN PARAMETERS

The basic circuit diagram for the dc-dc buck converter with an output voltage lower than the input voltage is shown in Fig.1. In the first stage of the design, it is necessary to determine the operating modes and circuit parameters. As it is known, in switching mode converters operate continuously, discontinuously and in threshold conditions depending on whether the inductance current falls to zero or not. Since the inductance current does not decrease to zero in a converter operating in a continuous current mode, the output-inductance current ripple may be at a lower value compared to other operating modes. In the discontinuous current mode, it has advantages in terms of absorbing the energy in inductance, especially at high powers.

In a buck converter operating in continuous current operating mode, as it is seen in Fig.2, when the *S*-switch is in on state, the diode will switch off because the diode is reverse polarized and during this time (*DT*) input circuit will provide energy to both the load and the inductance and the inductance current will increase with a certain slope (See. Fig.1a). When the *S*-switch is in *off* state, the voltage on the inductance will change direction (*1-D*) and the inductance current will provide current to the output during *T* and complete its circuit through the diode. (See Fig.1b). Since the average capacitor current in steady state is zero (open circuit with direct voltage), the average inductance current is equal to the average output current. Where *D* represents duty cycle and *T* represents the switching period. The voltage falling on the inductance is equal to the difference between the input voltage (*V<sub>i</sub>*) and the output voltage (*V<sub>o</sub>*) when the switch is in on state. The voltage falling on the inductance is equal to the *-V<sub>o</sub>* voltage when the switch is in off state.

In the converter operating in continuous current mode, there is an equivalence as in Eq. (1) between the output and the input voltage, by taking advantage of the fact that the energy accumulated in the inductance and the energy consumed in the inductance in the ideal situation are equal to each other and the average inductance voltage is zero.

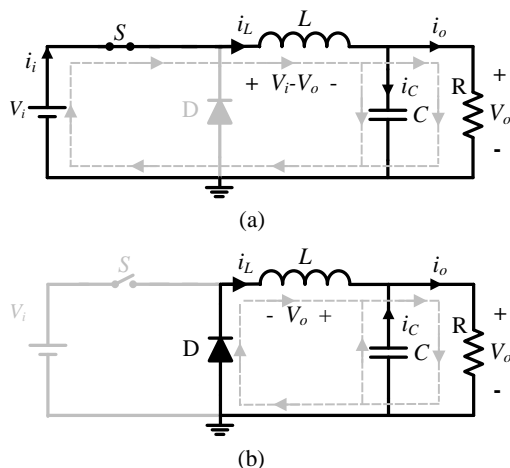


Fig.1. Buck converter basic circuit diagram

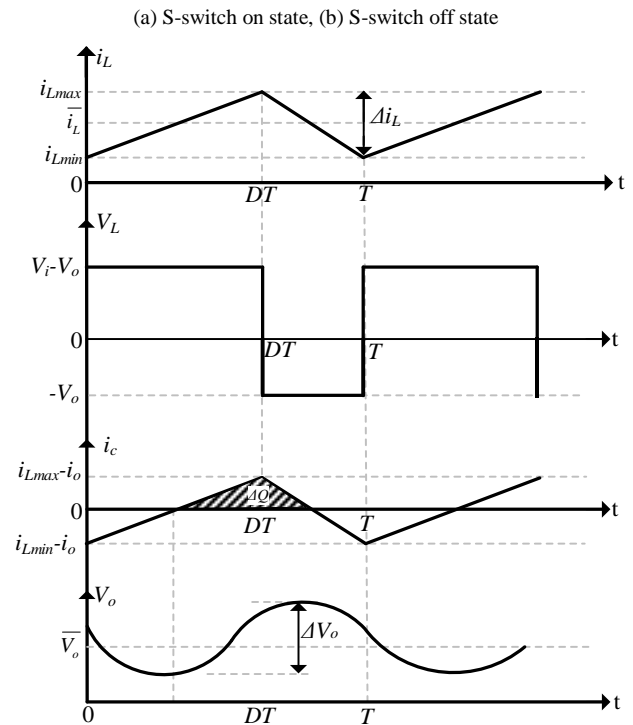


Fig.2. Analysis graphics of the buck converter [12]

TABLE I. BUCK CONVERTER DESIGN PARAMETERS

Parameters	Value
Input voltage, <i>V<sub>i</sub></i>	48
Output voltage, <i>V<sub>o</sub></i>	12
Switching frequency, kHz	100
Output power, <i>W</i>	9.6
Output voltage fluctuation, $\Delta V_o/V_o$	0.05

TABLE II. BUCK CONVERTER COMPONENTS VALUE

Parameters	Value
Load resistor, $\Omega$	15
Inductance, $\mu H$	100
Output Capacitor, $\mu F$	26

$$V_o = DV_i$$

$$D = \frac{t_{on}}{T} \tag{1}$$

Here, the *t<sub>on</sub>* indicates the time the switch remains in transmission. As seen in Eq. (1), there is a ratio between the output voltage and the input voltage as much as the duty cycle ( $0 < D < 1$ ). Since the duty cycle is less than 1, the output voltage will always be lower than the input.

The design criteria of the buck converter operating in continuous current mode with a power of approximately 10 Watt are given in Table I. By selecting the high switching frequency, the dimensions of the components to be used in the circuit are kept low.

Considering the parameters in Table I, the duty cycle  $D = 0.25$  and the output resistance is  $R = 15\Omega$ . The minimum

inductance ( $L_{min}$ ) value required for the converter to operate in continuous current mode can be calculated by Eq. (2) [21]:

$$L_{min} = \frac{(1-D)R}{2f} = 56.25\mu H \quad (2)$$

A converter operating at  $L_{min}$  value calculated in Eq. (2) operates under threshold condition. A value slightly larger than this specified value should be selected to operate in continuous current mode. In the design, this value was increased by 25% and the inductance value in Eq. (3) was determined.

$$L = 1.25 \times L_{min} = 70.31\mu H \quad (3)$$

The inductance current ripples depends on the inductance voltage and the inductance value. If the inductance current ripple is calculated considering the time the switch remains in conduction:

$$\Delta i_L = \left( \frac{V_i - V_o}{L} \right) DT = 1.28 A \quad (4)$$

Depending on this ripple amount ( $\Delta i_L$ ), the maximum inductance current and minimum inductance current can be easily calculated as in Eq. (5) and in Eq. (6) by considering the inductance current waveform in Fig. 2.

$$I_{L,max} = \bar{I}_L + \frac{\Delta I_L}{2} = 1.44A \quad (5)$$

$$I_{L,min} = \bar{I}_L - \frac{\Delta I_L}{2} = 0.16A \quad (6)$$

Buck converter output voltage ripple should generally be less than 1%. Since the inductance current ripples are also seen in the capacitor current, the capacitor value that ensures the output voltage ripple ( $\Delta V_o / V_o$ ) to be at the desired value can be calculated as in Eq. (6) [20]:

$$C_o = \frac{1-D}{8L(\Delta V_o / V_o)f^2} = 26 \mu F \quad (7)$$

The values calculated for the components to be used in the circuit are combined in Table II.

Considering the circuit design criteria and design parameters, the values of the elements used in the circuit in a basic buck converter operating in continuous current mode were determined. In the next section, closed loop control of the Buck converter is explained.

### III. VOLTAGE MODE CONTROLS OF BUCK CONVERTER

The block diagram of the voltage mode digital  $PI$  controlled buck converter consisting of power and feedback stages is shown in Fig.3. Voltage mode control is based on sensing the output voltage. Output voltage  $V_o$  is sensed and converted by a signal conditioning circuit to a suitable voltage value for the analog input channel and applied into the  $DSP$  via the analog input channel. The sensed output voltage digitized by ADC is compared with the reference voltage  $V_{ref}$ . The obtained error  $e[n]$  is tried to be minimized by  $PI$  control. The output  $K_2e[n]$  of this controller is used to generate duty cycle in  $DPWM$

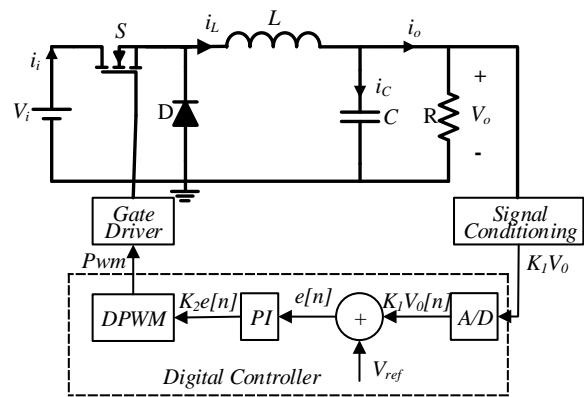


Fig.3. Digitally controlled buck converter block diagram

module.  $DPWM$  is used as a  $D/A$  converter to provide the duty cycle and generates  $PWM$  signal. The  $PWM$  is used to turn the switch on and off through the driver.

The close loop controller is designed to ensure that the output voltage  $V_o$  follows the reference voltage  $V_{ref}$ .  $PI$  control is widely used for feedback control in buck converters due to its easy implementation and low cost.  $PI$  control can be defined by the following transfer function.

$$u(t) = K_p e(t) + K_i \int_0^t e(\tau) d\tau \quad (8)$$

Here  $u(t)$  represents the control signal and  $e(t)$  the error.  $K_p$  represents the proportional gain and  $K_i$  the integral gain. The proportional term aims to reduce the error by multiplying the error coming from the system with a coefficient. For a small error in large values of  $K_p$  there may be large variations in output. This may cause system instability. Compensation for input distortions is slow at small values of  $K_p$ . This causes delayed regulation of the controller. This is undesirable in most applications [12]. Integral means finding the area of the error. In each duty cycle, the error is summed by multiplying the coefficient  $K_i$ . The integral term reduces the small error left from the proportional controller. The performance of a closed loop converter is highly affected by the controller parameters. Methods such as empirical methods, analytical methods, methods based on optimization are developed in the literature to set the  $K_i$  and  $K_p$  parameters.

Microcontroller is used to generate the  $PWM$  signal in digitally controlled switched power supplies. The amplitude of the  $PWM$  signal generated by the microcontroller is low. For this reason, a driver circuit should be used between the  $PWM$  output of the microcontroller and the gate of the power switch to charge and discharge the gate capacitance of the high side switch. This driver circuit will increase the voltage in the 0-5V range at the microcontroller output to the required voltage level for switching [22]. The gate driver is important for fast switching of the power element, reducing power losses associated with switching, and reducing parasitic capacitances at switch nodes. In addition, the use of a gate driver will protect the microcontroller from voltage spikes and noise, and at the same time, the gate load will reduce power losses and thermal stress in the microcontroller by moving the power losses from the microcontroller to the drive [23-24].

Driving techniques such as floating supply gate drive, transformer coupled drive, charge pump drive, bootstrap drive can be used in buck converters to switch the semiconductor power switch [25-26]. However, the most appropriate solution for driving semiconductor power switches in buck converters is to use the bootstrap drive circuit in terms of cost and simplicity [23].

#### IV. SIMULATION MODEL AND RESULTS

In order to verify the efficiency of the designed digitally controlled buck converter, the *Matlab @ Simulink* model in Fig.5. is created before its experimental implementation. The simulation model has circuit parameters based on Table I and Table II. The simulation model has been operated under full load conditions, continuous current mode, closed loop control. In the simulation model, suitable oscilloscopes are used to observe the inductance current, inductance voltage, output current, input and output voltages.

In the simulink model, the output voltage is detected and compared to the 12V reference voltage. The obtained error is tried to be minimized by *PI* control. *PI* control parameters  $K_i$  and  $K_p$  can be determined using *PID* tuning tool in *Matlab @ Simulink*.  $K_p$  value is 0.02752 and  $K_i$  value is 8.1185. The saturation block limits the error signal at the output of the *PI* control to the upper and lower saturation values. The saturation block output is compared with the sawtooth waveform generated from the repeating sequence block to determine the duty cycle. The frequency of the sawtooth waveform corresponds to the desired converter switching frequency 100kHz. Mosfet switches when the error value is greater than the triangular wave. With the step block, the switch is activated 0.03 seconds after the operating moment, the load of the circuit is increased to 20W and the output voltage response of the circuit against load changes is observed.

Fig.4. shows the results of the simulation model created. As

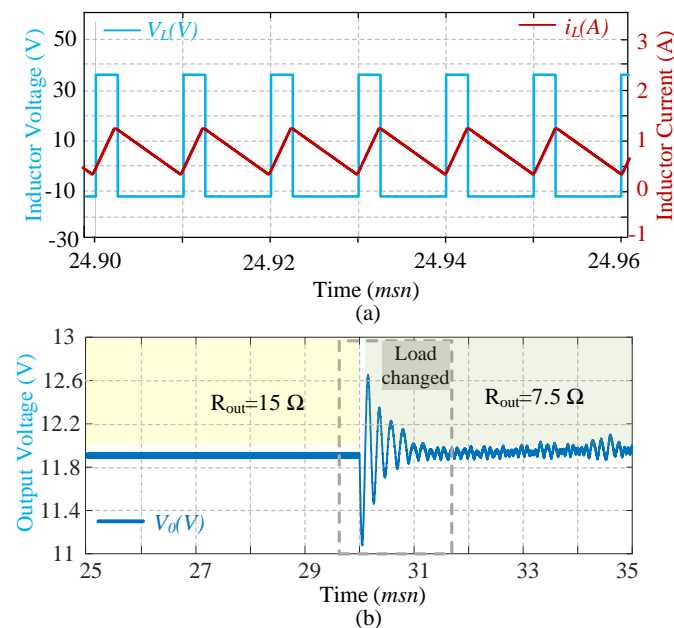


Fig.4. Simulink Results

(a) Inductance voltage and Inductance current (b) Output voltage

TABLE III.  
RISE TIME AND OVERSHOOT VALUE FOR DIFFERENT  $K_p$  AND  $K_i$  VALUES

Parameters	Rise time (Sn)	Overshoot (V)
$K_p = 0.02752, K_i = 8.1185$	0.022	5.1
$K_p = 0.05504, K_i = 8.1185$	0.015	6.8
$K_p = 0.01376, K_i = 8.1185$	0.030	3.4
$K_p = 0.02752, K_i = 16.237$	0.011	5.3
$K_p = 0.02752, K_i = 4.05925$	0.041	5.0

seen in Fig.4a, while the switch is in on state, the inductance current increases at a certain slope, it decreases when the switch is off state. In addition, inductance current ripple is approximately the same as design values calculated in Eq. (5) and in Eq. (6) and the current value is always greater than zero. This situation indicates that the designed converter works in continuous current mode. Fig.4b. shows the output voltage. It is seen at the output by decreasing the input voltage at the rate of duty cycle. When the load is increased to 20W, it is seen that the *PI* controller ensures the output voltage stability. The ripple in the output voltage is reduced to the value specified in Table II with the appropriate capacitor value.

The simulation results of the rise time and overshoot value of the output voltage for different values of  $K_p$  and  $K_i$  are given in Table III.  $K_p = 0.02752$  and  $K_i = 8.1185$  are used as reference values. First, the  $K_i$  value are kept constant and overshoot and rise time are observed for half and twice the  $K_p$  value. Afterwards, the  $K_p$  value are kept constant and overshoot and rise time are observed for half and twice the  $K_i$  value. It is seen from the simulation results that when  $K_p$  value is increased by keeping  $K_i$  value constant, rise time decreases and overshoot increases, and when  $K_p$  value is decreased, rise time increases and overshoot decreases. In addition, when the  $K_i$  value is increased by keeping the  $K_p$  value constant, it is seen that the rise time decreases and the overshoot increases, and when the  $K_i$  value is decreased, the rise time increases and the overshoot decreases.

#### V. EXPERIMENTAL SETUP AND RESULTS

In order to experimentally examine the dynamic performance of the designed converter, an experimental circuit setup consisting of the input power source, the designed buck converter and the microcontroller was established. Fig.6. shows the designed buck converter and circuit setup. *TI-C2000* series *F28379D* DSC control card, one of the high-performance microcontrollers of Texas Instruments was used to perform the voltage mode digital *PI* control of the buck converter. By using the output voltage applied to the analog inputs of this card, the duty cycle is adjusted in software and hardware. In addition, the *PWM* signal, inductance current and output voltage were observed using a digital oscilloscope.

The circuit block diagram of the digital voltage mode controlled buck converter is shown in Fig.7. It consists of five section. The 48V-12V section provides the + 12V voltage required for the mosfet driver supply and the 12V-3.3V section provides the + 3.3V voltage required for the opamp driver circuit supply.

The signal conditioning circuit consisting of voltage divider resistor circuit and voltage follower opamp circuit is used to

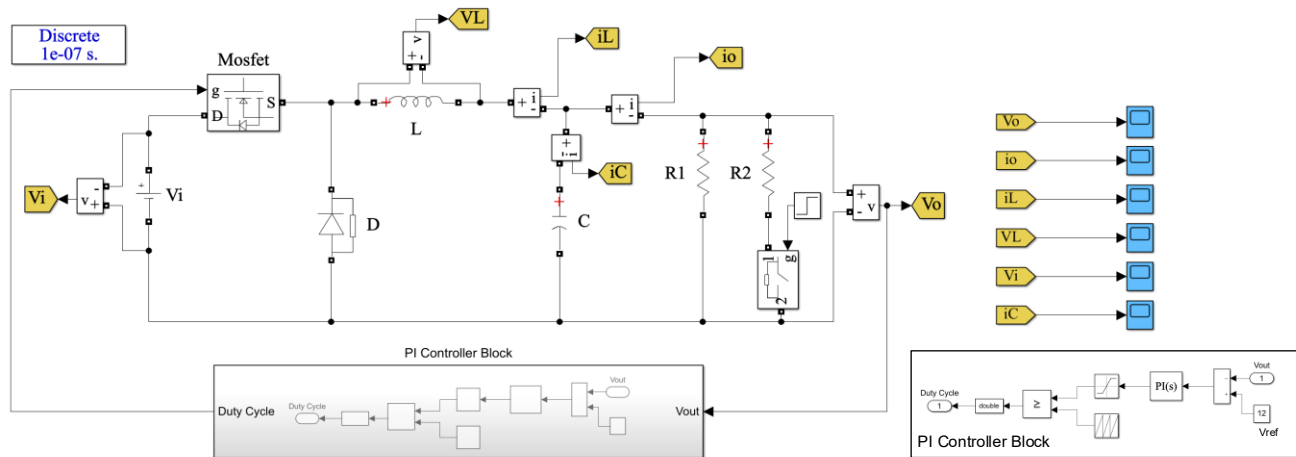


Fig.5. Digitally Controlled Buck Converter, Matlab @ Simulink Model

convert the output voltage to suitable voltage values for the ADCIN channels of the TMS320F28379D DSP and to protect the ADCIN channels of the TMS320F28379D DSP. The output voltage is detected and applied to the analog input channel of the DSP. The analog input voltage applied to the ADCIN channels of the TMS320F28379D DSP needs to be kept in the range of 0V-3.3V. For this purpose, in voltage mode control, the output voltage  $V_o$  is scaled by a voltage divider resistors circuit.

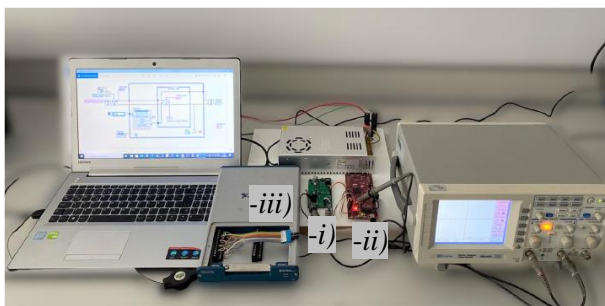
Since the feedback voltage is compared to an internal reference voltage to adjust the output voltage, any inaccuracy in the feedback voltage creates inaccuracies in the output voltage. Low noise and wide gain bandwidth opamp driver circuit with internal electrostatic discharge(ESD) protection circuit are used to protect ADC inputs. Opamp driver circuit

provides low / stable output impedance.

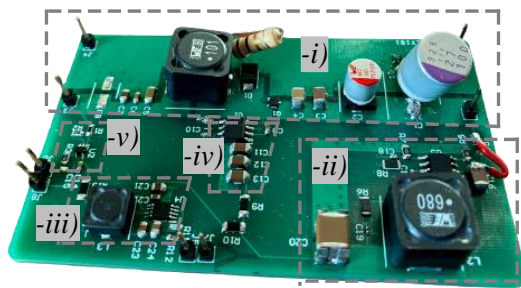
The opamp is connected as a unity gain, non-inverting buffer. This opamp circuit is a voltage follower circuit with high input impedance and low output impedance. Since there is no voltage difference between the opamp inputs, the output voltage  $V_o$  is the same as the input voltage  $V_{in}$ . In addition, the  $V = 3.3V$  voltage required to feed the opamp circuit is provided from the PCB board by designing a suitable voltage regulator circuit.

A bootstrap gate driver circuit is designed to drive the mosfet. Gate Driver IC are chosen to provide the required peak current. With gate driver circuit, about 5V PWM signal is converted to + VCC value and power switch is turned on and off properly. Also, the  $VDD = 12 V$  voltage required to feed the gate driver IC. With the suitable voltage regulator circuit, the input voltage is converted to the required 12V voltage for the gate driver IC supply. The gate driver IC is physically placed close to the power switch to minimize the effects of high frequency switching noise.

The Altium Designer program is used for the PCB drawing of the designed buck converter. In the PCB converter board drawing, the stray capacitance effect around the mosfet is reduced by selecting appropriate current paths and thickness. Short and wide current paths are used to reduce leakage inductance in loops with high current variation ( $di/dt$ ). In nodes where the voltage change rate ( $dv/dt$ ) with respect to time is high, it is tried to minimize the conductor area in the node in order to reduce the leakage capacitance.



(a)



(b)

Fig. 6. a) Test Bench Setup -i) Buck Converter -ii) F28379D DSC -iii) NI Data Acquisition Board b) Buck converter PCB Layout -i) Buck Circuit -ii) 48V-12V Circuit -iii) 12V-3.3V circuit -iv) Gate Driver Circuit -v) Signal Condition Circuit

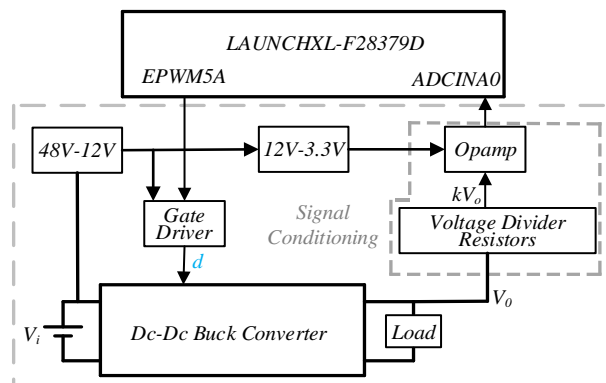
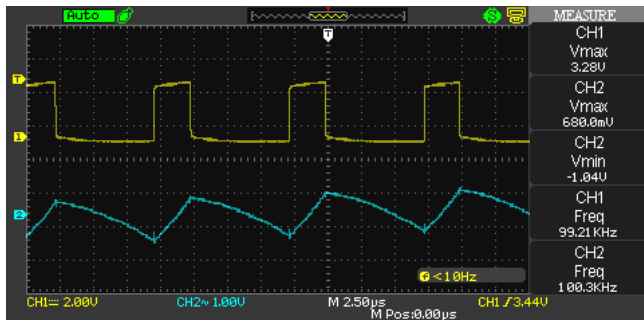
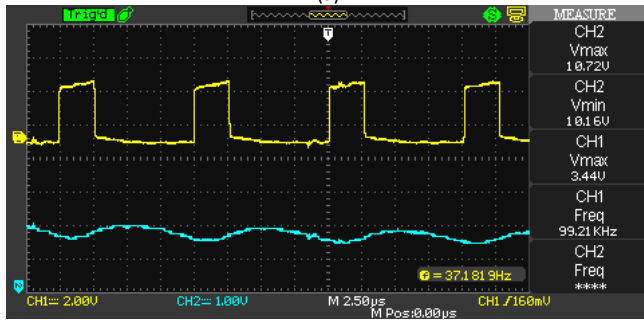


Fig.7. The General Schema of Designed PCB

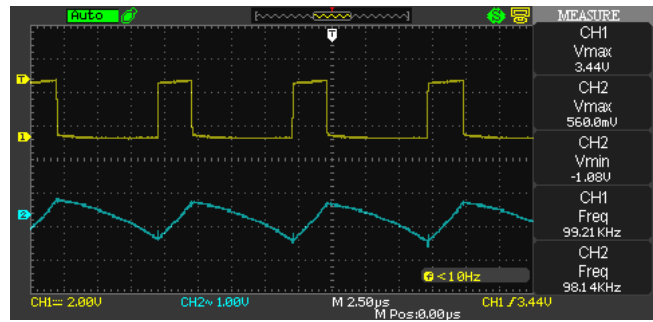


(a)

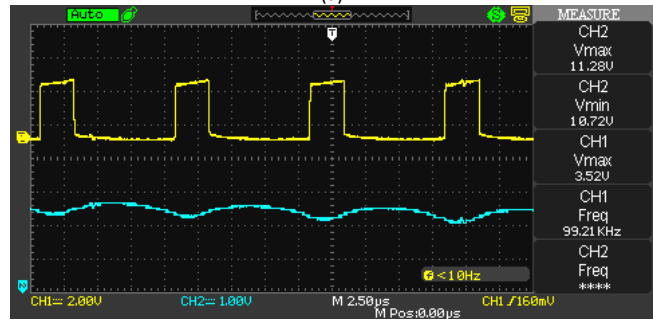


(b)

Fig.8. Experimental Results for  $V_i=48V$  and  $R=10\Omega$   
 (a) PWM, Inductance Current (b) PWM, Output Voltage

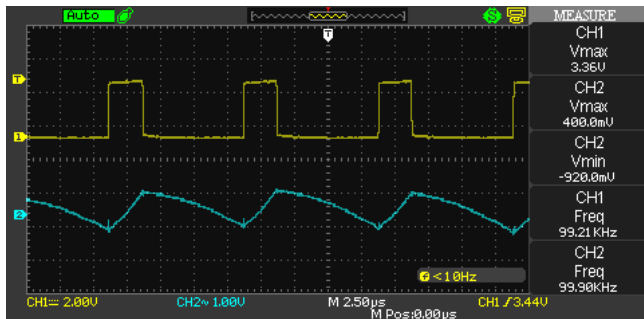


(a)

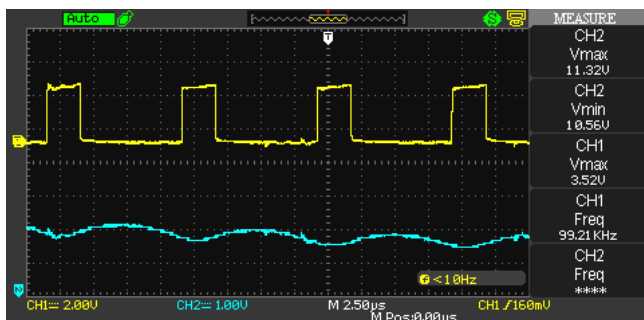


(b)

Fig.9. Experimental Results for  $V_i=48V$  and  $R=15\Omega$   
 (a) PWM, Inductance Current (b) PWM, Output Voltage

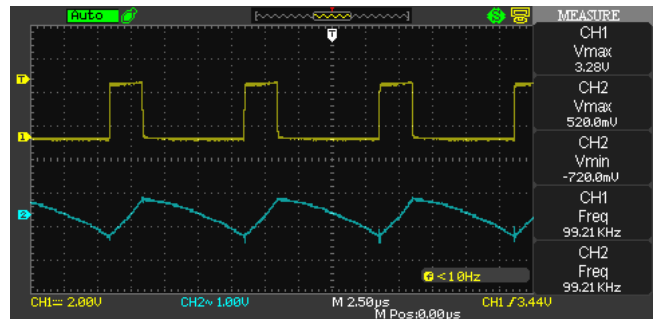


(a)

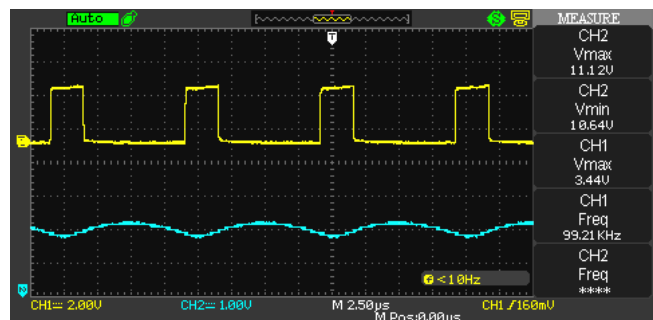


(b)

Fig.10. Experimental Results for  $V_i=48V$  and  $R=20\Omega$   
 (a) PWM, Inductance Current (b) PWM, Output Voltage



(a)



(b)

Fig.11. Experimental Results for  $V_i=48V$  and  $R=25\Omega$   
 (a) PWM, Inductance Current (b) PWM, Output Voltage

A ground plane is used to reduce the effect of return current noise of a device on other components and to minimize voltage drops caused by inductance and resistance with the short connections in the return path. By keeping the trace length, resistance is reduced and the susceptible to EMI is decreased.

Aluminum housed power resistors with different resistance values of 50W are used as load resistors: 10Ω, 15Ω, 20Ω, 25Ω. Thus, the stability of the circuit against output load changes is

observed. The Code Composer Studio (CCS) software development environment is used to digitize the analog voltage applied to the ADCIN channels of the TMS320F28379D DSP and to perform PI control. The codes developed with this program are compiled and loaded into the processor.  $K_p = 0.5$  and  $K_i = 0.001$  are chosen to obtain the desired control response with PI control. While determining  $K_p$  and  $K_i$  values, the effects of changing control parameters such as rise time, settling time,

overshoot, steady state error and stability are taken into consideration.

Fig.8, Fig.9, Fig.10. and Fig.11. shows the experimental results for different load resistance with  $V_i = 48V$ . The amplitude of the switching signal produced by *TI-F28379D* is about 3.3V. Switching frequency is 100kHz. This generated switching signal is connected to the power mosfet gate driver circuit as an input. As seen in Fig.8(a), Fig.9(a), Fig.10(a) and Fig.11(a), inductance current ripple match calculated values and Simulink results. Inductance currents are 1.044A, 0.733A, 0.547A and 0.435A for 10Ω, 15Ω, 20Ω, 25Ω resistors, respectively. When the inductance current waveforms are examined carefully, it is seen that the converter operates in continuous current mode. The output voltage contains only a small ripple caused by the parasitic parameters in the converter. As seen in Fig.8(b), Fig.9(b), Fig.10(b) and Fig.11(b), measurements show an under/overshoot voltage of -0.38V. The output voltage ripple is within permissible limit. In addition, the converter is stable, working at a switching frequency of 100 kHz without significant noise.

It is seen from the experimental results that the average values of output voltages are almost the same for all load resistance. The designed controller sets the duty cycle depending on load resistance.

Fig.12. shows the thermal performance of designed converter with 15Ω load resistor. This snapshot is taken at 25°C ambient temperature. The section of the PCB with the maximum heat is shown in red. This section includes a low power 1Ω resistor used to measure inductance current. This resistor is not included in the designed circuit and is added just before measurement. The yellow portion indicates the heat on inductance.

In order to calculate the efficiency of the circuit, the experimental results measured with a multimeter are given in Table IV. The input power is calculated as 8.92 W and the output power is 7.657W. The power efficiency is calculated as follow:

$$\% \eta = \frac{P_o}{P_i} \times 100 = 85.8 \quad (9)$$

As seen, the efficiency of the system is lower than 100% due to on-state resistances of mosfet and diode.

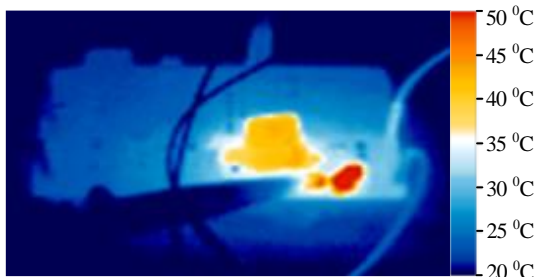


Fig.12. Thermal performance of designed converter

TABLE IV.  
BUCK CONVERTER EXPERIMENTAL RESULTS

Parameters	Value
Input voltage, V	48.22
Input current, A	0.185
Output voltage, V	11
Output current, A	0.696

## VI. CONCLUSION

In this study, the analysis, simulation and experimental application of a microcontroller-based dc-dc buck converter is carried out. The architecture and circuit implementation details are discussed in detail. The design parameters are verified with simulations and experiments. It is observed that the designed converter provides important design criteria such as high operating frequency, low output current ripple, and continuous current mode. Closed loop control technique is applied to the designed converter to hold the output voltages constants against to the load changes. The presented simulation and experimental results show the effectiveness of the developed controller in terms of overshoot limitations and accuracy.

## REFERENCES

- [1] A. A. A. Ismail and A. Elnady, "Advanced Drive System for DC Motor Using Multilevel DC/DC Buck Converter Circuit," in *IEEE Access*, vol. 7, pp. 54167-54178, 2019.
- [2] S. Kamat and S. Jadhav, "Design and Simulation of Low Power Charging Station for Electric Vehicle," 2019 International Conference on Advances in Computing, Communication and Control (ICAC3), Mumbai, India, 2019, pp. 1-4.
- [3] K. Hu, Y. Chen, H. Lin and C. Tsai, "Digital Buck Converter with Adaptive Driving Circuit for Cascode Power MOS," 2018 IEEE 7th Global Conference on Consumer Electronics (GCCE), Nara, 2018, pp. 126-127.
- [4] R. T. Yadlapalli and A. Kotapati, "Efficiency analysis of Quadratic buck converter for LED lamp driver applications," 2017 International Conference on Trends in Electronics and Informatics (ICEI), Tirunelveli, 2017, pp. 210-214.
- [5] N. Rigogiannis et al., "Experimental Investigation of a Digitally Current Controlled Synchronous Buck DC/DC Converter for Microgrids Applications," 2019 Panhellenic Conference on Electronics & Telecommunications (PACET), Volos, Greece, 2019, pp. 1-5.
- [6] A. A. Patil, et al., "Output voltage control scheme for standalone wind energy system," 2016 Int. Conf. on Computation of Power, Energy Information and Com. Chennai, 2016, pp. 534-541.
- [7] K. Pal and M. Pattnaik, "Performance of a Synchronous Buck Converter for a Standalone PV System: an Experimental Study," 2019 IEEE 1st International Conference on Energy, Systems and Information Processing (ICESIP), Chennai, India, 2019, pp. 1-6.
- [8] C. Fei, M. H. Ahmed, F. C. Lee and Q. Li, "Two-Stage 48 V-12 V/6 V-1.8 V Voltage Regulator Module With Dynamic Bus Voltage Control for Light-Load Efficiency Improvement," in *IEEE Transactions on Power Electronics*, vol. 32, no. 7, pp. 5628-5636, July 2017.
- [9] Y. Chen, J. Chen and D. Lai, "Dual mode digital buck converter controller without current sensor," 2018 IEEE International Conference on Industrial Electronics for Sustainable Energy Systems (IESES), Hamilton, 2018, pp. 118-123.
- [10] J. Yu, I. Hwang and N. Kim, "High performance CMOS integrated PWM/PFM dual-mode DC-DC buck converter," 18th Int. Scientific Conf. on Electric Power Engineering (EPE), Kouty nad Desnou, 2017, pp. 1-4.
- [11] Y. Moursy, R. Khalil, S. Lecce, V. Poletto, R. Iskander and M. Louerat, "Mixed-signal PI controller in current-mode DC-DC buck converter for automotive applications," 2016 IEEE International Symposium on Circuits and Systems (ISCAS), Montreal, QC, 2016, pp. 1610-1613.
- [12] A. Platon, S. Oprea, A. Florescu and S. G. Rosu, "Simple and Digital Implementation of PI Controller Used in Voltage-Mode Control," 2018 10th International Conference on Electronics, Computers and Artificial Intelligence (ECAI), Iasi, Romania, 2018, pp. 1-6.
- [13] Q. Huang, C. Zhan and J. Burm, "A 4-MHz Digitally Controlled Voltage-Mode Buck Converter With Embedded Transient Improvement Using Delay Line Control Techniques," in *IEEE Transactions on Circuits and Systems I: Regular Papers*, vol. 67, no. 11, pp. 4029-4040, Nov. 2020.
- [14] Y. Yan, A. Shehata, A. R. Beig and I. Boiko, "Auto-Tuning of PID Controller with Phase Margin Specification for Digital Voltage-Mode Buck Converter," 2020 IEEE Conference on Control Technology and Applications (CCTA), Montreal, QC, Canada, 2020, pp. 801-806.
- [15] P. Suskis and D. Nikonov, "Buck Converter Digital Control System Design and Performance Evaluation," 2018 IEEE 6th Workshop on

- Advances in Information, Electronic and Electrical Engineering (AIEEE), Vilnius, 2018, pp. 1-4.
- [16] M. Deshmukh and M. K. Namboothiripad, "DSP Based Second Order Sliding Mode Controller for Buck Converter," 2018 3rd International Conference for Convergence in Technology (I2CT), Pune, 2018, pp. 1-5.
- [17] M. K. Asy'ari, A. Musyafa' and K. Indriawati, "Design of Wind Turbine Output Voltage Control Systems in Multi-Input Buck Converter Using Fuzzy Logic Control for Battery Charging," 2019 Int. Conference on Advanced Mechatronics, Intelligent Manufacture and Industrial Automation (ICAMIMIA), Batu, Malang, Indonesia, 2019, pp. 249-252.
- [18] S. Seshagiri, E. Block, I. Larrea and L. Soares, "Optimal PID design for voltage mode control of DC-DC buck converters," 2016 Indian Control Conference (ICC), Hyderabad, 2016, pp. 99-104.
- [19] S. Ghosh, S. Satpathy, S. Das, S. Debbarma and B. K. Bhattacharyya, "Different Controlling Method of Closed Loop DC-DC Buck Converter: A review," 2018 International Conference on Smart Systems and Inventive Technology (ICSSIT), Tirunelveli, India, 2018, pp. 29-33.
- [20] M. M. Garg, Y. V. Hote, M. K. Pathak and L. Behera, "An Approach for Buck Converter PI Controller Design Using Stability Boundary Locus," 2018 IEEE/PES Transmission and Distribution Conference and Exposition (T&D), Denver, CO, 2018, pp. 1-5.
- [21] Daniel W. Hart., "Power Electronics", McGraw-Hill, New York-Americas, 2011
- [22] B. Yuan, J. Ying, W. T. Ng, X. Lai and L. Zhang, "A High-Voltage DC-DC Buck Converter With Dynamic Level Shifter for Bootstrapped High-Side Gate Driver and Diode Emulator," in IEEE Transactions on Power Electronics, vol. 35, no. 7, pp. 7295-7304, July 2020.
- [23] Design and Evaluation of A High-Current Gate Driver Circuit for Six Paralleled 1.2kV 36A SiC MOSFETs
- [24] "UCC27211A-Q1 120V Boot, 4A Peak, High Frequency High Side and Low Side Driver," SLUSCG0A datasheet, 2015
- [25] MH Rashid, "Power Electronics Circuits, Devices and Applications", 3rd Ed., Prentice-Hall, 2003, pp 761~789
- [26] Fairchild Application Note AN-6076 : Design and Application Guide of Bootstrap Circuit for High Voltage Gate Drive IC.

## BIOGRAPHIES



**HASAN SUCU** received B.S. degrees in electrical engineering from Inonu University, Malatya, Turkey, in 2009. Since 2018, he has been a student of B.S. degree in Inonu University, Malatya, in the Electrical and Electronics Engineering department. He is currently with the Arapgir Vocational High School, Electric Program, Malatya Turgut Ozal University, Malatya, Turkey. His research interests include design of dc-dc converters and power electronics circuits.



**TANER GOKTAS** received B.S and M.S degrees in electrical engineering from Firat University, Elazig, Turkey, in 2006 and 2010, respectively, and the Ph.D. degree in Electrical Engineering from the Inonu University, Malatya, Turkey, in 2015. He was a visiting scholar in the Power Electronic and Drives Lab, University of Texas at Dallas from 2014 to 2015. Since 2016, he has been with Inonu University as an Assistant Professor. His research interests include electric machines drives, power electronics, condition monitoring, motor design and diagnostic techniques in electric machines.



**MUSLUM ARKAN** received B.Sc. degree in Electrical and Electronics Engineering from University of Gaziantep, Turkey and his Ph. D. degree in Electrical Engineering from University of Sussex, Brighton, UK, in 1994 and 2000 respectively. Since 1994, he has been with the Electrical and Electronics Engineering Department, Inonu University, Malatya, Turkey, where he is currently a full Professor. His research activities include the use of digital signal analysis for diagnostic, condition monitoring and motor failure prediction by sensorless methods and modeling of electrical machines for diagnosis purpose.

# Comparison of PO and INC MPPT Methods Using FPGA In-The-Loop under Different Radiation Conditions

Reşat Çelikel and Ahmet Gündoğdu

**Abstract**— In photovoltaic (PV) systems, the Maximum Power Point Tracking (MPPT) algorithms are applied to obtain maximum efficiency under different atmospheric conditions. Among the MPPT methods, Perturb & Observe (PO) and Incremental Conductance (INC) methods are the oldest algorithms that have been used. Field Programmable Gate Arrays (FPGA) are used especially in applications requiring high speed. FPGA in-the-loop feature is used to test algorithms designed in MATLAB/Simulink environment. In this study, PO and INC methods were designed to work in FPGA environment. Both algorithms were tested under different radiation conditions by using FPGA-in-the-loop feature. The FPGA in-the-loop simulation result of PO and INC methods was shown graphically. Altera DE2-115 development board was used to test PO and INC MPPT algorithms. In addition, PO and INC methods were synthesized using the Quartus-II program. Comparisons of the simplicity of the algorithms were made based on the synthesis results. Thus, by using the FGPA in-the-loop feature and performing the synthesis process, both of the algorithms were tested and the areas covered by the algorithms in the FPGA were compared.

**Index Terms**—Solar Energy, PV systems, MPPT Algorithms, FPGA, Perturb and Observe, Incremental Conductance, Photovoltaic Energy Conversion.

## I. INTRODUCTION

SOLAR ENERGY is used extensively in renewable energy systems. However, due to the low efficiency of photovoltaic (PV) systems, various algorithms have been developed to obtain maximum energy from PV modules [1-2]. Among these algorithms, the oldest and most heavily used

algorithms are the Perturb and Observe (PO) and Incremental Conductance (INC) methods.

Many studies related to Maximum Power Point Tracking (MPPT) algorithms and their various derivatives have been conducted in the literature. The efficiencies of PO and INC methods were experimentally measured on the dynamic performance of a PV system according to the EN50530 standard, which is a European efficiency test standard. Accordingly, it was shown that as a result of tests conducted under the same conditions, the INC method had slightly higher efficiency than the PO Method [3]. In a literature study comparing conventional and modern MPPT methods, PO and INC methods were also examined in detail. In that study, by using a simulation study, it was shown that the power fluctuations occurring in the INC method were higher than in the PO method [4]. In addition to these studies, these two conventional methods have been the subject of many review articles [5-8]. In a study conducted using a low-cost microprocessor, comparisons of PO, INC, Fuzzy Logic Controller (FLC), Fractional Short-Circuit Current (FSCC), Fractional Open-Circuit Voltage (FOCV), and Neural Network (NN) MPPT methods were made. Also, the introduction of various low-cost microprocessors was carried out in that study [9]. In another study, on the other hand, by using the PO method together with various DC-DC converters, their performances were examined [10].

The conventional PO MPPT method has been modified using the variable-step PO method, and many studies have been conducted on this topic. In reference [11], the conventional PO MPPT method was reorganized as variable-step. In addition, the size of the variable step in the PO method was ensured by the PID controller. The parameters of the controller were calculated by using the genetic algorithm (GA). A power performance that had lower fluctuation was achieved in the proposed method. In reference [12], Hill Climb (HC), PO, INC, FLC, and the proposed Sliding Mode Controller (SMC) methods were compared under partial shading conditions. It was shown that the proposed method drew more power from the PV system and the drawn power had lower oscillation. A variable-step INC algorithm was

REŞAT ÇELİKEL, is with Department of Mechatronics Engineering, University of Firat University, Elazığ, Turkey, (e-mail: resat.celikel@gmail.com).

 <https://orcid.org/0000-0002-9169-6466>

AHMET GÜNDOĞDU, is with Department of Electrical Engineering University of Batman, Turkey, (e-mail: agundogdu23@gmail.com).

 <https://orcid.org/0000-0002-8333-3083>

Manuscript received February 22, 2018; accepted April 02, 2021.

DOI: [10.17694/bajece.884815](https://doi.org/10.17694/bajece.884815)

introduced in reference [13]. By adding a driving technique with a voltage reference to this algorithm at start time, a power with lower oscillation was drawn both at startup and in steady state. By modifying the INC algorithm, Xu et al. [14] developed an effective MPPT method under both uniform radiation and partial shading conditions.

Devi et al. [15] modified the PO algorithm and developed an effective MPPT method that worked with high efficiency under fast-changing atmospheric conditions. In another study, a modified PO method that could work in two different modes was proposed. Compared to the conventional PO method, the proposed method was working with high efficiency under fast-changing atmospheric conditions [16]. In addition to these methods, many different modified MPPT algorithms have been developed. In the developed methods, the main goal is to achieve speed, high efficiency, and high adaptability to environmental conditions [17-20]. In another study, a new soft-MPPT algorithm that could be realized with low-level microprocessors and also used in conjunction with both PO and INC algorithms was proposed [21]. Both simulation and experimental study of the INC method used in conjunction with the CUK converter were carried out and compared [22].

The main goal of modified conventional MPPT algorithms and different control methods is to get the maximum possible efficiency from PV systems. There are many studies conducted for this purpose in the literature [23-26]. Conventional PO, modified PO and Learning Automata Optimization-supported hybrid PO methods were compared in reference [27]. Simulation studies of the proposed hybrid PO method were conducted for many different environmental conditions, and the success of the proposed method was shown. In another study, the superiority of the linear tangents-based PO method over conventional methods was revealed by simulation studies [28]. A two-step PO method was developed to ensure that the power drawn from the PV system in steady state was higher [29]. The high performance of a new hybrid MPPT algorithm, which was created by combining the ABC (Artificial Bee Colony) optimization method and the PO method in a single-phase PV system, was shown under partial shading conditions [30, 31]. The main purpose of adaptive MPPT algorithms is to ensure the improvement of dynamic performance in both the transient and steady state. Furthermore, using these algorithms, maximum power point monitoring is ensured with high efficiency under variable atmospheric conditions [32-35].

In addition to PO MPPT algorithms, INC MPPT methods and derivatives of these methods are also widely used in the literature [36]. A modified INC MPPT algorithm was compared with conventional PO and INC algorithms [37]. A variable-step INC MPPT algorithm was performed both as simulation and experimentally [38]. Optimization of

parameters of a fractional order control-based INC MPPT algorithm was carried out [39]. An INC MPPT application was performed with a low-cost Arduino control card [40]. As an effective method under partial shading conditions, an Artificial Neural Network (ANN)-based INC MPPT method was proposed [41]. An evaluation study comparing the INC MPPT method with the PO method was conducted. A DC motor and pump were used as load [42]. By creating its model in the Proteus program of the PV panel, the INC MPPT algorithm was performed experimentally in a simulation environment [43]. By using a low-cost microcontroller and SEPIC converter, an INC MPPT application was carried out experimentally [44]. In a PV system where a CUK type DC-DC converter was used, the success of the INC algorithm in which the step ratio was determined with FLC was tested [45]. A modified INC algorithm that could monitor the maximum power point under variable load and partial shading conditions was developed [46]. In another study, an INC MPPT algorithm that can work with high performance under fast-changing atmospheric conditions was introduced [47].

In addition to the conventional methods, solar monitoring systems using algorithms such as ANN and FLC, which work with higher performance but require high-level processors in practice, are also quite widespread [48-50]. In the application of these complex methods, Field Programmable Gate Arrays (FPGAs), whose use in control applications has increased in recent years, are used. Unlike the conventional processor structure, FPGA has a system making parallel processing. Therefore, it stands out with high processing speeds [51-53]. Apart from studies conducted with FPGA, the FPGA-in-the-loop (FIL) feature has also been the subject of studies recently. FIL is used to test whether designed control methods or algorithms work with expected performance. The developed software has been designed so that it runs in FPGA. In reference [54], an estimation of the motor shaft angle was made via the ANN method by using resolver signals. The ANN structure was tested using the FIL feature. A new algorithm developed for energy measurement was run in the FIL environment [55]. An algorithm developed for fast detection of switching errors in a voltage-source inverter was first tested with FIL and then its experimental study was carried out [56]. The predictive current control algorithm developed for a grid-connected PV system was run in the FIL environment [57].

In this study, PO and INC MPPT algorithms were compared in terms of places they occupy in the microprocessor. For this purpose, the Altera Cyclone IV EP4CE115F29 FPGA chip on the Altera DE2-115 development platform was used. Primarily, these two algorithms, which were conventional, were reorganized so that they could work within FPGA. Moreover, the synthesizing

process of the algorithms was carried out using the Quartus II program. Since the FPGA in-the-loop feature runs in the MATLAB/Simulink environment, the results obtained from running the PO and INC algorithms were graphically compared. As a result of the synthesizing, a comparison of the total areas covered by the algorithms was made. Thus, it was shown that MPPT algorithms could be tested without experimental study. In addition, information about the place that algorithms would occupy in the microprocessor was obtained. This study can be seen as a preliminary study for conducting studies in terms of simplifying the algorithms if it would be deemed necessary in the future.

## II. PHOTOVOLTAIC SYSTEM

When creating a PV system, the desired power level can be achieved by connecting PV modules in series and parallel. In order for MPPT algorithms to be implemented, a DC-DC converter is connected to the output of the PV system. Thus, by setting the current and voltage drawn from the PV system, a maximum power is achieved in variable atmospheric conditions. The electrical equivalent circuit model of a PV cell can be obtained as shown in Figure 1 [58, 59].

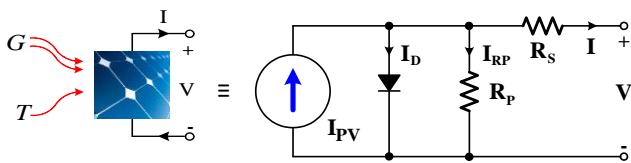


Fig.1. Electrical equivalent circuit model of a PV cell

The current produced by the PV cell here is given in Equations 1 and 2.

$$I = I_{PV} - I_D - I_{R_p} \quad (1)$$

$$I = I_{PV} - I_0 \left[ \exp\left(\frac{V + R_s I}{a}\right) - 1 \right] - \frac{V + R_s I}{R_p} \quad (2)$$

where  $I_0$  is the leakage current of the diode.  $a$  is an ideality factor and is given in Equation 3.

$$a = \frac{N_s n k T}{q} \quad (3)$$

where  $N_s$  is the number of series-bound cells,  $n$  is the diode ideality constant,  $k$  is the Boltzmann constant ( $1.3806503 \times 10^{-23}$  J/K),  $T$  is the cell temperature in Kelvin, and  $q$  is the electron charge ( $1.60217646 \times 10^{-19}$  C). The cell current

generated by the PV panel by the effect of light is given in Equation 4.

$$I_{PV} = \left( I_{PV,n} + K_I(T - T_n) \right) \frac{G}{G_n} \quad (4)$$

where  $I_{PV,n}$  is the current generated at  $25^\circ\text{C}$  and  $1000 \text{ W/m}^2$ ,  $T$  is the current temperature (Kelvin),  $T_n$  is the nominal temperature (Kelvin),  $G$  is the radiation value on the panel surface ( $\text{W/m}^2$ ), and  $G_n$  is the nominal radiation value ( $\text{W/m}^2$ ). The saturation current ( $I_0$ ) of the diode is given in Equation 5.

$$I_0 = \frac{I_{SC,n} + K_I(T - T_n)}{\exp\left(\frac{V_{OC,n} + K_V(T - T_n)}{a}\right) - 1} \quad (5)$$

where  $I_{SC,n}$  is the rated short-circuit current,  $V_{OC,n}$  is the rated open circuit voltage,  $K_I$  is the current coefficient, and  $K_V$  is the voltage coefficient.

In this study, a PV power system with 10 kW power was created using Trina TSM-250PA05.08 model PV panels in MATLAB/Simulink environment. Figure 2 shows current-voltage graph of the panel under standard test conditions-STC.

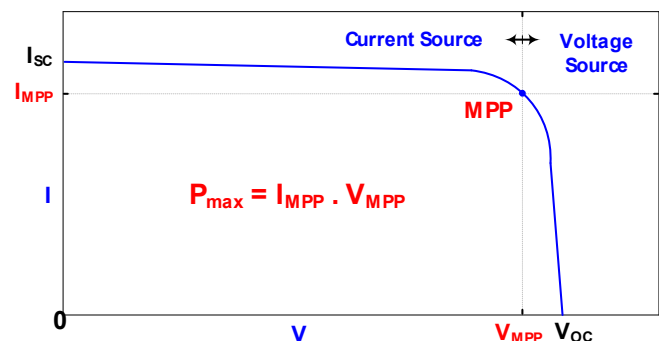


Fig.2. I-V curve of the PV panel

### A. Boost Converter

The circuit structure of an ideal boost converter is seen in Figure 3. For the case where the switch is off, the  $V_s$  voltage source is serially connected to the  $L$  coil and the tension formula can be written as in Equations 6 and 7.

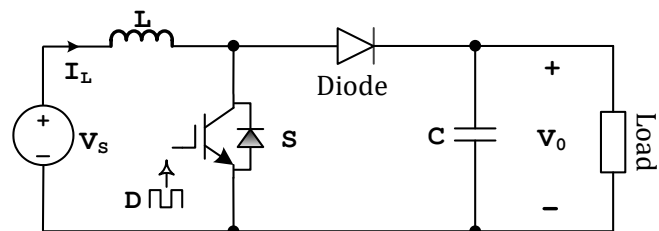


Fig.3. Boost converter

$$V_s(t) = L \frac{dI_L}{dt} \tag{6}$$

$$\frac{\Delta I_L}{\Delta t} = \frac{V_s}{L} \tag{7}$$

The time of the switch to remain in transmission ( $\Delta t$ ) can be written as  $DT_s$ , and the time to remain in cutoff can be written as  $(1-D)T_s$ . Here, while  $D$  refers to the task period of the switch,  $T_s$  refers to the switching period. Accordingly, the expression of the current during the transmission time of the switch is seen in Equation 8, and the expression of the current during the cutoff time of the Switch is seen in Equation 9.

$$\Delta I_L = \frac{V_s}{L} DT_s \tag{8}$$

$$\Delta I_L = \frac{V_s - V_0}{L} (1 - D) T_s \tag{9}$$

The sum of the change in current seen in Equations 8 and 9 will be zero within one period. When this expression is written, the change of output voltage depending on the task period is given in Equation 10.

$$V_0 = \frac{V_s}{1 - D} \tag{10}$$

### III. PO AND INC MPPT METHODS

In the conventional PO MPPT method, voltage and power changes in each step are measured. Taking into account the change in power and voltage, the switching task period of the boost converter is changed in a way that the voltage will be increased and decreased at the magnitude of  $\Delta V_{ss}$ . The flow diagram for the application of the PO method is shown in Figure 4(a).

The conventional INC MPPT method is created by observing the peak of the power-voltage curve of the PV system (i.e. by finding the point where the slope is zero, and also observing the current-voltage curve). The flow diagram for the implementation of the INC method is shown in Figure 4(b). While the maximum output power of the PV system is given in Equation 11, the restatement of power by using differential equations is given in Equations 12 and 13.

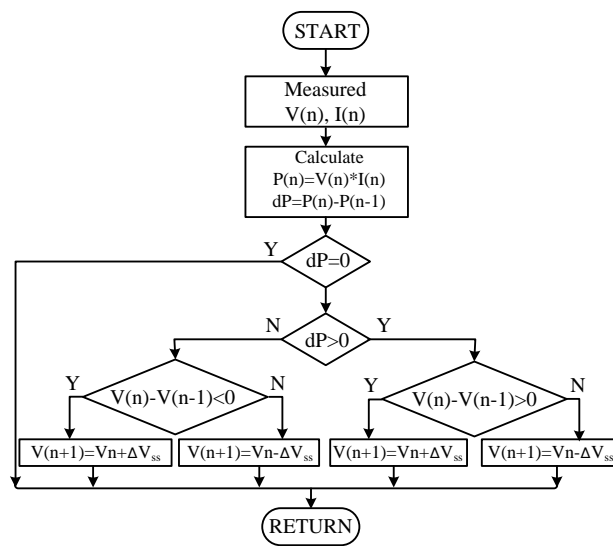
$$P_{MPP} = V_{MPP} \times I_{MPP} \tag{11}$$

$$\frac{dP}{dV} = I + V \frac{dI}{dV} = 0 \tag{12}$$

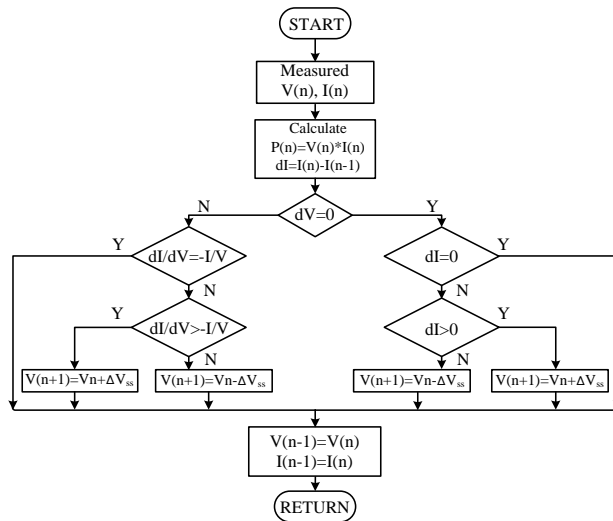
$$\frac{dI}{dV} \cong \frac{\Delta I}{\Delta V} = -\frac{I_{MPP}}{V_{MPP}} \tag{13}$$

The three applied derivatives associated with catching the MPP point are seen in Equation 14.

$$\begin{cases} \frac{dP}{dV} = 0, & \frac{\Delta I}{\Delta V} = -\frac{I}{V} \\ \frac{dP}{dV} > 0, & \frac{\Delta I}{\Delta V} > -\frac{I}{V} \\ \frac{dP}{dV} < 0, & \frac{\Delta I}{\Delta V} < -\frac{I}{V} \end{cases} \tag{14}$$



a)



b)

Fig.4. Flow diagrams for a) PO MPPT method and b) INC MPPT method

IV. FPGA IN-THE-LOOP (FIL) AND RESULTS

FIL is performed by using the Altera FPGA, which operates in line with MATLAB/Simulink. The FIL feature is used to test whether a control algorithm developed in the MATLAB/Simulink environment or a different model works or not. In this way, before the installation of large-cost systems, the accuracy of the algorithms and models that will work on the system is ensured. In order for the FIL feature to be able to operate, the algorithm to be tested must be synthesized first. Therefore, it is required that the algorithm to be tested is designed in a way that it can work within FPGA. In this study, the areas covered by PO and INC algorithms, which are among the conventional MPPT algorithms, in an FPGA and their performances were compared. In this way, it was shown that the determination of the areas covered by MPPT algorithms in a microprocessor and analysis of their

performances can be made with the FIL feature. Because the software would run in FPGA, the sample time of the simulation was set to 20 ns, which was the operating frequency of the used FPGA. Since the switching frequency of the Boost converter was 20 kHz in the simulation study, the measurement time of current and voltage was set to 50  $\mu$ s. In addition, in both algorithms, time settings were made in accordance with the order of current, voltage, and power changes in the flow diagram and the sampling time. Figure 5(a) and 5(b) show the sampling times of the MATLAB/Simulink simulation of PO and INC methods, respectively. These sampling times were set in a way that they would run in FPGA.

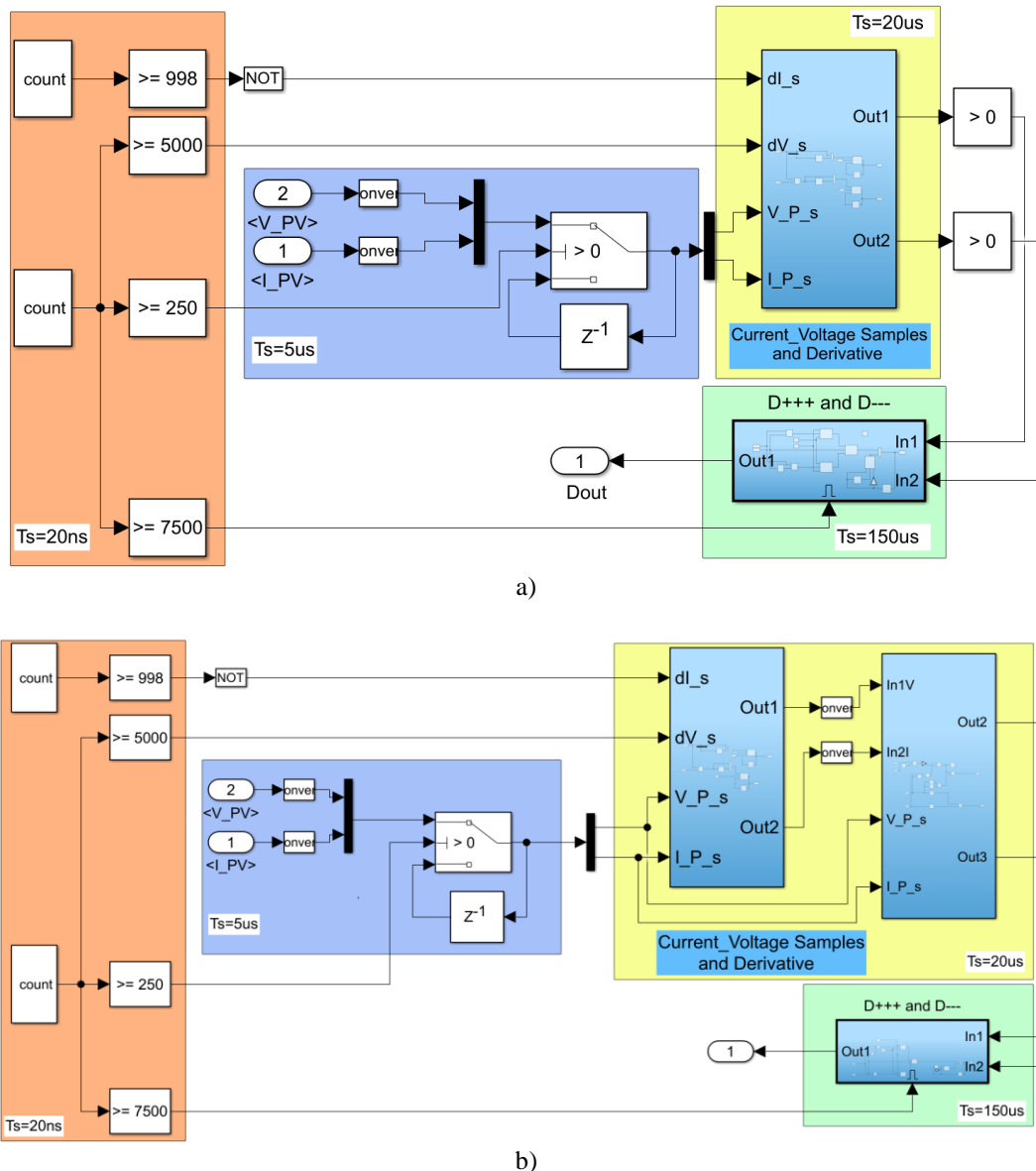


Fig.5. MATLAB/Simulink blocks synthesized by FPGA: a) PO method b) INC method

In algorithms running in FPGA, operations do not work in double format. Therefore, inputs, outputs and operations were reorganized in fixed point or integer formats. The

MATLAB/Simulink simulation study, which also includes the FIL block, is seen in Figure 6.

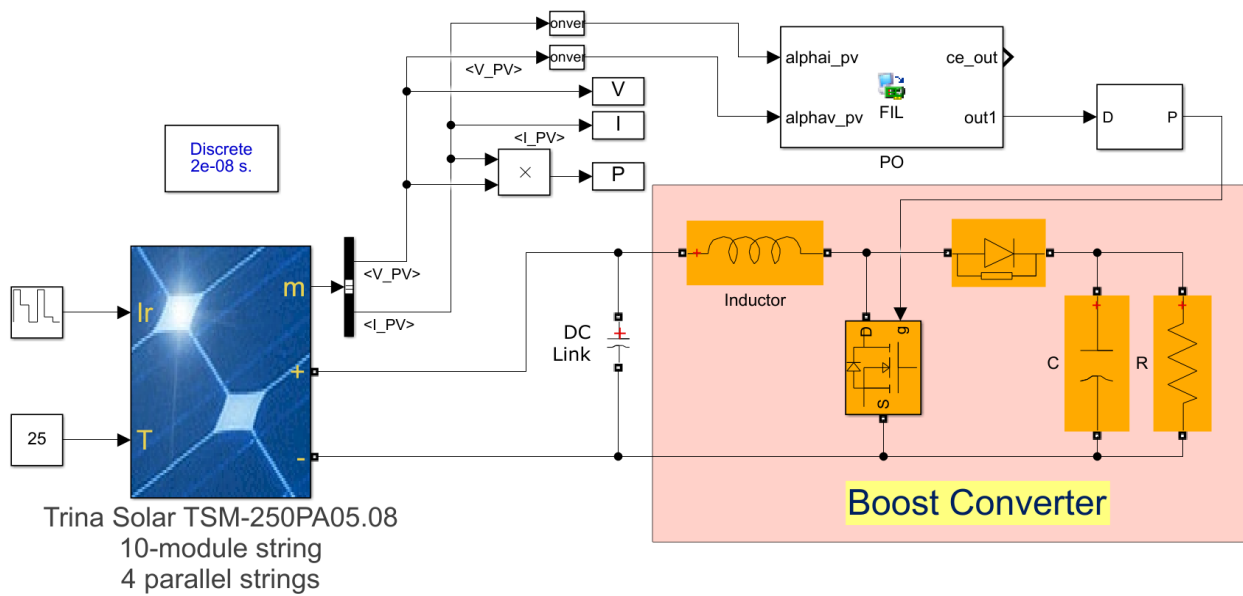


Fig.6. MATLAB/Simulink simulation including FIL block

The simulation study was carried out using MATLAB/Simulink and Altera DE2-115 Development Board. The FPGA used on the board is a product of Cyclone IV EP4CE115F29. Both algorithms were run together with FPGA by using the FIL block under the same conditions. Figure 7

shows the power obtained by PO and INC method at different radiation values (1000-700-400 W/m<sup>2</sup>) under a temperature of 25 °C. Figure 8 shows graphs of current and voltage generated at the same radiation values.

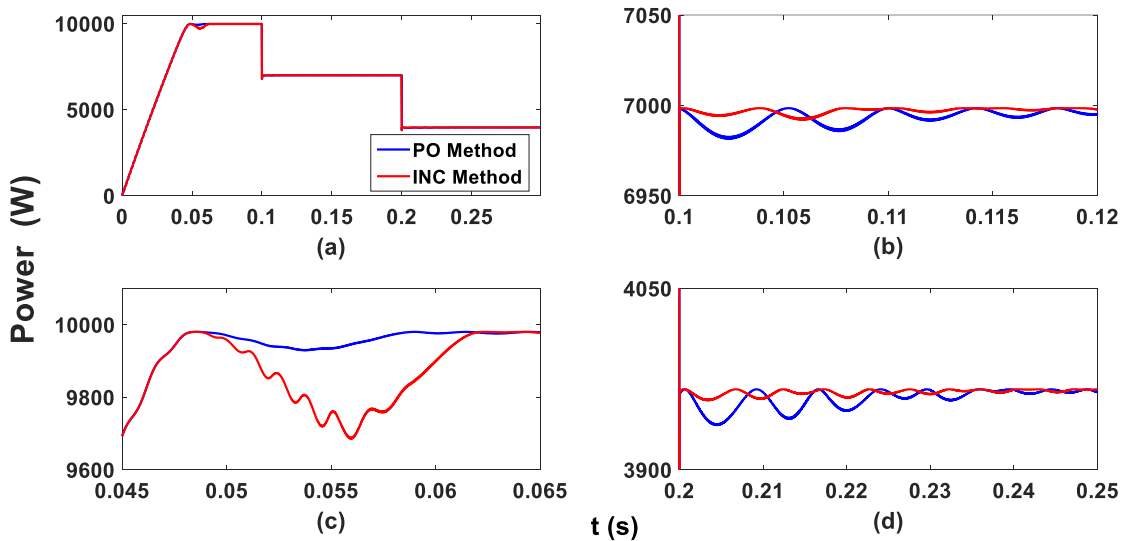


Fig.7. Power obtained by PO and INC method at 25 °C; a) at different radiation values b) at 1000 W/m<sup>2</sup> radiation value c) at 700 W/m<sup>2</sup> radiation value d) at 400 W/m<sup>2</sup> radiation value

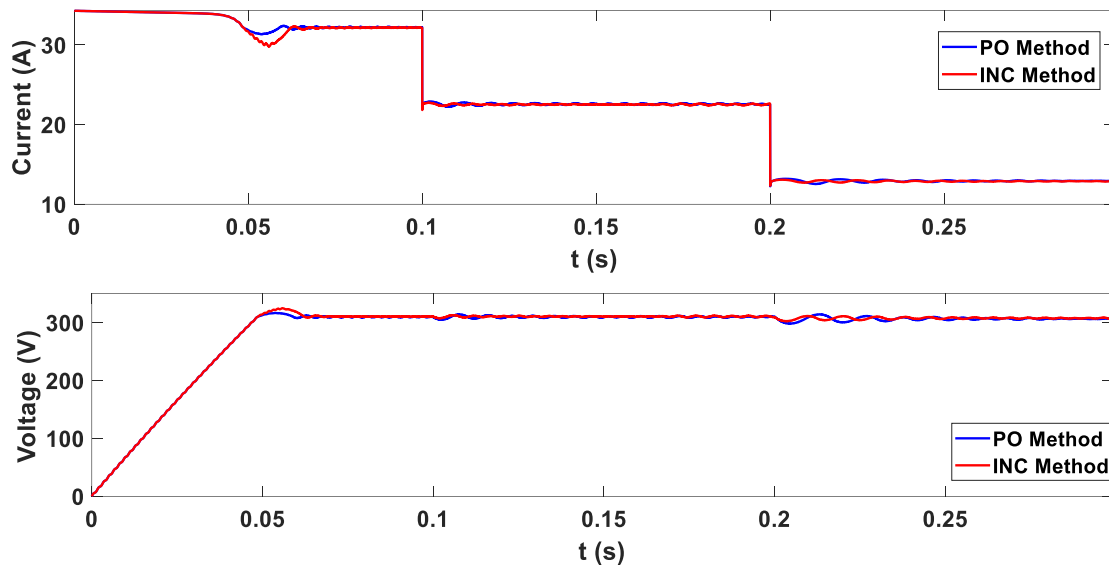


Fig.8. Current and voltage obtained by PO and INC methods under the same atmospheric conditions

Flow Summary	
Flow Status	Successful - Sun Jan 10 20:13:05 2021
Quartus II Version	10.0 Build 218 06/27/2010 SJ Web Edition
Revision Name	PO
Top-level Entity Name	Subsystem1
Family	Cyclone IV E
Device	EP4CE115F29C7
Timing Models	Final
Met timing requirements	N/A
Total logic elements	456 / 114,480 (< 1 %)
Total combinational functions	456 / 114,480 (< 1 %)
Dedicated logic registers	195 / 114,480 (< 1 %)
Total registers	195
Total pins	84 / 529 (16 %)
Total virtual pins	0
Total memory bits	0 / 3,981,312 (0 %)
Embedded Multiplier 9-bit elements	8 / 532 (2 %)
Total PLLs	0 / 4 (0 %)

a)

Flow Summary	
Flow Status	Successful - Sun Jan 10 20:17:06 2021
Quartus II Version	10.0 Build 218 06/27/2010 SJ Web Edition
Revision Name	INC
Top-level Entity Name	Subsystem1
Family	Cyclone IV E
Device	EP4CE115F29C7
Timing Models	Final
Met timing requirements	N/A
Total logic elements	5,125 / 114,480 (4 %)
Total combinational functions	5,125 / 114,480 (4 %)
Dedicated logic registers	195 / 114,480 (< 1 %)
Total registers	195
Total pins	84 / 529 (16 %)
Total virtual pins	0
Total memory bits	0 / 3,981,312 (0 %)
Embedded Multiplier 9-bit elements	24 / 532 (5 %)
Total PLLs	0 / 4 (0 %)

b)

Fig.9. Flow summary of synthesis with FPGA: a) PO algorithm b) INC algorithm

When Figure 7 is examined, it is seen that at the first starting time, the oscillation in the PO method was less when it caught the MPP point. At 700 W/m<sup>2</sup> and 400 W/m<sup>2</sup> radiation values, the power fluctuation in the PO method was more compared to the INC method. However, in steady state, these power

oscillations were very close to each other. In order for that the power oscillations were not too much at the first starting time, a task period locking method was used to fix the task period to 0.05 if the task period went negative. Accordingly, there were no major differences in the application of PO and INC methods. In order to understand the space these two algorithms, which have superiority over each other in various regions, occupy in the microprocessor, a synthesis process was performed using the Quartus II program. Figure 9 shows the results of the synthesis process.

Figure 9(a) shows a summary of the flow occurring as a result of synthesizing the PO method, while Figure 9(b) shows a summary of the flow occurring as a result of synthesizing the INC method. The synthesis result shows that the INC algorithm takes up more space in FPGA than the PO algorithm. Accordingly, it is clearly seen that the processing load is greater in the implementation of the INC algorithm. In terms of tracking the MPP point, it has been observed that these algorithms, which have different advantages over each other in different regions in transient state, have too little superiority over each other in steady state. The fact that the processing load in the INC algorithm is excessive is due to the division operations contained in the algorithm. At the end of the synthesis process, it was seen that the division process was a significant processing load for FPGAs.

## V. CONCLUSIONS

PO and INC, which are among the conventional MPPT algorithms, are two of the most commonly used methods. Comparisons of these algorithms and their various derivatives are quite common in the literature. FIL is a feature used to test algorithms that work and are designed in the

MATLAB/Simulink environment together with Altera FPGA. In this study, PO and INC MPPT algorithms were tested in the MATLAB/Simulink environment by using the FIL feature. These algorithms prepared in MATLAB/Simulink environment with Altera DE2-115 development platform, working synchronously. In order for algorithms to be able to run on a real system, time settings were made. In the next stage, to examine the areas covered by PO and INC methods in FPGA, the synthesis process was carried out using the Quartus II program. As a result of the FIL simulation performed at constant temperature and different radiation values, it was observed that the PO and INC methods had little superiority over each other in different regions. As a result of the synthesis process, on the other hand, it was shown that the PO method takes up less space in FPGA than the INC method. Accordingly, thanks to graphics obtained by FIL application and flow summary obtained as a result of synthesis process, it was clearly seen that in terms of ease of application, the PO method was superior to the INC method.

#### REFERENCES

- [1] C. Larbes, S.M.A. Cheikh, T. Obeidi, A. Zerguerras. "Genetic algorithms optimized fuzzy logic control for the maximum power point tracking in photovoltaic system." *Renew Energy*. Vol. 34, 2009, pp 2093-2100.
- [2] R. Celikel, A. Gundogdu. "System identification-based MPPT algorithm for PV systems under variable atmosphere conditions using current sensorless approach." *International Transactions on Electrical Energy Systems*, 2020, e12433.
- [3] K. Ishaque, Z. Salam, G. Lauss. "The performance of perturb and observe and incremental conductance maximum power point tracking method under dynamic weather conditions." *Applied Energy*, vol. 119, 2014, pp 228-236.
- [4] A. Gupta, Y. K. Chauhan, R. K. Pachauri. "A comparative investigation of maximum power point tracking methods for solar PV system." *Solar Energy*, vol. 136, 2016, pp 236-253.
- [5] X. Li, H. Wen, Y. Hu, Y. Du, Y. Yang. "A comparative study on photovoltaic MPPT algorithms under EN50530 dynamic test procedure." *IEEE Transactions on Power Electronics*, vol. 36. 4, 2020, pp 4153-4168.
- [6] A. R. Reisi, M. H. Moradi, S. Jamasb. "Classification and comparison of maximum power point tracking techniques for photovoltaic system. A review." *Renewable and Sustainable Energy Reviews*, vol. 19, 2013, pp 433-443.
- [7] M. A. Husain, A. Tariq, S. Hameed, M. S. B. Arif, A. Jain. "Comparative assessment of maximum power point tracking procedures for photovoltaic systems." *Green Energy & Environment*, vol. 2. 1, 2017, pp 5-17.
- [8] H. Bounechba, A. Bouzid, K. Nabti, H. Benalla. "Comparison of perturb & observe and fuzzy logic in maximum power point tracker for PV systems." *Energy Procedia*, vol. 50. 1, 2014, pp 677-684.
- [9] S. Motahhir, A. El Hammoumi, A. El Ghzizal. "The most used MPPT algorithms: Review and the suitable low-cost embedded board for each algorithm." *Journal of Cleaner Production*, vol. 246, 2020, 118983.
- [10] M. E. Başoğlu. "Analyzes of Flyback DC-DC Converter for Submodule Level Maximum Power Point Tracking in Off-grid Photovoltaic Systems." *Balkan Journal of Electrical and Computer Engineering*, vol. 7. 3, 2019, pp 269-275.
- [11] A., Harrag, S. Messalti. "Variable step size modified P&O MPPT algorithm using GA-based hybrid offline/online PID controller." *Renewable and Sustainable Energy Reviews*, vol. 49, 2015, pp 1247-1260.
- [12] Z. M. Ali, N. V. Quynh, S. Dadfar, H. Nakamura. "Variable step size perturb and observe MPPT controller by applying  $\theta$ -modified krill herd algorithm-sliding mode controller under partially shaded conditions." *Journal of Cleaner Production*, vol. 271, 2020, 122243.
- [13] F. Liu, S. Duan, F. Liu, B. Liu, Y. Kang. "A variable step size INC MPPT method for PV systems." *IEEE Transactions on Industrial Electronics*, vol. 55. 7, 2008, pp 2622-2628.
- [14] L. Xu, R. Cheng, J. Yang. "A Modified INC Method for PV String Under Uniform Irradiance and Partially Shaded Conditions." *IEEE Access*, vol. 8, 2020, pp 131340-131351.
- [15] V. K. Devi, K. Premkumar, A. B. Beevi, S. Ramaiyer. "A modified Perturb & Observe MPPT technique to tackle steady state and rapidly varying atmospheric conditions." *Solar Energy*, vol. 157, 2017, pp 419-426.
- [16] A. Ghamrawi, J. P. Gaubert, D. Mehdi. "A new dual-mode maximum power point tracking algorithm based on the Perturb and Observe algorithm used on solar energy system." *Solar Energy*, vol. 174, 2018, pp 508-514.
- [17] S. C. Wang, H. Y. Pai, G. J. Chen, Y. H. Liu. "A Fast and Efficient Maximum Power Tracking Combining Simplified State Estimation With Adaptive Perturb and Observe." *IEEE Access*, vol. 8, 2020, pp 155319-155328.
- [18] R. Balasankar, G. T. Arasu, J. C. M. Raj. "A global MPPT technique invoking partitioned estimation and strategic deployment of P&O to tackle partial shading conditions." *Solar Energy*, vol. 143, 2017, pp 73-85.
- [19] S. Mohanty, B. Subudhi, P. K. Ray. "A grey wolf-assisted perturb & observe MPPT algorithm for a PV system." *IEEE Transactions on Energy Conversion*, vol. 32. 1, 2016, pp 340-347.
- [20] S. Lyden, H. Galligan, M. E. Haque. "A Hybrid Simulated Annealing and Perturb and Observe Maximum Power Point Tracking Method." *IEEE Systems Journal*, 2020, DOI: 10.1109/JSYST.2020.3021379.
- [21] S. Bhattacharyya, D. S. K. Patnam, S. Samanta, S. Mishra. "Steady Output and Fast Tracking MPPT (SOFT MPPT) for P&O and InC Algorithms." *IEEE Transactions on Sustainable Energy*, vol. 12. 1, 2021, pp 293-302.
- [22] A. Safari, S. Mekhilef. "Simulation and hardware implementation of incremental conductance MPPT with direct control method using cuk converter." *IEEE Transactions on Industrial Electronics*, vol. 58. 4, 2010, pp 1154-1161.
- [23] E. Bianconi, J. Calvente, R. Giral, E. Mamarelis, G. Petrone, C. A. Ramos-Paja, M. Vitelli. "Perturb and observe MPPT algorithm with a current controller based on the sliding mode." *International Journal of Electrical Power & Energy Systems*, vol. 44. 1, 2013, pp 346-356.
- [24] D. Sera, L. Mathe, T. Kerekes, S. V. Spataru, R. Teodorescu. "On the perturb-and-observe and incremental conductance MPPT methods for PV systems." *IEEE Journal of Photovoltaics*, vol. 3. 3, 2013, pp 1070-1078.
- [25] K. Yan, Y. Du, Z. Ren. "MPPT perturbation optimization of photovoltaic power systems based on solar irradiance data classification." *IEEE Transactions on Sustainable Energy*, vol. 10. 2, 2018, pp 514-521.
- [26] V. Kumar, M. Singh. "Derated Mode of Power Generation in PV System Using Modified Perturb and Observe MPPT Algorithm." *Journal of Modern Power Systems and Clean Energy*, 2020, DOI: 10.35833/MPCE.2019.000258
- [27] S. S. Mohammed, D. Devaraj, T. I. Ahamed. "A novel hybrid maximum power point tracking technique using perturb & observe algorithm and learning automata for solar PV system." *Energy*, vol. 112, 2016, pp 1096-1106.

- [28] V. R. Kota, M. N. Bhukya. "A novel linear tangents-based P&O scheme for MPPT of a PV system." *Renewable and Sustainable Energy Reviews*, vol. 71, 2017, pp 257-267.
- [29] E. Mamarelis, G. Petrone, G. Spagnuolo. "A two-steps algorithm improving the P&O steady state MPPT efficiency." *Applied Energy*, vol. 113, 2014, pp 414-421.
- [30] D. Pilakkat, S. Kanthalakshmi. "Single phase PV system operating under Partially Shaded Conditions with ABC-PO as MPPT algorithm for grid connected applications." *Energy Reports*, vol. 6, 2020, pp 1910-1921.
- [31] D. Pilakkat, S. Kanthalakshmi. "An improved P&O algorithm integrated with artificial bee colony for photovoltaic systems under partial shading conditions." *Solar Energy*, vol. 178, 2019, pp 37-47.
- [32] Y. Yang, H. Wen. "Adaptive perturb and observe maximum power point tracking with current predictive and decoupled power control for grid-connected photovoltaic inverters." *Journal of Modern Power Systems and Clean Energy*, vol. 7. 2, 2019, pp 422-432.
- [33] Y. Yang, F. P. Zhao. "Adaptive perturb and observe MPPT technique for grid-connected photovoltaic inverters." *Procedia Engineering*, vol. 23, 2011, pp 468-473.
- [34] J. Ahmed, Z. Salam. "An enhanced adaptive P&O MPPT for fast and efficient tracking under varying environmental conditions." *IEEE Transactions on Sustainable Energy*, vol. 9. 3, 2018, pp 1487-1496.
- [35] R. Alik, A. Jusoh. "An enhanced P&O checking algorithm MPPT for high tracking efficiency of partially shaded PV module." *Solar Energy*, vol. 163, 2018, pp 570-580.
- [36] J. L. Díaz-Barnabé, A. Morales-Acevedo. "Experimental study of the equivalence of the Adaptive Incremental Conductance (AIC) and the Adaptive Perturb and Observe (APO) algorithms for PV systems maximum power tracking." *IEEE Latin America Transactions*, vol. 17. 8, 2019, pp 1237-1243.
- [37] S. Motahhir, A. El Hammoui, A. El Ghzizal. "Photovoltaic system with quantitative comparative between an improved MPPT and existing INC and P&O methods under fast varying of solar irradiation." *Energy Reports*, vol. 4, 2018, pp 341-350.
- [38] A. Loukriz, M. Haddadi, S. Messalti. "Simulation and experimental design of a new advanced variable step size Incremental Conductance MPPT algorithm for PV systems." *ISA transactions*, vol. 62, 2016, pp 30-38.
- [39] M. Al-Dhaifallah, A. M. Nassef, H. Rezk, K. S. Nisar. "Optimal parameter design of fractional order control-based INC-MPPT for PV system." *Solar Energy*, vol. 159, 2018, 650-664.
- [40] O. Oussalem, M. Kourchi, A. Rachdy, M. Ajaamoum, H. Idadoub, S. Jenkal. "A low cost controller of PV system based on Arduino board and INC algorithm." *Materials Today: Proceedings*, vol. 24, 2020, pp 104-109.
- [41] K. Punitha, D. Devaraj, S. Sakthivel. "Artificial neural network based modified incremental conductance algorithm for maximum power point tracking in photovoltaic system under partial shading conditions." *Energy*, vol. 62, 2013, pp 330-340.
- [42] M. A. Elgendy, B. Zahawi, D. J. Atkinson. "Assessment of the incremental conductance maximum power point tracking algorithm." *IEEE Transactions on Sustainable Energy*, vol. 4. 1, 2012, pp 108-117.
- [43] S. Motahhir, A. Chalh, A. El Ghzizal, A. Derouich. "Development of a low-cost PV system using an improved INC algorithm and a PV panel Proteus model." *Journal of Cleaner Production*, vol. 204, 2018, pp 355-365.
- [44] S. Necaibia, M. S. Kelaiaia, H. Labar, A. Necaibia, E. D. Castronuovo. "Enhanced auto-scaling incremental conductance MPPT method, implemented on low-cost microcontroller and SEPIC converter." *Solar Energy*, vol. 180, 2019, pp 152-168.
- [45] T. Radjai, L. Rahmani, S. Mekhilef, J. P. Gaubert. "Implementation of a modified incremental conductance MPPT algorithm with direct control based on a fuzzy duty cycle change estimator using dSPACE." *Solar Energy*, vol. 110, 2014, pp 325-337.
- [46] K. S. Tey, S. Mekhilef. "Modified incremental conductance algorithm for photovoltaic system under partial shading conditions and load variation." *IEEE Transactions on Industrial Electronics*, vol. 61. 10, 2014, pp 5384-5392.
- [47] K. S. Tey, S. Mekhilef. "Modified incremental conductance MPPT algorithm to mitigate inaccurate responses under fast-changing solar irradiation level." *Solar Energy*, vol. 101, 2014, pp 333-342.
- [48] R. Çelikel, A. Gündoğdu. "ANN-Based MPPT Algorithm for Photovoltaic Systems." *Turkish Journal of Science and Technology*, vol. 15. 2, 2020, pp 101-110.
- [49] F. Kentli, M. Yilmaz. "Mathematical modelling of two-axis photovoltaic system with improved efficiency." *Elektronika Ir Elektrotehnika*, vol. 21. 4, 2015, pp 40-43.
- [50] A. Youssef, M. El Tebany, A. Zekry. "Reconfigurable generic FPGA implementation of fuzzy logic controller for MPPT of PV systems." *Renewable and Sustainable Energy Reviews*, vol. 82, 2018, pp 1313-1319.
- [51] A. Senthilvel, K. N. Vijeyakumar, B. Vinothkumar. FPGA Based Implementation of MPPT Algorithms for Photovoltaic System under Partial Shading Conditions. *Microprocessors and Microsystems*, 2020, 103011.
- [52] A. Messai, A. Mellit, A. M. Pavan, A. Guessoum, H. Mekki. "FPGA-based implementation of a fuzzy controller (MPPT) for photovoltaic module." *Energy Conversion and Management*, vol. 52. 7, 2011, pp 2695-2704.
- [53] A. Mellit, H. Rezzouk, A. Messai, B. Medjahed. "FPGA-based real time implementation of MPPT-controller for photovoltaic systems." *Renewable Energy*, vol. 36. 5, 2011, 1652-1661.
- [54] R. Celikel. "ANN based angle tracking technique for shaft resolver." *Measurement*, vol. 148, 2019, 106910.
- [55] S. Jaiswal, M. S. Ballal. "FDST-based PQ event detection and energy metering implementation on FPGA-in-the-loop and NI-LabVIEW." *IET Science, Measurement & Technology*, vol. 11. 4, 2017, pp 453-463.
- [56] S. Karimi, P. Poure, S. Saadate. "Fast power switch failure detection for fault tolerant voltage source inverters using FPGA." *IET Power Electronics*, vol. 2. 4, 2009, pp 346-354.
- [57] M. Morales-Caporal, J. Rangel-Magdaleno, H. Peregrina-Barreto, R. Morales-Caporal. "FPGA-in-the-loop simulation of a grid-connected photovoltaic system by using a predictive control." *Electrical Engineering*, vol. 100. 3, 2018, pp 1327-1337.
- [58] E. Deniz. "ANN-based MPPT algorithm for solar PMSM drive system fed by direct-connected PV array." *Neural Computing and Applications*, vol. 28. 10, 2017, pp 3061-3072.
- [59] O. Aydogmus. "Design of a solar motor drive system fed by a direct-connected photovoltaic array." *Advances in Electrical and Computer Engineering*, vol. 12. 3, 2012, pp 53-58.

## BIOGRAPHIES



**REŞAT ÇELİKEL** was born in 1980. He received B.S, M.S and PhD degrees from Firat University, Elazığ, Turkey. He has been working as an Assist. Prof. Dr. at Batman University. His current interests are electric machines, flywheel energy storage, FPGA, renewable energy.



**AHMET GÜNDOĞDU** Elazığ in 1974. He received the B.S. and M.S. degrees in electrical teaching from the University of Firat, Elazığ, in 2004 and the Ph.D. degree in electrical engineering from Firat University, Elazığ, in 2012.

# Comparison of T-Type Converter and NPC for the Wind Turbine Based on Doubly-Fed Induction Generator

Altan Gencer

**Abstract**—A three-phase T-type converter topology proposes for wind turbine based on doubly fed induction generator (DFIG). The proposed converter consists of only twelve power switches without flying capacitors or any clamping diodes. The proposed system is implemented to grid side converter of wind turbine. Fuzzy logic controllers are more widely used in wind turbines compared to traditional control systems. Fuzzy logic PI controller has been applied to T-type and the conventional neutral-point clamped (NPC) converters control circuits. Total harmonic distortion (THD) value of current of presented system is measured as 1.76%. Also, DC-link voltage utilization can be maintained. Comparisons are conducted with T-type converter and a 3L-NPC method under same operation conditions. The proposed scheme has been carried out to verify in simulation results.

**Index Terms**— T-type converter topology, doubly fed induction generator, wind turbine.

## I. INTRODUCTION

IN RECENT YEARS, wind turbines have gained considerable importance among renewable energy sources. The various types of generators are used in wind turbines such as doubly-fed induction generator (DFIG), squirrel-cage induction generator (SCIG), and permanent magnet synchronous generator (PMSG). DFIG is the most widely used of these generator types. DFIG cannot be connected directly to the grid system. The DFIG needs to the converters in order to connect to the grid system. [1, 2] The converter is made in various types. The two level three phase converters (traditional type) are used quite a lot in wind turbine. Traditional type converters have very simple structure and control system. On the other hand, the energy quality of traditional converters is low and they are not used for high voltage values. For this reason, multi-level converters have started to be applied for wind turbines in recent years [3].

ALTAN GENCER, is with Department of Electrical Engineering University of Nevşehir Hacı Bektaş Veli University, Nevşehir, Turkey, (e-mail: [altangencer@nevsehir.edu.tr](mailto:altangencer@nevsehir.edu.tr)).

 <https://orcid.org/0000-0002-5592-4070>

Manuscript received November 16, 2020; accepted February 06, 2021.  
DOI: [10.17694/bajece.826624](https://doi.org/10.17694/bajece.826624)

The high number of switches in multi-level inverter is a disadvantage. On another hand, multi-level converters have superior features compared to conventional converters. It can be used in applications that require high power and voltage. In addition to, it has a great advantage in terms of energy quality. Also, switching losses are low due to the fact that they operate at low switching frequency [4].

Three-level converter topologies are two types which name as Neutral-Point Clamped (3L-NPC) and T-type. 3L-NPC consists of 12 switching and 6 diodes. T-type consists of 12 switching elements. At the same time, T-type are not required high voltage and current diodes. T-type has a simpler structure than 3L-NPC, it is cheap, and it produces energy quality [4-7].

In this study, a three-phase 3-level T-type converter is proposed for wind turbines based on DFIG. Fuzzy logic PI controller has been applied to the control system of the proposed converter. Fuzzy logic controllers obtain more effective results in complex systems compared to conventional control systems. THD values of current and voltage at the output of both converters systems have been measured under same operation conditions. The THD value of the proposed system is lower 3L-NPC converter. High harmonic causes distortions in the system and decreases efficiency. The proposed system are used less electronic components compared to 3L-NPC. Therefore, the proposed system reduces the switching losses and the cost of the system. The efficiency of proposed converter type has been proven by compared to 3L-NPC converters.

The organization of this paper is as given: dynamic model of the wind turbine is expressed in Sec. 2. Proposed model is expressed in Sec. 3. T-type converter is explained in Sec. 4. Then, simulation results are explained in Sec. 5. The conclusion is given in Sec. 6.

## II. DYNAMIC MODEL OF WIND TURBINE

The wind turbine system consists of a generator, blade, electronic converters, filter, and control system. A generator converts from a mechanical power to an electrical power. A wind turbines converts from wind power to electrical power. The electrical energy generated by a generator is not suitable for connecting directly to the electrical grid system. Therefore, converters are used to connect a wind turbine to electrical grid system. The converters regulate the generated voltage of the generator by means of control systems.

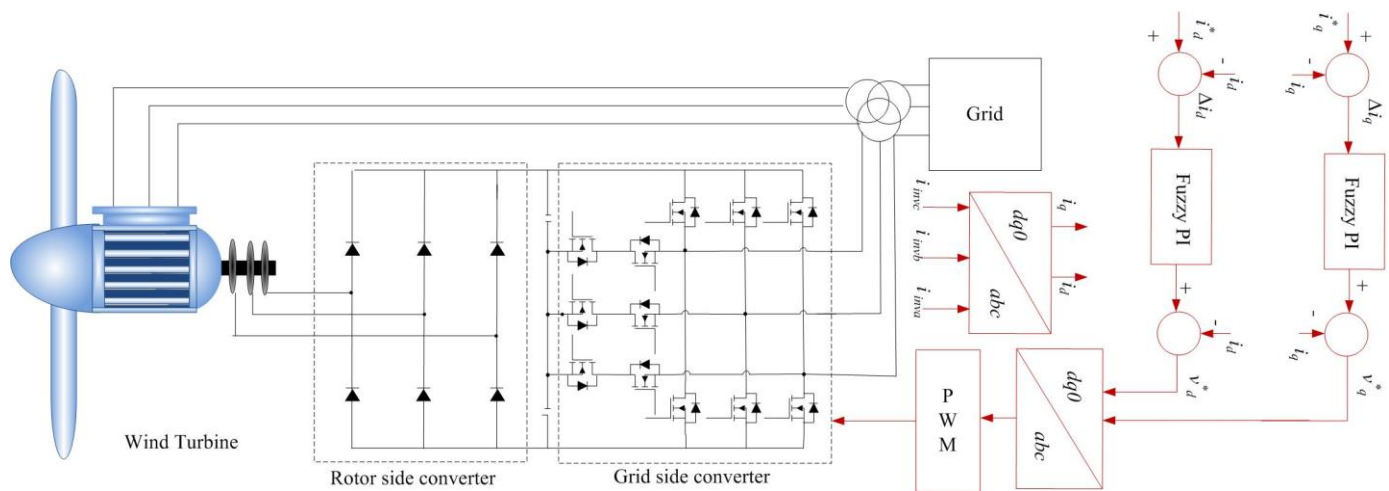


Fig. 1. Configuration with T-type converter of wind turbine based on DFIG.

### A. Wind Turbine

Wind turbines; It can be defined as mechanical systems that convert kinetic energy present in the wind into mechanical energy. The wind turbine cannot capture all the wind energy. For this reason, a mechanical power obtains from the wind turbine and is given in Eq. 1 [8].

$$P_m = \frac{1}{2} \rho A C_p(\lambda, \beta) v^3 \quad (1)$$

Where, the swept area of the rotor blades depicts  $A$ ,  $\rho$  represents the air density, the power conversion coefficient depicts  $C_p$ , the wind speed represents  $v$ . In this equation, if the swept area, air density and wind speed are taken as constant, aerodynamic power is obtained by the power factor of the wind turbine.  $\lambda$  represents a ratio between an angular velocity of a wind turbine and a wind speed. This ratio is expressed as the type speed ratio and is given in Eq. 2 [8]

$$\lambda = \frac{\omega_m R}{v} \quad (2)$$

### B. Mathematical model of DFIG

The mathematical model of DFIG is explained to simulate the whole system which consists of the stator and rotor. Several losses of DFIG are neglected such as hysteresis, magnetic saturation, stator, and rotor core losses. This model is the most widely accepted mathematical model of DFIG [1, 2].

$$v_s = R_s i_s + \frac{d\psi_s}{dt} + j\omega_e \psi_s \quad (2)$$

$$v_r = R_r i_r + \frac{d\psi_r}{dt} + j(\omega_e - \omega_r) \psi_r \quad (3)$$

The flux components of rotor and stator are expressed by:

$$\psi_s = L_s i_s + L_m i_r \quad (4)$$

$$\psi_r = L_r i_r + L_m i_s \quad (5)$$

### III. THE PROPOSED MODEL

The proposed model for DFIG based on T-type converter is illustrated in Fig. 1. Proposed system consists of the wind turbine, power electronic converters, and controller. The rotor side converter consists of a three-phase full-wave uncontrolled rectifier. Grid side converter consists of T-type converter. Grid and rotor side converters are used to supply the electrical energy produced by the double feed induction generator to the grid. The 2-level converter has a simple operating principle. Total harmonic distortion (THD) value of conventional converter is higher than multi-level converters, while the 2-level converter has a simple operating principle. Therefore, a three-phase T-type converter is built for the grid side converter of wind turbine system in this study. Grid and rotor side converters are used to supply the electrical energy generated by the double feed induction generator. The grid and rotor side controllers are designed to correct the electrical energy produced in the generator to meet the requirements of the load [9-19]. The three-phase T-type converter is given in Fig. 1.

In this study, a rotor and grid side converters were used to connect the wind turbine to the grid. Rotor side converter consists of three phase uncontrolled rectifier circuit. Rotor side converter converts 3-phase AC voltages generated by the double feed induction generator into DC voltage. A grid side converter converts from DC voltage to 3-phase AC voltage and provides it to be connected to the network. In this study, NPC and T type 3-phase converter types are applied for grid side converter. Fuzzy logic PI controller has been applied to these two converters control circuits. Fuzzy logic PI controller is more widely used in wind turbines compared to traditional control systems. Conventional control systems do not give effective results in varying operating conditions because its parameters are fixed. In this study, fuzzy logic PI controller block diagram applied to the controller of grid side converter and is given in Fig 2.a. In Fig. 2.b., the fuzzy logic PI controller consists of an input and an output. The error of the current value is read as an analog input from an input value of a fuzzy logic controller. A fuzzification is the process of transforming this analog input into fuzzy sets with some degree of membership. The input sets of the fuzzy controller

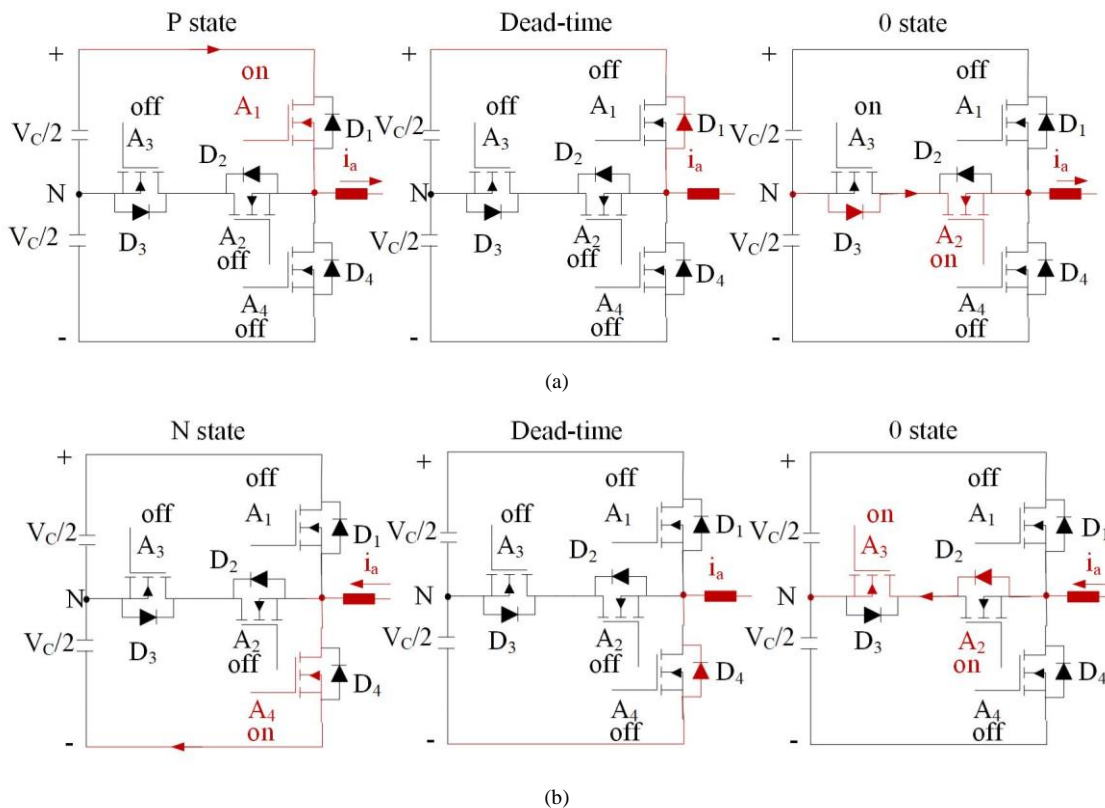


Fig.3. Current commutation during switching transition a) positive output current b) negative output current [5,14,15].

are divided into seven sections consisting of triangular and trapezoid shaped curves. These seven variables are called Positive Small (PS), Positive Medium (PM), Positive Large (PB) Zero (Z), Negative Large (NB), Negative Medium (NM), and Negative Small (NS). In this study, the output sets of the fuzzy controller are divided into seven sections consisting of triangular and trapezoidal shaped curves. Defuzzification converts a fuzzy truth values to continuous output variable [2, 10, 11, 12, 13]. The defuzzification is expressed by:

$$y = \frac{\sum_{i=1}^m y_i + \mu_i(y_i)}{\sum_{i=1}^m \mu_i} \quad (6)$$

Where,  $\mu_i(y_i)$  depicts the membership function,  $m$  represents the output quantificational index,  $y_i$  represents the output variable,  $y$  is the defuzzified output. [2, 10, 11].

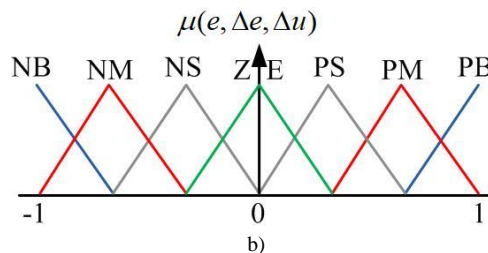
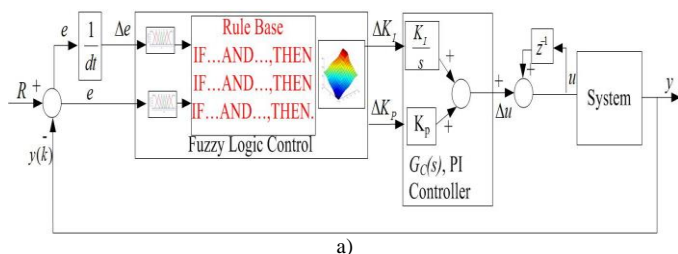


Fig.2. a)The general block diagram of fuzzy PI control method. b) MFs of  $e$ ,  $\Delta e$ , and  $\Delta u$  [2, 10, 11].

IV. T-TYPE CONVERTER

A three level T-type converter method is illustrated in Fig. 3. The switching states of T-type converter are illustrated in Table I [5, 14-19]. The switching states are the negative (N), neutral (0), and the positive (P) of dc-link voltage level. Three voltage levels of phase-neutral voltage are obtained by these switching states. The T-type method uses the same switch signals of the three-level NPC method modulation. A simple delay between switching on and off is applied to avoid a short circuit in a DC link [14-16].

TABLE I. Switching States [5, 14, 15, 16]

State	Q1	Q2	Q3	Q4
P	1	1	0	0
0	0	1	1	0
N	0	0	1	1

The current flows towards the AC terminal when the output voltage is positive. As seen in Fig. 3. a. [5, 14-16], the current flows from  $V_{DC}$  (+) via  $A_1$  to output terminal when  $A_1$

switches on. A simple delay between switching on and off is applied to avoid a short circuit in a DC link. A simple delay time is 1ms and all switches are off during this time. The current commutates to the inner switches  $A_2/D_3$  when  $A_1$  is switched off. The current flows from N via  $D_3$  and  $A_2$  to output terminal. [15, 16].

The current flows towards the  $V_{DC}$  (-) when the output voltage is negative. As seen in Fig. 3. b. [5, 14-16], the current flows from output terminal to  $V_{DC}$  (-) via  $A_4$  when  $A_4$  switches on. A simple delay between switching on and off is applied to avoid a short circuit in a DC link. A simple delay time is 1ms and all switches are off during this time. The current commutates to the inner switches  $A_3/D_2$  when  $A_4$  is switched off. The current flows from output terminal via  $A_3$  and  $D_2$  to N. [15, 16].

A 3L-NPC phase leg consists of 10 semiconductors which are 2 two diodes, 4 IGBTs, and 4 antiparallel free-wheeling diodes, while T-type phase leg composed of 8 semiconductors. The difference between NPC and T-type method is not only the number of power electronics. To achieve the same current THD value as 3L topology, switching frequency is reduced, resulting in reduced switching power losses [15, 16].

V. SIMULATION RESULTS

Both the proposed and NPC systems are implemented to the wind turbine which has the same power and control structures. The presented system is built-in Matlab / Simulink. Simulation parameters are applied to simulation time  $2\mu s$  and active power of wind turbine are 9MW. The switching signals required for the semiconductors are generated with priority in the Simulink study. The switching signals of a phase leg are illustrated in Fig. 4. T-type topology uses same switching signals of three-level NPC topology. The switching signals are obtained by comparing the reference sinusoidal wave with the triangular carriers. Also, switching signals are derived by means of control systems.

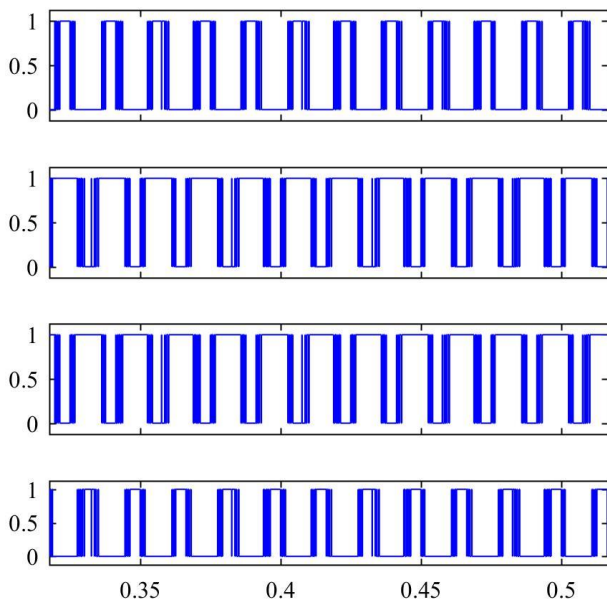


Fig.4. A phase leg switching signals

A phase of grid side converter output is given in Fig. 5. Blue line illustrates no filter of an output phase to phase voltage in Fig.5. Red line illustrates the filter of an output phase to phase voltage.

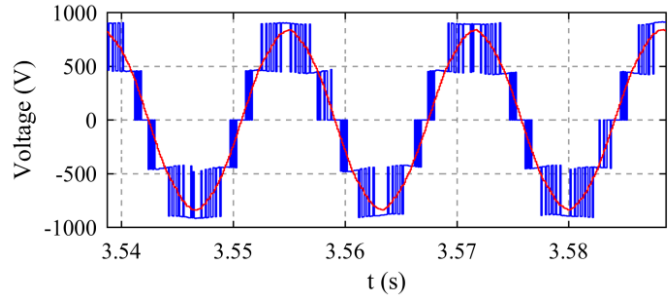


Fig.5. Filter and non-filter of output voltages of the converter

Output voltages of grid side converter are given in Fig. 6. The output voltage values are 1 p.u. The output currents of grid side converter are given in Fig. 7. The output current values are 1 p.u. The simulation tests are realized to confirm the dynamic performance of proposed system. From the current graph in Fig. 8, it is observed that there is no high level of disturbance effect on the signal. The THD value of current of proposed system is 1.76%. Also, this value is below the 5% limit specified in the IEEE 1547 standard.

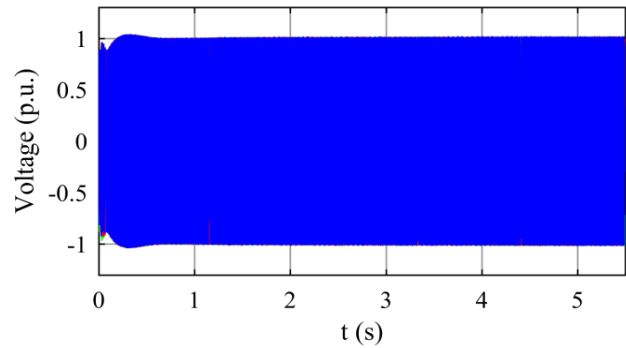


Fig.6. Three phase output voltages of the T-type converter

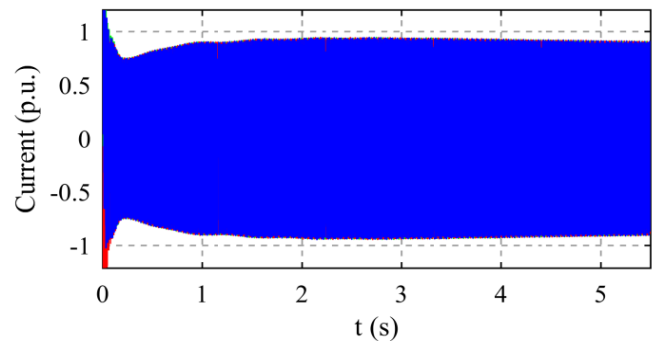
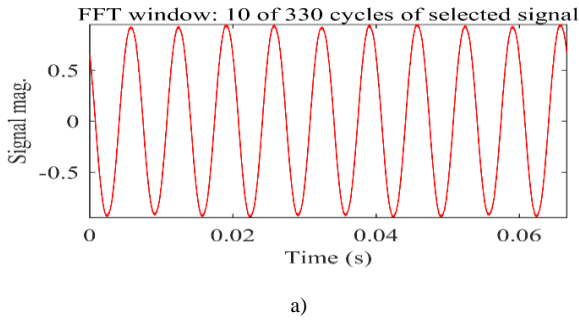
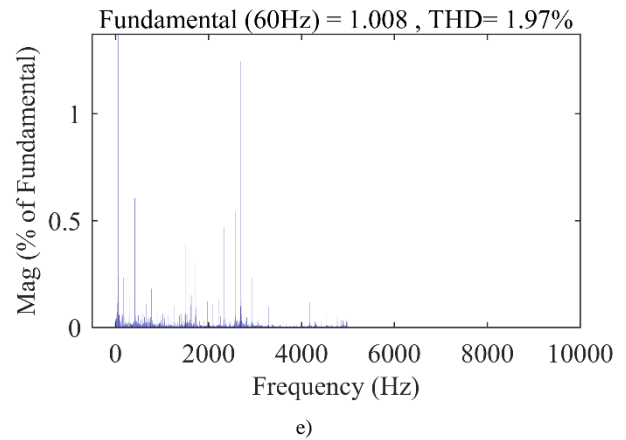


Fig.7. Three phase output currents of the T-type converter

Signal



FFT analysis



FFT analysis

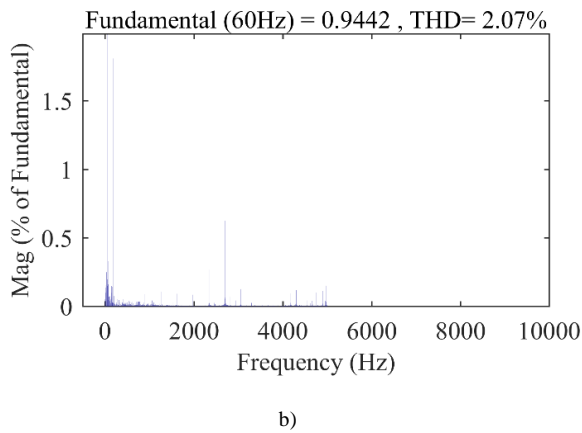


Fig.8. FFT analysis of load current and phase voltage a) signal of current b) THD value of voltage of T-type c) THD value of current of T-type d) THD value of voltage of 3L-NPC e) THD value of current of 3L-NPC

Active power of presented system is illustrated in Fig. 9. The values of active power are 9 MW. A voltage (Vdc) of presented system is given in Fig. 10. The value of Vdc is 1150 V. The simulation tests are realized to confirm the dynamic performance of proposed system.

FFT analysis

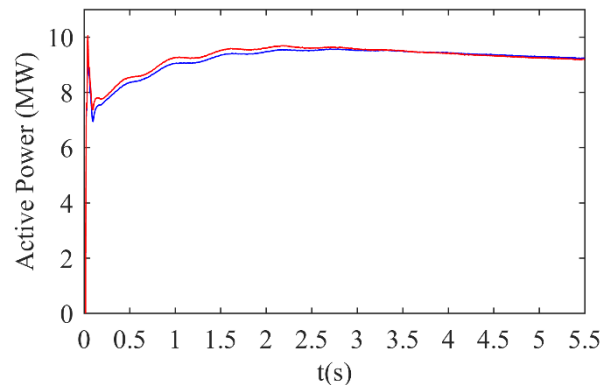
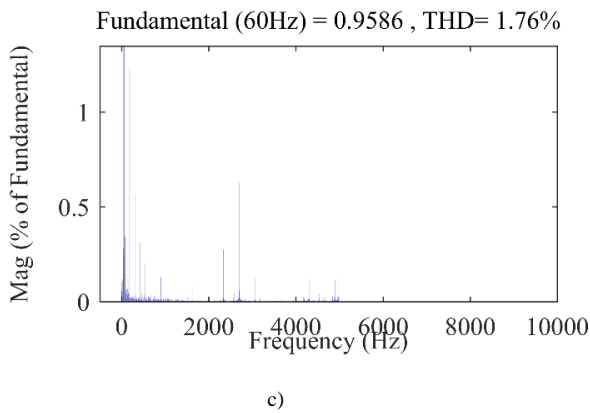


Fig.9. Active Power

FFT analysis

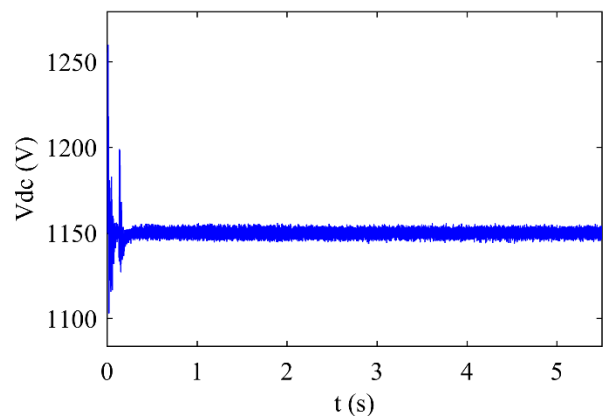
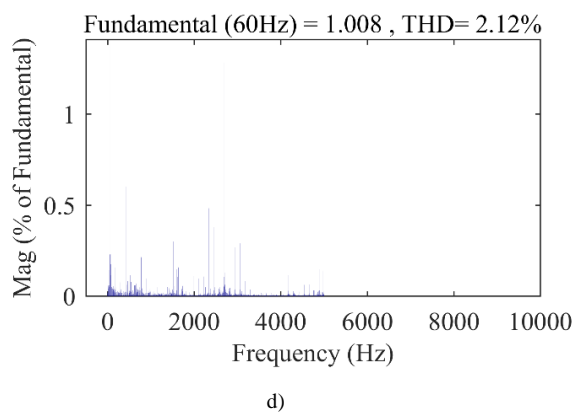


Fig.10. DC link voltage

## VI. CONCLUSION

A three-phase T-type converter topology is presented for wind turbine based on DFIG. The proposed converter system

is implemented to grid side converter of wind turbine. Fuzzy logic PI controller is applied in the control systems of both converters. THD values of the output voltage and current of the system are measured under same operation conditions. In addition to, DC link and active power values of the system are measured. The DC link voltage value is kept constant at 1150 V. The THD value of the current of the system presented is measured as 1.76%. Also, this value is below the 5% limit specified in the IEEE 1547 standard. The proposed system are used less electronic components compared to 3L-NPC. Therefore, the proposed system decreases the switching losses and the cost of presented system. The efficiency of proposed converter type has been proven by compared to 3L-NPC converters.

## REFERENCES

- [1] S. Bayhan, S. Demirbas and H. Abu-Rub, "Fuzzy-PI-based sensorless frequency and voltage controller for doubly fed induction generator connected to a DC microgrid," in *IET Renewable Power Generation*, vol. 10, no. 8, pp. 1069-1077, 9 2016, doi: 10.1049/iet-rpg.2015.0504.
- [2] S. Demirbas, "Self-tuning fuzzy-PI-based current control algorithm for doubly fed induction generator," in *IET Renewable Power Generation*, vol. 11, no. 13, pp. 1714-1722, 15 11 2017, doi: 10.1049/iet-rpg.2016.0700.
- [3] M. Z. Sujod and I. Erlich, "A new protection scheme for three-level NPC converter based DFIG using zero state control," *IEEE PES ISGT Europe 2013*, Lyngby, 2013, pp. 1-5, doi: 10.1109/ISGTEurope.2013.6695240.
- [4] C. Qin, C. Zhang, A. Chen, X. Xing and G. Zhang, "A Space Vector Modulation Scheme of the Quasi-Z-Source Three-Level T-Type Inverter for Common-Mode Voltage Reduction," in *IEEE Transactions on Industrial Electronics*, vol. 65, no. 10, pp. 8340-8350, Oct. 2018, doi: 10.1109/TIE.2018.2798611.
- [5] M. Schweizer and J. W. Kolar, "Design and Implementation of a Highly Efficient Three-Level T-Type Converter for Low-Voltage Applications," in *IEEE Transactions on Power Electronics*, vol. 28, no. 2, pp. 899-907, Feb. 2013, doi: 10.1109/TPEL.2012.2203151.
- [6] M. Barzegar-Kalashani, B. Tousi, M. A. Mahmud and M. Farhadi-Kangarlu, "Non-linear integral higher-order sliding mode controller design for islanded operations of T-type three-phase inverter-interfaced distributed energy resources," in *IET Generation, Transmission & Distribution*, vol. 14, no. 1, pp. 53-61, 17 1 2020, doi: 10.1049/iet-gtd.2019.0795.
- [7] Z. Zhang, A. Anthon and M. A. E. Andersen, "Comprehensive loss evaluation of neutral-point-clamped (NPC) and T-Type three-level inverters based on a circuit level decoupling modulation," *2014 International Power Electronics and Application Conference and Exposition*, Shanghai, 2014, pp. 82-87, doi: 10.1109/PEAC.2014.7037833.
- [8] S. Tohidi, P. Tavner, R. McMahon, H. Oraee, MR. Zolghadri, S. Shao S, et al. "Low voltage ride-through of DFIG and brushless DFIG: similarities and differences" *Electric Power System Research*, vol. 110, p.p. 64-72, 2014. doi: 10.1016/j.epr.2013.12.018.
- [9] R. Çelikel "Speed control of BLDC using NARMA-L2 controller in single link manipulator." *Balkan Journal of Electrical and Computer Engineering* 7.2 (2019): 143-148.
- [10] A. Gencer, "Modelling and control of permanent magnet synchronous generator based on three level NPC using fuzzy PI" . *Balkan Journal of Electrical and Computer Engineering* 6 (2018 ): 172-177
- [11] A. Gencer, "Analysis of Speed/Position Controller Based on Several Types of a Fuzzy Logic for Travelling Wave Ultrasonic Motor," *2019 1st Global Power, Energy and Communication Conference (GPECOM)*, Nevşehir, Turkey, 2019, pp. 170-174, doi: 10.1109/GPECOM.2019.8778619.
- [12] M. R. Tur, M. Wadi, A. Shobole and S. Ay, "Load Frequency Control of Two Area Interconnected Power System Using Fuzzy Logic Control and PID Controller," *2018 7th International Conference on Renewable Energy Research and Applications (ICRERA)*, Paris, 2018, pp. 1253-1258, doi: 10.1109/ICRERA.2018.8566890.
- [13] M. Wadi, A. Shobole, M. R. Tur and M. Baysal, "Smart hybrid wind-solar street lighting system fuzzy based approach: Case study Istanbul-Turkey," *2018 6th International Smart Grids and Cities Congress and Fair (ICSG)*, Istanbul, 2018, pp. 71-75, doi: 10.1109/SGCF.2018.8408945.
- [14] Z. Wang, Y. Wu, M. H. Mahmud, Z. Zhao, Y. Zhao and H. A. Mantooth, "Design and Validation of A 250-kW All-Silicon Carbide High-Density Three-Level T-Type Inverter," in *IEEE Journal of Emerging and Selected Topics in Power Electronics*, vol. 8, no. 1, pp. 578-588, March 2020, doi: 10.1109/JESTPE.2019.2951625.
- [15] Semikron "Application Note AN-11001: 3L NPC & TNPC Topology" <http://www.semikron.com>, crawled on July 2020.
- [16] N. Güler ve E. İrmak , "Nötr Kenetlemeli Eviriciler için Çok Giriş – Çok Çıkışlı DA-DA Çevirici Tasarımı ve Kontrolü", *Gazi Üniversitesi Fen Bilimleri Dergisi Part C: Tasarım ve Teknoloji*, c. 7, sayı. 1, ss. 49-62, Mar. 2019, doi:10.29109/gujsc.490144
- [17] A. Gündoğdu, R. Çelikel, and Ş. Fidan. "Analysis and Simulation of A Three-Phase Delta Inverter for A Star-Connected RL Load." *European Journal of Technice* 10.2, 2020, 274-288.
- [18] M. Yılmaz, "Real measure of a transmission line data with load fore-cast model for the future." *Balkan Journal of Electrical and Computer Engineering* 6.2 (2018): 141-145.
- [19] Shuhui Li, T. A. Haskew and J. Jackson, "Power generation characteristic study of integrated DFIG and its frequency converter," *2008 IEEE Power and Energy Society General Meeting - Conversion and Delivery of Electrical Energy in the 21st Century*, Pittsburgh, PA, 2008, pp. 1-9, doi: 10.1109/PES.2008.4596058.

## BIOGRAPHY



**ALTAN GENCER** was born in 1978. He received the M.Sc. degree of Electrical Education at Technical Education Faculty of Fırat University, 2002. He received Ph. D. degree of Electrical Education at Technical Education Faculty of Gazi University, 2011. From 2014, he is assistant professor by in Department of Electrical and Electronics Engineering, Faculty of Engineering in the Nevşehir H.B.V. University in Turkey. His research interests include of wind farm dynamic modeling, fuzzy logic control system.

# Reconstruction of the Taguchi Orthogonal Arrays with the Support Vector Machines Method

Selçuk Yazar

**Abstract**—Design of Experiment (DOE) is a widely used method for examining experiments especially in industrial production and robust design processes. This method is a set of statistical approaches in which mathematical models are developed through experimental testing to estimate possible outputs and given input values or parameters. The method aims to determine the main factors that affect the results with the smallest number of experimental studies. In this study, L16 ( $2^{15}$ ) orthogonal array, which was used in the Taguchi parameter design was reconstructed with the Support Vector Machines learning model and the Pearson VII kernel function. With this model, array elements were successfully classified in 87.04%. The new and original array were compared and 3.8% difference was measured between their Signal to Noise (S / N) ratios in an exemplary experiment.

**Index Terms**— Machine Learning, Support Vector Machine, Taguchi Design, Design of Experiments, Robust Design.

## I. INTRODUCTION

TODAY, IN many manufacturing applications, Taguchi's orthogonal array catalogs are used for industrial designs. Genichi Taguchi redesigned offline quality control methods [1], which were developed in Japan after World War II in the 1980s under the name of robust design in AT & T Bell laboratories. This method is generally called Taguchi orthogonal array design. For instance, in this method, determining the optimum levels of the nine control variables requires 6.000 possible combinations, while only 18 different controllable variables are adequate [2]. To give another example, let's assume that eight factors are affecting the experiment during the development of a robust model. If one of these factors affects two and seven of them at three levels,  $2 \times 3^7 = 4.347$  experiments should be performed to reach optimum values. If there are 15 parameters per three levels in this instance,  $3^{15} = 14.348.907$  distinct experiments are required. Taguchi's orthogonal array method is the solution in this type of experiment designs in which applying is practically difficult. This technique is used conventionally for industrial production areas.

**SELÇUK YAZAR**, is with Department of Computer Engineering Trakya University, Edirne, Turkey, (e-mail: selcukyazar@trakya.edu.tr).

 <https://orcid.org/0000-0001-6567-4995>

Manuscript received December 11, 2020; accepted March 29, 2021.

DOI: [10.17694/bajece.839449](https://doi.org/10.17694/bajece.839449)

Also, Taguchi designs use in Environmental Sciences [3, 4], Agricultural Sciences [5], Physics [6], Chemistry [7], Statistics [8], and Medicine [9] frequently. However, Genichi Taguchi did not share any information about the methods that are used to construct these arrays. Furthermore, it is difficult to distinguish the links between Taguchi's arrays and the published similar arrays elsewhere [10, 11].

In this study, we aimed to regenerate the L16 ( $2^{15}$ ) Taguchi array using support vector machines methods, based on two-level L4, L8, L12 arrays which are found in the Taguchi arrays catalog. We compared the array that we obtained and the original array with a sample experiment. In addition, the variation of the factors are affecting the results is discussed in the sample experiment.

This paper is organized as follows: In Section 2 we present information about orthogonal arrays. In section 3 we briefly describe the support vector machines and the Pearson VII function. Also, we provide a description of the sequential minimal optimization algorithm that we used for classification. Finally, in section 4 we describe our proposal and discuss our results.

## II. ORTHOGONAL ARRAYS AND EXPERIMENT DESIGN

Orthogonal arrays were first described by C.R.Rao as hypercube in 1946 [12] and introduced as statistical combinatorial arrangements methods. An orthogonal array consists of  $N$  rows and  $k$  columns, selected entries from a set of  $s$  symbols or levels defined as  $S = \{0, 1, \dots, s-1\}$ . The term "Level" in the array definition is used to indicate the level of factors and variables that have an impact on the test components in the experimental designs using these arrays. An  $N \times k$  matrix  $A$  formed in this way is called an orthogonal array of level  $s$  and strength  $t$ . In such a notation  $s$  denotes the number of levels. If the number  $s$  is equal to 2, there are two levels in the array, 0 and 1.

The  $t$  value is defined in the interval ( $0 \leq t \leq k$ ). This value tells us the number of  $s^t$  possible  $t$ -tuples belonging to  $N \times t$  subarrays that can be defined in array  $A$ . These  $t$ -tuples are also equal to the number of rows of the array. In addition, the value of  $\lambda$  is used to define the index of these arrays. The  $\lambda$  value indicates the number of repetitions of  $t$ -tuples up to  $s^t$ . When  $\lambda = 1$ , it is stated that the orthogonal array has the index unity. The orthogonal arrays are briefly denoted as  $OA(N, k, t, s)$  or  $OA(N, s^k, t)$ . In summary, integers that are defined as  $N, k, s, t$

are parameters of orthogonal arrays. The number of rows  $N$  is the number of runs indicating the number of experiments performed. The number of  $k$  columns refers to the combination of factors affecting the experiment.  $s$  is the number of levels,  $t$  is the strength. Let  $OA(12,11,2,2)$  be the 12 rows (number of runs), 11 columns(number of factors), 2 levels, and with strength 2 and of index unity orthogonal array. This array is shown in Table 1.

TABLE I: EXAMPLE OF A STANDARD 2 LEVELS ORTHOGONAL ARRAY.

0	0	0	0	0	0	0	0	0	0	0	0
1	1	1	0	1	1	0	1	0	0	0	0
0	1	1	1	0	1	1	0	1	0	0	0
0	0	1	1	1	0	1	1	0	1	0	0
0	0	0	1	1	1	0	1	1	0	1	0
1	0	0	0	1	1	1	0	1	1	0	0
0	1	0	0	0	1	1	1	0	1	1	1
1	0	1	0	0	0	1	1	1	0	1	0
1	1	0	1	0	0	0	1	1	1	1	0
0	1	1	0	1	0	0	0	1	1	1	1
1	0	1	1	0	1	0	0	0	1	1	1
1	1	0	1	1	0	1	0	0	0	1	1

For instance, let the first and last columns be selected of the exemplary orthogonal array described in Table 1. In this case, obtained new array shown in Table 2.

TABLE II: RANDOMLY SELECTED ARRAY COLUMNS

0	0
1	0
0	0
0	0
0	1
1	0
0	1
1	1
1	0
0	1
1	1
1	1

If pay attention to Table 2, four distinct rows can be seen. These are  $0\ 0$ ,  $0\ 1$ ,  $1\ 0$ ,  $1\ 1$  matrices in order and can be seen they repeat three times. 0 and 1 values in this array can be defined statistically as two different elements. For instance, consider that an experiment is conducted on food ingredients. Designers have standardized all other ingredients except sugar amount and fat type. The values in Table 2 could be changed, “sugary”, “sugarless”, “margarine”, “butter” respectively. It shows that there are two factors in this experiment and these factors have two levels. In this respect, this array is called a two-level array. 11 columns in the matrix, 11 different variables, 12 rows tell 12 different experiments can be done depending on these 11 variables.

Also, Mixed-level orthogonal arrays are defined as well as sequences with two levels. In cases where factors affecting an experiment have different levels, the orthogonal arrays that are used may expand accordingly. In mixed-level orthogonal arrays, there are more than one  $S$  sets where the levels are obtained. In this case, the mixed-level arrays are

shown as  $OA(N, s_1^{k_1}, s_2^{k_2}, \dots, s_n^{k_n}, t)$ . The first  $k_1$  column in the array is obtained from the  $S_1$  set, the next  $k_2$  column from the  $S_2$  set. However, there is no index definition in mixed-level arrays.

The algorithms for constructing standard orthogonal arrays have been clearly explained mathematically over time. Although Taguchi arrays are formed from existing arrays, there is no known method for all. Taguchi has a total of 21 orthogonal arrays of 2, 3, and 4 levels, in order. Unlike existing orthogonal notations, Taguchi arrays are denoted like below.

$$L \text{ (number of experiments) (Level}^{Factor})$$

Here, for example, the array denoted as  $L4(2^3)$ , 4 is the numbers of experiments(runs), 3 factors with 2 levels (variable) for each factor. Similarly, mixed-level sequences are defined in the Taguchi catalog. For example, an  $L8(2^3 4^1)$  means that the design has 8 runs, 3 factors with 2 levels, and 4 factors with 1 level.  $L4(2^3)$  and  $L8(2^3 4^1)$  are shown in Table 3.

TABLE III: (A)  $L4(2^3)$  2-LEVEL ORTHOGONAL ARRAY, (B)  $L8(2^3,4^1)$  MIXED-LEVEL ORTHOGONAL ARRAY

	1	2	3
1	1	1	1
2	1	2	2
3	2	1	2
4	2	2	1

	1	2	3	4	5
1	1	1	1	1	1
2	1	2	2	2	2
3	2	1	1	2	2
4	2	2	2	1	1
5	3	1	3	1	2
6	3	2	1	2	1
7	4	1	2	2	1
8	4	2	1	1	2

In Taguchi designs, for the analysis of the results are obtained from the experiments, the performance statistics method called Signal to Noise (S / N) ratio is used. Performance statistics are used to measure the effects of uncontrollable factors (noise factors) in the experiment. Noise factors (uncontrollable factors) cause deviation in the values that are obtained from the results of the experiment. There are three S/N ratios in the Taguchi design shown in Table 4.

TABLE IV: SIGNAL-TO-NOISE RATIO CALCULATION METHODS

S/N Characteristic	S/N Ratio	Comments
Smaller is better	$-10 \log\left(\frac{1}{n} \sum y_i^2\right)$	$n$ = Number of responses in the factor level combination. $y_i$ = Responses for the given factor level combination.
Nominal is best	$-10 \log\left(\frac{\bar{y}}{s^2}\right)$	$\bar{y}$ = Mean of responses for the given factor level combination $s$ = Standard deviation of the responses for the given factor level combination
Larger is better	$-10 \log\left(\frac{1}{n} \sum \frac{1}{y_i^2}\right)$	$y_i$ = Responses for the given factor level combination $n$ = Number of responses in the factor level combination.

As the ratio S/N increases, the result variance decreases around the target value. While determining the factor level is preferred for effective factors, the value with the highest S/N ratio is taken into consideration in experiment design.

### III. SUPPORT VECTOR MACHINES AND PEARSON VII KERNEL

Support vector machines (SVM) are located in supervised learning in the machine learning paradigm. It is used for case classification and pattern recognition in many different research disciplines such as medicine [13] and signal processing [14]. It is also an effective method to use decision trees with SVM to solve multi-class problems. Decision trees are preferred to determine measurement performances and make predictions [15]. The algorithms are used in SVM applications are very successful in classification problems. They are used to classify data sets that cannot be separated linearly. In summary, the algorithms are used herein look for a linearly separable hyperplane or a decision boundary that separates members of one class from another. If this decision boundary is found to be immensely successful, the desired classification result is achieved. An SVM classification model requires two main components: the support vector itself and the optimal decision limit.

Assuming that there is a set of two classes that can be easily separated from each other, there can be an infinite number of linear planes separating these two classes. If any  $i$  indexed point represented as  $(X_i, Y_i)$  has definite values such as +1 or -1, it is necessary to identify the planes separating these points

from each other and to determine which of these planes makes the best classification. The example classification result is shown in Fig. 1.

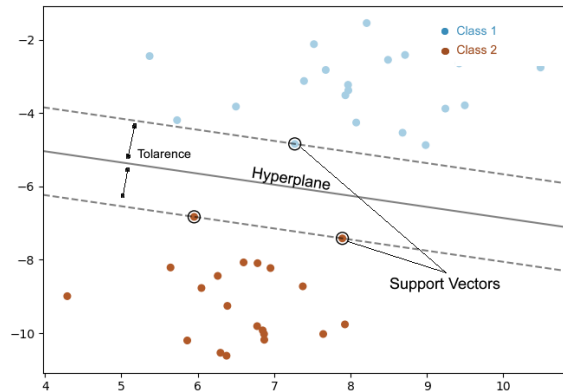


Fig. 1: Example of two-dimensional support vector machines classification.

When the values in classes 1 and 2 are displaced over time, there is a need to reconstruct the obtained planes to determine the optimum state and to rebuild the model. SVM algorithms are used for this purpose. Two classification methods are used in the SVM. These methods are called C-SVM and nu-SVM.

C-SVM is an error function is used conventionally to improve the compatibility of SVM. In the C-SVM model, the C value is used to systematically control the tolerance of discrete values. The coefficient C is an empirical parameter that works with grid search management. C-SVM function shown in equation 1, where  $w$  is the vector indicates the coefficients and  $\varphi_i$  is the slack variable and is also known as the training error for the training vector.

$$\tau(w, \varphi) = \frac{1}{2} \|w\|^2 + C \sum_{i=1}^N \varphi_i \quad (1)$$

nu-SVM models have been developed as an alternative to the C parameter. In the solution of nonlinear problems, the C value is used as a weight parameter to measure learning errors and tolerance of plane and support vectors in the classification process. In equation 1 the parameter C is replaced by  $\vartheta$  parameter. The parameter  $\vartheta$  in the nu-SVM model represents the fraction of the support vectors expected in the solution of the problem. Thus, for any given value of  $(0, 1]$ , the shape of the classifier can be predetermined. nu-SVM classifier shown in equation 2.

$$\tau(w, \varphi, \rho) = \frac{1}{2} \|w\|^2 - \vartheta \rho + \frac{1}{N} \sum_{i=1}^N \varphi_i \quad (2)$$

subject to  $\varphi_i \geq 0, \rho \geq 0$

In  $n$ -dimensional space, a hyperplane is an  $n-1$ -dimensional flat subspace. As it can be seen in Fig. 1, the hyperplane is a one-dimensional line, which is found as a separator in 2-dimensional space. The hyperplane of the classes distributed in 3-dimensional space will be a 2-dimensional plane. If expressed mathematically; In a space with  $n$  dimensions, a separating

hyperplane will be the linear combination of dimensions with a sum of 0.

$$\theta_0 + \theta_1 x_1 + \theta_2 x_2 + \dots + \theta_n x_n = 0 \quad (3)$$

The value  $\theta_0$  in equation 3 is often referred as a deviation. If the value  $\theta_0$  equals zero, the hyperplane will be at the origin point.

However, most classification problems cannot be solved by a linear function. There is various type of functions to obtain the hyperplane between the two classes and these functions are called the kernel. Besides the linear kernel function, polynomial, radial based, and sigmoid functions are also used. The kernel functions are expressed as  $K(X_i, X_j)$ . In the kernel functions, the data set classes are separated by using the C and  $\mathcal{S}$  parameters [16, 17].

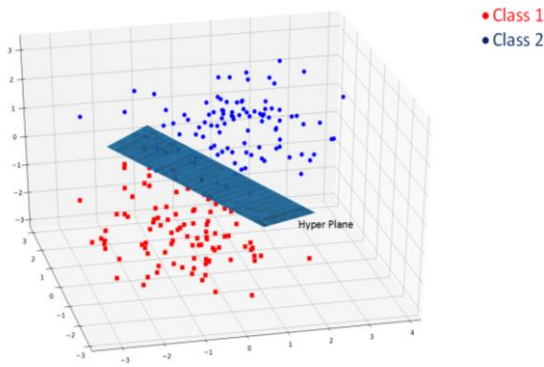


Fig. 2: Example of three-dimensional support vector machine classification.

As shown in Fig. 2, when classification solutions cannot always be easily solved by a linear function, alternative solutions can be found in spaces with increased dimensions. The kernel functions and dependent parameters should be determined according to the solution. In addition to linear solutions, different kernel functions should be used to separate and classify data sets belonging to multiple and nested classes.

#### A. Pearson VII kernel function

The Pearson VII function was used for classification that was developed in 1895 for X-ray diffraction scanning and for more accurate estimation of Gauss and Lorentz graphs with the parameter  $\omega$ . Thus, these graphs, which are formed by the control of  $\omega, \sigma$  parameters, have behaved similarly to the sigmoid function which is frequently used in artificial neural network research [18]. The kernel functions which are used in support vector machines are symmetric and semi-defined positive. In general, any kernel function fulfilling the Mercer's theorem conditions belongs to the class of valid kernel functions. The Mercer's theorem implies that a valid kernel function must be symmetric [19]. The resulting symmetrical matrix representing the kernel matrix must be positive semi-definite. The Pearson VII function is as follows:

$$K(x_i, x_j) = \frac{1}{\left[ 1 + \left( \frac{2 \sqrt{\|x_i - x_j\|^2 \sqrt{2^{(1/\omega)} - 1}}}{\sigma} \right)^2 \right]^\omega} \quad (4)$$

where  $x_i$  and  $x_j$  are two vector arguments. The single variable in the original version of the function is replaced by two vector arguments so that the Euclidean distance is measured between them. If one of the symmetrical or positive semi-definite conditions is met, then the conditions of the Mercer's are supplied. As a consequence, the PUK function satisfies all these requirements.

#### B. Sequential minimal optimization-SMO

The SMO algorithm is used to train support vector machines classifier functions. The SMO is developed to solve the known optimization problem in quadratic programming [20]. The optimization problem is shown as follows,

$$\max_{\alpha} \psi(\alpha) = \sum_{i=1}^N \alpha_i - \frac{1}{2} \sum_{i=1}^N \sum_{j=1}^N y_i y_j k(x_i, x_j) \alpha_i \alpha_j \quad (5)$$

Equation 5 is dependent on the terms  $\sum_{i=1}^N y_i \alpha_i = 0, 0 \leq \alpha_i \leq C$  and  $i = 1, \dots, n$ . Here,  $x_i$  represents the training example,  $y_i \in \{-1, +1\}$  the dependent target value,  $\alpha_i$  represents the Lagrange multiplier and  $C$  represents an SVM hyperparameter.

This method solves the main optimization problem of SVM by accepting two Lagrange multipliers  $\{\alpha_1, \alpha_2\}$  as a starting value of  $\alpha_1^{old} = \alpha_2^{old} = 0$  in a previous set of solutions  $\{\alpha_1^{old}, \alpha_2^{old}, \alpha_3^{old}, \dots, \alpha_n^{old}\}$  for a classification problem.

In equation 5, given  $t = y_1 y_2$ ,  $y_1 \alpha_1 + y_2 \alpha_2 = y_1 \alpha_1^{old} + y_2 \alpha_2^{old} = constant$  and  $\alpha_1 = \sigma - t \alpha_2$  values are replaced and also eliminating  $\alpha_2$  via the first and second derivatives;

$$\alpha_j^{new} = \alpha_j^{old} + \frac{y_j (E_j^{old} - E_i^{old})}{\eta} \quad (6)$$

The  $\alpha_j^{new}$  value is obtained in equation 6. Here  $E_i$  prediction error and the value  $\eta$  is defined as  $2k_{ij} - k_{ii} - k_{jj}$ . The value  $E_i$  is the error that the  $i$ th training example and  $E_i = (u_i - y_i)$  where  $u_i$  is the plane of the classification.

The main problem encountered in the training of data sets in the SVM method is that time performance in the training sets into chunks is poor. This is called a constrained quadratic programming problem in the literature. The SMO algorithm greatly improves the training performance of sparse data sets in these classification tasks. Although SMO offers a fast solution for sparse datasets, especially for linear SVMs, this algorithm can be extremely slow in non-sparse datasets. In this paper, we did not have a performance problem as we are using a small dataset and a nonlinear kernel function.

## IV. CLASSIFICATION RESULTS AND CONCLUSION

In this study, in order to reconstruct the L16 ( $2^{15}$ ) Taguchi array, we formed the classification model by using the support vector machine model which belongs to L4 ( $2^3$ ), L8 ( $2^7$ ), L8 ( $2^4$ ), and L12 ( $2^{11}$ ) 2-level arrays [21]. During the creation of the model, we also tested with various kernel functions that were used for SVM. Moreover, we achieved the highest performance classification with the Pearson VII kernel (PUK)

function that was used with Sequential Minimal Optimization algorithm.

Firstly, we created the model for the L16 2-level orthogonal array with the PUK kernel. At the time of the model creation, the maximum successful classification results were obtained by changing the classifier parameters  $C$ ,  $\vartheta$ , and Pearson VII kernel function parameters  $\omega$ ,  $\sigma$  is shown in Table 5.

TABLE V  
COMPARISON OF CLASSIFICATION RESULTS WITH VARIOUS KERNEL FUNCTIONS.

Method	Sigmoid	RBF	Linear	Polynomial	PUK
C-SVM	%54,4	%57,24	%47,03	%42	%66,4 (Same with SMO)
nu-SVM	%46,4	%67,2	%54,7	%47	<b>%87,04 (SMO)</b>

To classify the array data, we prepared a data set using the matrix elements of other 2-level orthogonal arrays. The confusion matrix of the results we obtained in Table 5 is shown in Fig. 3. As seen in Fig 3, most of the matrix elements are classified correctly thanks to the kernel function we use.

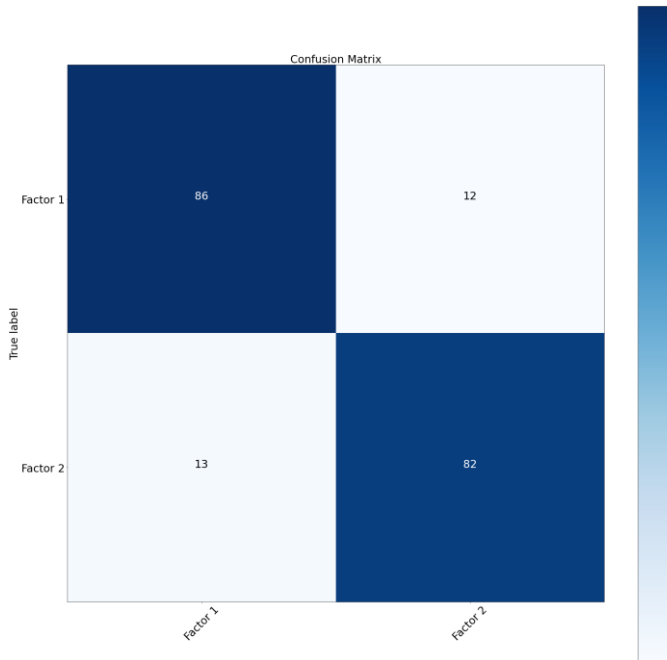


Fig. 3: The confusion matrix of the classification results we get from the 2-level arrays with nu-SVM and PUK kernel (SMO).

During the study, we observed that nonlinear core functions had higher performance in the classification of orthogonal arrays. The performance of the RBF and PUK cores is noticeably better than the other kernels, especially while classifying in 2-level classes. The output in the two-dimensional space obtained during the PUK classification process is shown in Fig. 4.

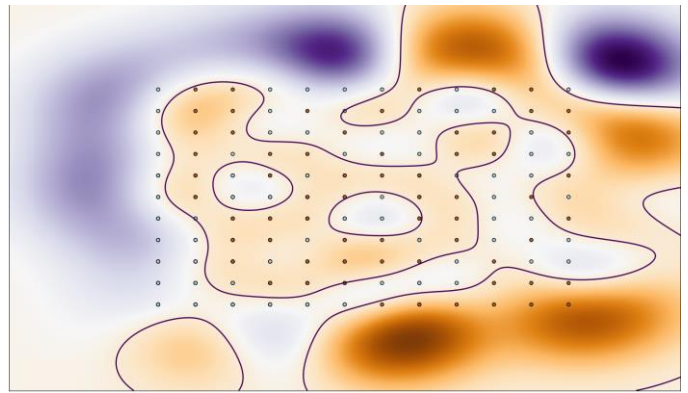


Fig. 4: Classification result with nu-SVM with Pearson kernel function without SMO. ( $\vartheta=0.5$ ,  $\sigma=0.001$ ,  $\omega=0.001$ , these values are obtained with experimentally for best results)

In this study, we have used the sequential minimal optimization algorithm for the values in the classification of the support vector machine. We achieved higher classification results with the SMO rather than the model that we applied without this algorithm. The plot of the classification results using the SMO algorithm is shown in Fig. 5.

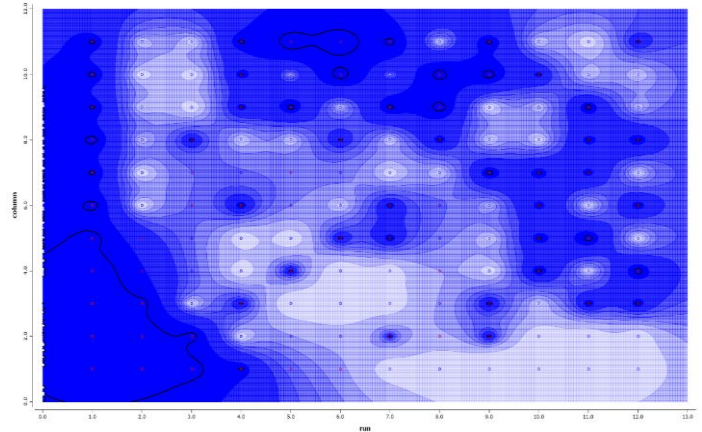


Fig. 5: nu-SVM classification plot, Pearson kernel function with SMO. ( $\vartheta=0.5$ ,  $\sigma=0.001$ ,  $\omega=0.001$ , these values are obtained with experimentally for best results)

We created the plot of the solution function and examined this graph in three dimensions to see if it is a sufficient hyperplane to differentiate the basic array values that we used and obtained during classification.

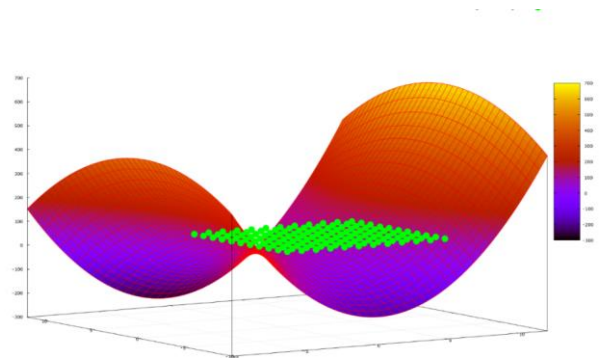


Fig. 6: Result function of our classification model.

Fig. 6 shows the values of the 2-level class shown in green, and the solution function of the classification with the highest performance is shown as a convex curve.

As a result of the most successful classification, we obtained the new orthogonal array is shown in Table 6. The red variables in Table 6 show values that differ from the original array. When we examined the distribution of elements in the array, we found it had a 40% difference from the original array.

Besides, the Taguchi arrays catalog contains mixed-level arrays as well as 2-level arrays which are defined in section 2.

We applied the model that is obtained for the L16 ( $2^{15}$ ) array to find the L16 ( $2^3 4^4$ ) mixed-level orthogonal array. To find the array L16 ( $2^3 4^4$ ), we classified the arrays L16 ( $2^6 4^3$ ), L16 ( $2^9 4^2$ ), L16 ( $2^{12} 4^1$ ), L8 ( $2^4 4^1$ ), but we could not achieve satisfactory results. These results are shown in Table 7.

TABLE VI  
NEW ARRAY CONSTRUCTED BY CLASSIFYING WITH nu-SVM(SMO).

Factors Experiment Number (runs)	1	2	3	4	5	6	7	8	9	10	11	12	13	14	15
1	1	1	1	1	1	1	1	1	1	1	1	1	1	1	1
2	1	1	1	1	1	2	2	2	2	2	2	1	1	1	1
3	1	1	2	1	2	2	2	1	2	2	2	1	1	1	1
4	1	2	1	2	2	1	2	2	1	1	1	1	1	1	1
5	1	2	2	1	2	2	2	2	1	2	1	1	1	1	1
6	2	2	2	2	1	2	2	1	2	1	1	1	1	1	1
7	2	1	2	2	1	1	2	2	1	2	1	1	1	1	1
8	2	2	2	2	2	2	2	1	1	1	2	1	1	1	1
9	2	1	1	2	2	2	1	2	2	1	1	1	1	1	1
10	2	2	2	1	1	1	1	2	2	1	2	2	1	1	1
11	2	2	1	2	1	2	1	1	1	2	2	2	1	1	1
12	2	2	1	1	2	1	2	1	2	2	1	1	1	1	1
13	2	2	1	1	1	1	1	1	2	2	1	1	1	1	1
14	2	2	2	1	1	1	1	2	2	2	2	1	1	1	1
15	2	2	2	2	2	1	1	2	2	2	1	1	1	1	1
16	2	2	2	2	2	2	1	1	2	1	1	1	1	1	1

The reason why our method fails on mixed-level arrays is the SMO algorithm is used to solve an optimization problem with two variables. According to the results in Table 7, we saw that the algorithm we use in the classification method is not suitable for different factors and levels in mixed-level arrays.

On the other hand, the new array we obtained was not orthogonal. Therefore we could not fully analyze it in accordance with the principles of experimental design. However, in non-orthogonal variance analysis, we examined the S/N ratio values using the ANOVA (Analysis Of Variance) method. These results are shown in Table 8 and Table 9.

TABLE VII  
CLASSIFICATION RESULTS FOR MIXED-LEVEL ARRAYS USING THE LAST SUCCESSFUL MACHINE LEARNING MODEL

Method	Sigmoid	RBF	Linear	Polynomial	PUK
C-SVM	%42,2	%47,2	%41,6	%32	%36,4 (Same with SMO)
nu-SVM	%37,6	%37,2	%44	%47	<b>%43,61(SMO)</b>

TABLE VIII  
STANDARD L16 TAGUCHI 2-LEVELS ARRAY SIGNAL TO NOISE RATIOS / LARGER IS BETTER

Factor	A	B	C	D	E	F	G	H	J	K	L	M	N	O	P
1	3,763	3,763	4,515	1,505	2,258	3,763	3,010	3,763	3,010	3,010	2,258	2,258	3,010	3,010	2,258
2	2,258	2,258	1,505	4,515	3,763	2,258	3,010	2,258	3,010	3,010	3,763	3,763	3,010	3,010	3,763
Delta	1,505	1,505	3,010	3,010	<b>1,505</b>	1,505	0,000	<b>1,505</b>	0,000	0,000	1,505	1,505	0,000	0,000	1,505
Rank	6,5	6,5	1,5	1,5	6,5	6,5	13	6,5	13	13	6,5	6,5	13	13	6,5

TABLE IX  
RECONSTRUCTED TAGUCHI 2-LEVELS ARRAY WITH nu-SVM(SMO), SIGNAL TO NOISE RATIOS / LARGER IS BETTER

Factor	A	B	C	D	E	F	G	H	J	K	L	M	N	O	P
1	3,612	2,736	2,006	2,257	2,257	3,010	3,762	3,762	2,580	3,344	2,408	3,440	3,010	3,010	3,010
2	2,734	3,612	4,300	3,762	3,762	3,010	2,257	2,257	3,344	2,580	4,013	<b>0,000</b>	?	?	?
Delta	0,875	0,875	2,293	1,505	<b>1,505</b>	0,000	1,505	<b>1,505</b>	0,764	0,764	1,605	3,440	<b>0,000</b>	<b>0,000</b>	<b>0,000</b>
Rank	8,5	8,5	2	5,5	5,5	13,5	5,5	5,5	10,5	10,5	3	1	13,5	13,5	13,5

We examined the parameters of the sample experiment (Drought survey) shown in Table 8 for the reconstructed array. The important factor for the experiment here is, of course, which varies depending on the type of experiment, the characteristics of the components in the subject matter, and which change has a greater effect on the outcome of the experiment or process. Without changing the value and factor information in the original array, our results are obtained in the new array are shown in Table 9.

In addition to the results in Table 9, when we examined the data averages related to signal/noise ratios, we also observed that inactive parameters in the standard orthogonal array can be effective in the newly constructed array, taking into account the order of parameters. For instance, in the sample experiment in this study, the effect of the North-South aspect parameter (factor J), on the result of the newly constructed array is shown in Figs 7 and 8.

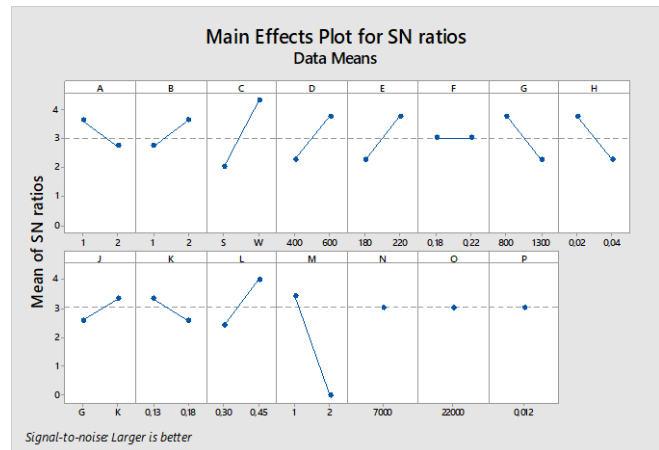


Fig. 8: Effects of new-generated 2-levels Taguchi orthogonal array parameters S/N ratios.

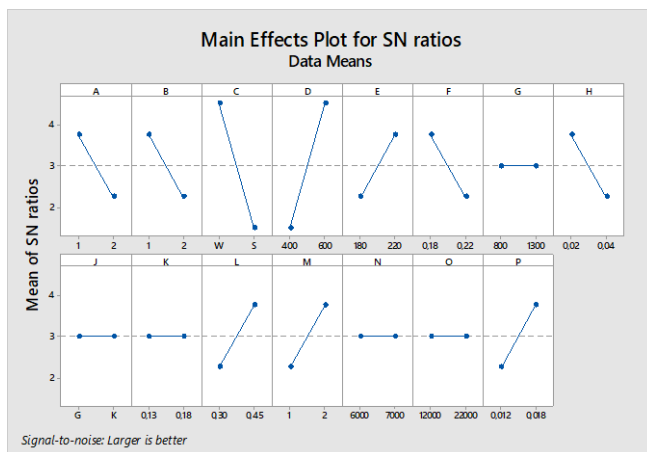


Fig. 7: Effects of standard L16 2-levels Taguchi orthogonal array parameters S/N ratios.

Another effect can be seen in Figures 7 and 8, in which we could not examine the effect of the last three parameters (N, O, P) on the experiment depending on the success of the classification. A better kernel function is used for the classification will eliminate the failure here. However, when these parameters are specific to the experiment are evaluated, it is seen if the effect of the results is low, and the classification is sufficient rather than unsuccessful. As a result of the classification we made under normal conditions, the deterioration of orthogonality seems to prevent the parameter effect research. Comparisons of our results are shown in Table 10.

TABLE X  
COMPARISONS OF PREVIOUS STUDIES AND THE PROPOSED METHODS.

Author(s)	Array Size	Method	Intended for
Kenny Q. et al[22]	12	Combinatorial isomorphism.	New arrays generation
Sorana D. Bolboacă, Lorentz Jäntschi[23]	16	Computational algorithm	New arrays generation
H. Bayrak and A. Alhan [24]	8,9	Projective geometry algorithm	Array classification
Our Proposal	16	SVM with SMO	Array classification and reconstruction

As in the studies we have compared in Table 10, orthogonal array researches are particularly focused on creating new variations of 2, 3, 4, and mixed-level arrays with mathematical approaches. It is envisaged to develop and simplify the experimental designs with the arrays to be found in this way. Thus, a more useful optimization of production designs can be achieved using multiple factor levels and minimal experimental studies. In this paper, we used a novel approach that includes machine learning methods to obtain existing 2-level and mixed-level orthogonal arrays by classifying existing arrays. However, the model we obtained more successfully in fixed arrays, did not make the same performance in mixed-level arrays.

The effects of column values are more important in optimal design approaches in the non-orthogonal row-column structure [25]. It is known that non-orthogonal approaches are not suitable for optimal design methods. In addition, in some of the studies that inspired this study, artificial neural network training methods [26, 27], compared with the Taguchi method give more realistic results than orthogonal arrays. In this study, depending on the type of experiment and the relationship between physically investigated values, we investigated whether a Taguchi array can be obtained to approach the results of artificial neural networks. As shown in Table 9, we could not obtain the second level values of the factors in the last three columns. The effects of these columns need to be examined in more depth. Considering the order of factors affecting the experiment, forming an orthogonal array can give more accurate results.

Nowadays, as the usage areas of artificial intelligence are increasing, it is possible to improve the robust design approach, which is an important value in product design with machine learning methods. This requirement in production activities is very important in terms of more efficient use of resources.

#### REFERENCES

[1] G. Taguchi and S. Konishi, *Taguchi Methods: Orthogonal Arrays and Linear Graphs*. Tools for Quality Engineering. Dearborn: MI: American Supplier Institute, 1987.

[2] L. E. Katz and M. S. Phadke, "Macro-Quality with Micro-Money," in *Quality Control, Robust Design, and the Taguchi Method*, K. Dehnad, Ed. Boston, MA: Springer US, 1989, pp. 23-30.

[3] P. T. Dhorabe, D. H. Lataye, A. R. Tenpe, and R. S. Ingole, "Adsorption of p-nitrophenol onto acacia glauca saw dust and waste orange peels

activated carbon: application of Taguchi's design of experiment," *SN Applied Sciences*, journal article vol. 1, no. 3, p. 250, February 20 2019.

[4] M. Rahmani, M. Kaykhaii, and M. Sasani, "Application of Taguchi L16 design method for comparative study of ability of 3A zeolite in removal of Rhodamine B and Malachite green from environmental water samples," *Spectrochimica Acta Part A: Molecular and Biomolecular Spectroscopy*, vol. 188, pp. 164-169, 2018/01/05/ 2018.

[5] S. Sadr, V. Mozafari, H. Shirani, H. Alaei, A. Tajabadi Pour, and A. Rajabi Behjat, "Control of pistachio endocarp lesion by optimizing the concentration of some nutrients using taguchi method," *Scientia Horticulturae*, vol. 256, p. 108575, 2019/10/15/ 2019.

[6] H.-A. Mehedi et al., "Synthesis of graphene by cobalt-catalyzed decomposition of methane in plasma-enhanced CVD: Optimization of experimental parameters with Taguchi method," *Journal of Applied Physics*, vol. 120, no. 6, p. 065304, 2016.

[7] L. Zhang et al., "Taguchi method assisted multiple effects optimization on optical and luminescence performance of Ce: YAG transparent ceramics for high power white LEDs," *Journal of Materials Chemistry C*, 10.1039/C9TC03916C 2019.

[8] R. Romero-Villafranca, L. Zúnica, and R. Romero-Zúnica, "Ds-optimal experimental plans for robust parameter design," *Journal of Statistical Planning and Inference*, vol. 137, no. 4, pp. 1488-1495, 2007/04/01/ 2007.

[9] E. Y. Ng and W. K. Ng, "Parametric study of the biopotential equation for breast tumour identification using ANOVA and Taguchi method," (in eng), no. 0140-0118 (Print).

[10] R. N. Kacker, E. S. Lagergren, and J. J. Filliben, "Taguchi's Orthogonal Arrays Are Classical Designs of Experiments," *Journal of research of the National Institute of Standards and Technology*, vol. 96, no. 5, pp. 577-591, Sep-Oct 1991.

[11] P. J. Rahul Davis, "Application of Taguchi-Based Design of Experiments for Industrial Chemical Processes," in *Statistical Approaches With Emphasis on Design of Experiments Applied to Chemical Processes*, 2017.

[12] C. R. Rao, "Hypercube of Strength "d" leading to Confounded Designs in Factorial Experiments," *Bull. Calcutta Math. Soc.*, vol. 38, pp. 67-68, 1946.

[13] O. D. OLANLOYE, O. OLASUNKANMÍ, and O. E. ODUNTAN, "Comparison of Support Vector Machine Models in the Classification of Susceptibility to Schistosomiasis," *Balkan Journal of Electrical and Computer Engineering*, vol. 8, no. 3, pp. 266-271.

[14] Y. Kaya, "Classification of PVC beat in ECG using basic temporal features," *Balkan Journal of Electrical and Computer Engineering*, vol. 6, no. 2, pp. 10-4, 2018.

[15] E. Aydemir and F. Kaysi, "Development of Short Forms of Scales with Decision Tree Algorithms," *Balkan Journal of Electrical and Computer Engineering*, vol. 8, no. 4, pp. 285-290, 2020.

[16] B. E. Boser, I. M. Guyon, and V. N. Vapnik, "A training algorithm for optimal margin classifiers," presented at the Proceedings of the fifth annual workshop on Computational learning theory, Pittsburgh, Pennsylvania, USA, 1992.

[17] B. Scholkop and A. Smola., *Learning with kernels*. M.I.T. Press, 2001.

[18] B. Üstün, W. J. Melssen, and L. M. C. Buydens, "Facilitating the application of Support Vector Regression by using a universal Pearson VII function based kernel," *Chemometrics and Intelligent Laboratory Systems*, vol. 81, no. 1, pp. 29-40, 2006/03/01/ 2006.

[19] J. Mercer, "Functions of Positive and Negative Type, and their Connection with the Theory of Integral Equations," *Philosophical Transactions of the Royal Society of London Series A*, vol. 209, p. 415, January 01, 1909 1909.

[20] J. Platt, "Sequential minimal optimization: A fast algorithm for training support vector machines," 1998.

[21] Catalogue of Taguchi designs. Available: <https://support.minitab.com/en-us/minitab/18/help-and-how-to/modeling-statistics/doe/supporting-topics/taguchi-designs/catalogue-of-taguchi-designs/>

[22] K. Q. Ye, D. Park, W. Li, and A. M. Dean, "Construction and classification of orthogonal arrays with small numbers of runs," *Statistics and Applications*, vol. 6, no. 1, pp. 5-15, 2008.

[23] S. D. Bolboacă and L. Jäntschi, "Design of experiments: Useful orthogonal arrays for number of experiments from 4 to 16," *Entropy*, vol. 9, no. 4, pp. 198-232, 2007.

- [24] H. Bayrak and A. Alhan, "On the construction of orthogonal arrays," Hacettepe Journal of Mathematics and Statistics, vol. 31, pp. 45-51, 2002.
- [25] J. Kunert, "A note on optimal designs with a non-orthogonal row—column-structure," Journal of Statistical Planning and Inference, vol. 37, no. 2, pp. 265-270, 1993/11/01/ 1993.
- [26] I. H. Kurt, M. Oduncuoglu, F. N. Yilmaz, E. Ergul, and R. Asmatulu, "A Comparative Study on the Effect of Welding Parameters of Austenitic Stainless Steels Using Artificial Neural Network and Taguchi Approaches with ANOVA Analysis," Metals, vol. 8, no. 5, 2018.
- [27] A. Alizadeh and H. Omrani, "An integrated multi response Taguchi-neural network- robust data envelopment analysis model for CO2 laser cutting," Measurement, vol. 131, pp. 69-78, 2019/01/01/ 2019.

#### BIOGRAPHIES



**SELÇUK YAZAR** received the B.S. degree in engineering physics from the Ankara University in 1997.

From 1998 to 2010, he worked as DevOps engineer and software developer. He received the M.S. and Ph.D. degrees in computer engineering from the Trakya University. His research interest include

Internet of Things, Deep Learning and Virtualization.

# Spectrum Occupancy Measurements in Cellular Frequency Band in Samsun

Begüm Korunur Engiz and Yousif Ali Rajab

**Abstract**— In this study, available spectrum parts in GSM900, LTE800, LTE900, GSM1800, LTE1800, UMTS2100 and LTE2600 were determined. The measurement campaigns were performed at 115 different locations in Samsun city center at the most active time of a day using RF Explorer 6G Combo analyzer device. The spectrum utilization rates were determined using energy detection technique (EDT), and average spectrum occupancy technique (ASOT). The thresholds were chosen manually as -40, -45, -50, -55, -60, -65, -70, -75 dBm, and as 10-dB above the noise floor, as recommended by International Telecommunication Union (ITU), and spectrum utilization was evaluated through EDT and ASOT. Obtained results show that at most of the measurement locations spectrum occupancy percentages calculated via EDT and ASOT very close to each other. Based on the results UMTS2100 band showed the highest average spectrum occupancy i.e. 33.91% and the overall average spectrum occupancy rate was found to 22.72%. Additionally, at 50% of the measurement locations occupancy percentage was below 33% for all services. The average occupancy over GSM900 band was between 0.87% - 66.61% according to the predetermined threshold. It was also found that the bands LTE1800 and LTE2600 were mostly occupied for the thresholds below -60 dBm whereas the measured spectrum was mostly vacant for -40 dBm. This led us to infer that there is a great potential for share some of UHF band for cognitive radio applications and future 5G systems.

**Index Terms**— Average Spectrum Occupancy Technique, Cognitive Radio, Energy Detecting Technique, Spectrum Occupancy Measurement

## I. INTRODUCTION

In order to meet the growing demand for wireless communication systems and applications, operators are pushed to establish new techniques to solve the shortage of radio spectrum resources problem. Efficient utilization of

radio frequency spectrum of fundamental importance. During recent years, the rapid increase in the number of users around the world has led the enormous growth of wireless applications and services to be developed [1]. However, there is less opportunity to find an available band (spatially or temporally) to deploy new wireless communication services or improve the existing ones.

Cognitive radio (CR) stands out as a promising solution for the competent administration an access control to the spectrum [2]. The concept of CR based on allowing so-called unlicensed, secondary user, for access to spectrum bands that are available, without make interference with the primary user [3]. In order to allow access, and deployment of CR, unused part of the spectrum must be determined. In [4], TV white space spectrum was evaluated for VHF (174-230 MHz) and UHF bands (470-860 MHz), in 8 different urban environment locations in Prishtina, the capital of Republic of Kosovo by using the NARDA Selective Radiation Meter SRM-3006. It is shown in the study that availability of TV bands varies between 87.5% and 100%, and give the opportunistic use of spectrum by CR. Available Television White Space (TVWS) spectrums in Samsun were determined in [5] with the aid of measurements conducted within 470 MHz -790 MHz band at 73 different locations. The maximum spectrum occupancy was found as 70% while the average spectrum occupancy was 20.7%. For long-term spectrum monitoring and occupancy, a study was performed by [6] within the band 174MHz and 1000MHz. This study proves that big portions of spectrum are free, and suitable for spectrum sharing. Also, multi-band and multi-location spectrum measurements campaign conducted in Nigeria in 80-2200 MHz frequency range in [7], and it was shown that the actual spectral occupancy in Nigeria was less than 10.00%. Furthermore, it was evaluated through spectral occupancy measurements conducted in Konya, Turkey from 30 to 3000MHz frequency range that many frequency bands are suitable for CR [8]. Available spectrum in the Global Mobile Communications (GSM) 900 MHz band in Palestine was validated through the simulations, and an efficient and interference robust CR system was proposed [9]. Unused spectrum parts in GSM900 band are evaluated through outdoor spectrum measurements performed in Samsun, and spectral usage in the band was found as 8.5% for -40 dBm [10]. For instance, the spectrum occupancy measurements carried out in South Africa for UHF, GSM900 MHz and GSM1800 MHz bands. Occupancy in the UHF band was approximately 20% while the GSM900 and 1800 MHz bands were occupied 92% and 40% respectively [11]. Similar study

BEGÜM KORUNUR ENGİZ, is with Department of Electrical and Electronics Engineering, Ondokuz Mayıs University, Samsun, Turkey, (e-mail: [bkengiz@omu.edu.tr](mailto:bkengiz@omu.edu.tr)).

 <https://orcid.org/0000-0002-3905-1791>

YOUSIF ALI RAJAB, is with Department of Electrical Engineering, Sakarya University, Sakarya, Turkey (e-mail: [yousif.ali.rajab@gmail.com](mailto:yousif.ali.rajab@gmail.com)).

 <https://orcid.org/0000-0002-8186-3742>

Manuscript received January 24, 2021; accepted March 29, 2021  
2018. DOI: [10.17694/bajece.867294](https://doi.org/10.17694/bajece.867294)

carried out in Kampala for GSM900, GSM1800, and the universal mobile telecommunications system 2100 (UMTS2100) and long term evolution 2600 (LTE2600) bands in [12]. The result of the study indicated an average uplink occupancy rate for GSM900, GSM1800, UMTS2100 and LTE2100 bands are of 8.8%, 0.6%, 0.56% and 0% respectively. Spectrum experiments were conducted in Barcelona for the frequencies of 75 MHz to 3 GHz [13]. The spectrum usage in Beijing was determined through continuous 24 h measurements over the frequencies from 450 to 2700 MHz [14], and shown that GSM900 band had the highest occupancy with 45.52%. The spectrum occupancy measurements were performed in three different locations. The target band was sub-6 GHz, and the results show that the average duty cycle of the sub-6 GHz is 4.73% [15]. In order to determine the spectrum occupancy, the measurements conducted within 850 MHz to 2 GHz using Software Radio Peripheral. Energy detection method was used with the threshold 6 dB above the noise floor. Average occupancy is calculated as 17.3 % and opportunities for CR systems were determined [2]. The spectrum measurements performed at frequency band of 700 MHz to 2.7 GHz in India for indoor and outdoor using DA5000 that is a compact discone aerial antenna and R&S FSH3 Handheld Spectrum Analyzer (HSA) connected to a laptop. Indoor and outdoor spectrum occupancies were examined and compared. According to results that the use of spectrum was very low, and spectrum was available for CR [16]. Spectrum measurements were conducted in Czech Republic and France at three different regions for the frequencies within 400 MHz–3 GHz. The average occupancies at three different regions were found as 6.5%, 10.7% and 7.7 % [17]. In [18], the spectrum in the frequency range 50 MHz – 6 GHz was scanned using deep radio based RF measurement systems. The spectrum usage analysis showed that a large amount of spectrum in the Digital Video Broadcasting (DVB) and GSM bands were under-utilized, and occupied bandwidth percentages in many cellular bands were low. The relationship between spectrum detection

performance and antenna numbers in MIMO systems was examined in [19]. The simulation results showed that the increase in the antenna numbers yielded better detection performance and channel capacity.

In this study, in order to determine the spectrum occupancy within cellular frequency bands (range from 700 MHz – 2.7 GHz) widespread measurements were conducted in Samsun – Turkey using RF Explorer 6G Combo spectrum analyzer. Spectrum occupancies were calculated by applying energy detecting and average spectrum occupancy techniques. The rest of the paper is organized as follows. Brief description of measurement setup is given in Section 2, measurement and occupancy results were presented in Section 3, and the paper is concluded in the final section.

## II. MATERIAL AND METHOD

In this study in order to find the holes within cellular frequency bands, widespread spectrum measurements conducted at various locations in Samsun-Turkey with an estimated area of 7 square kilometers. The measurements were performed using RF Explorer 6G Combo spectrum analyzer, and the results were recorded. Then, the recorded data which represent the measurement data from all measurement locations was assessed through MATLAB. Spectrum occupancies were calculated at chosen thresholds through EDT and ASOT. The details of the measurement process and spectrum occupancy calculation are given in the following sections.

### A. Spectrum Measurement

In order to have the necessary knowledge about the current spectrum usage in Samsun province, 115 locations were selected for coverage of all city center. Measurements were performed within the band 700 MHz to 2700 MHz that contain all cellular frequency bands, 2G capabilities GSM900, GSM1800, 3G capabilities UMTS2100, 4G capabilities LTE800, LTE900, LTE1800, and LTE2600.



Fig. 1. Measurement locations

The measurements were taken from 1 August 2018 to 7 August 2018, in the busiest hours of a day starting from 6:00 pm to 10:00 pm. Measurement locations are shown in Fig. 1, service names and measured frequencies are given in Table I.

TABLE I  
THE TARGETED CELLULAR FREQUENCY BANDS

Index	Service Name	Lower Frequency (MHz)	Upper Frequency (MHz)
1	LTE800	791	820.9
2	LTE900	925.1	935.1
3	GSM900	935.1	961.0
4	GSM1800	1805	1820
5	LTE1800	1820	1879
6	UMTS2100	2010	2120
7	LTE2600	2570	2670

Measurements were taken using RF Explorer 6G Combo spectrum analyzer. After installing device's Open Source software, and connecting dongle to the laptop, the device will be ready to take measurements. The software shows radio frequency spectrum bandwidth including Normal, Peak Max, Max Hold, Overwrite and Averaging modes. Span of the analyzer is 0.112-600 MHz and 2-600 MHz, and frequency range is 15-2700 MHz and 4850-6100 MHz according to the antennas used. Frequency resolution is 1 kHz and average noise level is -105 dBm. RF Explorer 6G Combo spectrum analyzer's software enables the follow the change in received signal strength and detection of the empty band by saving the instantaneous power in dBm. Measurement setup and an image of spectrum measurement with analyzer is shown in Fig. 2.



Fig. 2. An example of spectrum measurement with spectrum analyzer

### B. Occupancy Calculation Methods

In this study, the first technique that followed to determine the unused spectrum parts is Energy Detection Technique (EDT). In EDT, the spectrum is considered as occupied if the received signal power is above a certain threshold. Then the occupation rate of communication channels or frequency band can be determined according to the measurement's location

and time. Because EDT has low computational complexity, and easy to implement it is widely applied. After the completion of the measurements, the average power of the specific frequency at the location is calculated using (1).

$$P_{avg} = \sum_{i=1}^m \frac{p_i}{m} \quad (1)$$

Where: the average power is represented by  $P_{avg}$ , number of reading times presented by  $m$ , and the power of specific frequency at a specific moment is shown by  $p_i$ . In a measurement, the spectrum occupancy is calculated through (2):

$$F_{(f_i, p_i)} = \begin{cases} 0, & p_i < \beta \\ 1, & p_i \geq \beta \end{cases} \quad (2)$$

In the equation,  $F_{(f_i, p_i)}$  shows the spectrum occupancy at a measurement frequency,  $\beta$  is the threshold, and  $p_i$  is the average power. Then, if  $L$  shows the number of frequency span, the band's average spectrum occupancy is calculated using (3).

$$F_{avg} = \sum_{i=1}^L \frac{F_{(f_i, p_i)}}{L} \quad (3)$$

The second is; average spectrum occupancy technique (ASOT) that depends on finding the spectrum occupancy rate for a frequency point at specific time slot determined by equation (4).

$$\phi_{f(n), t(s)} = \begin{cases} 0, & p_n < \beta \\ 1, & p_n \geq \beta \end{cases} \quad (4)$$

In the equation,  $\phi_{f(n), t(s)}$  shows the spectrum occupancy of specific frequency point  $f(n)$  at time slot  $t(s)$ , and  $p_n$  represents the received power spectral density measured in specific frequency point, and  $\beta$  presents the threshold.

After finding the spectrum occupancy for each frequency point, spectrum occupancy of a band in all time slots can be determined through (5).

$$\phi = \frac{1}{mk} \sum_{s=1}^m \sum_{n=1}^k \phi_{f(n), t(s)} \quad (5)$$

Where:  $\phi$  is the average spectrum occupancy,  $m$  is the total number of time samples at a frequency, and  $k$  is the number of the frequency points in the chosen band.

In order to apply the methods above; the thresholds should be determined. In this study two different methods were used to determine the thresholds. First, seven different threshold value was selected manually as -40 dBm, -45 dBm, -50 dBm, -60 dBm, -65 dBm, -70 dBm, -75 dBm. In the second

method, to determine the noise floor (NF); power spectral density values of individual frequencies are averaged over time and the median is taken. Then M dB, ITU recommendation is 10 dB for spectrum monitoring, was added to the NF value to set the threshold. After the determination of the thresholds, spectrum occupancy percentages were calculated using both methods and results were given in the following section.

III. RESULTS AND DISCUSSIONS

In order to detect available parts of the spectrum, detailed measurements were conducted within cellular frequency bands, then techniques that described in the previous section have been applied. For the sake of brevity, figure for EDT at -55 dB for all services is given in Fig. 3. Overall occupancy evaluations are shown in stacked bar plot (Fig. 4.a, and Fig. 4.b) for EDT and ASOT respectively. It can be seen from Fig. 3 that spectrum utilization varies significantly by location and the service. The maximum average occupancies are 85.71%, 100%, 80%, 80%, 54.55%, 66.67%, and 15.52% for the services of LTE800, LTE900, GSM900, GSM1800, LTE1800, UMTS2100 and LTE2600 respectively. The figure also indicates that utilization level of LTE2600 band is very low. It can be concluded from Fig. 4 that average occupancy percentages vary from 0.05% to 85.22% for all services considered. Additionally, LTE800 and UMTS2100 bands are highly occupied, and GSM900, GSM1800 bands are almost equally occupied for all thresholds. Furthermore, the overall average occupancy of the services are 1.02%, 2.79%, 8.08%, 16.06%, 27.95% and 40.76% for thresholds from -40 dBm to -75dBm respectively.

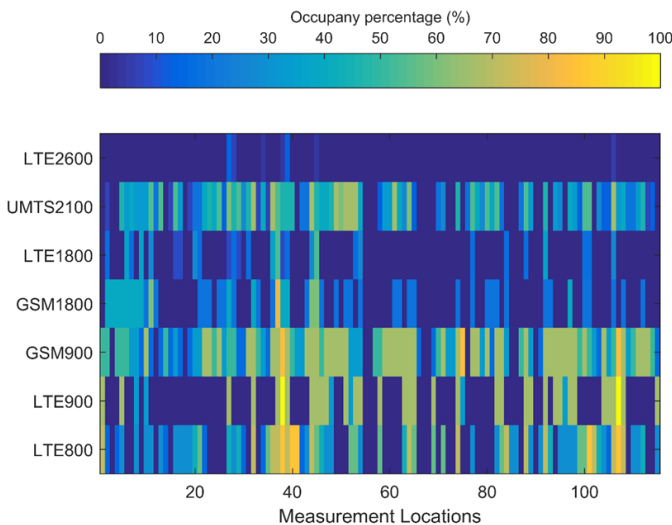


Fig. 3. Occupancy percentages at -55 dBm for EDT

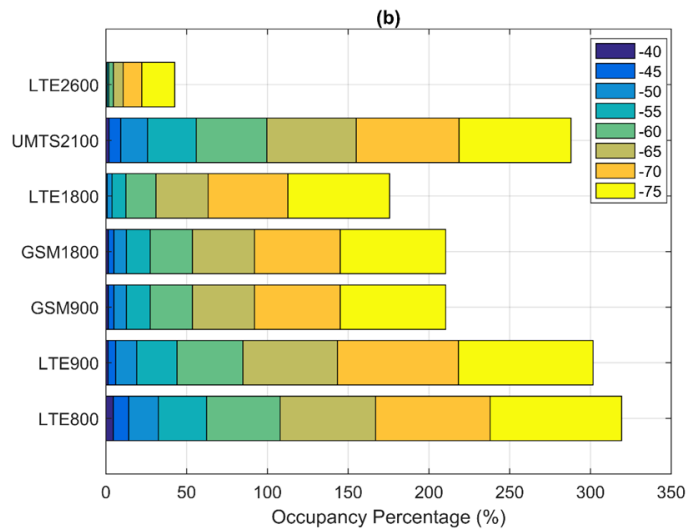
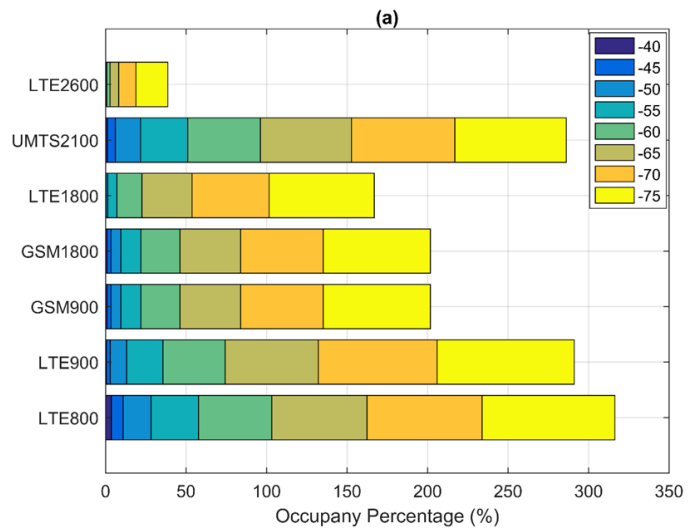


Fig. 4. Overall occupancy percentages for (a) EDT (b) ASOT

The decision thresholds were calculated according to the noise floor and ITU recommendation as -52.85,-53.22, -48.83, -59.24, -60.79, -56.18, and -72.97 dBm for the services LTE800, LTE900, GSM900, GSM1800, LTE1800, UMTS2100, and LTE2600 respectively. The occupancy percentages at these thresholds were calculated using EDT and ASOT, the results were given in Fig. 5.a and 5.b respectively. As seen from the figures that there are some slight differences at the measurement locations of i.e. 94, 46, and 52 for services of LTE900, LTE1800, and UMTS2100 respectively. However, occupancy percentages calculated through EDT and ASOT are closely follows each other, despite the difference in the calculation of spectrum occupancy. The differences between the results were in the range of 1% to 15%. Therefore, both methods can be used for spectrum sensing, as they are both simple and easy to implement.

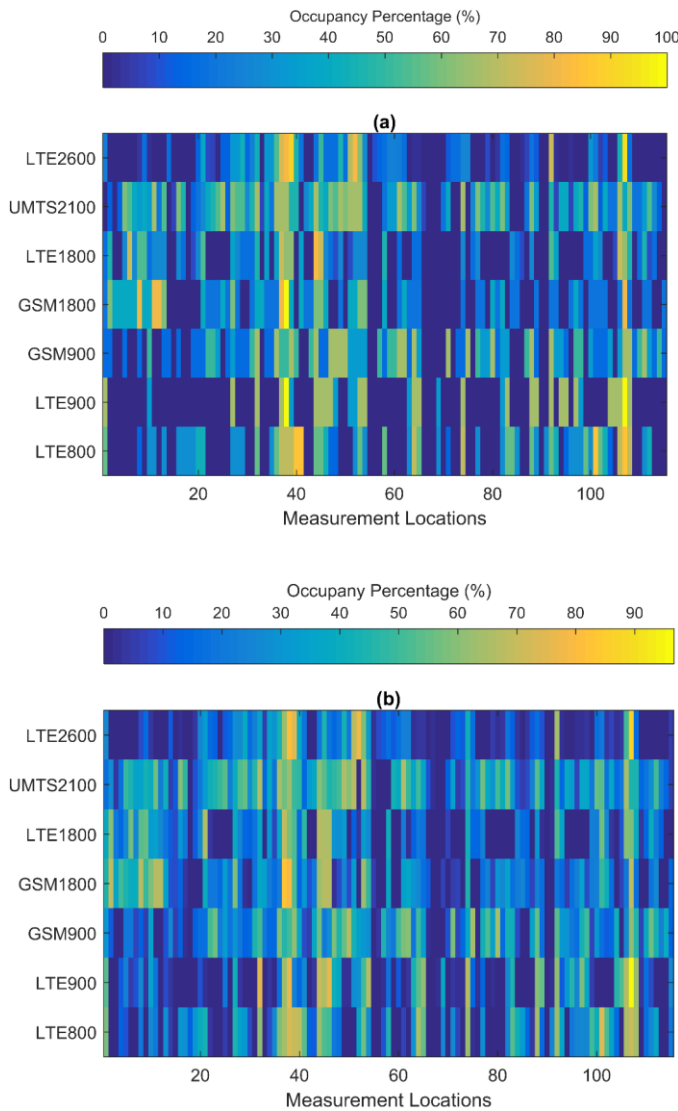


Fig. 5. Overall occupancy percentages at decision thresholds for (a) EDT (b) ASOT

Comparison of the overall average occupancy percentages were given in Table II. It can be concluded from the table that the average occupancy percentages calculated for all measurement locations through EDT and ASOT methods are almost equal. The maximum difference is obtained for the service of GSM1800 as 2.12%.

TABLE II  
THE TARGETED CELLULAR FREQUENCY BANDS

Service Name	Average Occupancy percentages for EDT (%)	Average Occupancy percentages for ASOT (%)
LTE800	23.48	23.83
LTE900	18.20	19.41
GSM900	27.83	27.07
GSM1800	<b>21.74</b>	<b>23.86</b>
LTE1800	17.94	19.73
UMTS2100	33.91	32.88
LTE2600	15.91	15.25

Generalized cumulative distribution functions were given in Fig. 6.a and 6.b for EDT and ASOT respectively. As seen from the figures that in 50% of the measurement locations occupancy percentage is below 20% for the services of LTE900, LTE1800 and LTE2600, while above 25% for LTE800, GSM900, GSM1800 and UMTS2100. The results show that at 90% of measurement locations approximately 36% of the bands are vacant, and available for CR utilization.

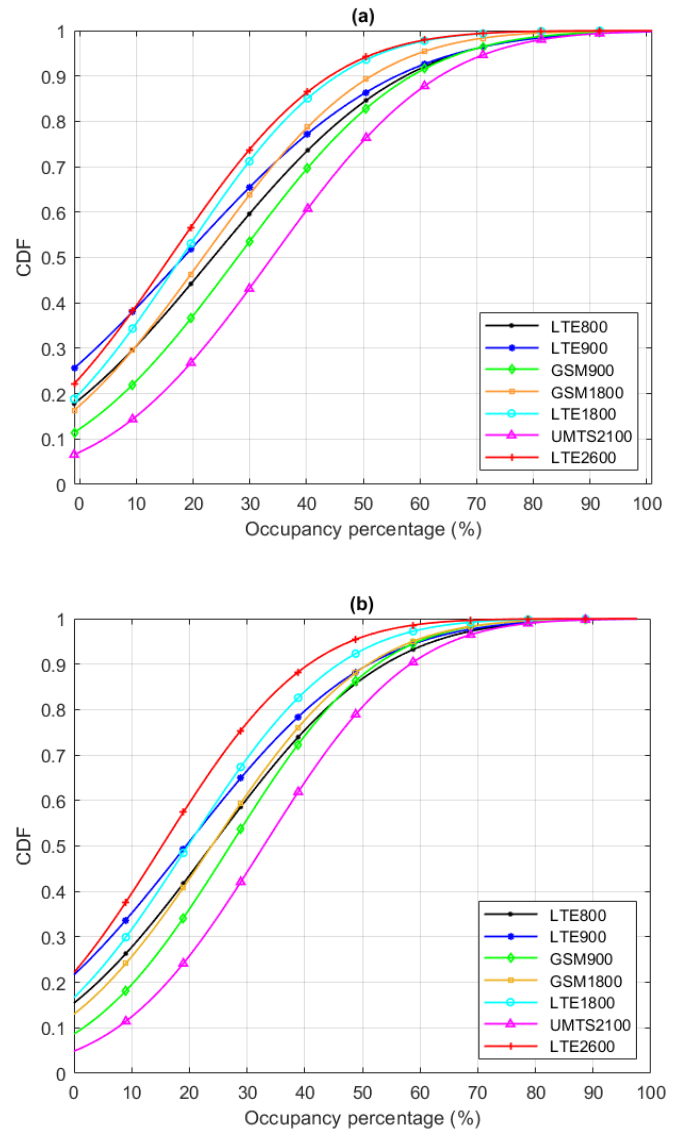


Fig. 6. Generalized cumulative distribution functions for (a) EDT (b) ASOT

#### IV. CONCLUSION

In this study, to evaluate the availability of the cellular frequency bands, extensive spectrum measurements were performed in Samsun at 115 different locations. Energy detection and average spectrum occupancy techniques were used for spectrum sensing. In order to calculate the spectrum occupancy percentages, received signal energy was compared with the decision threshold which was chosen manually and according to noise floor. Evaluations and analysis show that

spectrum utilization varies significantly by location and the service. Additionally, the maximum average occupancy of UMTS2100 is approximately 67%, and utilization level of LTE2600 band is very low. Furthermore, average occupancy percentage of all services is 16.06% at -55 dBm threshold. Based on the mean occupancy percentages calculated, among the seven cellular bands UMTS2100 had the highest occupancy about 33 % while LTE2600 had the lowest with about 15%. The results show that 50% of the measurement locations occupancy percentage is below 20% for the services of LTE900, LTE1800 and LTE2600, while below 33% for GSM900 and UMTS2100. The detailed analyses of the measurement results indicated that most of the bands are vacant and available for deployment of cognitive radio.

#### REFERENCES

- [1] S. Grönroos, K. Nybom, J. Björkqvist, J. Hallio, J. Auranen and R. Ekman. "Distributed spectrum sensing using low cost hardware." *Journal of Signal Processing Systems*. 83:1, 2016, pp.5-17.
- [2] M. S. Melo, G. R. Arroyave, and J. A. Quijano. "Spectrum Occupation Assessment in Bogota and Opportunities for Cognitive Radio Systems." *IEEE-APS Topical Conference on Antennas and Propagation in Wireless Communications (APWC)*, 10-14 September, Cartagena des Indias, Colombia, 2018, pp. 932-935.
- [3] F. Kiftaro, M. El-Tarhuni and K. Assaleh. "UHF Spectrum Occupancy Measurements in Sharjah-UAE." *9th IEEE-GCC Conference and Exhibition (GCCCE)*, 8-11 May, Sharjah, U.A.E, 2017, pp. 1-5.
- [4] H. Maloku, Z. L. Fazliu, M. Ibrani, A. Mekuli, E. Sela and M. Rajarajan. "Measurement of Frequency Occupancy Levels in TV Bands in Urban Environment in Kosovo." *18th Mediterranean Microwave Symposium (MMS)*, 31 October. -2 November, Prishtina, Kosovo, 2018, pp. 268-271.
- [5] C. Kumaz, Z. Albayrak. "Measuring and evaluating TV white spaces in Samsun, Turkey." *Journal of New Results in Science*, 5, 2016, pp. 139-148.
- [6] E. Wiles, K. Negus. "Long-term Spectrum Monitoring and Occupancy from 174 to 1000 MHz in Rural Western Montana." *12th European Conference on Antennas and Propagation (EuCAP 2018)*, 9-13 April, Butte, USA, 2018, pp. 1-5.
- [7] J. Popoola, U. Otuu. "Assessment of radio spectrum profile in Nigeria using multi-band and multi-location radio spectrum occupancy measurements." *Eskişehir Technical University Journal of Science and Technology A - Applied Sciences and Engineering*, 19 (4) , 2018, pp.948-962.
- [8] I. Şeflek, E. Yıldız. "Spectrum occupancy measurements at University Campus in Turkey." *International Journal of Electronics and Electrical Engineering*, 5 (1), 2017, pp.1-6.
- [9] A. Abdou, O. Najajri and A. Jamoos. "Developing a Secondary Mobile Network in the Palestinian GSM Band Using Cognitive Radio." *2017 IEEE Jordan Conference on Applied Electrical Engineering and Computing Technologies (AEECT)*, 11-13 October, Jerusalem, Palestine, 2017.
- [10] B. K. Engiz, Y. A. Rajab. "Investigation of Spectrum Occupancy in GSM Band in Samsun, Turkey." *6th International Conference on Electrical and Electronics Engineering (ICEEE)*, Istanbul, Turkey, 2019, pp. 158-161.
- [11] S. D. Barnes, P. A. Jansen van Vuuren and B. T. Maharaj. "Spectrum occupancy investigation: Measurements in South Africa." *Measurement*, vol. 46, no. 9, 2013, pp. 3098- 3112.
- [12] G. Ayugi, A. Kisolo and T. W. Ireeta. "Telecommunication frequency band spectrum occupancy in Kampala Uganda. " *International Journal of Research in Engineering and Technology*, (4), 2015, pp.390-396.
- [13] M. López-Benitez, A. Umbert and F. Casadevall. "Evaluation of Spectrum Occupancy in Spain for Cognitive Radio Applications." *IEEE 69th Vehicular Technology Conference*, 26-29 April, Barcelona, Spain, 2009, pp.1-5.
- [14] J. Xue, Z. Feng and P. Zhang. "Spectrum occupancy measurements and analysis in Beijing. " *IERI Procedia*, (4), 2013, pp.295–302.
- [15] D. A. Ramirez, M. Cardenas-Juarez, U. Pineda-Rico, A. Arce and E. Stevens-Navarro. "Spectrum Occupancy Measurements in the Sub-6 GHz Band for Smart Spectrum Applications." *IEEE 10th Latin-American Conference on Communications (LATINCOM)*, 14-16 November, Mexico, 2018, pp. 1-6.
- [16] N. Khoja, S. Anpat, V. Kale, P. Gadiya, S. Suryawanshi, M. Naikwadi and K. Patil. "Opportunistic Spectrum Access Measurements and Analysis in Urban Area for a Better Cognitive Approach." *2017 International Conference on Computing, Communication, Control and Automation (ICCUBEA)*, 17-18 August, Pune, India, 2017, pp.1-6.
- [17] V. Valenta, R. Marsalek, G. Baudoin, M. Villegas, M. Suarez and F. Robert. "Survey on Spectrum Utilization in Europe: Measurements, Analyses and Observations." *2010 Proceedings of the Fifth International Conference on Cognitive Radio Oriented Wireless Networks and Communications*, June 9–11, Cannes, 2010, pp.1-5.
- [18] P. Chandhar and V. U. Pai. "On Collaborative Radio Frequency Observatory in India." *2020 IEEE International Conference on Advanced Networks and Telecommunications Systems (ANTS)*, New Delhi, India, 2020, pp. 1-6.
- [19] F. Y. Ilgin. "Antenna Selection and Detection Performance on Correlation Based Detection Systems. " *Balkan Journal of Electrical&Computer Engineering*, Vol. 9, No. 1, 2021, pp.48-52.

#### BIOGRAPHIES



**BEGÜM KORUNUR ENGİZ** She received the B.S., M.S. and Ph.D. degrees in Electrical and Electronics Engineering from Ondokuz Mayıs University, Samsun, in 2001, 2007 and 2014 respectively. From 2006 to 2011, she was a research assistant at department of Electrical and Electronics Engineering. Between the years of 2011-2014 she was a lecturer at Ünye Vocational School, Ordu University. Since 2016 she has been an Assistant Professor Dr. at the Department of Electrical and Electronics Engineering, Ondokuz Mayıs University. Her research interests include wireless communication systems, cognitive radio, radio frequency electromagnetic field measurement and signal processing.



**YOUSIF ALI RAJAB** Iraq, Baghdad City, in 1991. He received the B.S. in computer engineering from Al Salam University college, Baghdad, and M.S. degree in Electrical and Electronics Engineering from Ondokuz Mayıs University, Samsun, in 2019. He is doing his Ph.D. on electronic engineering in Sakarya University. His research interests include cellular systems, cognitive radio and 4G.

# Kidney X-ray Images Classification using Machine Learning and Deep Learning Methods

Işıl Karabey Aksakallı, Sibel Kaçdioğlu and Yusuf Sinan Hanay

**Abstract**—Today, kidney stone detection is performed manually by humans on medical images. This process is time-consuming and subjective as it depends on the physician. This study aims to classify healthy or patient individuals according to the status of kidney stones from medical images using various machine learning methods and Convolutional Neural Network (CNN). We evaluated various machine learning methods such as Decision Trees (DT), Random Forest (RF), Support Vector Machines (SVM), Multilayer Perceptron (MLP), K-Nearest Neighbor (kNN), Naive Bayes (BernoulliNB), and deep neural networks using CNN. According to the experiments, the Decision Tree Classifier (DT) has the best classification result. This method has the highest F1 score rate with a success rate of 85.3% using the S+U sampling method. The experimental results show that the Decision Tree Classifier (DT) is a feasible method for distinguishing the kidney x-ray images.

**Index Terms**—kidney disease detection, classification, deep learning, machine learning, artificial intelligence in medicine.

## I. INTRODUCTION

**K**IDNEY STONE disease occurs due to the accumulation of salt and mineral crystals excreted in the urine and turning into stones. Kidney stones have been affecting people for centuries. It is one of the most common diseases of the kidneys and urinary tract. It affects approximately 1-15% of the world population, and its prevalence is increasing with each passing year [1]. The prevalence of kidney stones was 1–5% in Asia, 5–9% in Europe, and 7–15% in North America [1]. Kidney stone formation can occur at any age, gender, and

race. It is more common in men than in women. Kidney stones are thought to be caused by reasons such as lack of physical activity and eating habits. Chronic diseases such as blood pressure, diabetes, and obesity may affect stone formation. After the kidney stone is treated, it may recur and become chronic.

Prevention of kidney stone formation and recurrence is still a significant problem for human health. Impairment of kidney function due to the formation of kidney stones endangers human life. Therefore, early diagnosis of kidney stones is critical. In recent years, machine learning and deep learning approaches have been widely adopted to diagnose diseases thanks to the development of technology. These methods provide a reliable tool for making definitive diagnostic decisions that require long and complex processes, as they shorten the diagnosis time and increase the diagnostic accuracy. Along with deep learning, computer vision can categorize the images, extract the properties of an image and enable the classification of images by predicting them based on the model it creates. Until today, many studies have been conducted in which diseases were diagnosed with the deep learning methods. In a previous study, deep learning methods have been used to detect and classify brain tumors from medical images [2]. In another study, recognizing the pathological characteristics of diabetic patients was provided with deep learning [3]. Besides, deep learning methods were used to diagnose thyroid nodules from ultrasound images [4].

## II. RELATED WORK

In medicine, diseases are diagnosed with the experience and knowledge of doctors. The use of an automatic diagnosis system can facilitate the work of doctors. Some studies [2, 3, 4, 5] use deep learning methods to diagnose eye diseases caused by diabetes to help diagnose and classify diseases. In the United States, the prevalence of diabetic retinopathy is approximately 28.5% among individuals that have diabetes, while this rate is 18% in India [5]. Most physicians refer their diabetic patients to the ophthalmologist at regular intervals for retinopathy or macular edema screening, depending on the severity of the disease. Automatic grading of diabetic retinopathy has the benefits of increasing efficiency, reproducibility, and the scope of screening programs. It can improve patient outcomes by reducing access barriers and providing early diagnosis and treatment. A type of Convolutional Neural Network (CNN) named Inception-v3 is generally used to aid image analysis and object detection. In

**İŞİL KARABEY AKSAKALLI**, is with Department of Computer Engineering University of Erzurum Technical University, Erzurum, Turkey, (e-mail: [isil.karabey@erzurum.edu.tr](mailto:isil.karabey@erzurum.edu.tr)).

 <https://orcid.org/0000-0002-4156-9098>

**SİBEL KAÇDIOĞLU**, is with Department of Computer Engineering University of Erzurum Technical University, Erzurum, Turkey, (e-mail: [sibel.kacdioglu@erzurum.edu.tr](mailto:sibel.kacdioglu@erzurum.edu.tr)).

 <https://orcid.org/0000-0003-0578-998X>

**YUSUF SINAN HANAY**, is with Department of Computer Engineering, University of Erzurum Technical University, Erzurum, Turkey, (e-mail: [sinan.hanay@erzurum.edu.tr](mailto:sinan.hanay@erzurum.edu.tr)).

 <https://orcid.org/0000-0002-3331-5936>

Manuscript received February 10, 2021; accepted April 19, 2021.  
DOI: [10.17694/bajece.878116](https://doi.org/10.17694/bajece.878116)

the EyePACS-1 data set, the sensitivity of the algorithm was 97.5%, and the specificity was 93.4%. In the Messidor-2 data set, the sensitivity was 96.1%, and the specificity was 93.9% [3]. In literature, CNN is also used for brain tumor detection. In [2], a deep learning-based brain tumor detection and classification system have been proposed using skull MR images. In the study, ELM-LRF (Local receptive field extreme learning machine) method was proposed for tumor classification. As a result of the experiments, the classification accuracy of MR images is 97.18%. The performance of the proposed method is better than recent studies conducted with commonly used methods such as CNN. In another study, a transfer learning method using the Inception-v3 model, which was previously adapted to medical image analysis, was proposed to classify nodules in the thyroid glands from ultrasound images [4]. By classifying 20 of the 21 FNA malignant glands as malignant, they obtained 95.2% sensitivity and 61.8% specificity values by classifying 21 of the 34 FNA benign glands as benign. Besides, in the external test set (100 gland appearance 50 benign, 50 malignant), 50 FNA classified 47 malignant glands as malignant and obtained 94% sensitivity, 50 FNA classified 28 benign glands and obtained 56% specific values [4]. Today, the fine needle aspiration ((FNA)) method is used when evaluating nodules. Computer-based nodule detection and classification can help doctors avoid unnecessary FNA.

There are many studies on the diagnosis and classification of kidney diseases by machine learning methods. In this study, a synthetic kidney function test (KFT) data set including age, gender, urea, creatinine, and glomerular filtration rate was created for the analysis of kidney disease. The study aims to compare the performance of the two methods under two headings as accuracy and working time by using the

the KNN classifier was found to be 89%, and the accuracy of the SVM classifier to 84% [7]. In a similar study, classification of kidney disease (stone or tumor) and segmentation was provided on ultrasound images [8]. Artificial neural networks are proposed for classification and multi-core k-means algorithm for segmentation. A median filter was used to remove noise in ultrasound images. GLCM (Level Co-occurrence Matrix) features were removed from each image after the noise was removed. As a result, it is seen that the system proposed as linear + quadratic-based segmentation has reached a maximum accuracy of 99.61% when compared to all other methods. Besides, the type of these stones is also important for treatment. To determine the type of stones, the type of kidney stone was classified from endoscopic video images with a deep learning network trained with digital photographs of five types of kidney stone components. This classification aims to automatically determine the laser energy settings manually adjusted according to the kidney stone component and size [9]. Deep convolutional neural network (CNN), as well as pre-trained ResNet-101, were used for classification. For recall values; UA (Uric acid) component 94.12%, COM (calcium oxalate monohydrate) component 90.48%, CHPD / brushite (calcium hydrogen phosphate dihydrate) component 85.71%, cystine (cystine) component 75%, MAPH / struvite (magnesium ammonium the phosphate hexahydrate component is stated to be 71.42%. For precision values; UA (Uric acid) component 94.12%, COM (calcium oxalate monohydrate) component 95%, CHPD / brushite (calcium hydrogen phosphate dihydrate) component 75%, cystine (cystine) component 75%, MAPH / struvite (magnesium ammonium the phosphate hexahydrate component is stated to be 71.43%. According to the researchers who conducted this study, it is the first study to

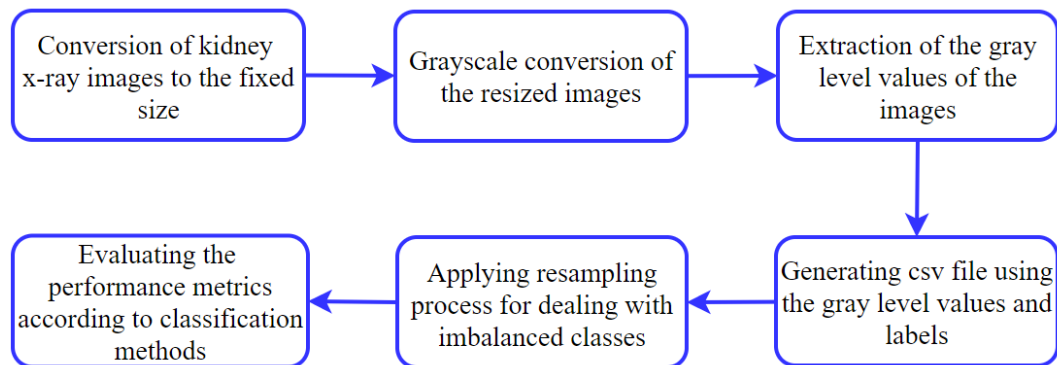


Fig.1. Block diagram of the proposed method

information of kidney patients and Support Vector Machine (SVM) and Artificial Neural Network (ANN) to predict four types of kidney disease [6]. Support Vector Machine (SVM) and Artificial Neural Network (ANN) methods were used. Classification accuracies were calculated as SVM 76.32%, ANN 87.70%. In another study, kidney stones are detected from low contrast ultrasound images. Median filter, Gaussian filter, and blunt masking are applied to improve the images. Subsequently, KNN and SVM classification techniques were used for the analysis of kidney stone images. The accuracy of

use a convolutional neural network to classify kidney stone type. In addition, the positions, shapes and sizes of kidney stones are different from each other. Therefore, kidney stone segmentation with machine learning is challenging. In the literature, preprocessing studies have been carried out to reduce this difficulty. In a study, a preprocess algorithm was developed for kidney stone detection and segmentation from CT images [10]. Three thresholding algorithms based on density, size, and location were applied to extract unrelated organ and bone structures from the images. CT images of 30

patients were studied. As a result, a 95.24% sensitivity value was obtained with the proposed algorithm [10]. In another study [11], the effects of morphological operations on kidney stone classification and analysis were investigated. The location and size of the kidney stone have been tried to be determined using GAC segmentation besides extraction and morphological operations. The proposed algorithms have been applied on several kidney images, and high efficiency has been achieved [11]. In one of the studies in the same direction, SVM was used for classification in automatic kidney stone detection. In the study, before classification, the image histogram equalization and embossing method, which evaluates color differences directionally, was tried. The proposed method was tested on 156 CT images with stones and healthy kidneys, achieving 98.71% accuracy [12]. In another study, a thresholding-based model has been developed with deep learning for the detection and scoring of kidney stones from abdominal non-contrast computed tomography (NCCT) images. The model is divided into four stages. Initially, 3D U-Nets were created for kidney and kidney sinus segmentation. Later, deep 3D dual-path networks were developed for hydronephrosis grading. Thresholding methods were used to identify and segment stones in the renal sinus area. Finally, the location of the stone was determined. As a result, the stone detection method reached 95.9% sensitivity and 98.7% positive predictive value (PPV) [13].

### III. OVERVIEW OF THE PROPOSED METHOD

Kidney x-ray images are used to detect whether a person has kidney stones or not. According to this information, a person is detected to be healthy or patient. This detection is generally decided by a specialist doctor. A sample of healthy or patient images is shown in Fig. 2. Although a specialist doctor can distinguish the images given in the figure, some images cannot be detected by the specialist, or the detection process by humans takes time. Therefore, an algorithmic detection system is needed for the classification of the x-ray images. In this study, a decision support mechanism that determines whether an individual is patient or healthy is proposed by applying various machine learning and deep learning methods to kidney x-ray images. The block diagram of the proposed mechanism is shown in Fig. 1. In the first step of Fig.1, each image was scaled to  $64 * 80$  dimensions because kidney x-ray images were obtained with different sizes. Then fixed-size images were converted into grayscale images to extract gray level values in the second step. In the third step, gray level binary values were extracted from these grayscale images, and these values were saved in a CSV file with their tags. Since the number of data with a healthy label in the data set is quite low compared to the patient label, resampling methods were applied to the dataset to deal with imbalanced classes. After all these processes were performed, various classification methods, including machine learning and deep learning have been applied to the balanced dataset, and the test dataset has been evaluated in terms of precision, recall, and F1 score.

#### A. Dataset

The dataset is prepared by using 221 kidney x-ray images obtained from the Urology Department of Ataturk University.

Before the classification process has been applied, these images are subjected to various preprocesses. In the first step, different-sized x-ray images are converted into  $64 \times 80$  fixed-size images. Then resized images are subjected to grayscale conversion processes in the second step. In the third step, the gray level values obtained from the image are extracted in the CSV file. These values consist of 5120 columns are labeled as patient or healthy according to the presence of kidney stones, catheters, or both found from the x-ray images. Images without any kidney stones or catheters are labeled as healthy, while images with stones or catheters are labeled as patients. This labeling process has been done by taking into account the opinions of the specialist doctors working in the Urology department. In the obtained dataset, 182 images have a patient label, while 39 images have a healthy label.

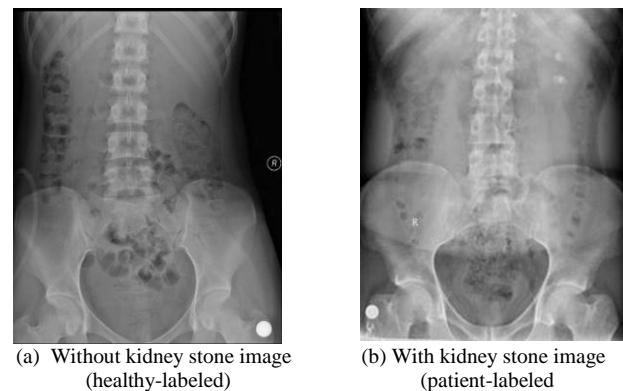


Fig. 2. Sample kidney x-ray images

#### B. Method

In this study, a decision support system based on machine learning and deep learning that detects whether a kidney x-ray image is patient or healthy is proposed. Machine learning (ML) is a branch of artificial intelligence, and it offers powerful classification techniques to make predictions on test data by training existing data and analyzing big data inaccessible to the human mind alone [14]. Machine learning methods are widely used mainly in data classification, pattern recognition, and prediction. Machine learning concepts are used for many applications such as data classification, email filtering, face detection, disease prediction, fraud detection, and traffic management. Deep learning (DL) is a type of machine learning method, and the learning process takes place on an artificial neural network model with more intermediate layers. Deep learning methods can classify large amounts of data with higher accuracy to provide analytical results based on the parameters and objectives of a particular framework [15]. Deep learning is mainly used in image segmentation, disease prediction, and recommendation systems such as convolutional neural networks, autoencoders, and restricted Boltzmann machines [16].

Within the scope of the study, various machine learning methods named Decision Tree (DT) [17], Random Forest (RF) [18], Support Vector Machine (SVM) [19], Multilayer Perceptron (MLP) [20], k Nearest Neighbor (kNN) [21] and Naive Bayes (BernoulliNB) [22] and deep learning

Convolutional Neural Network (CNN) which is a feed-forward neural network [23] have been applied. In the model training phase, the StratifiedKFold cross-validation method is applied to split the dataset. Also, the grid-search method is used to determine the best parameters belonging to the classification methods giving the highest accuracy rate

### 1) Resampling process

Since the data with the healthy label in the data used within the scope of the study are less than the data with the patient label, resampling is performed on the dataset. Among the resampling methods; undersampling, oversampling and SMOTETomek method, which is a combination of two methods, is applied in the scope of this study. Undersampling takes place by deleting a randomly selected section from the data belonging to the dominant class. In addition to bringing the data more stable, this method can shorten the running time of the classification method since it enables running with smaller data, especially when the data size is very large. On the other hand, as the information in the deleted data is lost, it can lead to underfitting problems. Oversampling can be defined as increasing the number of data belonging to this class by repeating a randomly selected part of the data belonging to the minority class. Since there is no loss of information in this method, it may be a superior method compared to undersampling. However, since some of the data are repeated precisely, it can lead to overfitting problems.

### 2) Classification

After resampling on the data set, train-test splitting is performed to be used as 80% training and 20% test data. The obtained train data is trained using StratifiedKFold cross-validation (kFold = 5). Then, test data that are not used in model training is evaluated in terms of Precision, Recall, and F1 score metrics. Performance percentages according to the resampling methods and classification algorithms used are given in Tables II and III.

TABLE I  
THE BEST PARAMETER VALUES FOR THE DATA SET ACCORDING TO MACHINE LEARNING METHODS

Algorithm	Best parameter values
Decision Tree (DT)	<i>criterion='gini', max_depth=3</i>
Random Forest (RF)	<i>criterion='entropy', max_depth= 4, max_features='log2', n_estimators= 200</i>
Support Vector Machine (SVM)	<i>C=0.1, gamma=1, kernel='rbf'</i>
Multilayer Perceptron (MLP)	<i>random_state=1, max_iter=300</i>
k Nearest Neighbor (kNN)	<i>n_neighbors= 16</i>
Naive Bayes (BernoulliNB)	<i>alpha= 10.0</i>

A general description of all classification methods applied within the scope of this study is given below:

**Decision Tree (DT):** Decision Tree is a supervised learning method generally used for classification and regression

analysis [24]. DT is expressed as a structural flow chart. Each internal node represents a test on an attribute, each branch describes a test result, and each leaf represents a class label [17, 25, 26].

**Random Forest (RF):** Random Forest, which consists of a combination of many decision trees, is used for more classification problems besides regression. A collection of tree-structured classifiers ( $h(x, \Theta_k), k = 1, \dots$ ) represents RF where  $\Theta_k$  are independent distributed random vectors and  $h_1(x), h_2(x), \dots$  represents the training set obtained from random vector  $Y$ .  $X$  is a margin function that is calculated by  $mg(X, Y) = \text{av}_k I(h_k(X)=Y) - \max_{j \neq Y} \text{av}_k I(h_k(X)=j)$  where  $I(\cdot)$  is an indicator. The  $mg$  representing the margin gives the measure of the change in the average number of votes in  $X, Y$  with any other class. The larger  $mg$  value means, the more confidence in the classification [25].

**Support Vector Machine (SVM):** Support Vector Machine is a supervised machine learning method proposed by Vapnik [19]. SVM classifies the samples dividing the training dataset into distinct classes by using a hyperplane. When the dataset consists of two-dimensional data, a linear classifier is used with a linear hyperline [19, 27]. In this study, we use the linear classifier to distinguish the healthy and patient-labeled data. In the mathematical expression,  $x$  is a vector point, and  $w$  is a weight. This classifier aims to find the optimal plane where the distance between the two classes is the greatest to keep the margin value at the highest level. This case is called the maximum margin linear classifier, and the calculation of the margin is expressed in Fig. 3 and equation 1.

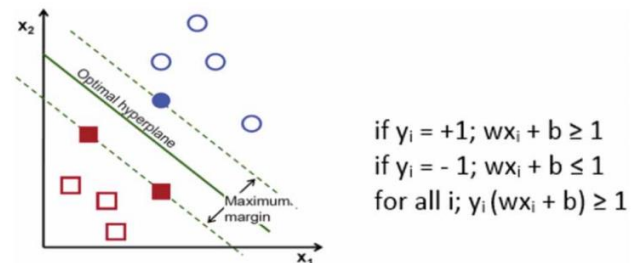


Fig. 3. Linear classification using SVM

$$\text{margin} \equiv \arg \min_{x \in D} d(x) = \arg \min_{x \in D} \frac{|\mathbf{x} \cdot \mathbf{w} + b|}{\sqrt{\sum_{i=1}^d w_i^2}} \quad (1)$$

**Multilayer Perceptron (MLP):** Multilayer Perceptron is a popular feed-forward neural network due to its fast operation, easy applicability, and small dataset requirements [26]. In this network structure, units consist of an input layer, one or more hidden layers, and an output layer [20]. The input layer takes an activation vector externally and transmits it to the units in the first hidden layer via weighted links. After each layer calculates its activation, it transfers the activation to the neurons in the successive layers, as shown in Fig. 4.

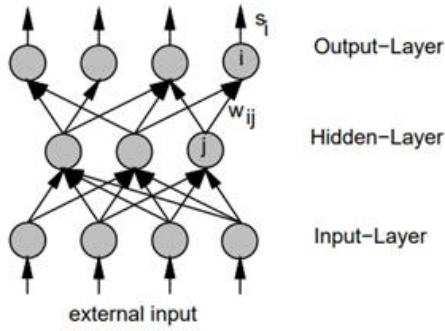


Fig. 4. Multilayer Perceptron with one hidden layer

Each neuron  $i$  in the network is a simple processing unit that calculates the activation  $s_i$  based on incoming excitation called the  $net_i$ .  $net_i$  is calculated as seen in equation 2:

$$net_i = \sum_{j \in pred(i)} s_j w_{ij} - \theta_i \quad (2)$$

In this equation,  $pred(i)$  indicates the set of predecessors of unit  $i$ , while  $w_{ij}$  represents the weight of the connection from unit  $j$  to unit  $i$ .  $\theta_i$  is the bias value of the unit  $i$ . The activation of the unit  $i$  is calculated by passing the net input through a nonlinear activation function. Usually the sigmoid logistic function is calculated as follows:

$$s_i = f_{log}(net_i) = \frac{1}{1 + e^{-net_i}} \quad (3)$$

Having an easily computable derivative of this function makes the method advantageous. The derivation is shown below:

$$\frac{\partial s_i}{\partial net_i} = f'_{log}(net_i) = s_i * (1 - s_i) \quad (4)$$

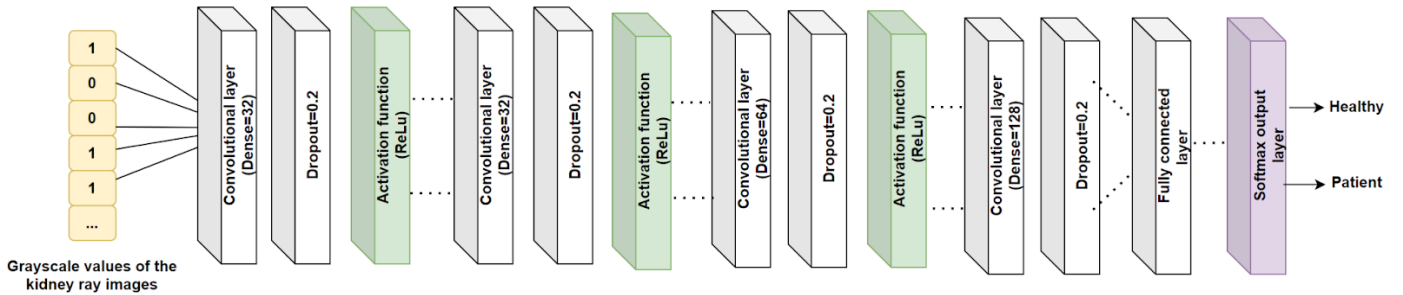


Fig.5. Designed CNN model for classification of kidney x-ray images

*k Nearest Neighbor (kNN)*: kNN is a supervised learning method that estimates test data based on the samples closest to  $k$  values given in the feature space [27, 28]. After training all existing samples, the method classifies new samples according to the similarity measure. As a result of the experiments performed with the Grid Search method, the optimal  $k$  value is found as 16.

*Naive Bayes (BernoulliNB)*: Naive Bayes method calculates the probability of finding the correct tag of a data from a test dataset by multiplying the probabilities of all factors affecting that result [29]. In the equation below;  $C$  is the class label,  $F$  values are the input data:

$$P(C | F_1, F_2, \dots, F_n) = \frac{P(C) P(\bar{F}_1, \bar{F}_2, \dots, F_n | C)}{P(F_1, F_2, \dots, F_n)} \quad (5)$$

with the operation, there is a probability value that the input data whose class is unknown belongs to the  $C$  class. As a result of probability calculations, the number of class labels is determined as the class of the test data [29].

*Convolutional Neural Network (CNN)*: CNN is one of the most famous successful methods that has been widely used in image processing in recent years. This method is based on artificial neural networks, whose network structure contains more intermediate layers, neurons with learnable weight, and bias. CNN input data, which consists of any image or digital data, differs according to the problem in terms of the dropout value, the number of layers, the activation function used, and the number of neurons [30]. Within the scope of this study, the CNN model is created using Keras library and Python programming language. The best result has been tried to be achieved by changing the learning rate, optimization algorithm, number of hidden layers, number of epochs, weight starting values, and activation functions as hyperparameters. Fig. 5 shows the developed CNN model to classify whether the person is healthy or patient.

#### IV. EXPERIMENTAL RESULTS

After the resampling process is completed, 80% of the dataset (182 image values) is trained, and precision, recall, and F1 score performance metrics are evaluated with the StratifiedKFold cross-validation method. The classification performance of the methods depends on the number of correctly detected classes (TP-Correct Positive), the number of healthy people identified as patients (FP-False Positive), and the number of patients identified as healthy (FN-False Negative). Using these values, the Precision and Recall values

are calculated. F1 score value gives the harmonic average of the precision and recall values. Therefore, a high F1 score value is an essential criterion for a suitable decision support mechanism. General formulas of metrics used in the study are given in equations (6) - (8).

$$\text{Precision} = TP / (TP + FP) \quad (6)$$

$$\text{Recall} = TP / (TP + FN) \quad (7)$$

TABLE II CROSS VALIDATION SCORE FOR TRAINING MODEL (S: SMOTE, U: RANDOMUNDERSAMPLER, ST: SMOTETOMEK, S+U: COMBINIG SMOTE – RANDOMUNDERSAMPLER)

	Cross_val_score											
	Precision (%)				Recall (%)				F1 Score (%)			
	S	U	ST	S+U	S	U	ST	S+U	S	U	ST	S+U
DT	85.8	88	83.8	90.2	85.8	88	83.8	90.2	85.5	70	77.5	77.2
RF	85.5	85.5	85.9	85.8	85.5	85.5	85.5	85.9	91	81.6	87	87.5
SVM	85.8	85.8	85.8	85.8	85.8	85.8	85.8	85.8	92.4	92.4	92.4	92.4
MLP	84.7	88.3	87.2	87.6	84.7	88.3	87.2	87.6	90.3	77.6	85	82.7
kNN	86.2	84.6	80.7	87.4	86.2	84.6	80.7	87.4	87	88.6	32.8	66.6
Bayes	85.8	85.8	79.3	85.8	85.8	85.8	79.3	85.8	92.4	92.4	27.2	92.4
CNN	77.9	77.9	77.9	77.9	100	100	100	100	87.4	87.4	87.4	87.4
<b>AVG</b>	<b>84.5</b>	<b>85.1</b>	<b>82.9</b>	<b>85.6</b>	<b>87.7</b>	<b>88.3</b>	<b>86.1</b>	<b>88.9</b>	<b>89.4</b>	<b>84.3</b>	<b>69.9</b>	<b>83.7</b>

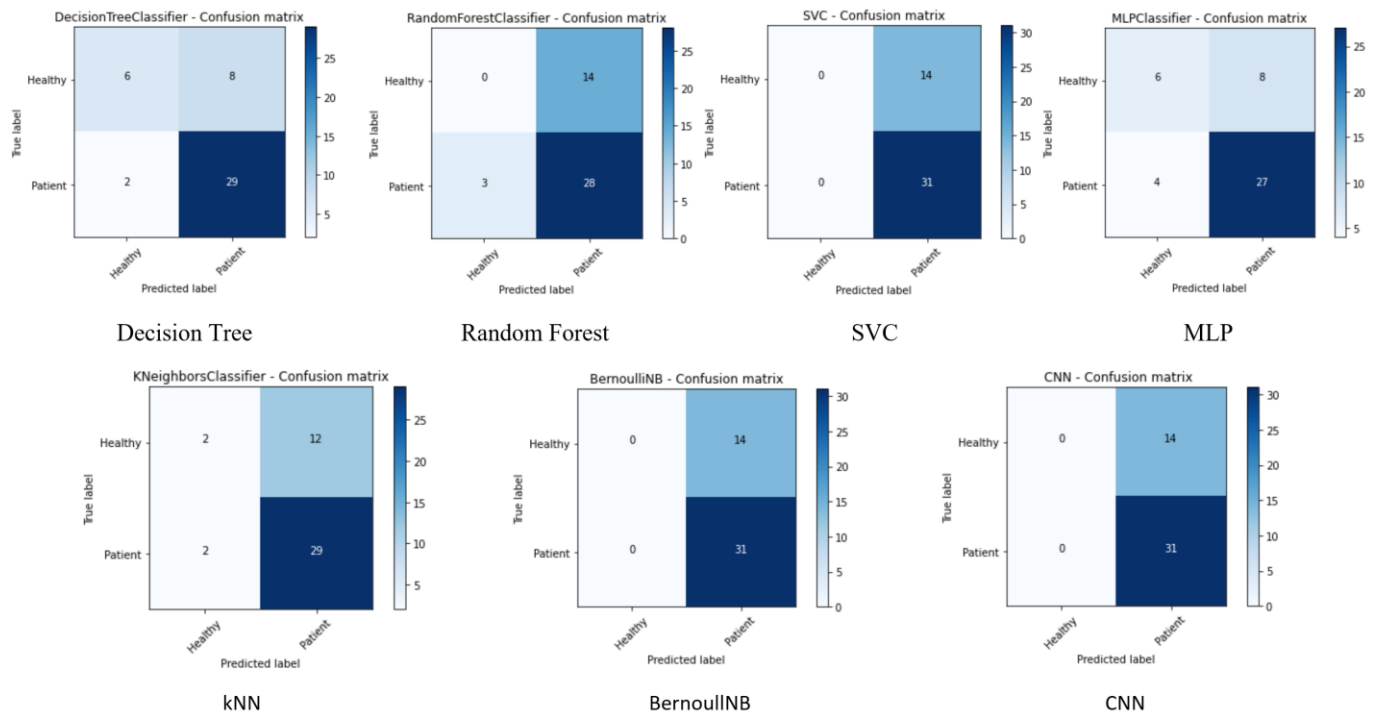


Fig. 6. Confusion matrices obtained from combining SMOTE+RandomUnderSampler method according to classification methods

$$F1\_score = 2 * (\text{Precision} * \text{Recall}) / (\text{Precision} + \text{Recall}) \quad (8)$$

Table II shows the performances of the cross-validation method applied to the training model according to algorithms and sampling methods. While the average highest values in terms of precision (85.6%) and recall (88.9%) metrics are obtained with the combining SMOTE+ RandomUnderSampler (S + U) method, when evaluated in terms of algorithms, the average highest value for F1 Score (89.4%) is obtained using SMOTE sampling method. According to cross-validation scores of the applied algorithms, MLP and CNN achieve the highest values in terms of the evaluation metrics. MLP has an 87.2% precision rate and 92.4% F1 score rate, while CNN has a 100% recall rate.

Table III shows the performance values by applying the cross\_val\_predict method to 45 images that have not been used before on the trained model. In terms of precision, the highest rate (78.4%) is obtained with the Decision Tree Classifier (DT) using the S + U method. When looking at the results of the prediction for the test data (cross\_val\_predict), 100% Recall value is obtained with the CNN method in all samples, while the Precision and F1 score values as a result of ST and S + U sampling are quite low compared to other methods. Furthermore, it is seen that the Decision Tree Classifier (DT) has the highest F1 score by 85.3.1% rate using S+U.

Also, this method gives the highest precision rate (78.4%)

TABLE III CROSS VALIDATION PREDICT FOR TEST MODEL (S: SMOTE, U: RANDOMUNDERSAMPLER, ST: SMOTETOMEK, S+U: COMBINIG SMOTE – RANDOMUNDERSAMPLER)

	Cross_val_predict											
	Precision (%)				Recall (%)				F1 Score (%)			
	S	U	ST	S+U	S	U	ST	S+U	S	U	ST	S+U
DT	72.7	80	69.6	<b>78.4</b>	77.4	77.4	51.6	93.5	75	78.7	59.3	<b>85.3</b>
RF	70.7	68.6	63.9	66.7	93.5	77.4	74.2	90.3	80.6	72.7	68.7	76.7
SVM	68.9	68.9	70.3	68.9	<b>100</b>	<b>100</b>	83.9	<b>100</b>	81.6	81.6	76.5	81.6
MLP	71.9	72.7	76.5	77.1	74.2	77.4	83.9	87.1	73	75	80	81.8
kNN	72.5	68.2	33.3	70.7	93.5	96.8	6.5	93.5	81.7	80	1.08	80.6
Bayes	68.9	68.9	70.4	68.9	<b>100</b>	<b>100</b>	61.3	<b>100</b>	81.6	81.6	65.5	81.6
CNN	68.9	68.9	68.9	68.9	<b>100</b>	<b>100</b>	<b>100</b>	<b>100</b>	81.6	81.6	81.6	81.6
<b>AVG</b>	<b>70.6</b>	<b>70.9</b>	<b>64.7</b>	<b>71.3</b>	<b>91.2</b>	<b>89.7</b>	<b>65.9</b>	<b>94.1</b>	<b>79.3</b>	<b>78.7</b>	<b>61.8</b>	<b>81.3</b>

among the other methods. According to both Table II and Table III, it is examined that all of the sampling methods give the same results in the CNN method.

When the methods are evaluated in terms of sampling, it is seen that the S + U combined sampling strategy gives the highest average recall (94.1%) value, Precision (71.3 %), and F1 score (81.3 %) values. Fig.6 shows complexity matrices obtained as a result of the classification of test data using S+U oversampling. When the confusion matrices seen in Fig. 3 are examined, it is seen that the BernoulliNB and CNN models classify the patient data 100%. Therefore the recall value obtained from these models is 100%. However, these methods couldn't correctly classify the healthy labeled data.

## V. CONCLUSION

In this study, kidney x-ray images obtained from Atatürk University Research Hospital are used to classify patients and healthy individuals implementing machine learning and deep learning approaches. By using these methods, a decision support mechanism is proposed in a shorter time that enables the diagnosis of images that the specialist doctor has difficulty in diagnosing. Firstly, images are converted to the gray level values after they are scaled to fixed sizes. Then, a data set is created by obtaining gray-level numerical values from the images. Since this data set has imbalance classes, various oversampling and undersampling methods are used. In this way, the performance metrics of the methods increase significantly. Accurate detection of healthy individuals is as important as the detection of patient individuals in the detection of kidney diseases. In this respect, achieving high performance in the F1 score is one of the most important criteria. According to the experiments, DT has the highest F1 score rate with a success rate of 85.3% using the S+U sampling method.

## ACKNOWLEDGMENT

The authors thank the Department of Urology at Ataturk University Education and Research Hospital to share kidney x-ray images anonymously,

## REFERENCES

- [1] D. Aune, Y. Mahamat-Saleh, T. Norat, and E. Riboli, "Body fatness, diabetes, physical activity and risk of kidney stones: a systematic review and meta-analysis of cohort studies," *European journal of epidemiology*, vol. 33, no. 11, pp. 1033-1047, 2018.
- [2] A. Ari and D. Hanbay, "Deep learning based brain tumor classification and detection system," *Turkish Journal of Electrical Engineering & Computer Sciences*, vol. 26, no. 5, pp. 2275-2286, 2018.
- [3] V. Gulshan et al., "Development and validation of a deep learning algorithm for detection of diabetic retinopathy in retinal fundus photographs," *Jama*, vol. 316, no. 22, pp. 2402-2410, 2016.
- [4] J. Song et al., "Ultrasound image analysis using deep learning algorithm for the diagnosis of thyroid nodules," *Medicine*, vol. 98, no. 15, 2019.
- [5] R. Raman et al., "Prevalence of diabetic retinopathy in India: Sankara Nethralaya diabetic retinopathy epidemiology and molecular genetics study report 2," *Ophthalmology*, vol. 116, no. 2, pp. 311-318, 2009.
- [6] S. Vijayarani, S. Dhayanand, and M. Phil, "Kidney disease prediction using SVM and ANN algorithms," *International Journal of Computing and Business Research (IJCBR)*, vol. 6, no. 2, pp. 1-12, 2015.
- [7] J. Verma, M. Nath, P. Tripathi, and K. Saini, "Analysis and identification of kidney stone using K th nearest neighbour (KNN) and support vector machine (SVM) classification techniques," *Pattern Recognition and Image Analysis*, vol. 27, no. 3, pp. 574-580, 2017.
- [8] A. Nithya, A. Appathurai, N. Venkatadri, D. Ramji, and C. A. Palagan, "Kidney disease detection and segmentation using artificial neural network and multi-kernel k-means clustering for ultrasound images," *Measurement*, vol. 149, p. 106952, 2020.
- [9] K. M. Black, H. Law, A. Aldouhki, J. Deng, and K. R. Ghani, "Deep learning computer vision algorithm for detecting kidney stone composition," *BJU international*, 2020.
- [10] N. Thein, H. A. Nugroho, T. B. Adji, and K. Hamamoto, "An image preprocessing method for kidney stone segmentation in CT scan images," in *2018 International Conference on Computer Engineering, Network and Intelligent Multimedia (CENIM)*, 2018: IEEE, pp. 147-150.
- [11] M. Shahina and H. S. Mahesh, "Renal Stone Detection and Analysis by Contour Based Algorithm," in *2019 International Conference on Recent Advances in Energy-efficient Computing and Communication (ICRAECC)*, 2019: IEEE, pp. 1-5.
- [12] A. Soni and A. Rai, "Kidney Stone Recognition and Extraction using Directional Emboss & SVM from Computed Tomography Images," in *2020 Third International Conference on Multimedia Processing, Communication & Information Technology (MPCIT)*, 2020: IEEE, pp. 57-62.
- [13] Y. Cui et al., "Automatic Detection and Scoring of Kidney Stones on Noncontrast CT Images Using STONE Nephrolithometry: Combined

- Deep Learning and Thresholding Methods," *Molecular Imaging and Biology*, pp. 1-10, 2020.
- [14] L. E. McCoubrey, M. Elbadawi, M. Orlu, S. Gaisford, and A. W. Basit, "Harnessing machine learning for development of microbiome therapeutics," *Gut Microbes*, vol. 13, no. 1, pp. 1-20, 2021.
- [15] B. Shah, A. Alsadoon, P. Prasad, G. Al-Naymat, and A. Beg, "DPV: a taxonomy for utilizing deep learning as a prediction technique for various types of cancers detection," *Multimedia Tools and Applications*, pp. 1-23, 2021.
- [16] A. K. Sahoo, C. Pradhan, and H. Das, "Performance evaluation of different machine learning methods and deep-learning based convolutional neural network for health decision making," in *Nature inspired computing for data science*: Springer, 2020, pp. 201-212.
- [17] J. R. Quinlan, "Induction of decision trees," *Machine learning*, vol. 1, no. 1, pp. 81-106, 1986.
- [18] L. Breiman, "Random forests," *Machine learning*, vol. 45, no. 1, pp. 5-32, 2001.
- [19] V. N. Vapnik, "An overview of statistical learning theory," *IEEE transactions on neural networks*, vol. 10, no. 5, pp. 988-999, 1999.
- [20] M. W. Gardner and S. Dorling, "Artificial neural networks (the multilayer perceptron)—a review of applications in the atmospheric sciences," *Atmospheric environment*, vol. 32, no. 14-15, pp. 2627-2636, 1998.
- [21] D. W. Aha, D. Kibler, and M. K. Albert, "Instance-based learning algorithms," *Machine learning*, vol. 6, no. 1, pp. 37-66, 1991.
- [22] K. P. Murphy, "Naive bayes classifiers," *University of British Columbia*, vol. 18, no. 60, 2006.
- [23] K. Fukushima and S. Miyake, "Neocognitron: A self-organizing neural network model for a mechanism of visual pattern recognition," in *Competition and cooperation in neural nets*: Springer, 1982, pp. 267-285.
- [24] K. C. Kandpal, S. Kumar, G. S. Venkat, R. Meena, P. K. Pal, and A. Kumar, "Onsite age discrimination of an endangered medicinal and aromatic plant species *Valeriana jatamansi* using field hyperspectral remote sensing and machine learning techniques," *International Journal of Remote Sensing*, vol. 42, no. 10, pp. 3777-3796, 2021.
- [25] M. A. Friedl and C. E. Brodley, "Decision tree classification of land cover from remotely sensed data," *Remote sensing of environment*, vol. 61, no. 3, pp. 399-409, 1997.
- [26] S. Naaz, "Detection of Phishing in Internet of Things Using Machine Learning Approach," *International Journal of Digital Crime and Forensics (IJDCF)*, vol. 13, no. 2, pp. 1-15, 2021.
- [27] M. Riedmiller, "Advanced supervised learning in multi-layer perceptrons—from backpropagation to adaptive learning algorithms," *Computer Standards & Interfaces*, vol. 16, no. 3, pp. 265-278, 1994.
- [28] E.-H. S. Han, G. Karypis, and V. Kumar, "Text categorization using weight adjusted k-nearest neighbor classification," in *Pacific-asia conference on knowledge discovery and data mining*, 2001: Springer, pp. 53-65.
- [29] G. Yang et al., "Tree Species Classification by Employing Multiple Features Acquired from Integrated Sensors," *Journal of Sensors*, vol. 2019, 2019.
- [30] I. Karabey and L. Bayındır, "An evaluation of fingerprint-based indoor localization techniques," in *2015 23rd Signal Processing and Communications Applications Conference (SIU)*, 2015: IEEE, pp. 2254-2257.
- [31] İ. K. AKSAKALLI and L. BAYINDIR, "Derin Öğrenme Kullanılarak Parmak izi Tabanlı İç Ortam Konumlandırma," *Erzincan Üniversitesi Fen Bilimleri Enstitüsü Dergisi*, vol. 13, no. 2, pp. 483-501.

## BIOGRAPHIES



**ISIL KARABEY AKSAKALLI** graduated from Gazi University in 2013 and started to work as a research assistant at Atatürk University in 2014. After receiving her MSc degree from Atatürk University in 2015, she was appointed as a research assistant to Erzurum Technical University in the

Department of Computer Engineering. She started her PhD. in 2016 at Hacettepe University and still continues to this program. Her research topics include microservice architectures, optimization methods, distributed systems, machine learning and deep learning techniques.



**SIBEL KACDIOĞLU** obtained a bachelor degree in Computer Engineering from Anadolu University in 2016. She received her M.Sc. in 2020 in Computer Engineering Department at the Atatürk University, Erzurum. Currently she pursues her Ph.D. in Computer Engineer at Computer Engineering Department of Atatürk University, Erzurum. Along with her Ph.D. she works as a research assistant in Erzurum Technical University. Her areas of interest are Machine Learning, Computer Vision and Image Processing.



**Y. SINAN HANAY** received Ph.D. in Electrical and Computer Engineering from University of Massachusetts (UMass), Amherst in 2011. He joined Osaka University in 2011 as a post-doctoral researcher. From 2012 to 2016, he worked at Center for Information and Neural Networks (CiNet) of NICT Japan. During that time, he also held visiting researcher and lecturer positions at Osaka University. He is a co-author of a paper which received the best paper award in IEEE International Conference on High Performance Switching and Routing 2011. He is currently an assistant professor at Erzurum Technical University in Turkey.

# Automatic Positioning of Mobile Users via GSM Signal Measurements

Ercan Demir and Abdulkemir Öztekin

**Abstract**—Today the need for mobile communication systems and the high increase in the number of users have also made the development of new generation mobile applications indispensable. Obtaining location information has been one of the most interesting and significant areas of improvement. The purpose of the services used to determine the location is generally to obtain the information of the users such as approximate location, speed, and time. The GPS is the most preferred and globally accurate positioning system among global positioning systems. However, in addition high installation cost of the system; galactic and meteorological factors, high buildings, other physical obstacles, and especially indoor areas are some of the main constraints that can lead to serious signal degradation and losses which may cause the system to be out of service. In this context, there is an urgent need for positioning systems that will be alternative and complementary to global positioning systems. The cellular network is widely used by almost everyone and its coverage area is increasing day by day. The network has been trained and tested in the simulation environment using machine learning algorithms, namely, extreme learning machine (ELM), generalized regression neural network (GRNN), and k nearest neighborhood (kNN). When compared to other cellular localization methods in the literature, the proposed system performs positioning with much higher accuracies with distance error rates below a meter (m) at minimum, and between 76-216 m on average. The test results show that it can successfully localize the mobile users with a significant accuracy for indoor, where GPS signals are very weak or cannot be received at all; and it can also stand in the breach for outdoor, where GPS may be disabled for different reasons.

**Index Terms**—GSM positioning, GPS, localization, machine learning.

**ERCAN DEMİR** is with Department of Electrical Electronics and Engineering Batman University, Batman, Turkey, (e-mail: [ercandemir23.ed@gmail.com](mailto:ercandemir23.ed@gmail.com)).

 <https://orcid.org/0000-0002-3234-8728>

**ABDULKERİM ÖZTEKİN** is with Department of Electrical and Electronics Engineering Batman University, Batman, Turkey, (e-mail: [abdulkemirimoztekin@gmail.com](mailto:abdulkemirimoztekin@gmail.com)).

 <https://orcid.org/0000-0002-0698-3525>

Manuscript received January 04, 2021; accepted April 27, 2021.  
DOI: [10.17694/bajece.852963](https://doi.org/10.17694/bajece.852963)

## I. INTRODUCTION

THE HIGH interest in mobile communication systems triggers the development of new technologies and applications. Geolocation techniques are one of the most important developments in this field. Positioning techniques enable the position estimation of people, mobile devices or equipment. Global positioning systems are the most widely used positioning systems in many areas in today's technology. Global geolocation systems are mainly used in military fields (fighter jets, smart weapons and bombs, positioning vehicles and equipment) and scientific studies (geological studies, remote sensing research, geophysical measurements, cartography, etc.). On the other hand, such positioning systems are widely used in many transportation systems, mining activities, all kinds of security applications, especially in search and rescue operations, agricultural activities, and sports activities [1].

Among the satellite systems used for global positioning, the most widely used positioning system with the widest user mass is the global positioning system (GPS). This system developed by the USA was used for military purposes in the early days. The GPS global positioning system consists of two main parts: satellites positioned in the earth orbit and ground stations that control these satellites. Such global positioning systems are costly to install. However, these systems may not work because sufficient signal levels cannot be generated in closed areas such as tunnels, under bridges, and inside buildings, as well as blind spots created by obstacles. In addition to the high number of complex, multi-storey, and wide-spread buildings in today's modern settlements, this number is increasing day by day. Due to the fact that the buildings consist of tens of floors, hundreds of rooms, and corridors, they are both complex and the number of population they accommodate gives the appearance of small cities [2]. The inadequacy of global positioning systems such as the inability to work in such closed areas indicates the need for effective positioning systems that can also work in closed areas.

In this context, the Global System for Mobile Communications (GSM-Global System for Mobile Communications) emerges as a good alternative in determining the location of the mobile user. In addition to the increasing need for daily use of mobile devices used for communication, their popularity has also increased day by

day. In addition to the fact that cellular base stations are more and more frequent in metropolitan areas, the coverage area is rapidly increasing to include rural areas. However, the ability to receive signals from cellular base stations even in closed areas and in worse physical conditions brings the GSM-based positioning system one step further to determine the location of the mobile user.

There are different studies in the literature for cellular network-based location determination. Magro et al. have estimated the user's location with an average margin of error of 324 m using a genetic algorithm exploiting network parameters, such as cell ID and transmitted signal strength that can be accessed by mobile devices in 3G networks [3]. Türkyılmaz has proposed an environment aware location estimation method based on signal strength measurements for cellular networks, where it has been reported that the average error has been reduced from 642 m to 573 m (10.75% improvement), the standard deviation from 689 m to 481 m (30.19% improvement), and the maximum error from 4762 m to 2638 m (44.6% improvement) [4].

In the study conducted by Kurt, a positioning system using the fingerprint in cellular networks has been employed using received signal strengths (RSS) collected from mobile stations in two different regions, resulting in an average distance error of 435 m and 405 m, respectively [5]. Fritsche et al. have worked on obtaining approximate location information over the GSM network in case of interruption of GPS information [6]. A geolocation algorithm has been developed using Kalman filter exploiting the information with the help of both GPS satellites and measured information from the GSM network. Xuereb and Debono have proposed a mobile terminal location estimation using support vector machines with an error margin of 314m [7].

In this paper, a study has been carried out to obtain approximate location information via cellular networks. A data set including the location information of these base stations together with a sufficient number of real signal measurements obtained from different GSM base stations from different points of the region, both indoor and outdoor, was created by means of a mobile application that have been developed in the Android Studio environment. In Matlab simulation environment, the training of the network has been provided with this obtained data set using machine learning methods: extreme learning machine (ELM), generalized regression neural network (GRNN) and k nearest neighbors (kNN) algorithm. Thus, a study was conducted to obtain approximate real location information by using signal measurements on the test data.

The study consists of four sections. After this introduction section, in the second section, a brief background on extreme learning machines, generalized regression neural network and k nearest neighbor algorithm are given. The third section includes the application findings. The last section concludes the paper by discussion and suggestion of further studies.

## II. MATERIALS AND METHOD

### A. Collection of the Data Set

The data used in this study consists of signal measurement records obtained from indoor and outdoor locations in a certain region in the city center of Siirt (a province in Turkey) via a convenient and easy-to-access mobile application that we have developed in the Android Studio environment. The developed application has been installed and runs on an android based mobile phone to collect and record data. The map of the scanned area where the data collection process has been taken is shown in Figure 1, using the Google Earth application.



Fig.1. Google Earth output illustrating the scanned area for data collection

The collected data consists of the actual signal strengths measured in dBm from different base stations of the serving cellular network and the geographic coordinates (i.e., latitude and longitude) of the currently serving cell location taken via internet and the actual position of the mobile user taken via GPS, which have been recorded instantly at certain time intervals that can be easily adopted according to the relative speed of the mobile user to ensure sufficient amount of data. The record has been arranged in a suitable form and has been purified from redundant data to acquire consistent information since it may inherently contain repetitive information from the same cells according to the availability of the cells of the serving network. Therefore, the data set has been ensured to contain measurements from at least three different cells, namely the camping cell and other neighboring cells, as the proposed algorithm relies on. The obtained parameters to be used in the simulation environment have been classified in Table 1.

TABLE I  
THE CONTENT OF THE DATA SET

RSS1	RSS measured from serving cell
RSS2	RSS measured from neighboring cell
RSS3	RSS measured from neighboring cell
Lat1	Latitude information of the serving cell
Lon1	Longitude information of the serving cell
Lat2	Latitude information of the mobile user
Lon2	Longitude information of the mobile user

TABLE II  
AN ARRANGED SAMPLE DATA SET

Record #	RSS1 (dBm)	RSS2 (dBm)	RSS3 (dBm)	Lat1 (°)	Lon1(°)	Lat2(°)	Lon2(°)
1	-94	-102	-102	37.9362619	41.9339838	37.93444416	41.94037064
2	-90	-103	-104	37.9362619	41.9339838	37.93438009	41.94037293
3	-92	-101	-102	37.9333024	41.9348472	37.93426857	41.94035169
4	-94	-99	-103	37.9333024	41.9348472	37.93428212	41.94035159
:	:	:	:	:	:	:	:
:	:	:	:	:	:	:	:
985	-102	-98	-105	37.9324745	41.9422683	37.93430771	41.94339912
986	-70	-83	-84	37.9351614	41.9419484	37.93448996	41.94061816
987	-72	-81	-83	37.9351614	41.9419484	37.93437705	41.94047073
:	:	:	:	:	:	:	:

In addition to the two basic data sets obtained by both indoor and outdoor measurements, a third data set has been formed by combining these two data sets to obtain a mixed type data to provide a more general and realistic model. Finally, the acquired data sets reflecting the three types of scenarios, namely indoor, outdoor and general, are then ready to be tested in the simulation environment. The arranged data set consists of a total of 2040 data, categorized as 1203 data for indoor and 837 data for outdoor, where a sample of the data set is given in Table 2.

**B. Extreme Learning Machine**

Extreme learning machine (ELM) is a method developed to be used in training feed-forward artificial neural networks (ANN) with only one hidden layer [8]. The scheme of the network is given in Figure 2.

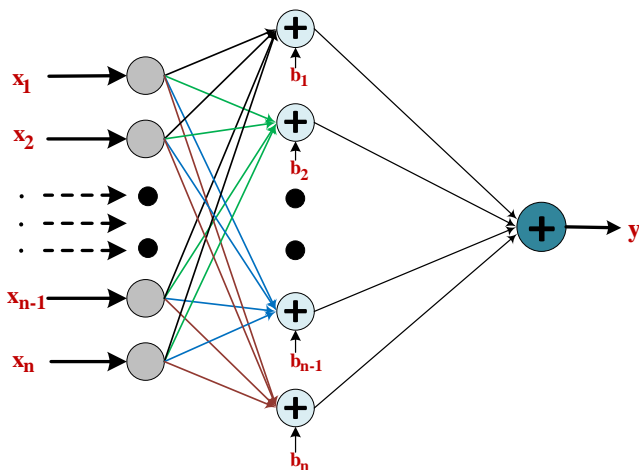


Fig.2. A feed-forward ANN model with one hidden layer

The output equation of the network is given as

$$Y(p) = \sum_{j=1}^m \beta_{j,k} g \left( \sum_{i=1}^n w_{i,j} x_i + b_j \right) \tag{1}$$

where  $x_{1...n}$  are the input vectors,  $y_{1...p}$  are the output vectors,  $\beta_{1...m}$  are the output layer weights,  $w_{1...n,1...m}$  are the connection weights between input layer and hidden layer,  $b_{1...m}$  are the biases and  $g(\cdot)$  is the activation function [9].

In order for ANN to be able to learn successfully, the transfer function, the biases and weights of the system to be modeled have to be selected properly.

In order to minimize the error that will occur during training in gradient-based approaches, the process of changing the given weights and biases continue until the most appropriate parameters are obtained. In the ELM method, the input weights and biases are given randomly, and the output weights are calculated accordingly [10]. Equation 1 can be rewritten in a more compact form as follows

$$y = H\beta \tag{2}$$

where  $H$  represents the hidden matrix of the network.  $H$  can be calculated as follows

$$H = \begin{bmatrix} g(w_{1,1}x_1 + b_1) & \dots & g(w_{1,m}x_m + b_m) \\ g(w_{n,1}x_n + b_1) & \dots & g(w_{n,m}x_m + b_m) \end{bmatrix} \tag{3}$$

Calculation of the inverse matrix of  $H$  matrix is performed with the generalized Moore-Penrose matrix. So the output weights ( $\beta$ ) can be calculated as

$$\beta = H^\dagger y \tag{4}$$

where  $H^\dagger$  in Equation 4 indicates the Moore-Penrose generalized inverse matrix [11].

### C. Generalized Regression Neural Network

Generalized regression neural network (GRNN) is a controlled type of feed-forward neural network (FFNN) and is one of the most popular neural networks. It was first introduced by Donald F. Specht in 1991. The training of GRNN networks is very fast, because unlike other networks where most of the data can be propagated back and forth many times until an acceptable error is found, in GRNN data only needs to be moved forward once [12]. The GRNN network works well on interpolation problems, a mathematical method developed to calculate missing data in a series. GRNN networks are used for estimating continuous variables as in standard regression techniques. By taking the function prediction directly from the training data, it approximates any function between the input and output vectors. In addition, as the size of the training set increases the prediction error approaches zero, but there are only slight restrictions on the function [13].

A GRNN consists of four layers: input layer, pattern layer, summation layer and output layer. The number of input units on the input layer depends on the total number of observation parameters. The first layer is connected to the pattern layer, and each neuron in this layer provides a training pattern and its output. The pattern layer is connected to the summation layer. In training of the network, radial-based and linear activation functions are used in the hidden and output layers [14]. Each pattern layer unit is connected to  $S$ - and  $D$ -summation neurons. The  $S$ -summation neuron computes the sum of the weighted responses of the pattern layer. On the other hand, the  $D$ -summation neuron is used to calculate the non-weighted output of the pattern neurons.

$y_i$  is the target output value corresponding to the  $i$ th input pattern and represents the connection weight between the pattern layer and  $S$ -summation neuron. The connection weight for  $D$ -summation neuron is unity. The predicted value  $\hat{y}_i$  to an unknown input vector  $x$ , is obtained by the output layer which divides the output of each  $S$ -summation neuron by  $D$ -summation neuron

$$\hat{y}_i = \frac{\sum_{i=1}^n y_i \cdot \exp - D(x, x_i)}{\sum_{i=1}^n \exp - D(x, x_i)} \quad (5)$$

where  $n$  is the number of training patterns, and the Gaussian function  $D$  is defined as

$$D(x, x_i) = \sum_{k=1}^m \left( \frac{x_k - x_{ik}}{\sigma} \right)^2 \quad (6)$$

where  $m$  is the number of elements of the input vector, The  $x_k$  and  $x_{ik}$  are the  $k$ th element of  $x$  and  $x_i$ , respectively. The  $\sigma$  is generally called as spread and its optimal value is determined experimentally. It should be noted that in conventional GRNN applications all units in the pattern layer have the same single spread [15].

### D. $k$ Nearest Neighbor

The  $k$  nearest neighbor ( $k$ NN) is a sample based learning algorithm that performs the learning process according to the data in the training set. Classification of a new data is made according to the distance (similarity) between the data in the

training set [16]. In  $k$ NN regression, the algorithm is used for estimating continuous variables. The algorithm employs a weighted average of the nearest neighbors  $k$ , weighted by the inverse of their distance. In the  $k$ NN method, the data in the training set are recorded with numerical features. Each data represents a point in  $m$ -dimensional space and all of the data in the training set is included in an  $m$ -dimensional data area. In case a new data is encountered, the classification of the new data is performed by determining  $k$  pieces of data that are similar to the new data from the data in the training set [17].

One of the most important factors affecting the performance of the  $k$ NN is how to calculate the distance between data. The calculation process can be performed by Euclidean distance or other distance measurement parameters, such as Minkowsky, Hamming or Mahalanobis distance metrics or their variants, depending on the data. Since symmetrically non-propagated classes are often encountered while determining the class in the  $k$ NN, such classes are more dominant in determining the classes of new data. Therefore, methods that give weight values in different ways to the values that affect the distance measurement of the  $k$ NN are used [18].

The  $k$ NN is highly effective in training sets with a large number of data; it can achieve significant successful results. It can create a classification model even if there are data that are not similar to the data in the training set. The availability of such data increases the time required for training the data set [19]. Although the  $k$ NN is structurally simple, it has a high computational cost. Calculating the distance between the data to be classified and the data in the data set requires a very high calculation cost in training sets with a high number of data. In order to minimize such a high cost, methods that can be used with  $k$ NN can be preferred. For example, structurally powerful search trees or elementary component methods that can reduce data size can be used [20]. The  $k$ NN is not very successful in sets with high dimensions. In addition, it is very sensitive to factors such as neighborhood number and distance measurement and requires high memories [21].

Choosing of the optimal  $k$  parameter is a crucial task in  $k$ NN, and it is mostly dependent on the type of the employed data. Large values of  $k$  generally can improve the noise effect in classification, but it may cause to a distinction of the boundaries of the classes; however, an optimal selection of  $k$  neighbors can be obtained using various heuristic algorithms [22]. In the special case of selecting  $k = 1$  in prediction of the class to belong to the closest training sample is known as the nearest neighbor algorithm. In the two-class  $k$ NN (i.e. binary case classification), if  $k$  is chosen to be an odd number then it helps the algorithm to avoid tied votes. Bootstrap technique is one of the popular empirical method in selecting the optimal  $k$  value in the setting stage [23].

### E. Proposed Method

The block diagram of the proposed positioning system is illustrated in Figure 3. The arranged data set obtained via our developed application consists of a total of 2040 data, categorized as 1203 data for indoor and 837 data for outdoor. In the first preprocessing stage, the data is retrieved from the application, recorded to a database and categorized to the

relevant classes. In the next stage, all data sets are put through the machine learning algorithms, namely ELM, GRNN and, kNN to predict the position of the current location of the mobile user. Eventually, the predicted location information is compared with the actual location information obtained via GPS to calculate the distance between the predicted and actual location coordinates, thus enabling to measure the performances of each algorithm in terms of minimum/mean distance error and RMSE.

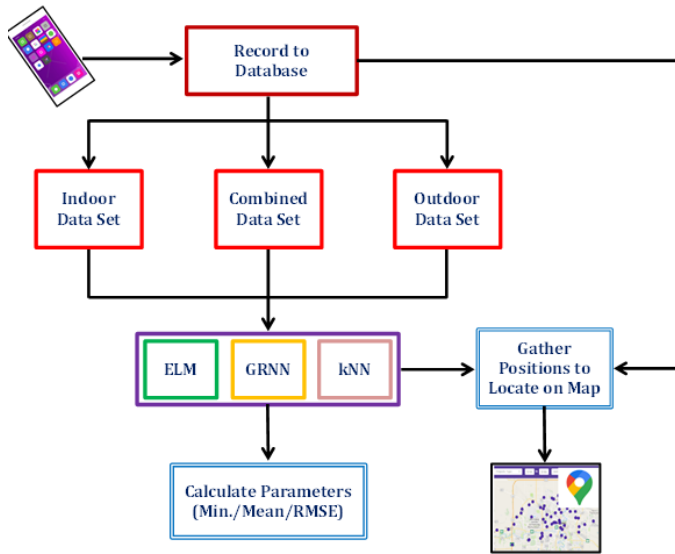


Fig.3. A general layout of the proposed algorithm

### III. RESULTS AND DISCUSSION

For the selection of the activation function, which is one of the most important parameters affecting the performance of ELM, 14 different activation functions have been tested. Another important parameter affecting the performance is the number of neurons in the hidden layer, and tests are carried out for different numbers of neurons (5, 10, 25, 50, 75, 100, 125) and thus the network parameters (input and output weights and biases) that will work with best accuracy are determined separately for each data set. The optimum spread value which is the most important parameter for GRNN, was determined by conducting experiments for each data set using a total of 10 spread values (0.3, 0.5, 0.7, 0.9, 1, 1.5, 2, 2.5, 3, and 4). In the kNN method, k neighborhood parameter was tested for different numbers of

neighborhood values (1, 2, 3, 5, 10, 25, and 50) in the simulation environment and the minimum k value that would be optimum for each data set was determined.

Depending on the used methods and related parameters, the distance between the estimated position (i.e., latitude & longitude) and the actual position was calculated using the Haversine formula given below

$$d = 2r \arcsin \left( \sqrt{\sin^2 \left( \frac{lat2 - lat1}{2} \right) + \cos(lat1) \cos(lat2) \sin^2 \left( \frac{lon2 - lon1}{2} \right)} \right) \quad (7)$$

where d is the distance in kilometer (km), and the parameter r is the radius of the Earth taken as r ≈ 6371 km. The parameters lat1, lon1, lat2, and lon2 represent the latitudes and longitudes of the actual and the estimated location in radians (rad), respectively. This distance expresses the amount of deviation from the actual position, i.e., the amount of error. The performances of all given methods were tested for each data set, namely: indoor, outdoor, and mixed data sets. The root mean square error (RMSE) metric, as well as the obtained distance errors, have been used as the performance parameters for evaluation.

#### A. Indoor Data Set

The RMSE values obtained in the tests performed with ELM method to determine the location with indoor data set are given in Table 3.

Among 14 activation functions, the best average RMSE values were provided by symmetric hard-limit, symmetric saturating linear, tangent sigmoid, pure linear and hyperbolic tangent activation functions. When all the activation functions and the number of neurons in the hidden layer are examined together, it can be seen that the best performance is achieved by the pure linear activation function with a value of 0.00145 RMSE and 10-125 neurons.

As a result of the tests obtained by cross validation using different activation functions and different number of neurons, the min. and mean distances between the estimated and actual locations are given in Table 4. The results show that each activation function has performed a min. error of approximately a few meters, and the best result was obtained as 0.9 m, using multiquadratic activation function with 75 neurons. It is seen that almost all of the activation functions used has performed an average error of 200 to 250 m, where the best mean error distance was achieved as 199 m using the pure linear activation function with 10-100 neurons. Also, the

TABLE III  
AVERAGE RMSE VALUES USING ELM / INDOOR

Activation Functions	Number of Hidden Neurons						
	5	10	25	50	75	100	125
Sym. Hard-limit	0.00167	0.00166	0.00166	0.00163	0.00163	0.00160	0.00159
Sym. Sat. Linear	0.00167	0.00165	0.00165	0.00162	0.00161	0.00160	0.00159
Tangent Sigmoid	0.00167	0.00167	0.00165	0.00163	0.00160	0.00159	0.00159
Pure Linear	0.00216	<b>0.00145</b>	<b>0.00145</b>	<b>0.00145</b>	<b>0.00145</b>	<b>0.00145</b>	<b>0.00145</b>
Hyp. Tangent	0.00167	0.00166	0.00163	0.00165	0.00161	0.00160	0.00160
Multiquadratic	0.00167	0.00166	0.00162	0.00160	0.00158	0.00157	0.00157

TABLE IV  
MIN. AND MEAN DISTANCE ERRORS (M) USING ELM/ INDOOR

Activation Functions	Number of Hidden Neurons													
	5		10		25		50		75		100		125	
	Min.	Mean	Min.	Mean	Min.	Mean	Min.	Mean	Min.	Mean	Min.	Mean	Min.	Mean
Sym. Hard-limit	22	5234	10	223	15	221	15	438	4	220	8	320	5	382
Sym. Sat. Linear	21	224	1	221	4	221	12	320	12	218	7	216	7	244
Tangent Sigmoid	11	228	5	224	10	229	5	220	4	238	8	227	7	239
Pure Linear	5	295	2	<b>199</b>	2	<b>199</b>	3	<b>199</b>	3	<b>199</b>	2	<b>199</b>	2	200
Hyp. Tangent	6	224	8	224	8	221	4	222	10	343	7	242	8	419
Multiquadratic	7	224	8	223	5	219	2	217	<b>0.9</b>	226	5	220	5	258

best performances were mostly obtained with the pure linear activation function.

The obtained min. and mean distance errors for each activation function depending on the number of neurons in the hidden layer is shown graphically in Figure 4. It can be seen from the figure that the best results are mostly obtained with the pure linear activation function.

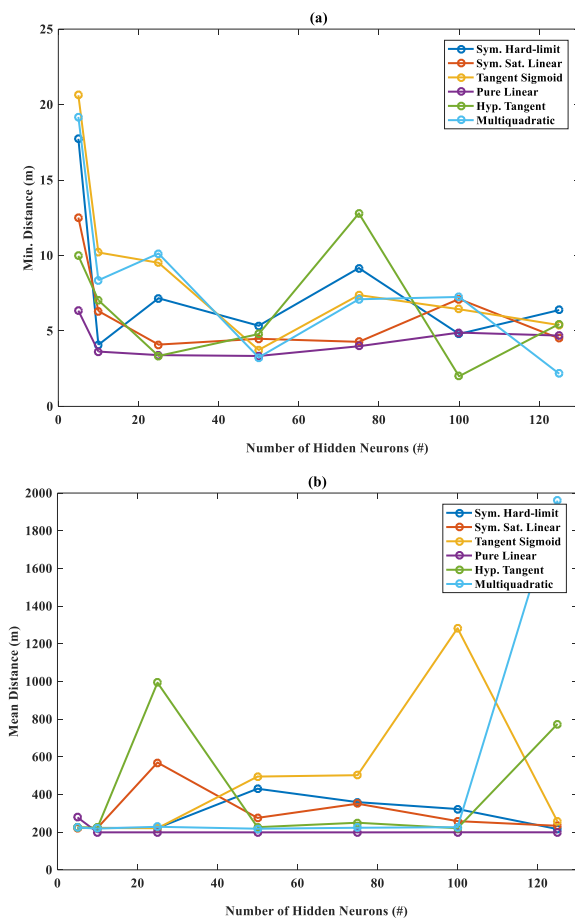


Fig.4 Distance errors vs number of hidden neurons, (a) Min. (b) Mean

The obtained test results using GRNN method for indoor data set depending on the spread values (0.3-4.0) is given in Table 5.

TABLE V  
MIN. AND MEAN DISTANCE ERRORS (M), AND RMSE VALUES USING GRNN / INDOOR

Spread Values	Min.	Mean	RMSE
0.3	<b>0.001</b>	228	0.0019
0.5	<b>0.001</b>	224	0.0018
0.7	<b>0.001</b>	217	0.0017
0.9	<b>0.001</b>	213	0.0017
1.0	<b>0.001</b>	212	<b>0.0016</b>
1.5	0.014	<b>210</b>	<b>0.0016</b>
2.0	0.021	<b>210</b>	<b>0.0016</b>
2.5	0.189	<b>210</b>	<b>0.0016</b>
3.0	2.153	211	<b>0.0016</b>
4.0	10.953	212	<b>0.0016</b>

When the results given in Table 5 are evaluated in general, the best performance in terms of RMSE values was obtained as 0.0016. The best min. distance error was obtained as 0.001 m with spread values 0.3-1.0, and the best mean distance error was found to be 210 m with spread values 1.5-2.5.

Finally the indoor data set was tested with *k*NN method, where Table 6 shows the min. and mean distances, as well as the corresponding RMSE values depending on the number of neighbors *k*.

TABLE VI  
MIN. AND MEAN DISTANCE ERRORS (M), AND RMSE VALUES USING *k*NN / INDOOR

<i>k</i>	Min.	Mean	RMSE
1	<b>0.0000</b>	<b>75</b>	<b>0.0009</b>
2	<b>0.0000</b>	85	<b>0.0009</b>
3	<b>0.0000</b>	103	0.0011
5	0.0024	130	0.0013
10	0.0024	170	0.0016
25	0.0024	203	0.0018
50	0.0000	254	0.0022

TABLE VII  
MIN. AND MEAN DISTANCE ERRORS (M) USING ELM/ OUTDOOR

Activation Functions	Number of Hidden Neurons													
	5		10		25		50		75		100		125	
	Min.	Mean	Min.	Mean	Min.	Mean	Min.	Mean	Min.	Mean	Min.	Mean	Min.	Mean
Sym. Hard-limit	28	236	24	237	12	233	8	231	<b>1</b>	422	9	517	6	348
Sym. Sat. Linear	21	237	15	939	28	511	15	577	10	224	9	236	19	452
Tangent Sigmoid	9	7097	15	238	4	269	11	244	8	9032	21	471	10	578
Pure Linear	8	316	5	<b>207</b>	6	<b>207</b>	5	<b>207</b>	4	<b>207</b>	5	<b>207</b>	9	<b>207</b>
Hyp. Tangent	20	244	27	245	17	299	22	1921	12	417	12	1052	9	8340
Multiquadratic	13	233	28	237	23	240	8	246	15	805	10	333	9	289

When the results in Table 6 are evaluated, the best performance in terms of RMSE values was obtained as 0.0009. The best min. distance error was obtained as 0 m with  $k = 1, 2$  and 3, and the best mean distance error as 75 m with  $k = 1$ .

### B. Outdoor Data Set

Using the same analogy used for indoor data set, the outdoor data set has been tested in the same manner using ELM, GRNN and kNN methods, and the results are given in Table 7, Table 8 and Table 9, respectively.

The results given in Table 7 shows that almost all activation functions have performed well in terms of min. distance and the best result was obtained as 1 m using symmetric hard-limit activation function with 75 neurons. Similarly, the best mean distances best distance error was obtained as 207 m using pure linear activation function with 10-125 neurons. When considering all the results together, it is seen that most of the activation functions reach an average error of between 200 to 300 m, and the best results (about 222 m on average) are mostly obtained with the pure linear activation function.

TABLE VIII  
MIN. AND MEAN DISTANCE ERRORS (M), AND RMSE VALUES USING GRNN / OUTDOOR

Spread Values	Min.	Mean	RMSE
0.3	0.905	237	0.0021
0.5	1.087	232	0.0020
0.7	1.087	220	0.0019
0.9	<b>0.638</b>	209	0.0018
1.0	1.087	207	0.0018
1.5	1.086	196	<b>0.0016</b>
2.0	1.087	193	<b>0.0016</b>
2.5	1.087	<b>191</b>	<b>0.0016</b>
3.0	1.087	193	<b>0.0016</b>
4.0	1.323	195	<b>0.0016</b>

The obtained test results using GRNN method for outdoor data set depending on the spread values (0.3-4.0) is given in Table 8, where the best min. distance error was obtained as 0.638 m with 0.9 spread value and the best mean distance error as 191 m with 2.5 spread value. Also, the best result in

terms of RMSE value was obtained with 1.5-4.0 spread values as 0.0016.

TABLE IX  
MIN. AND MEAN DISTANCE ERRORS (M), AND RMSE VALUES USING kNN / OUTDOOR

k	Min.	Mean	RMSE
1	<b>0.61</b>	<b>93</b>	<b>0.0011</b>
2	1.08	98	<b>0.0011</b>
3	1.38	108	0.0012
5	1.45	135	0.0014
10	1.45	195	0.0018
25	3.80	261	0.0022
50	7.31	353	0.0028

Finally, the test results of outdoor data set using kNN method are shown in Table 9, where the best min. and mean distance error was found as 0.61 m and 93 m with  $k = 1$ , respectively. And the best result in terms of RMSE value was obtained with  $k = 1$  and 2 as 0.0011.

### C. Combined Data Set

In order to generalize the results obtained from indoor and outdoor data sets, an integrated data set was created by combining these data sets. Similarly, the combined type data set was tested using ELM, GRNN, and kNN methods, where the obtained results are shown in Table 10, Table 11, and Table 12, respectively.

The results given in Table 10 shows that the best min. and mean distance errors was obtained as 1 m using the hyperbolic tangent activation function with 25 neurons and as 204 m using pure linear activation function with 10 neurons, respectively.

When Table 11 is examined, it is seen that the best performance in terms of RMSE values was obtained with 2.0 spread value as 0.0016, and the best min. distance error as 0.001 m with 0.3-1.0 spread values. The best mean distance error is seen to be 216 m with 1.5 spread value.

Finally, the test results of mixed data set using kNN method are shown in Table 12, where the best RMSE value was obtained as 0.0013 with  $k = 1$ . The best min. and mean distance errors were found as 0 m with  $k = 50$  and 120 m with  $k = 1$ , respectively.

TABLE X  
MIN. AND MEAN DISTANCE ERRORS (M) USING ELM/ COMBINED

Activation Functions	Number of Hidden Neurons													
	5		10		25		50		75		100		125	
	Min.	Mean	Min.	Mean	Min.	Mean	Min.	Mean	Min.	Mean	Min.	Mean	Min.	Mean
Sym. Hard-limit	4	232	5	231	11	230	11	479	11	227	4	226	8	608
Sym. Sat. Linear	6	231	6	231	4	234	9	228	5	229	6	225	8	227
Tangent Sigmoid	4	231	4	235	6	236	4	703	6	243	5	248	5	449
Pure Linear	27	3009	9	204	9	205	9	205	10	205	9	205	9	205
Hyp. Tangent	9	231	8	231	1	230	7	230	4	290	4	9858	8	655
Multiquadratic	11	535	9	242	13	232	4	261	12	234	5	980	6	583

TABLE XI  
MIN. AND MEAN DISTANCE ERRORS (M), AND RMSE VALUES USING GRNN / COMBINED

Spread Values	Min.	Mean	RMSE
0.3	<b>0.001</b>	241	0.0020
0.5	<b>0.001</b>	234	0.0019
0.7	<b>0.001</b>	224	0.0018
0.9	<b>0.001</b>	220	0.0017
1.0	<b>0.001</b>	219	0.0017
1.5	0.012	<b>216</b>	0.0017
2.0	0.026	217	<b>0.0016</b>
2.5	0.266	217	0.0017
3.0	2.187	218	0.0017
4.0	3.503	219	0.0017

TABLE XII  
MIN. AND MEAN DISTANCE ERRORS (M), AND RMSE VALUES USING kNN / COMBINED

k	Min.	Mean	RMSE
1	0.0009	<b>120</b>	<b>0.0013</b>
2	0.0009	135	0.0014
3	0.0011	160	0.0016
5	0.0045	198	0.0018
10	0.0125	253	0.0021
25	0.0138	326	0.0026
50	<b>0.0000</b>	380	0.0030

TABLE XIII  
A SUMMARY OF MIN. AND MEAN DISTANCE ERRORS (M) DEPENDING ON THE DATA SET

Location	ELM		GRNN		kNN	
	Min.	Mean	Min.	Mean	Min.	Mean
Indoor	0.89	199	0.001	210	0	<b>75</b>
Outdoor	1	207	0.638	191	0.61	<b>93</b>
Combined	1	204	0.001	216	0	<b>120</b>

All the results are given in Table 13 in order to summarize and compare the performances of the given methods depending on the used type of data sets. When the given results are compared, it is clearly seen that the best results yielding minimum distance errors have been achieved with indoor data set using *k*NN method, with a min. of 0 m and an average of 75 m. Although the performances of both ELM and GRNN are nearly the same in all data sets, the performance of *k*NN considerably drops for outdoor and combined data sets.

#### IV. CONCLUSION

The need for positioning of people and/or devices, either being for personal, scientific, judicial or commercial purposes, is in a big demand, especially in indoors and obstructed areas. This requirement can be met with the help of different systems such as global, cellular or wi-fi technologies. Positioning systems show a great improvement through auxiliary and complementary systems and applications developed in parallel with technology. It is expected that geolocation systems will continue to develop by taking the advantage of the properties of signals that can be obtained from different generation cellular communication networks, such as GSM, CDMA, WCDMA, and LTE via mobile devices.

In this study, indoor and outdoor locations in a certain region were chosen as the application area. The data used in the tests consist of real signal measurements obtained from cellular base stations via a convenient and easy-to-access mobile application we have developed in the Android Studio environment. Since accessing, saving and organizing the limited number of network data offered by GSM operators requires an important and time consuming process, the software of the developed mobile application constitutes one of the most critical and important parts of this study. The data we obtained in this study was trained in the simulation environment with ELM, GRNN, and *k*-NN, enabling the mobile user to estimate the real position using only instant GSM signal measurements.

The proposed study shows that better results were obtained with indoor data which is actually more critical in positioning and the *k*NN works with the highest accuracy in all data sets when compared to other algorithms. It is thought that the reason of high difference in the obtained minimum and mean error is due to the incompatible data in the data sets which causes large deviations in predictions. In some cases, namely according to the current occupancy rate, connection speed and other optimization priorities of the operator; the mobile user

may be camped to another base station at a longer distance; which then causes to a higher positioning error as the proposed algorithm uses the camped base station's location information as its input. In fact, obtaining mostly higher accuracies with indoor data supports this idea. Because, possible remote base stations that can be directed by the operator due to the aforementioned priorities, will be prevented due to weak signal levels indoor. Thus, with the proposed algorithm, the mobile user will be able to camp to nearby stations with higher signal levels leading to positioning with higher accuracy.

When our study is compared to similar localization methods using cellular network data in the literature, it is seen that it performs positioning with much higher accuracies with all three methods. It is considered that the proposed method can successfully position the mobile users with a good accuracy for indoor environments, where GPS signals are very weak or cannot be received at all; and that it can be also used as a good alternative for outdoor environments, in cases where GPS may be disabled for different reasons. Designing a hybrid positioning system by integrating wi-fi based technologies that provide successful results in indoor positioning with cellular and/or global positioning systems is considered as a future work.

#### REFERENCES

- [1] Sevindi, C. (2005). (Global Positioning System (GPS) and Its Usage in Geographical Researches. *Turkish Journal Geographical Sciences*, 3(1), 101-112.
- [2] Teunissen, P., & Montenbruck, O. (Eds.). (2017). *Springer handbook of global navigation satellite systems*. Springer.
- [3] Magro, M. J., & Debono, C. J. (2007, September). A genetic algorithm approach to user location estimation in umts networks. In *EUROCON 2007-The International Conference on "Computer as a Tool"* (pp. 1136-1139). IEEE.
- [4] Türkyılmaz, O. (2007). Environment aware location estimation in cellular networks. Master Thesis. Boğaziçi University, İstanbul.
- [5] Kurt, Ö. F. (2009) Location estimation by fingerprinting in cellular networks. Master Thesis. Boğaziçi University, İstanbul.
- [6] Fritsche, C., Klein, A., & Wurtz, D. (2009, March). Hybrid GPS/GSM localization of mobile terminals using the extended Kalman filter. In *2009 6th Workshop on Positioning, Navigation and Communication* (pp. 189-194). IEEE.
- [7] Xuereb, D., & Debono, C. J. (2010, March). Mobile terminal location estimation using Support Vector Machines. In *2010 4th International Symposium on Communications, Control and Signal Processing (ISCCSP)* (pp. 1-4). IEEE.
- [8] Huang, G. B., Zhu, Q. Y., & Siew, C. K. (2006). Extreme learning machine: theory and applications. *Neurocomputing*, 70(1-3), 489-501.
- [9] Ertuğrul, Ö. F., & Kaya, Y. (2014). A detailed analysis on extreme learning machine and novel approaches based on ELM. *American Journal of computer science and engineering*, 1(5), 43-50.
- [10] Öztekin, A., & Erçelebi, E. (2019). An efficient soft demapper for APSK signals using extreme learning machine. *Neural Computing and Applications*, 31(10), 5715-5727.
- [11] Huang, G. B., Wang, D. H., & Lan, Y. (2011). Extreme learning machines: a survey. *International journal of machine learning and cybernetics*, 2(2), 107-122.
- [12] Celikoglu, H. B., & Cigizoglu, H. K. (2007). Public transportation trip flow modeling with generalized regression neural networks. *Advances in Engineering Software*, 38(2), 71-79.
- [13] Cigizoglu, H. K., & Alp, M. (2006). Generalized regression neural network in modelling river sediment yield. *Advances in Engineering Software*, 37(2), 63-68.

- [14] Kim, B., Lee, D. W., Park, K. Y., Choi, S. R., & Choi, S. (2004). Prediction of plasma etching using a randomized generalized regression neural network. *Vacuum*, 76(1), 37-43.
- [15] Jang, J. S. R., Sun, C. T., & Mizutani, E. (1997). Neuro-fuzzy and soft computing-a computational approach to learning and machine intelligence [Book Review]. *IEEE Transactions on automatic control*, 42(10), 1482-1484.
- [16] Mitchell, T. M. (1997). *Machine Learning*. McGraw-Hill Higher Education. New York.
- [17] Han, J., Pei, J., & Kamber, M. (2011). *Data mining: concepts and techniques*. Elsevier.
- [18] Coomans, D., & Massart, D. L. (1982). Alternative k-nearest neighbour rules in supervised pattern recognition: Part 1. k-Nearest neighbour classification by using alternative voting rules. *Analytica Chimica Acta*, 136, 15-27.
- [19] Aha, D. W., Kibler, D., & Albert, M. K. (1991). Instance-based learning algorithms. *Machine learning*, 6(1), 37-66.
- [20] Shmueli, G., Patel, N. R., & Bruce, P. C. (2011). *Data mining for business intelligence: Concepts, techniques, and applications in Microsoft Office Excel with XLMiner*. John Wiley and Sons.
- [21] Duda, R. O., & Hart, P. E. (2006). *Pattern classification*. John Wiley & Sons.
- [22] Everitt, B. S., Landau, S., Leese, M., & Stahl, D. (2011). Miscellaneous clustering methods. *Cluster analysis*, 215-255.
- [23] Hall, P., Park, B. U., & Samworth, R. J. (2008). Choice of neighbor order in nearest-neighbor classification. *the Annals of Statistics*, 36(5), 2135-2152.

#### BIOGRAPHIES

**ERCAN DEMİR** Siirt, Turkey, in 1996. He received the B.S. degree in electrical and electronics engineering from Siirt University, Siirt, in 2018. He received the M.S. degree in electrical and electronics engineering from Batman University, Batman, in 2020.

He worked as an electrical and electronics teacher with the Private Siirt OSB Science Vocational and Technical Anatolian High School in 2019, and worked as an electrical and electronics engineer with the SAGTEK Biomedical Informatics in 2020. His research interests include machine learning, android programming, and signal processing.



**ABDULKERİM ÖZTEKİN** Berlin, Germany, in 1978. He received the B.S. degree in electrical and electronics engineering from Hacettepe University, Ankara, in 2001. He received the M.S. and the Ph.D. degrees in electrical and electronics engineering from Gaziantep University, Gaziantep, in 2018.

From 2001 to 2011, he worked as a Senior Engineer in several companies in the industry, and from 2012 to 2018; he was a Lecturer with the Electronic Communication Department, Batman University. Since 2018, he has been an Assistant Professor with the Electrical and Electronics Engineering Department, Batman University. His research interests include signal processing, video coding, communication systems, and machine learning.



# Energy Efficient Driving Optimization of Electrical Vehicles Considering the Road Characteristics

Hasan Eroğlu and Yasin Oğuz

**Abstract**— Electric vehicles, which are an important part of sustainable energy technologies, occupy an important place in our daily life. More efficient use of electric vehicles will ensure more efficient use of sustainable energy sources. It is not possible for the human brain to determine the most efficient driving characteristics. In this study, energy efficient driving optimization of electric vehicles was realized. Along the route, optimum speeds were determined in terms of energy, by using the road and engine characteristics. Geographical information systems and genetic algorithm have been used effectively in the solution of the problem. The effectiveness of the proposed algorithm was revealed with many test studies. With this study, an algorithm that provides an energy-efficient driving for electrical vehicles was developed. The results will contribute to the development of electric vehicle technologies.

**Index Terms**— Electric Vehicles, Energy optimization Autonomous vehicle.

## I. INTRODUCTION

RANGE OF electric vehicles (EV) is one of the most important parameters in the evaluation of EVs. Road condition, vehicle performance, driver profiles, traffic situation and similar factors are the main factors affecting the EVs range [1]. Increasing the efficiency of EVs can be achieved by developing battery, motor, communication, mechanical parts, shell, and similar technologies, as well as optimum vehicle driving according to the road conditions. The slope of the road and the number of bends in the road are the main road conditions that affect energy consumption.

HASAN EROĞLU, is with Department of Electrical and Electronics Engineering University of Recep Tayyip Erdogan, Rize, Turkey, (e-mail: [hasan.eroglu@erdogan.edu.tr](mailto:hasan.eroglu@erdogan.edu.tr)).

 <https://orcid.org/0000-0002-7233-5569>

YASİN OĞUZ, is with Department of Electrical and Electronics Engineering University of Gumushane, Gumushane, Turkey, (e-mail: [yasin.oguz@gumushane.edu.tr](mailto:yasin.oguz@gumushane.edu.tr)).

 <https://orcid.org/0000-0002-0324-0515>

Manuscript received March 24, 2021; accepted April 19, 2021.  
DOI: [10.17694/bajece.902485](https://doi.org/10.17694/bajece.902485)

Determining the ideal speed according to the slope and bend criterion of the road will reduce energy consumption considerably, allowing the EVs to travel over longer ranges. As known, it is very difficult for the driver to perform the most effective driving, considering the most efficient speed of the engine and the desired time to reach the destination depending on the slope and bend of the road. To this day, many studies have been conducted on the use of EVs more efficiently. Some of these studies have focused on identifying more economical road routes for electric vehicles. From these studies, a mathematical model was proposed [1] to find the fastest path for heavy vehicles by considering the slope of the road, radius of curves of the road, width, weight, carrying capacity and the sample application was carried out. The constrained shortest path (CSP) algorithm was developed, assuming the maximum and minimum battery capacity as the limit [2]. A new algorithm has been proposed [3] by considering the battery limit values and energy for determining an effective route. A new route-finding algorithm with data mining technique was introduced [4] by considering the speed characteristics of the driver from a data set. A dynamic route planning algorithm was developed [5] that calculates the energy consumption of the EVs in consideration of real-time traffic information. A multi-criteria route algorithm that provides time and energy optimization was proposed [6]. A study was conducted [7] using particle swarm optimization to find the least cost route between the two points. For this purpose, dynamic and static factors were considered. In this study, speed and road slope were accepted as constant.

A multi-purpose route optimization model based on model prediction control was created to determine the most appropriate way for drivers to manage wireless and plug-in charging states more effectively [8]. In all these studies, it was tried to determine a more efficient route.

On the other hand, some route independent studies were conducted to use EVs more efficiently. An optimization method was developed [9] by using indirect optimization method for serial hybrid EVs. In the developed method, the speed of the vehicle was regulated by considering the time, safety and comfort criteria and a reduction in energy consumption was recorded.

An Eco Adaptive Cruise Control System was developed [9] to increase the total energy costs and vehicle safety at the same time. The proposed controller captures the on-trip data to optimally adjust the speed of the EVs. The nonlinear model predictive control technique is used to adjust the vehicle speed.

In another study, for EV drivers in the United States, optimization of the driving range was performed by [10], considering battery charge, electricity charge and other factors limiting the range. A concurrent optimization of the hybrid EVs was made using multi-purpose evolutionary optimization tools using powertrain and driving strategy variables [11]. In this study, it was emphasized the importance of choosing the right transmission range as well as the correct choice of power train as well as the correct choice of driving strategy to provide economical driving of Hybrid EVs. In another study [12], a speed optimization algorithm was proposed in the US to collect real driving data on a 4 km long motorway, allowing EVs to pass green traffic lights immediately without delay. It has shown that the proposed optimization system reduces energy consumption by up to 17.5% compared to actual driving patterns without increasing driving time.

When all the above and other optimization studies [13]–[19] for EVs are examined, it is remarkable that there is a need for an algorithm achieves the least cost-effective driving with the appropriate speed values by using the EV's engine effectively

according to the road slope and bending values provided that the driver reaches the target in the desired time. In this study, in line the above-mentioned target, the least cost-effective driving characteristic is provided without compromising the time that the user wants to reach the target. Thus, the algorithm will contribute to the literature, related to autonomous driving studies in the world, not only to guide the vehicle, according to the road, but also to provide an economic driving model that can reach the target at the desired time for the user.

The major contributions of the paper can be summarized as follows:

- To achieve autonomous driving in electric vehicles, energy efficient driving optimization has been proposed.
- A software that provides an average of 13% less energy consumption has been realized.
- A software has been developed that considers the economic preference of the driver and increase the comfort of the driver on inclined and winding roads.

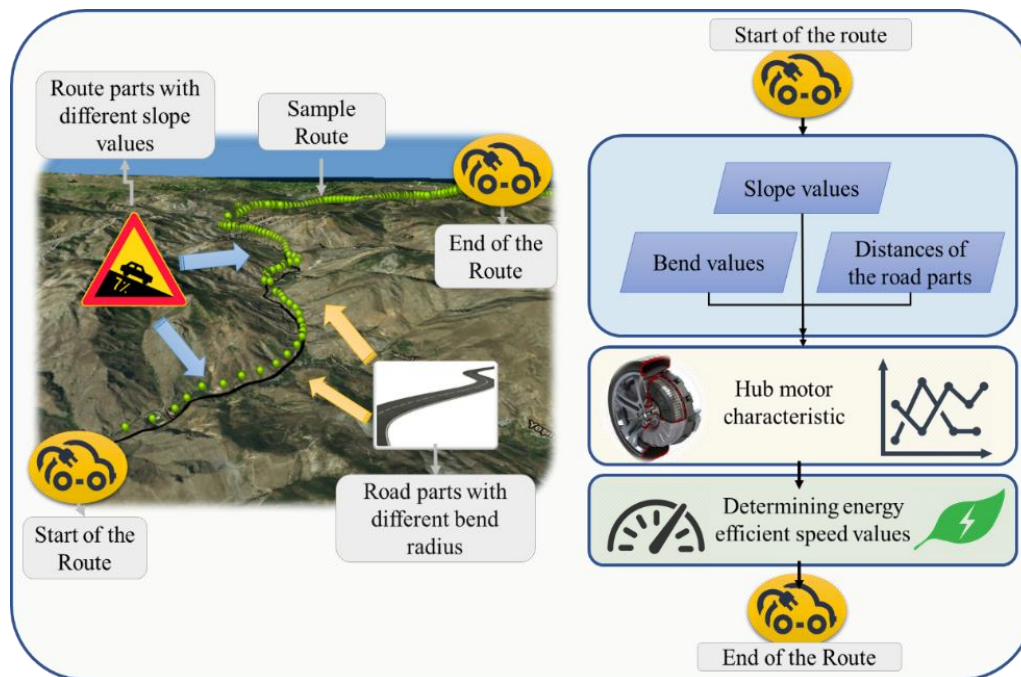


Fig. 1. General framework of the study

## II. PROBLEM DEFINITION

The optimization of EVs can be achieved by two methods. The first method is to solve the optimization problem considering the parameters such as slope, traffic, speed limits, toll roads, cornering, and to prefer roads with less energy consumption. This problem is called Energy efficient route optimization problem. The second method is to optimize the most efficient driving, considering the vehicle engine efficiency according to the road conditions. This optimization problem is called Energy efficient driving optimization.

This study focuses on the energy efficient driving optimization. General representation of the study is shown in Fig. 1.

### A. Optimization Problem Formulation

It is not possible for the driver to calculate at which speeds he/she should go for the most economical driving on different slope conditions. The driver is required to use the vehicle at the most efficient speeds, considering the road slope and bending characteristics of the road, constantly referring to the engine characteristics. The driver should also check whether the target has been reached at the desired time with these calculated speed values. This problem can only be solved by an optimization algorithm. The objective of the optimization problem is to deliver the vehicle to the target with the least possible energy consumption during the time the driver wants to reach the target. Therefore, the fitness function of the optimization problem depends on the current values  $I_n$ ,  $V$  battery voltage and

time values  $T_n$  drawn by the electric vehicle.  $n$  is the number of the road part that have different slope value.

The problem used in this study can be formulated as follows:

$$F_i = \min \sum_{n=0}^N I_n \times V \times T_n \quad (1)$$

where  $F_i$  is the fitness function of  $i$ th solution. Each set of solutions consists of the sum of the multiplication of the current values drawn by the vehicle on the different slope valued road segment and the time spent on the same road segment.

### B. Problem Assumptions

- Regenerative braking has not been performed on downward sloping road sections.
- EVs are equipped a navigation center that has the required data, such as  $x$ ,  $y$  and  $z$  coordinates of the road, EV motor characteristic and route information.
- EVs have a speed control system that controls the vehicle speed according to proposed algorithm's energy efficient speeds.
- Maximum car speed used in the proposed algorithm is limited to hub motor maximum speed.
- The electric vehicle has adaptive cruise control that regulates its own speed relative to the vehicle in front.

### III. ESTABLISHING THE EV MODEL

In optimization studies, all factors affecting energy consumption should be considered to model EVs correctly. In the modeling of EV used in this study, inertial force, gravitational force, rolling resistance force of wheels and aerodynamic force are considered [1], [4] as shown in Fig. 2.

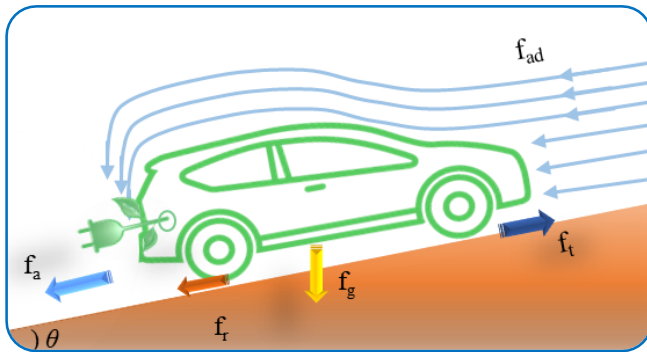


Fig. 2. Forces acting on an electric vehicle

All the forces in Fig. 2 can be expressed mathematically as in the following equation.

$$f_t = f_a + f_{gx} + f_r + f_{ad} \quad (2)$$

where  $f_t$  is the traction force required for the EV to move,  $f_a$  is the inertial force,  $f_{gx}$  is the gravitational force,  $f_r$  is the rolling resistance force and  $f_{ad}$  is the aerodynamic force. The aerodynamic force varies depending on the relative speed of the vehicle and the wind. The rolling resistance force depends on the friction between the tire and asphalt and does not change depending on the speed. The gravitational force depends on the slope of the road on which the vehicle climbs. The inertial force is a resistance which varies depending on the acceleration and mass of the vehicle.

Every force in (2) is calculated as follows.

#### 1) Aerodynamic Force

The aerodynamic force can be calculated by [1], [4]

$$f_{ad} = \frac{1}{2} \cdot \rho \cdot S \cdot C_D \cdot (v + v_{wind})^2 \quad (3)$$

where  $f_{ad}$  is the aerodynamic force,  $\rho$  is air density,  $S$  is the vehicle frontal area,  $C_D$  is the aerodynamic drag coefficient,  $v$  is the vehicle speed and  $v_{wind}$  is the head wind speed.

The vertical surface area of the electric vehicle used in this study is calculated from the three-dimensional drawing of the vehicle as  $1.57 \text{ m}^2$ . The air density  $\rho$  is taken as  $1.255 \text{ kg/m}^3$ , the drag coefficient  $C_D$  is taken as  $0.229$ .

#### 2) Rolling Resistance Force

Rolling resistance refers to the energy consumed because of deformation when the tire contacts the road. In each turn of the wheel, the wheel tread area bends and deforms as it contacts the surface of the ground. Rubber is heated due to deformation and energy is lost in the form of heat. The rolling resistance force is

$$f_r = m \cdot g \cdot \mu \quad (4)$$

where  $m$  is the vehicle's mass,  $g$  is the earth-surface gravitational acceleration and  $\mu$  is the rolling coefficient. The rolling resistance force has been neglected in the subtraction of engine consumption characteristics of the electric vehicle because it does not change with the speed of the vehicle or the slope of the road.

#### 3) Gravitational Force

Gravitational force is the force caused by the slope in the opposite direction to the direction of movement of the vehicle and can be calculated as follows

$$f_{gx} = m \cdot g \cdot \sin(\theta) \quad (5)$$

where  $m$  is the vehicle's mass and  $g$  is the earth-surface gravitational acceleration.

The weight of the electric vehicle used in the study was measured as  $280 \text{ kg}$ . This value has been used to add variable slope resistance according to the road slope of the vehicle.

#### 4) Inertial Force

When the speed of the moving objects changes, the force which is formed in the opposite direction to the movement direction is called inertial force. The inertial force is

$$f_a = (m/g) \cdot a \quad (6)$$

where  $m$  is the vehicle's mass,  $g$  is the earth-surface gravitational acceleration and  $a$  is the acceleration.

In this study, it was assumed that the EV was driven at constant speed in different slope intervals on the road by ignoring the acceleration resistance of the vehicle in determining the energy efficiency speed values. In addition, the resistance forces of other mechanical components were neglected as they did not change much with the vehicle speed and inclination value.

The total torque acting on the center of the wheel, since the total rim and tire radius of the vehicle is  $26.72 \text{ cm}$  can be calculated as below

$$t_t = f_t * 0.2672 \quad (7)$$

where  $t_t$  is the total torque and  $f_t$  is the traction force.

IV. DETERMINATION OF ROAD AND VEHICLE CHARACTERISTICS

A. Obtaining the Vehicle Characteristic

In this study, Mitsuba M2096II Hub engine was used in the EV. The motor characteristic curve of the Mitsuba M2096II Hub engine shown in Fig. 3 is transferred to the MATLAB environment. By considering the forces acting on the vehicle and calculated in the previous section, the current drawn by the vehicle is calculated according to the total torque applied to the motor shaft.

The proposed algorithm determines the most efficient speed values by referring to the curve in Fig. 3, considering the road slope and bend radius within the time required to reach the target on the planned route.

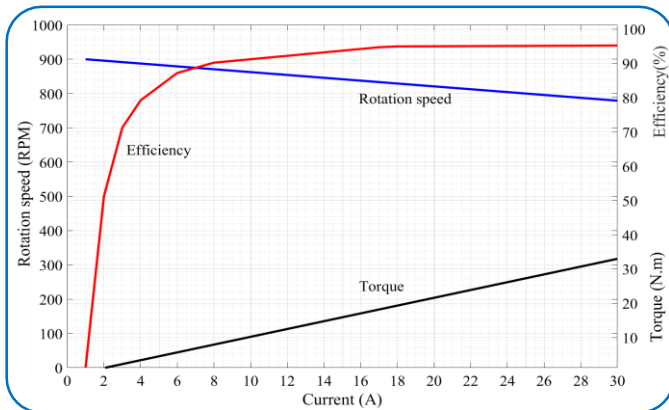


Fig. 3. Mitsuba M2096II hub engine curve

B. Reading the Road Characteristic Using GIS

Today, in the studies related to EVs, it is possible to collect, analyze and reach the results quickly with the help of Geographical Information Systems (GIS). GIS is a regular collection of computer hardware, software and geographic data designed to effectively collect, store, update, process, analyze and display all kinds of geographic information. GIS is also widely used in routing studies, such as data transformation, processing, arithmetic operations on database information, merging and determination of the route.

In this study, to test the developed algorithm, multiple different routes were used. GIS have been utilized to use the road characteristic of the route in the algorithm. A sample route and the characteristic road values are shown in Fig. 4.

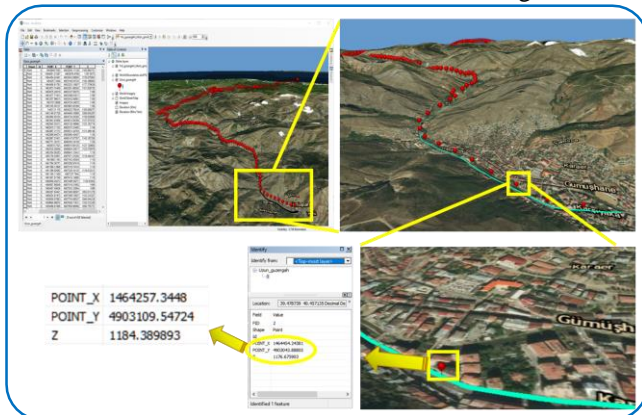


Fig. 4. Reading the route characteristic in GIS

All digital maps in GIS environment are stored in databases. To read the data of the sample road by the proposed algorithm, the road information in the GIS environment is converted to a text file so that the algorithm can read.

C. Determining the Road Bend

The Euclidean curvature approach can be used to the calculation of the bend radius of any part for the segmented road. The radius calculation for the circle given in Fig. 5. is formulated below.

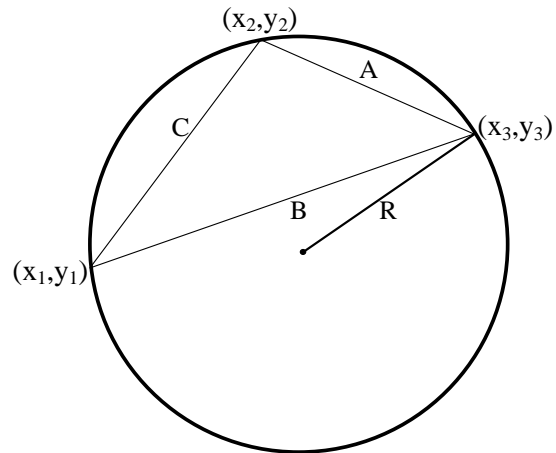


Fig. 5. Euclidean curvature calculation

$$R = \frac{ABC}{4\sqrt{L(L-A)(L-B)(L-C)}} \quad (8)$$

$$L = \frac{1}{2}(A + B + C) \quad (9)$$

$$A = \sqrt{(x_3 - x_2)^2 + (y_3 - y_2)^2} \quad (10)$$

$$B = \sqrt{(x_3 - x_1)^2 + (y_3 - y_1)^2} \quad (11)$$

$$C = \sqrt{(x_2 - x_1)^2 + (y_2 - y_1)^2} \quad (12)$$

where R is the radius road bending. The maximum speed of the vehicle for a curve with radius R can be calculated as follows [1]

$$\max V_{bend} \left( \frac{km}{h} \right) = \sqrt{127(\mu + \sigma)R} \quad (13)$$

where  $\mu$  is the lateral friction coefficient and  $\sigma$  is the horizontal slope of the road. In this study, the horizontal slope of the road is not taken into consideration.

V. OUTLINE OF THE ALGORITHM

In this study, electric vehicle dynamic driving optimization has been studied for more efficient driving. The problem is a linear optimization problem with constraints. The objective function of the problem is to minimize the total energy of EV as calculated in equation 1. The current to be consumed according to the torque acting on the drive system on different sloping parts of the road is taken from Fig. 3 according to equations 3-7. The two most important constraints are the maximum speed of the vehicle, according to the engine characteristics of the EV and the speed at which the EV can travel in the bends of the road.

For the problem described in this study, Genetic algorithm (GA) is used because of its ability to avoid local optimum

solutions and converge to a global one [20]. GA is a stochastic powerful optimization method based on a random-based study logic. It has been successfully adapted to solve many optimization problems, including planning, handling and engineering [21]. The flowchart of the algorithm is shown in Fig. 6.

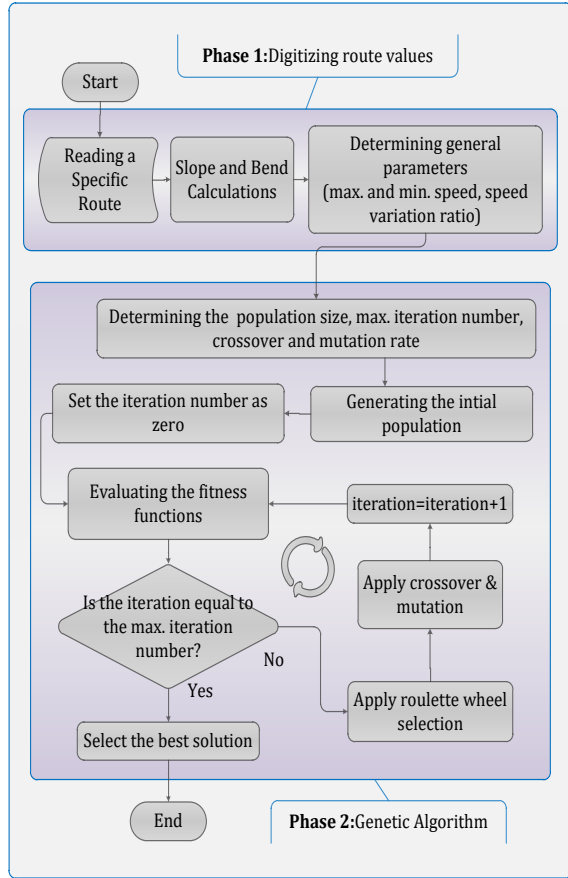


Fig. 6. Flowchart of the developed algorithm

In GA, each individual constituting the population represents a solution for the problem. In this study, each chromosome contains different speed values that the vehicle can travel along the route of the EVs. An individual gene contains the speed at which each vehicle can travel.

The main steps of the algorithm are as follows.

**A. Initializing the Population**

In this step the parameters of the study are determined. The main parameters are population size, maximum number of iterations, crossover, and mutation rate. The population consists of many chromosomes.

**B. Chromosome Generation**

Each individual in the population is called a chromosome. Identification of the number of the chromosomes in the population is very important. No definite judgment has been made for the size of the population set to be solved for different problems. When this value is too small, the algorithm is not able to find a good solution as a result of reducing the number of alternatives needed to find the best solution. The fact that the number of chromosomes in the solution set is too large also

appears to be an effect that slows down the algorithm considerably. The best value should be determined by the behavior of the problem. A sample chromosome representation is shown in Fig. 7.



Fig. 7. Sample chromosome used for the proposed algorithm

Every chromosome is determined according to the following equations.

$$X = \begin{cases} x_{i,j} = rand(minV_j, maxV_j) & , j = 1 \\ x_{i,j} = rand(smin_j, smax_j) & , j > 1 \end{cases} \quad (14)$$

Where  $X$  is the chromosome of the algorithm,  $i = 1, 2, \dots, n_p$ ,  $j = 1, 2, \dots, k$ ,  $n_p$  is the number of chromosomes in the population,  $V$  is the speed values and  $k$  is the number of the route parts.

$$smin_j = \begin{cases} minV_j & , x_{i,j-1} \times lb < minV_j \\ x_{i,j-1} \times lb & , x_{i,j-1} \times lb \geq minV_j \end{cases} \quad (15)$$

$$smax_j = \begin{cases} maxV_j & , x_{i,j-1} \times hb \geq maxV_j \\ x_{i,j-1} \times hb & , x_{i,j-1} \times hb < maxV_j \end{cases} \quad (16)$$

where  $lb$  is acceleration lower limit coefficient and  $hb$  is acceleration upper limit coefficient. These coefficients are used to determine the speed values that make up genes in the process of chromosome generation. Being extremely different from the previous speed value is not desirable as it is not possible in terms of the vehicle engine acceleration characteristic.

**C. Evaluating the Objective Functions**

The objective function shows how well the chromosomes in the population are. This function is very important for GA since the selection in GA is based on the objective function. The objective function is calculated from the fitness value as formulated in the second section of the study.

**D. Selection Procedure**

This procedure is the selection of two chromosomes from the population by considering their fitness values. Selection

methods commonly used are roulette wheel selection, tournament selection and sequential selection. The selection of the roulette wheel is related to the area occupied by the fitness values of the chromosomes in the solution set on the wheel. Thus, non-healthy chromosomes have a chance to be selected. The selection probability of each chromosome in the population can be found by calculating the ratio of each chromosome's fitness value to the sum of the fitness values of all the chromosomes in the population. Good fitness values increase the selection probability of a chromosome being selected from a set of solutions. We selected a chromosome with a probability calculated by the following equation.

$$p_i = \frac{f_i}{\sum_{j=1}^k (f_j)} \tag{17}$$

where k is the number of all chromosomes in the population,  $f_i$  is the fitness value of the  $i$ th chromosome and  $p_i$  is the selection probability  $i$ th chromosome.

**E. Crossover**

The crossover operator is based on the formation of elite parent chromosomes by combining the characteristics of different population members in new individuals. For this purpose, two parent chromosomes in the population are randomly selected. The two common parts of the two selected parents are mutually crossed. The most important constraint here is that the randomly selected parts of the randomly selected parent chromosomes must belong to the same road segments in the problem. Sample crossover operation used in the algorithm is shown in Fig.8.

If the fitness value of the child chromosome is better than the first selected parent chromosome, the child chromosome is taken to the population instead of the parent chromosome.

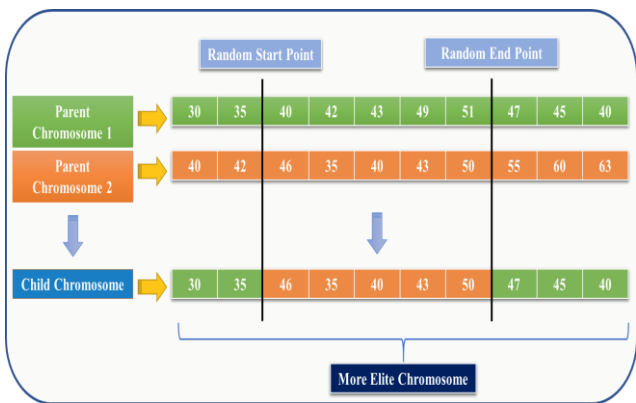


Fig. 8. Sample crossover operation used in the algorithm

**F. Mutation**

The mutation is the determination of the better chromosomes by changing the structure of the individuals to be transferred from the individuals in the solution set for the next

generation. The mutation is carried out in order to ensure diversity and to reach the result faster by preventing the new solution for just copying from the previous solutions. Sample mutation operation used in the algorithm is shown in Fig. 9.

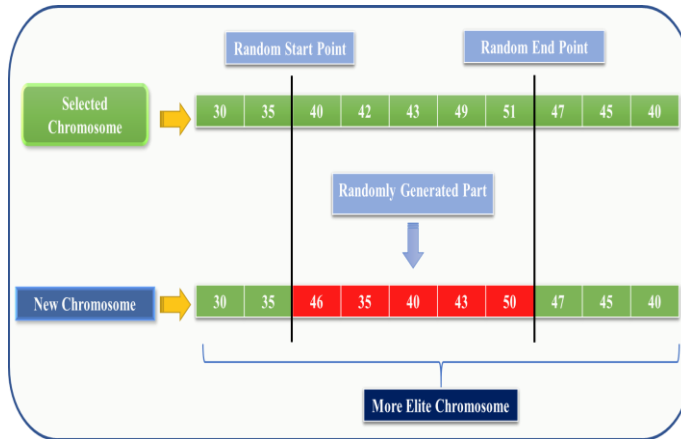


Fig. 9. Sample mutation operation used in the algorithm

**G. Determining the Termination Condition**

In this study firstly, the termination criterion is selected as the maximum number of iterations. At the end of many experimental studies, it is seen that the analytical convergence decreases when a certain number of cycles is exceeded. For this reason, it is chosen to reach the maximum efficiency value as the termination criterion of the algorithm.

**VI. RESULTS AND DISCUSSION**

In this section, different experimental studies about the problem, vehicle model, road slope characteristics and the proposed algorithm were carried out to reveal the efficiency of the study. In this respect, a sample route with different road slope and bending characteristics is selected and discussed in detailed below.

**A. Details of the Route**

As the proposed approach in the study is to achieve the most energy efficient driving, according to the engine characteristics and different bending values of the road, we have selected the motorway between Trabzon-Gumushane provincial centers, which is approximately 100 km long as the sample route. The details of the route are shown in Table 1. Each line in this table gives the average characteristic of the 5 km segments of the route. The reasons for choosing the route are as follows; Having 0-7% slope characteristics with different road segments, having low and high bending parts, performing efficiency analysis for short and long different route situations (10, 20, ... 100 km cases) along the 0-100 km route. The slope and bending view of the route is shown in Fig. 10.

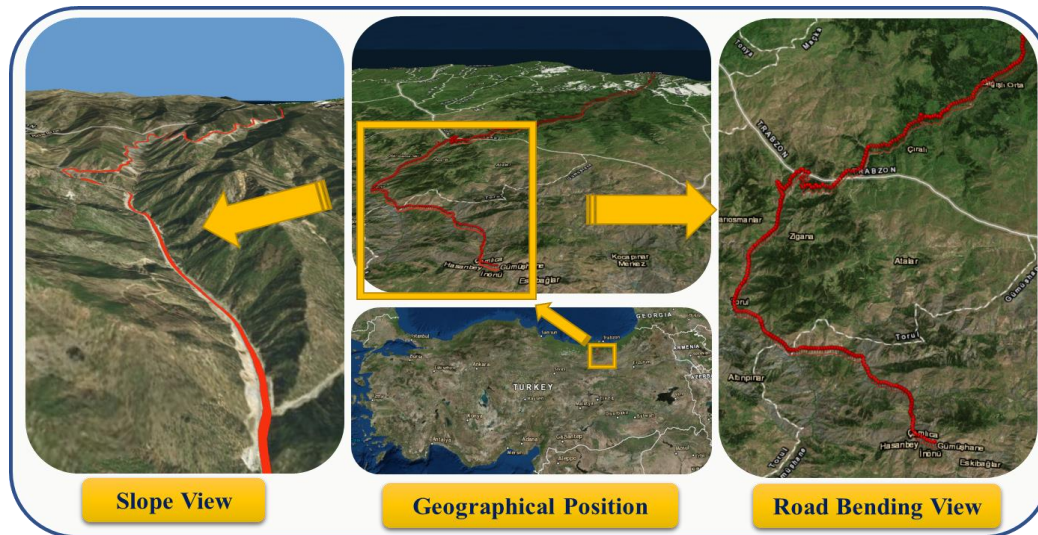


Fig. 10. Slope and bending view of the route

TABLE 1  
ROAD CHARACTERISTICS

Part number	Road part length	Average slope value	Average slope value (degree)	Minimum bend radius
1	5.19 km	-0.010	-0.58	357.96 m
2	5.07 km	-0.008	-0.44	350.42 m
3	5.38 km	-0.010	-0.56	266.75 m
4	5.10 km	-0.008	-0.45	416.74 m
5	5.36 km	0.004	0.23	315.02 m
6	5.06 km	0.006	0.34	500.51 m
7	5.30 km	0.044	2.52	127.43 m
8	5.21 km	0.029	1.68	117.23 m
9	5.26 km	-0.008	-0.47	157.46 m
10	5.13 km	-0.049	-2.80	216.78 m
11	5.29 km	-0.053	-3.05	124.01 m
12	5.23 km	-0.048	-2.73	237.74 m
13	5.31 km	-0.029	-1.64	440.19 m
14	5.10 km	-0.021	-1.23	342.20 m
15	5.35 km	-0.021	-1.23	256.40 m
16	5.17 km	-0.011	-0.66	229.77 m
17	5.07 km	-0.011	-0.62	460.59 m
18	5.23 km	-0.012	-0.71	1388.86 m
19	5.29 km	-0.009	-0.52	314.04 m
20	3.43 km	-0.006	-0.35	396.35 m

**B. Case Studies**

The algorithm was run at different distances along the route to reveal the efficiency of the algorithm. The proposed algorithm for 10, 20, 30, 100 km long driving distances and the results of the vehicle driving at average speeds at the same distances were compared. For comparison, it is assumed that the vehicle travels at fixed average speeds named Desired average speed on the sample route. *Current × Second* values calculated according to road distances and desired average speed values are shown in Table 2.

TABLE 2  
CONSTANT AVERAGE SPEED CASE STUDY RESULTS

	Desired Average Speeds (km/h)					
	50	60	70	80	90	100
10	9049	9252	9801	10601	11489	12563
20	15917	16928	18520	20744	23089	25705
30	31280	31628	33205	35755	38653	41993
40	59007	57339	57924	60065	62883	66359
50	68127	66036	66530	68787	71864	75758
60	70442	68411	69166	71822	75300	79851
70	76987	74867	75794	78977	83293	88933
80	83124	81596	83368	87543	93124	100044
90	89403	88695	91551	96948	103919	112308
100	94337	94633	98737	105380	113433	122823
	Current x Seconds (AxS)					

The desired average speed values given in Table 2 are not applicable at all points of the route. When the maximum speeds are calculated considering the bend radius of the road, some of the applied average speeds are calculated below the desired values. In this case, applied average speed values occur. The desired average speed values and the applied average speed values are shown in Table 3.

TABLE 3  
APPLIED AVERAGE SPEEDS

	Desired Average Speeds (km/h)						
	50	60	70	80	90	100	
10	50	60	70	80	89	98	
20	50	60	70	80	89	98	
30	50	60	70	80	89	98	
40	50	60	69	78	87	95	
50	50	60	69	78	86	94	
60	50	60	69	78	86	93	
70	50	60	69	78	86	94	
80	50	60	69	78	87	94	
90	50	60	69	78	87	95	
100	50	60	69	78	87	95	
	Applied Average Speeds (km/h)						

Gain value used in the comparisons is calculated by comparing the fitness function values obtained by the proposed algorithm and applied average speed case.

The gain value can be calculated by the following equation.

$$\eta = \frac{E_{as} - E_{pa}}{E_{as}} \times 100 \quad (18)$$

where  $E_{as}$  is the energy consumed using the applied average speed value, and  $E_{pa}$  is the energy consumed using the proposed algorithm.

To test the accuracy of the proposed algorithm, case studies have been carried out for many different situations. Case studies and results are as follows.

#### C. Constant average speed case

In this part, first, the energy consumptions for different arrival times on different routes were calculated using the developed algorithm and applied average speed. These two values were compared, and gains were calculated. In this case study, it is assumed that the driver chooses an average speed and goes constant at this speed. The results obtained from these two cases at different times are given in Table 4.

TABLE 4  
CONSTANT AVERAGE SPEED CASE STUDY RESULTS

Average Speed	60 km/h			
Distance	Time given	Energy (Proposed Algorithm)	Energy (Constant Speed)	Gain
9,77 km	586 sec	8192 A x sec	9254 A x sec	11,5%
19,84 km	1191 sec	15043 A x sec	16928 A x sec	11,1%
29,78 km	1787 sec	27511 A x sec	31628 A x sec	13,0%
39,87 km	2392 sec	51412 A x sec	57321 A x sec	10,3%
49,83 km	2990 sec	59002 A x sec	66011 A x sec	10,6%
59,91 km	3595 sec	61045 A x sec	68389 A x sec	10,7%
69,85 km	4191 sec	66987 A x sec	74849 A x sec	10,5%
79,97 km	4798 sec	72479 A x sec	81604 A x sec	11,2%
89,78 km	5387 sec	78476 A x sec	88735 A x sec	11,6%
98,00 km	5880 sec	83320 A x sec	94703 A x sec	12,0%

TABLE 5  
CONSTANT DISTANCE CASE STUDY RESULTS

Distance: 98,00 km				
Time given	Average Speed	Energy (Proposed Algorithm)	Energy (Constant Speed)	Gain
7840 sec	45 km/h	79842 A x sec	96448 A x sec	17,22%
7056 sec	50 km/h	81481 A x sec	94312 A x sec	13,60%
6415 sec	55 km/h	81871 A x sec	93857 A x sec	12,77%
5880 sec	60 km/h	83561 A x sec	94705 A x sec	11,77%
5428 sec	65 km/h	86325 A x sec	96485 A x sec	10,53%
5040 sec	70 km/h	90527 A x sec	102900 A x sec	12,02%

Table 5 shows that an average of 13 % gain is obtained. Also, the graphical representation of the results in Table is presented as in figure 11. With above different case studies, it is shown that the proposed algorithm is very useful in terms of energy efficiency.

As shown in Table 4, the energy consumed by the vehicle for the same arrival times on the same route is reduced by the proposed algorithm and an average of 11.25 % gain is obtained. This value shows that the driver is not able to make an energy efficient driving like the proposed algorithm considering the road characteristics and bending values.

In the proposed algorithm, the minimum arrival time for calculating the speed values was used. This value is essential for the vehicle and driver to reach the destination at the desired time. In determining the minimum arrival time of the proposed algorithm, 1 km/min, which is a suitable average value for cars, was taken into consideration.

#### D. Constant distance case

In contrast to the average speed case discussed in detail in the previous section, this section tested the performance of the algorithm at different speeds at the same distance. For this purpose, the performance of the algorithm was tested at different speeds between 45-70 km/h at 98 km. The results obtained are presented in Table 5

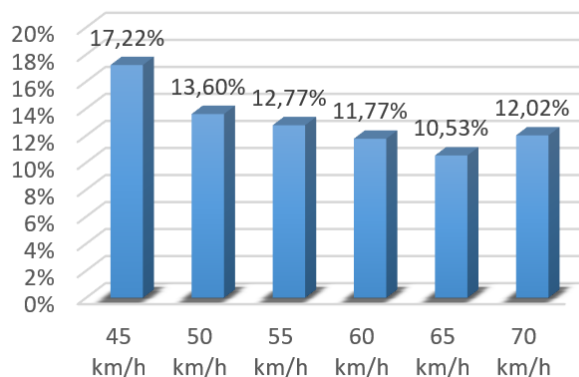


Fig. 11. Gain values according to different speeds.

## VII. CONCLUSIONS

Electric vehicle technologies are becoming more and more common every day. Basically, the subject of autonomous driving consists of two titles as autonomous tracking of the road and determination of autonomous speeds.

It is not possible for vehicle drivers to determine the most energy-efficient speed profile by considering road slope, bending and vehicle engine characteristics. For this purpose, artificial intelligence is needed.

In this study, efficient driving optimization of electric vehicles was realized. For this purpose, modelling of the electric vehicle was performed and as an optimization problem the problem parameters were calculated. The characteristics of a commonly used EV motor were modelled. In order to solve the problem with GA, which is a powerful method of artificial intelligence methods, the general working framework was determined, and the algorithm was integrated to the study. The interaction between GIS and GA was provided. The performance of the proposed algorithm was tested with different case studies on the determined sample routes. The results obtained showed that the developed algorithm achieved an average of 13% gain with an efficient driving profile.

With this study, electric vehicles will be used more efficiently in terms of energy. Thus, environmental efficiency will be achieved.

### VIII. FUTURE WORKS

In the future study, the integration of the developed algorithm on an electric vehicle and the autonomous driving of the electric vehicle is planned with the help of a navigation to be developed. Also, further development of the study can be realized by including parameters such as traffic, road condition etc. by using larger data.

### ACKNOWLEDGMENTS

This research was supported by Scientific Research Projects Coordination Unit of Gumushane University by the 16.F5112.02.01 project number. The authors thank the Scientific Research Projects Coordination Unit of Gumushane University and the editors and anonymous referees for helpful feedback on earlier drafts.

### REFERENCES

- [1] H. Kumaş, C. Gencer, and H. Maraş, "Ağır araçlar için yol eğimi ve viraj yarıçapı dikkate alınarak en hızlı güzergâhin belirlenmesi," *J. Fac. Eng. Archit. Gazi Univ.*, vol. 27, no. 2, pp. 385–395, 2012.
- [2] A. Artmeier and J. Haselmayr, "The optimal routing problem in the context of battery-powered electric vehicles," in *Workshop: CROCS at ...*, 2010, no. APRIL 2010, pp. 1–13, [Online]. Available: <http://www.cis.cornell.edu/ics/compsust-org/crocs-at-cpaio10/papers/crocs-at-cpaio10-Artmeier.pdf>.
- [3] M. Sachenbacher, M. Leucker, A. Artmeier, and J. Haselmayr, "Efficient Energy-Optimal Routing for Electric Vehicles," in *Proc. Twenty-Fifth AAAI Conference on Artificial Intelligence*, 2011, no. January 2011, pp. 1402–1407.
- [4] A. M. Bozorgi, M. Farasat, and A. Mahmoud, "A Time and Energy Efficient Routing Algorithm for Electric Vehicles Based on Historical Driving Data," *IEEE Trans. Intell. Veh.*, vol. 2, no. 4, pp. 308–320, 2017, doi: 10.1109/tiv.2017.2771233.
- [5] Y. Wang, J. Jiang, and T. Mu, "Context-aware and energy-driven route optimization for fully electric vehicles via crowdsourcing," *IEEE Trans. Intell. Transp. Syst.*, vol. 14, no. 3, pp. 1331–1345, 2013, doi: 10.1109/TITS.2013.2261064.
- [6] M. F. and O. Basir, "Optimal energy/time routing in battery-powered vehicles," 2016.
- [7] O. Rawashdeh and R. Abouleiman, "Electric vehicle modelling and energy-efficient routing using particle swarm optimisation," *IET Intell. Transp. Syst.*, vol. 10, no. 2, pp. 65–72, Mar. 2016, doi: 10.1049/iet-its.2014.0177.

- [8] C. Li, T. Ding, X. Liu, and C. Huang, "An Electric Vehicle Routing Optimization Model With Hybrid Plug-In and Wireless Charging Systems," *IEEE Access*, vol. 6, pp. 27569–27578, 2018, doi: 10.1109/ACCESS.2018.2832187.
- [9] M. Vajedi and N. L. Azad, "Ecological adaptive cruise controller for plug-in hybrid electric vehicles using nonlinear model predictive control," *IEEE Trans. Intell. Transp. Syst.*, vol. 17, no. 1, pp. 113–122, 2016, doi: 10.1109/TITS.2015.2462843.
- [10] Z. Lin, "Optimizing and Diversifying Electric Vehicle Driving Range for U.S. Drivers," *Transp. Sci.*, vol. 48, no. 4, pp. 635–650, 2014, doi: 10.1287/trsc.2013.0516.
- [11] R. Cook, A. Molina-Cristobal, G. Parks, C. Osornio Correa, and P. J. Clarkson, "Multi-objective Optimisation of a Hybrid Electric Vehicle: Drive Train and Driving Strategy," in *Evolutionary Multi-Criterion Optimization*, S. Obayashi, K. Deb, C. Poloni, T. Hiroyasu, and T. Murata, Eds. Berlin, Heidelberg: Springer Berlin Heidelberg, 2007, pp. 330–345.
- [12] L. Kang, H. Shen, and A. Sarker, "Velocity Optimization of Pure Electric Vehicles with Traffic Dynamics Consideration," in *2017 IEEE 37th International Conference on Distributed Computing Systems (ICDCS)*, Jun. 2017, pp. 2206–2211, doi: 10.1109/ICDCS.2017.220.
- [13] J. Huang, Y. Liu, M. Liu, M. Cao, and Q. Yan, "Multi-Objective Optimization Control of Distributed Electric Drive Vehicles Based on Optimal Torque Distribution," *IEEE Access*, vol. 7, pp. 16377–16394, 2019, doi: 10.1109/ACCESS.2019.2894259.
- [14] X. Wu, D. Freese, A. Cabrera, and W. A. Kitch, "Electric vehicles' energy consumption measurement and estimation," *Transp. Res. Part D Transp. Environ.*, vol. 34, pp. 52–67, 2015, doi: 10.1016/j.trd.2014.10.007.
- [15] H. Mehrjerdi and R. Hemmati, "Stochastic model for electric vehicle charging station integrated with wind energy," *Sustain. Energy Technol. Assessments*, vol. 37, no. October 2019, p. 100577, Feb. 2020, doi: 10.1016/j.seta.2019.100577.
- [16] F. Orecchini, A. Santiangeli, and F. Zuccari, "Hybrid-electric system truth test: Energy analysis of Toyota Prius IV in real urban drive conditions," *Sustain. Energy Technol. Assessments*, vol. 37, no. December 2018, p. 100573, Feb. 2020, doi: 10.1016/j.seta.2019.100573.
- [17] C. Bian, G. Yin, L. Xu, and N. Zhang, "Active collision algorithm for autonomous electric vehicles at intersections," *IET Intell. Transp. Syst.*, vol. 13, no. 1, pp. 90–97, 2019, doi: 10.1049/iet-its.2018.5178.
- [18] X. Dong, Q. Lin, M. Xu, and Y. Cai, "Artificial bee colony algorithm with generating neighbourhood solution for large scale coloured traveling salesman problem," *IET Intell. Transp. Syst.*, vol. 13, no. 10, pp. 1483–1491, Oct. 2019, doi: 10.1049/iet-its.2018.5359.
- [19] A. Fukushima, T. Yano, S. Imahara, H. Aisu, Y. Shimokawa, and Y. Shibata, "Prediction of energy consumption for new electric vehicle models by machine learning," *IET Intell. Transp. Syst.*, vol. 12, no. 9, pp. 1174–1180, Nov. 2018, doi: 10.1049/iet-its.2018.5169.
- [20] W. B. A. Karaa, A. S. Ashour, D. Ben Sassi, P. Roy, N. Kausar, and N. Dey, "Medline text mining: An enhancement genetic algorithm based approach for document clustering," *Intell. Syst. Ref. Libr.*, vol. 96, pp. 267–287, 2016, doi: 10.1007/978-3-319-21212-8\_12.
- [21] A. Hiassat, A. Diabat, and I. Rahwan, "A genetic algorithm approach for location-inventory-routing problem with perishable products," *J. Manuf. Syst.*, vol. 42, pp. 93–103, Jan. 2017, doi: 10.1016/j.jmsy.2016.10.004.

### BIOGRAPHIES

**HASAN EROĞLU** received the B.S., M.S., and Ph.D. degrees in Electrical and Electronics Engineering from the University of Selcuk, Konya, Turkey in 2007, 2009, and 2014. From 2010 to 2015, he was a research assistant in Gumushane University. He has been an assistant professor since 2015. He has been working at Recep Tayyip Erdogan University since 2020. His research and professional interests include: Electrical engineering, optimization of energy transmission lines, renewable energy systems, geographic



information systems in power systems, energy quality and decision support systems.



**YASİN OĞUZ** received the B.S., M.S., and Ph.D. degrees in Electrical and Electronics Engineering from Karadeniz Technical University, Trabzon, Turkey in 1998, 2002, and 2008.

From 1999 to 2001 he was a research assistant and from 2001 to 2011 he was a lecturer in Karadeniz Technical University.

He has been an assistant professor since 2011. Between 2011 and 2013, he worked as an assistant professor at Avrasya University. He has been working at Gumushane University since 2013. His research and professional interests include: Electronics, Communication, Electromagnetic, Microwave and Antenna Technologies.

# First-Principles Study of Graphene-6H SiC Surface Interactions

Ahmet Cicek and Bulent Ulug

**Abstract**— Interactions of graphene with 6H-SiC {0001} surfaces are numerically investigated from first principles. In order to describe the bulk structure and its 6 bilayer thick surfaces correctly, bare and dipole-corrected atomic relaxations are considered. The obtained lattice parameters and bulk modulus are in good agreement with experimental values. The calculated indirect band gap width of 2.10 eV is smaller than the experimental value due to the nature of the computational method. Geometrical optimization of the surfaces, where dipole correction is applied, reveals that the first two bilayers displace significantly, where the relaxations of the very top bilayer is more pronounced. Band structures of the {0001} surfaces possess two flat bands around the Fermi level due to unsaturated bonds on opposite faces. When one layer of C atoms are introduced on the Si-terminated surface, it behaves as a tightly-bound buffer layer. This is also the case for the C-terminated surface when van der Waals interactions are taken into account. In contrast, disregarding these interactions yields free-standing graphene like behavior for the first C overlayer. On both surfaces, the second C overlayer is free-standing where the corresponding band structures incorporate Dirac-cone like features.

**Index Terms**—Graphene, 6H Silicon Carbide, Density Functional Theory, Surface analysis, Band structure

## I. INTRODUCTION

GRAPHENE, monolayer of graphite, was first obtained in 2004 by mechanical exfoliation from graphite [1]. Since then, it has been extensively studied both theoretically and experimentally. Theoretically it has been drawing attention due to phenomena such as observation of quantum Hall effect at room temperature [2] and the Klein paradox, a phenomenon important in the context of relativity [3]. Due to its superior mechanical, electronic and optical properties, it has been finding applications in device physics [4, 5].

Among the most common methods for obtaining few-layer graphene are mechanical exfoliation from graphite [1], arc discharge [6] and intercalation of graphite by active elements

AHMET CICEK, is with Department of Nanoscience and Nanotechnology, Burdur Mehmet Akif Ersoy University, Burdur, Turkey, (e-mail: [ahmetcicek@mehmetakif.edu.tr](mailto:ahmetcicek@mehmetakif.edu.tr)).

 <https://orcid.org/0000-0002-7686-0045>

BULENT ULUG, is with Department of Physics, Akdeniz University, Antalya, Turkey, (e-mail: [bulug@akdeniz.edu.tr](mailto:bulug@akdeniz.edu.tr)).

 <https://orcid.org/0000-0003-1744-6861>

Manuscript received April 1, 2021; accepted April 27, 2021.

DOI: [10.17694/bajece.908183](https://doi.org/10.17694/bajece.908183)

like Li and K [7]. However, epitaxial growth on substrates such as silicon carbide (SiC) with 8% lattice mismatch [8] and boron nitride (BN) with 2% lattice mismatch [9] are preferred for large-scale crystal quality growth of graphene. In addition, epitaxial graphene growth can also be achieved on metallic substrates such as nickel (Ni), cobalt (Co), copper (Cu), rutherfordium (Ru) and platinum (Pt) [10-14]. Although high-quality monolayer (ML) graphene can be grown on metallic substrates, they are not suitable for microelectronic applications due to charge transfer to graphene. In contrast, SiC with approximately 3 eV band gap is more suitable for epitaxial graphene growth. Especially {0001} surfaces of hexagonal 4H-SiC [15-17] or 6H-SiC [18, 19] are preferred for high-quality graphene growth.

Graphene exhibits different physical properties on opposite surfaces of hexagonal SiC terminated by Si or C atoms [20, 21]. Thus, understanding of graphene-substrate interactions is vital for design of graphene based nanodevices and investigation of their physical properties. For instance, the first graphene layer grown on Si-terminated face of SiC is tightly bound to surface, which has a complex reconstruction, while free-standing graphene layers are obtained starting from the second layer [20]. In contrast, the first layer grown on the C-terminated face of SiC is free standing, where there exist rotational defects between graphene layers [22].

Considering the complex surface reconstruction of hexagonal SiC, first numerical studies employing density-functional theory (DFT) calculations on graphene-SiC interactions involved relatively small surface reconstructions [8, 23, 24]. Although these studies suggested that the very first layer on both Si-terminated and C-terminated surfaces were tightly-bound buffer layers, more recent studies indicate that the buffer layer does not appear on the C-terminated face [25, 26]. Thus, it is important to understand the correct behavior of graphene on opposite faces of hexagonal SiC.

In this work, graphene-substrate interactions for the commonly employed 6H-SiC{0001} surfaces are numerically investigated from first principles via DFT calculations. Structural and electronic properties of graphene on opposite surfaces are compared to understand the formation mechanism and physical properties of graphene on these surfaces.

## II. MATERIAL AND METHODS

Crystal structure of the 6H silicon carbide substrate in the  $S_3$  configuration [27] is seen in Fig. 1(a). Here, each carbon (silicon) atom is tetravalently bonded to four silicon (carbon) atoms, where the bond length is 1.89 Å and the C-Si-C bond angle is 109.57 degrees. It is designated 6H since its unit cell

in the hexagonal crystal class comprises 6 bilayers (BLs) in the ABCACB... stacking order [28]. The Si-C bonds follow a zig-zag pattern over the  $(11\bar{2}0)$  plane shown in Fig. 1(b). Positions of the atoms on this plane are denoted as  $z_i$  ( $i=1...12$ ) (Fig. 1(c)), whereas the vertical distances in a BL and between two BLs are denoted as  $d_i$  and  $h_i$ , respectively. Thus,  $6(d_i+h_i)=c$ , lattice constant in the  $[0001]$  ( $z$ ) direction. The first Brillouin zone for 6H SiC and the high-symmetry points over the  $\{0001\}$  surfaces are given in Fig. 1(d).

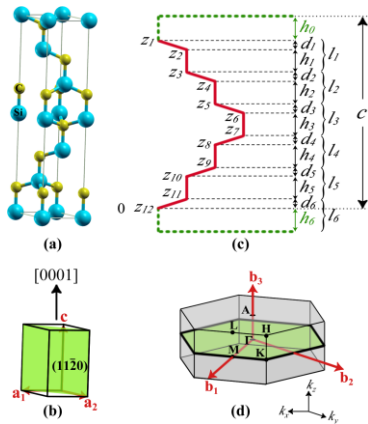


Fig.1. The crystal structure of 6H SiC (a), definition of  $(0001)$  direction and  $(11\bar{2}0)$  plane (b), definition of atomic positions over the  $(11\bar{2}0)$  plane (c) and the first Brillouin zone, as well as high-symmetry points for  $\{0001\}$  surfaces.

Graphene is grown on 6H SiC  $\{0001\}$  surfaces. Here, the  $(0001)$  surface is terminated by a sub-layer composed of only Si atoms, whereas the  $(000\bar{1})$  surface is terminated by a C sub-layer. Growth on 6H SiC takes place through a thermal process where Si atoms sublime and the remaining C atoms on the very top of the surface form surface reconstructions [29]. The most common surface reconstruction for epitaxial graphene growth is denoted as  $6\sqrt{3}\times 6\sqrt{3} R30^\circ$  [30]. However, in this study a more computationally affordable surface reconstruction of  $\sqrt{3}\times\sqrt{3} R30^\circ$  is considered [8, 23].

The top view of the  $(0001)$  surface of 6H SiC is seen in Fig. 2(a), where the enumeration of top BL atoms is also shown. Also in Fig. 2(a) is the graphene ML considered on 6H SiC surface and the enumeration of C atoms in this layer.

Geometry of a graphene ML on  $\sqrt{3}\times\sqrt{3} R30^\circ$  reconstruction of 6H SiC is on the right of Fig. 2(a). The side view of the geometry under study for the case of  $(0001)$  surface is given in Fig. 2(b). Here, a BL graphene is demonstrated, where  $d_{GA}$  and  $d_{GG}$  are graphene-substrate and graphene-graphene distances, respectively. In the case of graphene BL, the ABAB... stacking order is considered.

The numerical problems in Fig. 1 and Fig. 2 are three dimensional (3D) in nature. However, the study of solid surfaces requires termination of an otherwise infinite system along a given direction. While the unit cell in Fig. 1(a) defined with Bloch periodic boundary condition is sufficient for the study of bulk crystals, study of surfaces requires supercell

structures, where the finite-size crystal is surrounded by a vacuum layer of thickness  $d_{vac}$  ( $h_0$  and  $h_6$  in Fig. 1(c)).

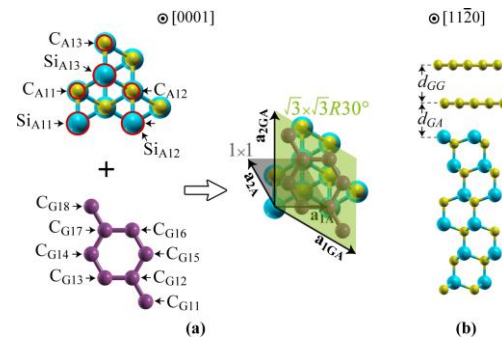


Fig.2. The  $\sqrt{3}\times\sqrt{3} R30^\circ$  model to investigate graphene-6H SiC interactions (a) and side view of the substrate-graphene BL model along the  $[11\bar{2}0]$  direction (b).

In this study, an asymmetric supercell, as seen in Fig. 3, due to electrical polarity of the 6H SiC  $\{0001\}$  surfaces is considered. Since the Si and C atoms on opposite faces have unequal electron affinities, a net surface charge density develops [31]. For large number of cells, this polarization can be ignored. However, for small supercells as in Fig. 3, ignoring it may result in significant error.

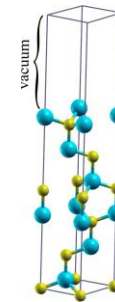


Fig.3. The numerical model employed for the investigation of 6BL-thick 6H SiC  $\{0001\}$  surfaces.

Graphene-6H SiC interactions are numerically investigated from first principles (*ab-initio*) via DFT calculations implemented in Quantum Espresso software [32]. This software employs a plane-wave basis set for the calculation of density functionals from Kohn-Sham equations. The local density approximation (LDA) and generalized gradient approximation (GGA) for the exchange-correlation functionals are utilized. Perdew-Zunger (1981) parametrization [33] in case of LDA and Perdew-Wang 91 (PW91) parametrization [34] for GGA are employed.

Brillouin zone integrals are discretized through Monkhorst-Pack (MP) [35]  $k$ -point meshes. In case of bulk 6H SiC and its  $\{0001\}$  surfaces, a  $12\times 12\times 2$  MP grid is used. In free-standing graphene calculations,  $6\times 6\times 6$  MP grids are employed. In addition, the cut-off energy in all calculations is 50 Ry.

The calculations are conducted in four stages. First, the equilibrium geometry for bulk 6H SiC in Fig. 1(a) is obtained through unconstrained geometric relaxation. Here, the convergence criterion is reduction of Hellmann-Feynman forces below  $2.0\times 10^{-4}$  Ry/Bohr ( $5.1\times 10^{-3}$  eV/Å). In addition, the band structure of bulk 6H SiC is obtained. In the second

stage, 6H SiC {0001} surfaces are geometrically optimized. Here, the 2D model in Fig. 1(c) is considered. In each case, 3 of 6 BLs are relaxed, while the rest are fixed. The vacuum layer thickness in these calculations is adopted as  $d_{vac}=20$  Å.

### III. RESULTS AND DISCUSSION

Numerically-obtained lattice constants ( $a$  and  $c$ ) from the Birch-Murnaghan equation of state fitting [36] are given in Table 1. They are in good agreement with both experimental [37-39] and previous numerical [28, 40-42] data. However, LDA approach resulted in a slightly closer value to the experimental value of  $a=3.081$  Å [37]. In addition, the bulk modulus ( $B_0$ ) values are also close to the experimentally-obtained values [38, 39], while GGA approach yields a closer value. Besides, the derivative of bulk modulus ( $B_0'$ ) is considerably larger than the experimental value [39].

TABLE 1  
COMPARISON OF THE LATTICE AND ELASTIC PARAMETERS OBTAINED IN THIS WORK WITH THE VALUES IN THE LITERATURE.

Parameter	This work		Literature	
	LDA	GGA	Experimental	Numerical
$a$ (Å)	3.094	3.050	3.081 <sup>a</sup>	3.077 <sup>d</sup> (LDA) 3.033 <sup>e</sup> (GGA) 3.099 <sup>f</sup> (GGA) 3.095 <sup>g</sup> (GGA)
$c/a$	4.909	4.908	4.909 <sup>a</sup>	4.910 <sup>d</sup> (LDA) 4.906 <sup>e</sup> (GGA) 4.908 <sup>f</sup> (LDA) 4.907 <sup>g</sup> (GGA)
$B_0$ (GPa)	210.94	228.94	230.2(±4.0) <sup>b</sup> 260(±9) <sup>c</sup>	
$B_0'$	3.92	4.57	2.9(±0.3) <sup>c</sup>	

<sup>a</sup>Ref. [37], <sup>b</sup>Ref. [38], <sup>c</sup>Ref. [39], <sup>d</sup>Ref. [28], <sup>e</sup>Ref. [40], <sup>f</sup>Ref. [41], <sup>g</sup>Ref. [42]

Results of geometrical relaxations of the bulk 6H SiC indicates that the relaxations exhibit repeating behavior with 3 BL periods. Therefore,  $d_{i+3}=d_i$  and  $h_{i+3}=h_i$  ( $i=1,2,3$ ). The values of  $d_i$  and  $h_i$  in Table 2 are in good agreement with the results of Käckell et al [40]. Overall, the atoms experience relaxations around 1 pm.

TABLE 2  
CALCULATED DISTANCES WITHIN AND BETWEEN BILAYERS FOR BULK 6H SILICON CARBIDE

	Fixed atoms		Relaxed		Literature (Ref. [40], LDA)
	LDA	GGA	LDA	GGA	
$d_1$ (Å)	<b>0.62</b>	0.63	<b>0.63</b>	0.64	0.63
$h_1$ (Å)	<b>1.87</b>	1.90	<b>1.87</b>	1.90	1.86
$d_2$ (Å)	<b>0.62</b>	0.63	<b>0.62</b>	0.63	0.62
$h_2$ (Å)	<b>1.87</b>	1.90	<b>1.87</b>	1.90	1.86
$d_3$ (Å)	<b>0.62</b>	0.63	<b>0.62</b>	0.63	0.62
$h_3$ (Å)	<b>1.87</b>	1.90	<b>1.88</b>	1.90	1.87

The band structure of geometrically optimized 6H SiC is given in Fig. 4. Here, an indirect band gap of  $E_G=2.10$  eV between the  $\Gamma$  and L points is obtained through LDA calculations, which is considerably smaller than the experimental value of 3.08 eV [43]. This is a well-known

underestimation in LDA band structure calculations [44]. A similar result is obtained for GGA calculations. To calculate the band gap correctly, hybrid functionals are utilized, which are not considered in this work.

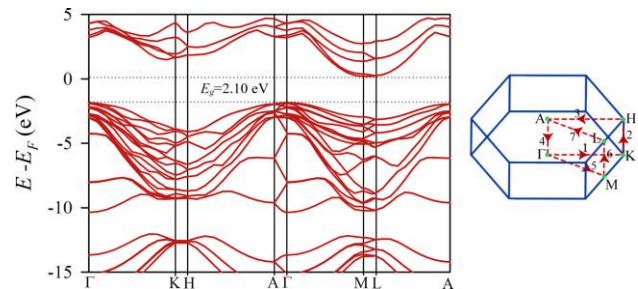


Fig.4. The band structure of 6H SiC through LDA calculations. The k-path is given in the first Brillouin zone on the right.

Since investigation of graphene-substrate interactions involves surfaces, the projection of the bulk band structure in Fig. 4 over the  $1 \times 1 \{0001\}$  surface is also investigated. Reduction of dimension is achieved by varying the  $z$  component of the wave vector ( $k_z$ ) between 0 and  $\pi/c$  and calculating the corresponding band structure for each  $k_z$  over the  $\Gamma MK\Gamma$  path seen in Fig. 4. The final projected band structure given in Fig. 5 is obtained through superposition of all individual band structures. The 6H-SiC {0001} surface bands are overlaid on this projected band structure to understand the effects of surface termination. In addition to the 2.10 eV band gap, pocket band gaps localized in the valence and conduction bands [23], as well as a stop band around  $E-E_F=-10$  eV are observed in Fig. 5.

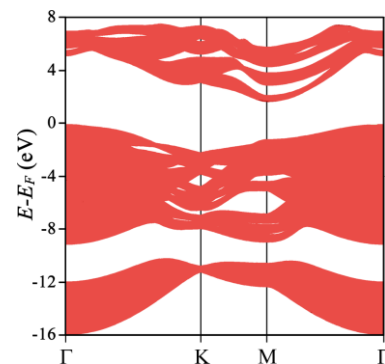


Fig.5. Projection of bulk 6H SiC electronic bands over the  $1 \times 1 \{0001\}$  surface.

By employing the supercell in Fig. 3 and dipole correction, geometrical optimization of 6H SiC (0001) (Si terminated) and (000 $\bar{1}$ ) (C terminated) surfaces are carried out. In both cases, only the first 3/6 BLs are relaxed and the variations of the  $d_i$  and  $h_i$  values with respect to the corresponding values in bulk 6H SiC are calculated. The results are presented in Table 3. It is clearly seen that the relaxation is largest in the top BL for both cases. Percent variations of  $d_i$  and  $h_i$  for the second BLs are considerably smaller, Table 3. Moreover, relaxations in the

third BLs are negligible. Besides, for relaxation from the Si-terminated surface, LDA calculations yield values almost twice of the values obtained through GGA calculations. Closer inspection of Table 3 reveals that relaxation of the first C sub-layer on the (000 $\bar{1}$ ) surface is relatively higher. This is related to the charge transfer towards the (000 $\bar{1}$ ) side, whose polarity is higher.

TABLE 3

PERCENT VARIATIONS OF THE DISTANCES WITHIN AND BETWEEN BILAYERS FOR 6H SILICON CARBIDE {0001} SURFACES WITH RESPECT TO THE VALUES FOR THE BULK CRYSTAL

Distance Variation		LDA	GGA
From Si	$\Delta d_1(\%)$	-6.8	-3.2
	$\Delta h_1(\%)$	1.0	0.6
	$\Delta d_2(\%)$	-1.6	-0.5
	$\Delta h_2(\%)$	0.5	0.3
From C	$\Delta d_6(\%)$	-37.4	-33.3
	$\Delta h_6(\%)$	4.3	3.6
	$\Delta d_5(\%)$	-5.7	-3.5
	$\Delta h_5(\%)$	1.0	0.8

Band structures of the 6H SiC {0001} surfaces overlaid on the projected bulk bands are given in Fig. 6. The presented band structures are obtained through LDA calculations by considering the relaxed surfaces. The Fermi level ( $E_F$ ) is above the valence band maximum of the bulk (0 eV) by 0.5 eV and 0.3 eV for the Si- and C-terminated surfaces, respectively. In both cases, two surface bands localized around  $E_F$  are observed, Figure 6. These bands originate from the dangling p states of the Si<sub>1</sub> and C<sub>6</sub> atoms on the opposite faces. The band due to C<sub>6</sub> is flat since this side is more planar [45]. In addition, a single band in the stop band around -10 eV is also seen for both surfaces, Fig. 6.

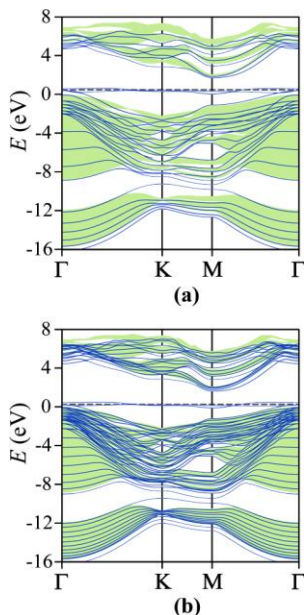


Fig.6. Band structures of the 6H SiC (0001) (a) and (000 $\bar{1}$ ) surfaces overlaid on the projected bands of the bulk. The horizontal dashed lines denote the Fermi levels ( $E_F$ ).

The band structures of ML and BL graphene are given in Fig. 7. Since results of LDA and GGA calculations agree well, only the results of LDA calculations will be given in the following band structures. Fig. 7(a) shows that the  $E_F$  and Dirac point ( $E_D$ ) coincide, as expected. Moreover, the Dirac cone is observed around these energies. In case of BL graphene in ABAB.. stacking, a slight band gap opening is observed, Fig. 7(b).

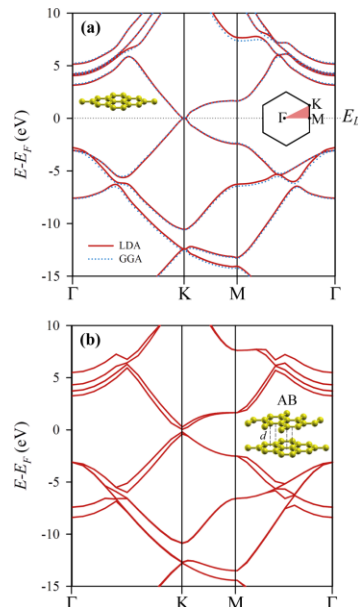


Fig.7. Band structures of ML (a) and BL (b) graphene.

The supercell employed in graphene-substrate calculations involves  $\sqrt{3} \times \sqrt{3} R30^\circ$  surface reconstruction in Fig. 2(a). It contains 18 Si and 18 C atoms belonging to the substrate and 8 C atoms belonging to the graphene superstrate. Fig. 8 shows that the first C layer on the (0001) surface does not exhibit free-standing graphene behavior, where it forms a buffer layer. When the first C layer initial distance to the (0001) surface is 2.6 Å or 3.0 Å, it approaches the surface upon relaxation, where the C<sub>G12</sub> and C<sub>G17</sub> atoms form mostly covalent bonds with the Si<sub>A12</sub> and Si<sub>A13</sub> atoms, Fig. 8(a). Besides, the Si<sub>A11</sub> atom, whose dangling bond is not saturated, experiences less upwards displacement than the Si<sub>A12</sub> and Si<sub>A13</sub> atoms. In case of the first C (buffer) layer, the value of the London  $s_6$  parameter (0 or 1) does not have significant effect on final relaxations on the (0001) surface.

The buffer layer in Fig. 8 is, on the average, separated from the top Si layer of the (0001) surface by 2.23 Å and exhibits a buckling of 0.27 Å (11% of graphene lattice constant). These results are close to the value (2.58 Å) reported by Mattausch and Pankratov [8]. Thus, the first C layer on the 6H SiC (0001) surface is a buffer layer.

The second C layer on the (0001) surface behaves like free-standing graphene, Fig. 8(b). The distance of this layer to the buffer layer is calculated as 3.39 Å and 3.02 Å, respectively, for  $s_6=0$  and 1. Furthermore, the buckling in the second C layer is much less significant (around 2 pm).

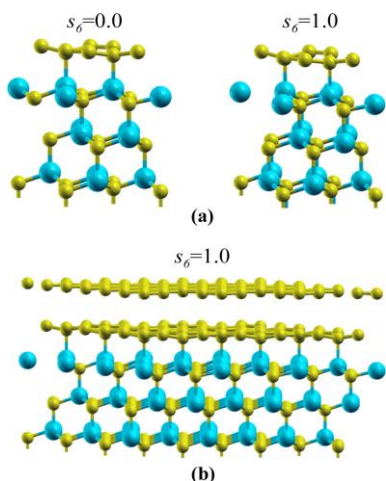


Fig.8. Final atom positions on the relaxed (0001) surface of 6H SiC in case of one (a) and two (b) C overlayers.

Band structures for one and two C overlayers on 6H SiC (0001) surface are given in Fig. 9. Inclusion of dispersion forces by varying the London  $s_6$  parameter does not have a significant effect on the obtained bands. The flat bands around 0.5 eV in each case are related to the unsaturated dangling states of the substrate. Fig. 9(a) reveals that the graphene Dirac cone does not appear for the buffer layer. On the other hand, although overlapping with the substrate bands, a Dirac-cone like behavior is observed in Fig. 9(b) for two C overlayers.

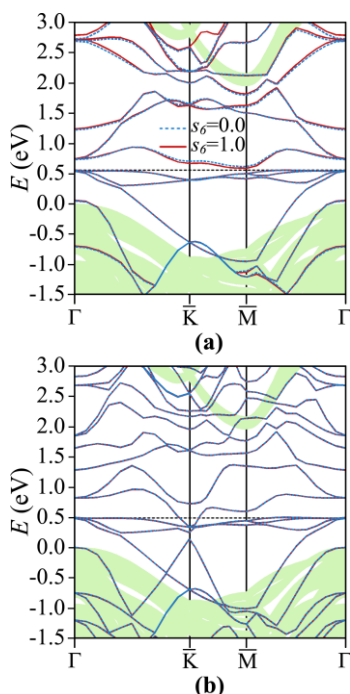


Fig.9. Band structure of one (a) and two (b) C overlayers on the 6H SiC (0001) surface.

The final atomic positions for the geometrically optimized system of one C overlayer on the (0001) surface of 6H SiC are given in Fig. 10(a). In contrast to Fig. 8(a), the first C layer is not bonded to the surface when London  $s_6=0$ . Thus, inclusion of the dispersion forces has a significant effect on the resulting

interactions. When  $s_6=1$ , the first C overlayer is covalently-bonded to the (0001) surface. The second case is similar to the results of Mattausch and Pankratov where local spin density approximation (LSDA) without explicitly considering dispersion forces [8, 23]. In contrast, calculations by Magaud et al [25] on C-rich  $(2 \times 2)_C$  surface reconstruction of 4H SiC suggest that the first C overlayer behaves like free-standing graphene. The latter is in agreement with experimental results and the DFT results for the  $\sqrt{13} \times \sqrt{13} R46.1^\circ$  surface reconstruction of 6H SiC [46].

When  $s_6=1$ , The relaxations for the (0001) surface are significantly larger than those on the (0001) surface for both one C overlayer and two overlayers. The vertical displacement in the buffer layer is as high as 0.37 Å. Due to buckling in the buffer layer, the minimum bond angle is found to be  $115.03^\circ$ . The average distance between the buffer layer and the (0001) decreases to 2.02 Å. In contrast, the second C layer behaves like free-standing graphene, Fig. 10(b), as in the case of (0001) surface in Fig. 8(b).

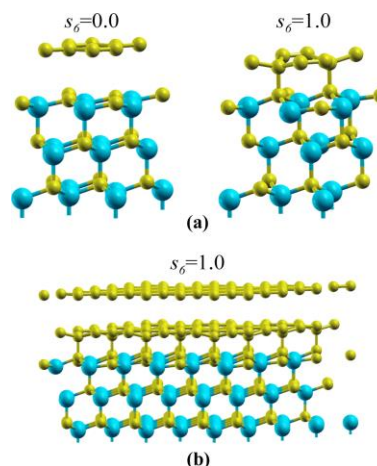


Fig.10. Final atom positions on the relaxed (0001) surface of 6H SiC in case of one (a) and two (b) C overlayers.

The fluctuations in the first C overlayer when  $s_6=0$  are as low as 2.0 pm, where the C layers behave like free-standing graphene. The bond length in this layer does not significantly change from the initial value of 1.52 Å. Moreover, the graphene-substrate is measured as 2.94 Å.

The covalent bonding to surface on the right of Fig. 10(a), where the van der Waals forces are included in LDA calculations, stems from the nature of the numerical method and the van der Waals radii ( $r_0=1.45$  Å) of the C atoms. While, the LDA calculations usually tend to over-bonding, the initial distance between the released C atoms is close to  $r_0$ . Thus, a tightly-bound atoms are obtained in these calculations.

The sharp contrast in Fig. 10(a) is also clearly visible in Fig. 11(a), where the band structure of one C overlayer on the (0001) surface is presented. While, a Dirac-cone like behavior, hallmark of graphene band structure, is observed for  $s_6=0$ , only four flat bands due the the buffer layer C atoms and unsaturated substrate C atoms appear for  $s_6=1$ . The discrepancy is also visible for two C overlayers, Fig. 11(b).

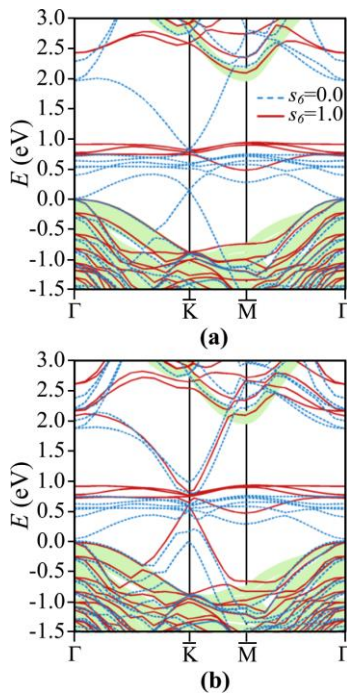


Fig.11. Band structure of one (a) and two (b) C overlayers on the 6H SiC (000 $\bar{1}$ ) surface.

#### IV. CONCLUSION

In conclusion, density-functional theory calculations of graphene on 6H silicon carbide {0001} surfaces reveal that the free-standing graphene behavior is observed starting from the second carbon overlayer on either surface. In case of the Si-terminated (0001) surface, the first C layer is a buffer layer, covalently bonded to the surface. This is the case irrespective of dispersion forces are accounted for. In contrast, the first C overlayer acts like a free-standing graphene layer on the C-terminated 6H SiC (000 $\bar{1}$ ) surface when the van der Waals interactions between the overlayer and surface are neglected. However, intrinsic nature of LDA calculations and the van der Waals radii of C atoms lead to covalently-bonded first C overlayer (i.e. a buffer layer) when van der Waals interaction is taken into account. In all cases, both first C overlayers and the top substrate bilayer experience significant displacement from their equilibrium positions. However, the fluctuations on the second C overlayer is negligible. The results of this work can be used in estimating behavior of epitaxially-grown graphene few layers on SiC surfaces and developing their applications.

#### ACKNOWLEDGMENT

This work is supported by Akdeniz University Scientific Research Projects Coordination Unit under the grant number 2008.01.0105.010.

#### REFERENCES

[1] K. S. Novoselov, D. Jiang, F. Schedin, T. Booth, V. Khotkevich, S. Morozov, and A. K. Geim, "Two-dimensional atomic crystals," *Proceedings of the National Academy of Sciences*, vol. 102, no. 30, 2005, pp. 10451-10453.

[2] Z. Jiang, Y. Zhang, Y.-W. Tan, H. Stormer, and P. Kim, "Quantum Hall effect in graphene," *Solid State Communications*, vol. 143, pp. 1-2, 2007, pp. 14-19.

[3] M. Katsnelson, K. Novoselov, and A. Geim, "Chiral tunnelling and the Klein paradox in graphene," *Nature Physics*, vol. 2, no. 9, 2006, pp. 620-625.

[4] Y.-M. Lin, C. Dimitrakopoulos, K. A. Jenkins, D. B. Farmer, H.-Y. Chiu, A. Grill, and P. Avouris, "100-GHz transistors from wafer-scale epitaxial graphene," *Science*, vol. 327, pp. 5966, 2010, pp. 662-662.

[5] P. Avouris, "Graphene: electronic and photonic properties and devices," *Nano Letters*, vol. 10, no. 11, 2010, pp. 4285-4294.

[6] K. Subrahmanyam, L. Panchakarla, A. Govindaraj, and C. Rao, "Simple method of preparing graphene flakes by an arc-discharge method," *The Journal of Physical Chemistry C*, vol. 113, no. 11, 2009, pp. 4257-4259.

[7] A. Kumar, A. L. M. Reddy, A. Mukherjee, M. Dubey, X. Zhan, N. Singh, L. Ci, W. E. Billups, J. Nagurny, and G. Mital, "Direct synthesis of lithium-intercalated graphene for electrochemical energy storage application," *ACS Nano*, vol. 5, no. 6, 2011, pp. 4345-4349.

[8] A. Mattausch and O. Pankratov, "Ab initio study of graphene on SiC," *Physical Review Letters*, vol. 99, no. 7, 2007, p. 076802.

[9] G. Giovannetti, P. A. Khomyakov, G. Brocks, P. J. Kelly, and J. Van Den Brink, "Substrate-induced band gap in graphene on hexagonal boron nitride: Ab initio density functional calculations," *Physical Review B*, vol. 76, no. 7, 2007, p. 073103.

[10] A. Reina, X. Jia, J. Ho, D. Nezich, H. Son, V. Bulovic, M. S. Dresselhaus, and J. Kong, "Large area, few-layer graphene films on arbitrary substrates by chemical vapor deposition," *Nano Letters*, vol. 9, no. 1, 2009, pp. 30-35.

[11] J. C. Swart, I. M. Ciobac, R. A. van Santen, and E. van Steen, "Intermediates in the formation of graphitic carbon on a flat FCC-Co (111) surface," *The Journal of Physical Chemistry C*, vol. 112, no. 33, 2008, pp. 12899-12904.

[12] L. Gao, J. R. Guest, and N. P. Guisinger, "Epitaxial graphene on Cu (111)," *Nano Letters*, vol. 10, no. 9, 2010, pp. 3512-3516.

[13] S. Marchini, S. Günther, and J. Wintterlin, "Scanning tunneling microscopy of graphene on Ru (0001)," *Physical Review B*, vol. 76, no. 7, 2007, p. 075429.

[14] P. Sutter, J. T. Sadowski, and E. Sutter, "Graphene on Pt (111): Growth and substrate interaction," *Physical Review B*, vol. 80, no. 24, 2009, p. 245411.

[15] D. Momeni Pakdehi, J. Aprojanz, A. Sinterhauf, K. Pierz, M. Kruskopf, P. Willke, J. Baringhaus, J. Stckmann, G. Traeger, and F. Hohls, "Minimum resistance anisotropy of epitaxial graphene on SiC," *ACS Applied Materials & Interfaces*, vol. 10, no. 6, 2018, pp. 6039-6045.

[16] Z. Liu, Q. Xu, C. Zhang, Q. Sun, C. Wang, M. Dong, Z. Wang, H. Ohmori, M. Kosinova, and T. Goto, "Laser-induced growth of large-area epitaxial graphene with low sheet resistance on 4H-SiC (0001)," *Applied Surface Science*, vol. 514, 2020, p. 145938.

[17] X. Zhang, C. Yan, C. Zeng, T. Sun, Z. Xing, W. Shi, Y. Wang, C. Pang, and B. Zhang, "Epitaxial synthesis of graphene on 4H-SiC by microwave plasma chemical vapor deposition," *Materials Research Express*, vol. 7, no. 11, 2020, p. 116410.

[18] N. Briggs, Z. M. Gebeyehu, A. Vera, T. Zhao, K. Wang, A. D. L. F. Duran, B. Bersch, T. Bowen, K. L. Knappenberger, and J. A. Robinson, "Epitaxial graphene/silicon carbide intercalation: a minireview on graphene modulation and unique 2D materials," *Nanoscale*, vol. 11, no. 33, 2019, pp. 15440-15447.

[19] T. Hu, H. Bao, S. Liu, X. Liu, D. Ma, F. Ma, and K. Xu, "Near-free-standing epitaxial graphene on rough SiC substrate by flash annealing at high temperature," *Carbon*, vol. 120, 2017, pp. 219-225.

[20] P. N. First, W. A. de Heer, T. Seyller, C. Berger, J. A. Strosio, and J.-S. Moon, "Epitaxial graphenes on silicon carbide," *MRS Bulletin*, vol. 35, no. 4, 2010, pp. 296-305.

[21] T. Cavallucci and V. Tozzini, "Intrinsic structural and electronic properties of the Buffer Layer on Silicon Carbide unraveled by Density Functional Theory," *Scientific Reports*, vol. 8, no. 1, 2018, pp. 1-10.

[22] C. Berger, Z. Song, X. Li, X. Wu, N. Brown, C. Naud, D. Mayou, T. Li, J. Hass, and A. N. Marchenkov, "Electronic confinement and coherence in patterned epitaxial graphene," *Science*, vol. 312, pp. 5777, 2006, pp. 1191-1196.

[23] A. Mattausch and O. Pankratov, "Density functional study of graphene overlayers on SiC," *Physica Status Solidi (b)*, vol. 245, no. 7, 2008, pp. 1425-1435.

- [24] F. Varchon, R. Feng, J. Hass, X. Li, B. N. Nguyen, C. Naud, P. Mallet, J.-Y. Veuillen, C. Berger, and E. H. Conrad, "Electronic structure of epitaxial graphene layers on SiC: effect of the substrate," *Physical Review Letters*, vol. 99, 12, 2007, p. 126805.
- [25] L. Magaud, F. Hiebel, F. Varchon, P. Mallet, and J.-Y. Veuillen, "Graphene on the C-terminated SiC (000 1) surface: An ab initio study," *Physical Review B*, vol. 79, 16, 2009, p. 161405.
- [26] C. P. Huelmo and P. A. Denis, "Unraveling the electromagnetic structure of the epitaxial graphene buffer layer," *Journal of Physics: Condensed Matter*, vol. 31, 43, 2019, p. 435001.
- [27] K. Hayashi, K. Morita, S. Mizuno, H. Tochihara, and S. Tanaka, "Stable surface termination on vicinal 6H-SiC (0001) surfaces," *Surface Science*, vol. 603, 3, 2009, pp. 566-570.
- [28] C. Park, B.-H. Cheong, K.-H. Lee, and K.-J. Chang, "Structural and electronic properties of cubic, 2H, 4H, and 6H SiC," *Physical Review B*, vol. 49, 7, 1994, p. 4485.
- [29] T. Seyller, A. Bostwick, K. Emtsev, K. Horn, L. Ley, J. McChesney, T. Ohta, J. D. Riley, E. Rotenberg, and F. Speck, "Epitaxial graphene: a new material," *Physica Status Solidi (b)*, vol. 245, 7, 2008, pp. 1436-1446.
- [30] K. Emtsev, F. Speck, T. Seyller, L. Ley, and J. D. Riley, "Interaction, growth, and ordering of epitaxial graphene on SiC {0001} surfaces: A comparative photoelectron spectroscopy study," *Physical Review B*, vol. 77, 15, 2008, p. 155303.
- [31] R. Helbig and F. Engelbrecht, "SiC: Polar properties and their influence on technology and devices," in *Advances in Solid State Physics 38*: Springer, 1999, pp. 75-86.
- [32] P. Giannozzi, S. Baroni, N. Bonini, M. Calandra, R. Car, C. Cavazzoni, D. Ceresoli, G. L. Chiarotti, M. Cococcioni, and I. Dabo, "QUANTUM ESPRESSO: a modular and open-source software project for quantum simulations of materials," *Journal of Physics: Condensed Matter*, vol. 21, 39, 2009, p. 395502.
- [33] J. P. Perdew and A. Zunger, "Self-interaction correction to density-functional approximations for many-electron systems," *Physical Review B*, vol. 23, 10, 1981, p. 5048.
- [34] J. P. Perdew, J. A. Chevary, S. H. Vosko, K. A. Jackson, M. R. Pederson, D. J. Singh, and C. Fiolhais, "Atoms, molecules, solids, and surfaces: Applications of the generalized gradient approximation for exchange and correlation," *Physical Review B*, vol. 46, 11, 1992, p. 6671.
- [35] H. J. Monkhorst and J. D. Pack, "Special points for Brillouin-zone integrations," *Physical Review B*, vol. 13, 12, 1976, p. 5188.
- [36] F. Birch, "Finite elastic strain of cubic crystals," *Physical Review*, vol. 71, 11, 1947, p. 809.
- [37] G. C. Capitani, S. Di Pierro, and G. Tempesta, "The 6 H-SiC structure model: Further refinement from SCXRD data from a terrestrial moissanite," *American Mineralogist*, vol. 92, 2-3, 2007, pp. 403-407.
- [38] W. Bassett, M. Weathers, T. C. Wu, and T. Holmquist, "Compressibility of SiC up to 68.4 GPa," *Journal of Applied Physics*, vol. 74, 6, 1993, pp. 3824-3826.
- [39] M. Yoshida, A. Onodera, M. Ueno, K. Takemura, and O. Shimomura, "Pressure-induced phase transition in SiC," *Physical Review B*, vol. 48, 14, 1993, p. 10587.
- [40] P. Käckell, B. Wenzien, and F. Bechstedt, "Influence of atomic relaxations on the structural properties of SiC polytypes from ab initio calculations," *Physical Review B*, vol. 50, 23, 1994, p. 17037.
- [41] J. Wang, L. Zhang, Q. Zeng, G. L. Vignoles, and L. Cheng, "Surface relaxation and oxygen adsorption behavior of different SiC polytypes: a first-principles study," *Journal of Physics: Condensed Matter*, vol. 22, 26, 2010, p. 265003.
- [42] J. Sołtys, J. Piechota, M. Łopuszyński, and S. Krukowski, "A comparative DFT study of electronic properties of 2H-, 4H- and 6H-SiC (0001) and SiC ( ) clean surfaces: significance of the surface Stark effect," *New Journal of Physics*, vol. 12, 4, 2010, p. 043024.
- [43] T. Dalibor, G. Pensl, N. Nordell, and A. Sch ner, "Electrical properties of the titanium acceptor in silicon carbide," *Physical Review B*, vol. 55, 20, 1997, p. 13618.
- [44] J. P. Perdew, "Density functional theory and the band gap problem," *International Journal of Quantum Chemistry*, vol. 28, S19, 1985, pp. 497-523.
- [45] M. Sabisch, P. Krüger, and J. Pollmann, "Ab initio calculations of structural and electronic properties of 6H-SiC (0001) surfaces," *Physical Review B*, vol. 55, 16, 1997, p. 10561.
- [46] J. Hass, F. Varchon, J.-E. Millan-Otoya, M. Sprinkle, N. Sharma, W. A. de Heer, C. Berger, P. N. First, L. Magaud, and E. H. Conrad, "Why multilayer graphene on 4H-SiC (000-1) behaves like a single sheet of graphene," *Physical Review Letters*, vol. 100, 12, 2008, p. 125504.

## BIOGRAPHIES



**AHMET CICEK** Finike, Antalya, in 1980. He received the B.S. degree in Physics from Bilkent University in 2003, M.S. and Ph.D. degrees in Physics from Akdeniz University in 2006 and 2012, respectively.

From 2005 to 2010, he was a Research Assistant with Physics Department of Akdeniz University. He was assigned as an Assistant Professor in the Physics Department, Burdur Mehmet Akif Ersoy University between 2014 and 2016. Later, he was assigned as an Associate Professor in the Department of Nanoscience and Nanotechnology, Burdur Mehmet Akif Ersoy University. He is currently working as a Professor at the same department since 2019. He is the author of three book chapters, 40 SCI articles, and 4 patent applications. His research interests include nanophotonics, plasmonic nanostructures, acoustic metamaterials, phononic crystals and numerical materials science.



**BULENT ULUG** Yozgat, in 1953. He received the B.S. and M.S. degrees in Physics from Hacettepe University, in 1976 and the Ph.D. degree in Electrical Engineering from the University of Edinburgh, UK, in 1982.

He was Assistant Professor from 1983 to 1986 and Associate Professor from 1986 to 1996 in the Physics department, İn nü University. He has been a Professor with the Physics Department, Akdeniz University between 1996 and 2020. He is the author of more than 40 articles. His research interests include high-temperature superconductors, photonic and phononic crystals, quantum well structures and green synthesis of metallic nanoparticles.

# Monitoring Medical Interventions for Multidimensional Evaluation of Changes in Patient Test Results with Principal Component Analysis

Mohammed Abebe Yimer\*, Özlem Aktaş, Süleyman Sevinç, Ali Rıza Şişman, Oktay Yildirim and Eminullah Yaşar

**Abstract**—Medical doctors of today are challenged with increasingly large volumes of high-dimensional, heterogeneous, and unstructured data from various sources that pose significant challenges for manual analysis. However, this unstructured data is mainly vital for decision making but there exists a shortage of intelligent tools to extract the hidden knowledge. Given these facts, the application of machine learning methods in healthcare is a growing phenomenon. This paper explores machine learning approaches for interpreting large quantities of continuously acquired, multivariate patient-based medical laboratory data, in intensive care unit (ICU) settings. The research hypothesizes that

principal component analysis (PCA) can be able to capture the changes in the outcomes after a medical intervention. We adopted PCA as the main method, to observe and capture the daily changes for intensive care unit patients. The approach will be able to inform the physicians, which laboratory tests are exhibiting variances after an intervention, and their associated epiphenomenon. This can be used as a clue to make decisions on which treatment or diagnosis to apply further. Experimental analysis results indicate that PCA was able to capture patient progression in terms of variances. Permutation tests for the validity and stability of the model exhibit an acceptable significance level with a p-value of 0.001. Results showed that the approach provides promising results for interpreting large quantities of patient data for establishing a cause-effect relationship from medical interventions and be used as an early warning system. The study retrospectively demonstrated the capability of PCA to monitor and provide an alert to the clinicians about the patient's changing conditions, thereby providing opportunities for timely interventions. If coupled with other machine learning models, the approach can also be able to support clinical decision making and enable effective patient-tailored care for better health outcomes.

**MOHAMMED ABEBE YIMER**, is with Department of Computer Engineering University of Dokuz Eylül University, Izmir, Turkey, (e-mail: [moshehio@gmail.com](mailto:moshehio@gmail.com)).

 <https://orcid.org/0000-0003-0622-4841>

**ÖZLEM AKTAŞ**, is with Department of Computer Engineering University of Dokuz Eylül University, Izmir, Turkey, (e-mail: [aktas.ozlem@deu.edu.tr](mailto:aktas.ozlem@deu.edu.tr)).

 <https://orcid.org/0000-0001-6415-0698>

**SÜLEYMAN SEVINÇ**, is with Department of Computer Engineering University of Dokuz Eylül University and Labenko Bilişim A.Ş., Izmir, Turkey, (e-mail: [suleysevinc@gmail.com](mailto:suleysevinc@gmail.com)).

 <https://orcid.org/0000-0001-9052-5836>

**ALI RIZA ŞIŞMAN**, is with Department of Medical Biochemistry University of Dokuz Eylül University, Izmir, Turkey, (e-mail: [aliriza.sisman@deu.edu.tr](mailto:aliriza.sisman@deu.edu.tr)).

 <https://orcid.org/0000-0002-9266-0844>

**OKTAY YILDIRIM**, is with Department of Computer Engineering University of Dokuz Eylül University, Izmir, Turkey, (e-mail: [oktay.yildirim@deu.edu.tr](mailto:oktay.yildirim@deu.edu.tr)).

 <https://orcid.org/0000-0001-7281-3623>

**EMINULLAH YAŞAR**, is with Department of Computer Engineering University of Dokuz Eylül University, Izmir, Turkey, (e-mail: [eminullah.yasar@gmail.com](mailto:eminullah.yasar@gmail.com)).

 <https://orcid.org/0000-0003-2298-4808>

Manuscript received August 12, 2020; accepted February 6, 2021.  
DOI: [10.17694/bajece.782510](https://doi.org/10.17694/bajece.782510)

**Index Terms**—Capture variances, Decision making, Intensive care unit, Medical intervention, Patient Care, Principal component analysis.

## I. INTRODUCTION

Several research studies postulate that the development of machine learning systems in healthcare is paramount both for the healthcare industry as well as the patients. The majority of healthcare systems nowadays use a basic visual representation of historical data for analysis by the doctors. This type of viewing is important however, this becomes overwhelming with the increasing number of patients and a vast amount of collected data. This necessitates the development of intelligent tools or systems that can extract insight and semantics from this bulk of data for decision-making processes.

Widanagamaachchi *et al.* [1], presents a system for interactive visualization and exploration of patient progression overtime for decision making using hierarchical clustering and tracking graph. Wang *et al.* [2], also developed a web-based visual mining system that supports explorative analysis of

high dimensional categorical electronic medical records (EMR) for chronic kidney disease (CKD). The proposed method uses Ochiai coefficients to compute patient similarity-based on seventeen CKD factors. This type of exploring and viewing is important, however, it won't be enough to uncover latent information. In addition, early studies such as [3 - 5] use generic patient vital signs to compute early warning scores to predict patient mortality for deteriorating patients. These systems are solely based on physiological parameters of the patient's vital signs such as heart rate, breathing rate, and systolic blood pressure. Moreover, these systems use the sum of assigned points of these vital signs from a subjectively fixed normal range to identify patients that are deteriorating but also can have their outcome changed by timely intervention. The aforementioned studies use ordinary methods and/or patient vital signs to monitor patient progressions. However, recent advancements in machine learning and EMR paves the way for the development of intelligent tools for medical data analysis to help in decision making. In line with this, numerous predictive and analytic models have been presented.

Ye *et al.* [6] applied a tree-based random forest algorithm on data collected from EMRs to predict patients at high risk of intra-hospital mortality and achieved a c-statistics of 0.884. On the other hand, the study by Cai *et al.* [7], presents a predictive model for real-time predictions of the length of stay (LOS), mortality, and readmission for inpatients from electronic health records (EHR). The study employed Bayesian network model to estimate the likelihood of a patient being in one of the following states; at home, in the hospital, or dead, and achieved an average daily accuracy of 80% and an AUROC of 0.82. Furthermore, other highly investigated categories of machine learning models in healthcare include disease-specific predictive models. For example, the work [8], performed experimental studies on data collected on mild cognitive impairments (MCI). The work conducted a comparative study on methods such as decision trees, different statistical t-tests to predict the chance of a patient being positive or negative. The study [9] also demonstrates the use of machine learning methods for predicting acute kidney injuries (AKI) from EHR for better assessment of existing and novel interventions to provide vital treatment. Also, the studies [10, 11] explored the use of PCA as a dimensionality reduction technique and proved that it helps improve both classification accuracy and model training time for classification tasks. Moreover, the authors [11] suggest the use of this approach as part of medical devices for non-invasive, inexpensive decision-making tool. There are a tremendous amount of studies and investigations conducted on predictive models for patient mortality and disease-specific predictions. However, there is little or no investigation conducted on machine learning models to extract hidden knowledge or semantics from electronic health records for decision making. Because of these facts, this research focuses on a non-disease specific model for observing outcome changes after a medical intervention in ICU settings. The proposed approach can serve as an EMR-based early warning system that can be used as

part of a daily routine clinical practice.

## II. MATERIALS AND METHODS

The study used a subset of data extracted from the publicly available Medical Information Mart for Intensive Care-III (MIMIC-III) v1.4 database [12, 13]. Some studies conducted using this database include [14 - 16]. The MIMIC-III dataset contains comprehensive, granular, deidentified ICU EHRs collected from hospital medical information systems (both patient bedside workstations and hospital archives). The data is collected from a single tertiary teaching hospital between the years 2001 and 2012. The dataset includes patient information that falls into several categories such as general, physiological, medications, fluid balance, notes, and reports. For our intended research, a total of 1,410 patients with a hospital LOS greater than or equal to 30 days is selected. Next, for each of these patients corresponding demographic and clinical data (laboratory data) is extracted from the original database. After careful inspection of the extracted dataset 1,306 (out of 1410) patients having at least 10 observations were selected for further analysis. This threshold is chosen to have extended observations and to ascertain that the approach captures the intended changes. Table I describes general information about the dataset used.

TABLE I  
USED DATASET GENERAL INFORMATION

Gender	Count	Average LOS (in days)
Male	732	55.2
Female	574	57.78
Total	1306	56.33

The dataset used for this work contains laboratory tests conducted over the specified period for multiple laboratory tests for each patient separately. The study conducted a detailed retrospective analysis on 1,306 ICU patients with a minimum hospital LOS of 30 days. The selected target patients were diagnosed with different diseases such as sepsis and pneumonia, with a mean hospital LOS of 56.33 days. At the end of their stay, the subjects were discharged alive or dead to home or another healthcare unit. Table II presents sample data used for a sample patient. Laboratory test dates are de-identified (from the source) according to the Health Insurance Privacy and Accountability Act (HIPAA) privacy rule i.e., 2/26/2191 for instance is not an error. It indicates a de-identified date according to the HIPAA rule not to disclose the actual patient laboratory test dates. However, date sequences are properly maintained.

The study hypothesizes that PCA can be able to capture the changes that may happen due to medical intervention. PCA is commonly used for linear dimensionality reduction and exploratory purposes through variance maximization. The intuition behind PCA is to use a special coordinate system that depends on the cloud of points. The axes are placed in the direction of the highest variance of the points to maximize the

variance along that direction [15]. This intuition can help us determine and show the patient's laboratory result exhibiting the highest variances after applying a certain medical intervention. Moreover, if applied to longitudinal data, it may help us explore patient progression from time T1 to T2. So that appropriate treatment or therapy can be prescribed or further diagnosis can be advised. In addition, each principal component (PC) is a linear combination of the original individual variables. This can be used to see the effect and contribution of each laboratory test in that direction. The succeeding PCs try to capture the next highest variances left out by the preceding PCs. This may show epiphenomenon or parallel medical events or conditions happening. Most studies use PCA as preprocessing for classification tasks [10-11]. However, based on the intuition of how PCA works, we believe that it can be used as part of a tool for early warning of medical conditions by showing laboratory tests with changes. To evaluate our primary hypothesis, a retrospective analysis was performed using PCA to monitor patient progress.

For this analysis, first non-numeric variables and variables with a single measured value (having no variance) throughout the ICU stay are discarded. Since the analysis is patient-based missing values are imputed using the most-frequent strategy along each column. This is followed by data standardization for PCA processing. Then the records are grouped based on the date the laboratory test is taken. A baseline of at least four observations should be available on a specific day to start or

apply the analysis. Otherwise, those observations are merged with the next day's test results. This process is repeated iteratively until we achieve the minimum (4 observations) amount of observations for analysis. Finally, the relevant patient data were fed into the model and principal components were computed and visualized. Once this is complete, model validation and stability test are conducted.

To evaluate the validity and stability of the proposed approach, a permutation test sometimes known as randomization test is employed without relying on a specific probability model. Total variance accounted for (TVAF) is computed as the statistics of interest. TVAF is equal to the sum of the Eigenvalues of the first  $n$  principal components. In our case  $n$  represents the number of principal components that make up 99% of the total variance in the data. This is followed by  $r$  number of permutation ( $r=1000$ ) and statistical estimates (estimated TVAF) for each permutation is computed. The statistical significance between the observed TVAF and the estimated TVAF is determined by comparing the  $p$ -value to a significance level. A significance level  $\alpha=0.05$  is adopted as a rejection rule for this study. The alternative hypothesis that the estimated TVAF values do not deviate significantly from the observed TVAF value is tested against the null hypothesis that it does. If  $p < \alpha$ , the result is marked significant, and  $H_0$  is rejected.

TABLE II  
SAMPLE DATASET CONTENT

Date	Anion Gap	Bicarbonate	Bilirubin, Direct	Bilirubin, Indirect	Bilirubin, Total	Chloride
2/26/2191 16:20	18	16	0.2	4.2	4.4	114
2/28/2191 0:30			0.3	4	4.3	115
3/1/2191 4:30	19	15	0.3	3.8	4.1	106
3/1/2191 13:55	19	13				110
3/2/2191 5:20	23	14	0.7	2.7	3.4	106
3/2/2191 12:45	23	13				105
3/3/2191 4:30	17	21	0.3	4.6	4.9	99
3/3/2191 23:35	21	20	0.3	6	6.3	97

### III. RESULTS

In the PCA analysis, principal components that make up 99% of the overall variance in the data are retained for each analysis. For example analysis results for a sample patient

(frequently diagnosed for respiratory failure) shows the first two PCs for the first day and the first three PCs for the next day that amount to approximately 99% of the variances explained in the data (Fig. 1).

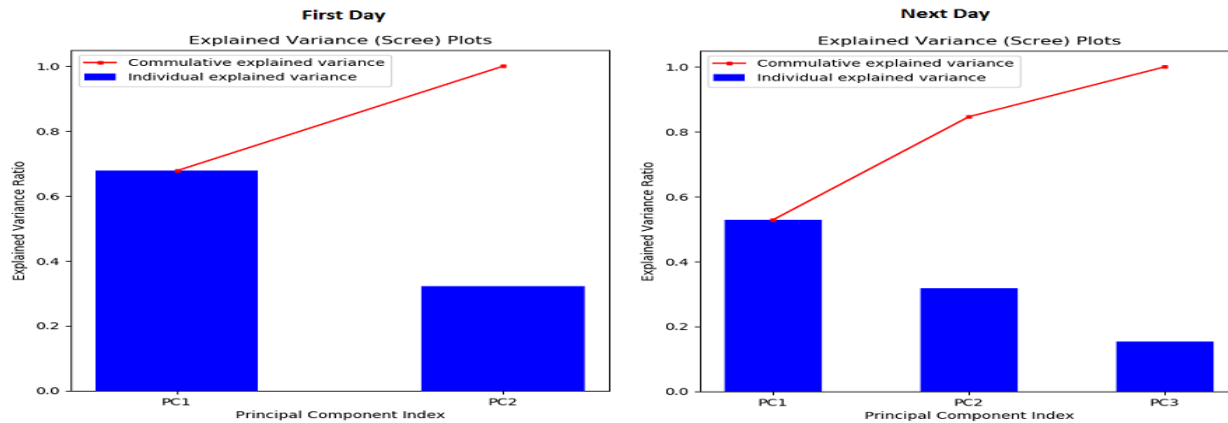


Fig. 1. Sample Principal Component Scree Plot

In addition, the contribution of each variable to a PC can be tabulated (see Table III) or presented using different formats for ease of use. For instance, Fig. 2 represents a 2-dimensional

plot representation of variable loadings/contributions of the original variables under their respective principal components.

TABLE III  
SAMPLE VARIABLE CONTRIBUTIONS/LOADINGS

PC.No	Chloride	Glucose	Oxygen	PT	Phosphate	Sodium	pCO2	pH
PC1	0.394	0.313	0.028	0	0.394	0	-0.193	0.167
PC2	0.114	0.138	0.078	0	0.114	0	0.357	-0.397
PC3	0	0.017	-0.106	0	0	0	0.096	-0.03
PC4	-0.041	0.007	-0.439	0	-0.041	0	0.26	0.029
PC5	0.023	-0.021	0.605	0	0.023	0	0.285	-0.346

plot visually shows the results for the first two components.

Table III shows sample variable loadings per principal components for a specific laboratory test date. The larger the absolute value of the coefficient is, the more important the corresponding variable is in calculating the principal component. Generally, how large the absolute value of a coefficient has to be to consider it significant is subjective. For instance, we can see from Table III that PT and Sodium do not contribute to any of the PCs, and this indicates the insignificance of these tests on that specific day. On the other hand, Phosphate and Chloride contribute the highest under PC1. Moreover, this tabular information can be presented using other representations for ease of use as depicted in Fig. 2 and show the daily changes after a certain treatment or intervention. To interpret each principal components, we can examine the magnitude and direction of the coefficients for the original variables. The plot on Fig. 2(a), (b), and (c) visually shows the component loading for day one, two, and three of the analysis, respectively. Note that laboratory tests with zero loadings are removed from the plots.

In these results, for day one of the ICU stay (Fig. 2(a)), the first principal component has large positive associations with MCHC, Potassium, White Blood Cells, and PTT. The second component has large positive associations with MCH, MCV, Red Blood Cells, Hematocrit, and Hemoglobin. The loading

The third component has large negative associations with Base Excess & pH and large positive associations with Hematocrit (Calculated), Potassium (Whole Blood), and Hemoglobin (see Table IV). Moreover, we can observe that there are changes in magnitude and direction on the second and third days of the ICU stay (Fig. 2(b) and (c)). This may mean that the condition of the patient is either getting better or worse. Or it may also show if medical treatment is working or not. The plots show comparison and progression of successive daily based contributions (negative or positive) of the laboratory tests under different PCs for a patient i.e. daily changes. They depict what changes happened on a specific day based on or in relation to a treatment applied on the previous day. This can be used to decide on further steps that need to be carried out. Based upon this, a trained physician can be able to easily infer the implication and make an informed decision.

The corresponding coefficient values for Fig. 2 are presented in Table IV below only for the top five variables for the first three PC along with changes for three consecutive days. As it can be seen from the table, MCHC, Potassium, White Blood Cells and PTT equally contribute the highest under PC1. On the other hand, MCH, MCV, and Red Blood

Cells equally contribute the highest under PC2 for day 1. contribute the highest under PC3 for the same day. Besides, Hematocrit (Calculated), Base Excess, and pH

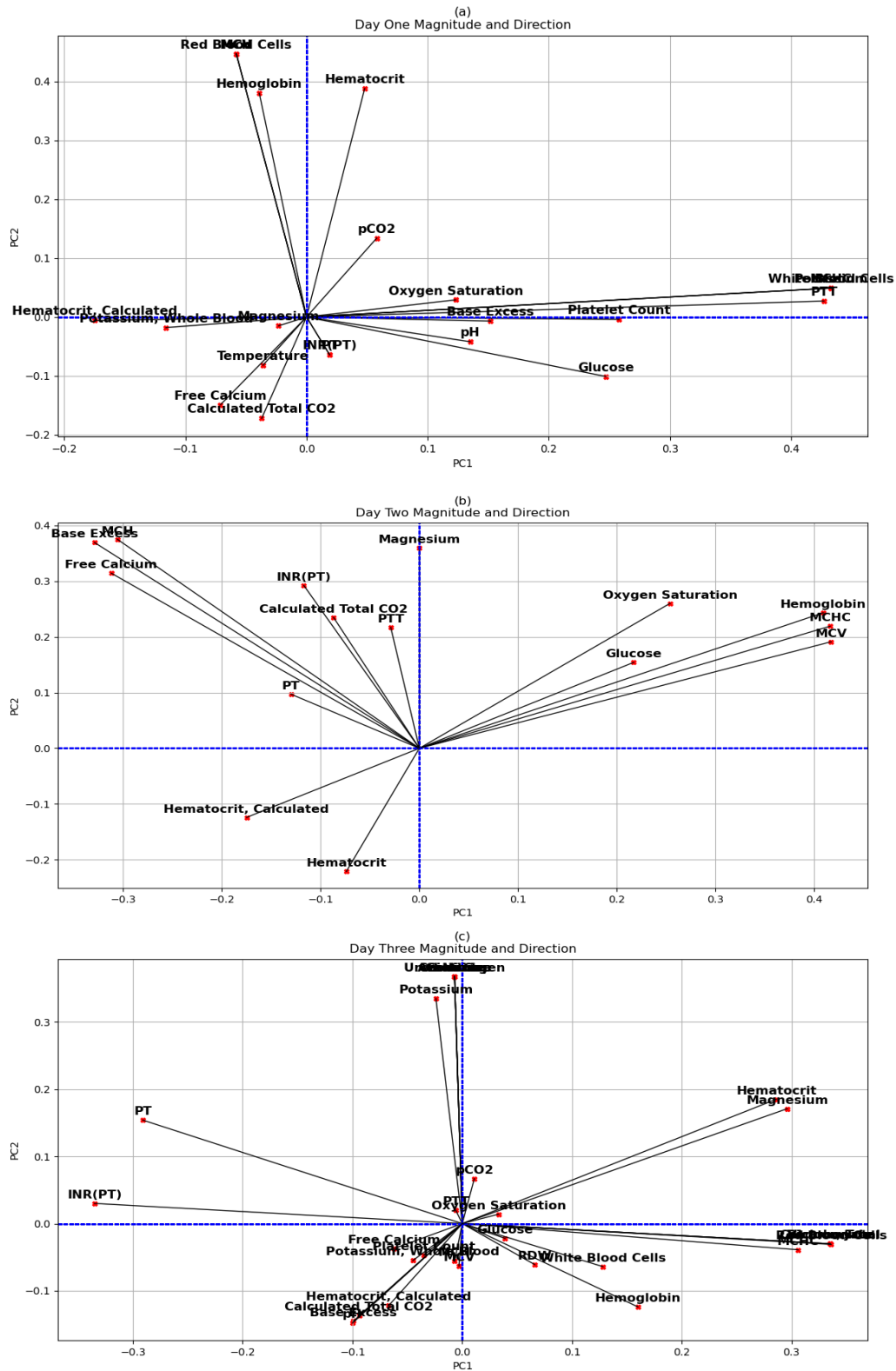


Fig. 2. Magnitude and direction of the coefficients for the original variables

TABLE IV  
TOP THREE PC DAILY CHANGES

Day	PC1		PC2		PC3	
1	MCHC	0.43	MCH	0.45	Hematocrit, Calculated	0.46
	Potassium	0.43	MCV	0.45	Base Excess	-0.45
	White Blood Cells	0.43	Red Blood Cells	0.45	pH	-0.40
	PTT	0.43	Hematocrit	0.39	Potassium, Whole Blood	0.28
	Platelet Count	0.26	Hemoglobin	0.38	Hemoglobin	0.26
2	PTT	0.42	Oxygen Saturation	0.38	Hemoglobin	0.56
	PT	0.42	Calculated Total CO2	0.37	Free Calcium	0.52
	INR(PT)	0.41	Platelet Count	0.36	Hematocrit, Calculated	0.49
	Calculated Total CO2	-0.33	Glucose	0.31	Magnesium	-0.21
	Glucose	-0.31	Magnesium	0.29	pH	0.20
3	Red Blood Cells	0.34	Anion Gap	0.37	PTT	0.34
	Bicarbonate	0.34	Chloride	0.37	MCV	0.33
	Calcium, Total	0.34	Creatinine	0.37	RDW	0.30
	INR(PT)	-0.34	Sodium	0.37	pH	-0.29
	Vancomycin	0.34	Urea Nitrogen	0.37	MCH	0.29

Finally, the dimensionality suggested by the scree plots of the analysis is variant depending on the number of variables and samples we have in the dataset, corresponding to 99% of the explained variance in the data. In the end, the stability and validity of the model for the overall analysis were confirmed by the p-values of estimated TVAFs. The estimated statistics achieved a significance level of 0.001 which is much less than the predetermined  $\alpha$ . This proves that the alternative hypothesis is accepted which posits the approach's stability and validity.

#### IV. DISCUSSION

Many variables must be considered when interpreting the results of any medical laboratory test. In clinical medicine, physicians use normal reference ranges as guidelines of what is normal or abnormal. However, using normal reference ranges for ICU patients may not be the most sought out strategy [16]. Furthermore, we believe that even if minor changes of successive measurements of patient vital signs are within normal reference ranges, in conjunction with other laboratory test results, those changes may reveal significant information. This in turn can be used to make informed decisions on a drug, therapy, or further diagnosis. In this study, we presented a model for observing changes in outcome after clinical interventions in ICU settings. To the best of our knowledge, this is a novel non-disease specific model that can observe and capture clinical changes and is built to provide non-disease specific analysis of patient progress over time. The results can be used to decide what treatment or therapy to prescribe or which diagnosis to perform further. From the results, we can be able to see which laboratory tests are contributing more and their combined directions. This insight

can be used to decide; 1) on which laboratory tests to perform further analysis and/or omit from further analysis so that redundant and anomalous tests will be avoided and 2) it can also be used to decide what prescription to provide or avoid, for the benefit of the patient. Moreover, each principal component is a linear combination of the original individual variables. With a closer look at this, a physician can be able to know or judge the combined effects of those variables and make medical inferences. Sometimes it may also be necessary to see which laboratory test is having a change more often than the others so that precautions can be taken, and this can also be achieved with the proposed approach. However, it is worth noting that we did not and cannot address the issue of whether the change happened due to the introduction of a treatment or by chance in this setting.

In any statistical model, where PCA is not an exception, model validation is imperative to generalize the results of a proposed model. However, Lebart [17] points out that conventional analytical approaches are both unrealistic and analytically intricate for computing precision estimates of models such as PCA. Parametric methods have been tried for PCA model validation [18], alternatively, the study [19] advocates nonparametric methods as theoretically better matches for the nonparametric nature of PCA. By applying nonparametric methods such as permutation tests or bootstrap tests, different matrices can be generated by permutation or resampling of the data, and their Eigen values and Eigen vectors will no longer be the same. In view of these facts, the study used permutation testing for model validation. Given all the bulk of data, the physician has to make the most out of it and try saving the lives of the patients. With this in mind, we proposed a model that can help the physicians as part of their daily routine clinical practice. The approach can be used to

look at the results of an ICU patients' treatment from different perspectives. Furthermore, results showed that the approach, if coupled with other machine learning models, can be able to provide a promising future for real-time, non-invasive patient monitoring and early warning system in ICU settings. However, it is worth mentioning that, the medical protocols used, prescriptions provided and input events recommended to the patients during the ICU stay were not taken into consideration in this study. We believe that if included, any one of these inputs can cause certain variables to change.

Based on the research results, we can point out that with the appropriate selection of relevant algorithms, applying machine learning models on EMRs can provide key insights for medical practitioners to facilitate the decision making processes. With the aid of the proposed model, inexperienced physicians may feel better confidence about their decisions. Nevertheless, this approach cannot replace or undermine the diagnostic skills and professional instincts of medical practitioners. The results of this research can provide an alternative means for the medical practitioners to consider only the significant factors instead of going through the whole patient data. Moreover, since the study used ICU admissions data from a single tertiary teaching hospital, there is no guarantee that similar results would be obtained in other locations, clinical settings, or specific patient groups. Although the study has done retrospective analysis, we are confident that the system can be implemented as a real-time early warning system. Finally, the proposed model should not be regarded as the sole solution for detecting patient progression over time. Rather, it should be used as part of the daily routine clinical practice.

## V. CONCLUSION

Given longitudinal data, numerous machine learning approaches can be applied to extract different semantic and latent knowledge, so that informed decisions can be made. The advantages of machine learning approaches in healthcare are multifold. It can be used to make timely, lifesaving, and effective decisions. On the other hand, it can save unnecessary wastage of resources both for the patient, healthcare industry, and medical practitioners.

Early studies such as [3 - 5] use the sum of assigned points of generic vital signs from a subjectively fixed normal range to compute early warning scores to identify patients that are deteriorating but also can have their outcome changed by timely intervention. These types of systems are solely based on physiological parameters of the patient's vital signs such as heart rate, breathing rate, and systolic blood pressure. In this study, we showed that PCA can be used as part of a tool for early warning of medical outcome changes and epiphenomenon in ICU settings. It can be used as a novel non-disease specific tool that can observe patient daily clinical changes and provide non-disease specific analysis of patient progress over time for proactive actions. Given the facts, the

user can be able to decide what treatment or therapy to prescribe or which diagnosis to perform further. However, additional investigation is required with other machine learning models to provide a full-fledged and more robust support for the medical practitioners.

## VI. AUTHOR CONTRIBUTION STATEMENT

The authors confirm contribution to the paper as follows: M. Abebe YIMER and S. SEVINÇ conceived and presented the idea. M. Abebe YIMER took the responsibility of data collection and preparation. M. Abebe YIMER carried out the model implementation with the help of O. YILDIRIM and E. YAŞAR. Analysis and interpretation of results are carried out by M. Abebe YIMER, S. SEVINÇ, and A. Rıza ŞİŞMAN. The draft manuscript is prepared by M. Abebe YIMER. Also, A. Rıza ŞİŞMAN contributed to the interpretation of the results from a medical perspective and S. SEVINÇ, & Ö. AKTAŞ helped supervise the project. A final and critical review of the article before submission not only for spelling and grammar but also for its intellectual content is conducted by M. Abebe YIMER, S. SEVINÇ, A. Rıza ŞİŞMAN, and Ö. AKTAŞ. Finally, all authors reviewed the results, provided critical feedback, and approved the final version of the manuscript.

## VII. ETHICS APPROVAL

The study used a publicly available, deidentified medical dataset, hence no ethics approval was required.

## VIII. CONFLICT OF INTEREST

The authors declare no conflicts of interest.

## REFERENCES

- [1] W. Widanagamaachchi, Y. Livnat, P.-T. Bremer, S. Duvall and V. Pascucci, "Interactive Visualization and Exploration of Patient Progression in a Hospital Setting," AMIA Annual Symposium Proceeding, vol. v2017, pp. 1773-1782, 2017.
- [2] C.-F. Wang, J. Li, K.-L. Ma, C.-W. Huang and Y.-C. Li, "A Visual Analysis Approach to Cohort Study of Electronic Patient Records," in IEEE International Conference on Bioinformatics and Biomedicine, Belfast, UK, 2014.
- [3] C. Mathukia, W. Fan, K. Vadyak, C. Biege and M. Krishnamurthy, "Modified Early Warning System improves patient safety and clinical outcomes in an academic community hospital," Journal of Community Hospital Internal Medicine Perspectives, vol. 5, no. 2, 2015.
- [4] G. B. Smith, D. R. Prytherch, P. Meredith, P. E. Schmidt and P. I. Featherstone, "The ability of the National Early Warning Score (NEWS) to discriminate patients at risk of early cardiac arrest, unanticipated intensive care unit admission and death," Elsevier Resuscitation, vol. 84, no. 4, pp. 465-470, 2013.
- [5] D. R. Prythercha, G. B. Smith, P. E. Schmidt and P. I. Featherstone, "ViEWS—Towards a national early warning score for detecting adult inpatient deterioration," Elsevier Resuscitation, vol. 81, no. 8, p. 932-937, 2010.
- [6] C. Ye, O. Wang, M. Liu, L. Zheng, M. Xia, S. Hao, B. Jin, H. Jin, C. Zhu, C. J. Huang, P. Gao, G. Ellrodt, D. Brennan, F. Stearns, K. G. Sylvester, E. Widen, D. B. McElhinney and X. Ling, "A Real-Time Early Warning System for Monitoring Inpatient Mortality Risk: Prospective Study Using Electronic Medical Record Data," Journal of Medical Internet Research, vol. 21, no. 7, 2019.

- [7] X. Cai, O. Perez-Concha, E. Coiera, F. Martin-Sanchez, R. Day, D. Roffe and B. Gallego, "Real-time prediction of mortality, readmission, and length of stay using electronic health record data," *Journal of American Medical Information Association*, vol. 23, no. 3, pp. 553-561, 2016.
- [8] F. Babić, M. Vadovský, M. Muchová, J. Paralić and L. Majnarić, "Simple Understandable Analysis of Medical Data to Support the Diagnostic Process," in *IEEE 15th International Symposium on Applied Machine Intelligence and Informatics*, Slovakia, 2017.
- [9] H. Mohamadlou, A. Lynn-Palevsky, C. Barton, U. Chettipally, L. Shieh, J. Calvert, N. R. Saber and R. Das, "Prediction of Acute Kidney Injury With a Machine Learning Algorithm Using Electronic Health Record Data," *Canadian Journal of Kidney Health*, vol. 5, pp. 1-9, 2018.
- [10] I. Babaoğlu, O. Fındık and M. Bayrak, "Effects of principal component analysis on assessment of coronary artery diseases using support vector machine," *Elsevier Expert Systems with Applications*, vol. 37, pp. 2182-2185, 2010.
- [11] S. Kara and F. Dirgenali, "A system to diagnose atherosclerosis via wavelet transforms, principal component analysis and artificial neural networks," *Elsevier Expert Systems with Applications*, vol. 32, pp. 632-640, 2007.
- [12] A. E. Johnson, J. T. Pollard, L. Shen, H. L.-W. Lehman, M. Feng, M. Ghassemi, B. Moody, P. Szolovits, L. A. Celi and R. G. Mark, "MIMIC-III, a freely accessible critical care database," *Scientific Data*, 2016.
- [13] A. Goldberger, L. Amaral, L. Glass, J. Hausdorff, P. Ivanov, R. Mark, J. Mietus, G. Moody, C. Peng and H. Stanley, "PhysioBank, PhysioToolkit, and PhysioNet: Components of a New Research Resource for Complex Physiologic Signals," *Circulation* 101(23):e215-e220, 2000.
- [14] J.-L. Vincent, N. D. Nielsen, N. I. Shapiro, M. E. Gerbasi, A. Grossman, R. Doroff, F. Zeng, P. J. Young and J. A. Russell, "Mean arterial pressure and mortality in patients with distributive shock: a retrospective analysis of the MIMIC-III database," *Annals of Intensive Care*, vol. 8, no. 107, 2018.
- [15] I. H. Witten and E. Frank, *Data Mining: Practical Machine Learning Tools and Techniques*, 2005: Elsevier Science.
- [16] P. D. Tyler, H. Du, M. Feng, R. Bai, Z. Xu, G. L. Horowitz, D. J. Stone and L. A. Celi, "Assessment of Intensive Care Unit Laboratory Values That Differ From Reference Ranges and Association With Patient Mortality and Length of Stay," *JAMA Network Open*, vol. 1, no. 7, 2018.
- [17] L. Lebart, "Which Bootstrap for Principal Axes Methods?," in *Selected Contributions in Data Analysis and Classification. Studies in Classification, Data Analysis, and Knowledge Organization*, Springer, Berlin, Heidelberg, 2007, pp. 581-588.
- [18] H. Ogasawara, "Asymptotic biases of the unrotated/rotated solutions in principal component analysis," *British Journal of Mathematical and Statistical Psychology*, vol. 57, p. 353-376, 2004.
- [19] M. Linting, B. van Os and J. J. Meulman, "Statistical Significance of the Contribution of Variables to the PCA Solution: An Alternative Permutation Strategy," *Psychometrika*, vol. 76, no. 3, pp. 440-460, 2011.

## BIOGRAPHIES



**Mohammed Abebe YIMER**, Born on June 1, 1985 at a city called Ukie estate farm, East Wollega, Oromia, Ethiopia. He completed his elementary school at Ukie elementary school, high school at Nekemte Derge Senior Secondary school and his preparatory education at Nekemte Comprehensive high school. Graduated with B.Sc. Degree in Computer Science and Information Technology from Arba Minch University and with MSc Degree in Computer Science from Addis Ababa University.

He has been employed and working as a lectures at Arba Minch University, Ethiopia since 2007. Currently he is pursuing his PhD in Computer Engineering at Dokuz Eylül University, Izmir-Turkey. His research interest include natural language processing, artificial intelligence, machine learning, deep learning, and data analytics.



**Özlem Aktaş** received the B.S. degree in 2003, M.Sc. degree in 2005 and Ph.D degree in 2010 from Computer Engineering Department of Dokuz Eylül University (DEU), Izmir, Turkey. She worked as a Computer Engineer in Gonen Information Technologies in 2003, worked as a Research Assistant from 2004-2009, and she has been working as Assistant Professor since 2010 in Dokuz Eylül University Department of Computer Engineering. Her research interests include natural language processing, artificial intelligence, machine learning and software engineering. She has many papers in journals and conferences in these interest areas since 2003.



**Süleyman Sevinç** obtained his BSc Degree from Istanbul Technical University in 1983. He completed his MSc and PhD degree from University of Arizona, USA between 1986 -1988. He has been serving in multiple universities as an academician both in Turkey and Australia on different levels and capacity. He has been working in Sydney University, Celal Bayar University, Halic University and Dokuz Eylül University as a professor. Moreover, he has been appointed and has been serving as Industry 4.0 coordinator of Dokuz Eylül University between the years 2017-2019. Currently, he is serving at Labenko Bilişim A.Ş. Izmir-Turkey both as a co-founder and CEO. Prof. Sevinç has numerous articles published in different international and reputable journals and has multiple citations. His main focus and interest is automation of medical laboratories, hospital laboratory information systems, robotics, and the application of artificial intelligence in medical laboratories.



**Oktay Şişman** is a Clinical Biochemistry specialist with 20 years of experience; He is a lecturer in the department of medical biochemistry of Dokuz Eylül University Faculty of Medicine. Dr. Şişman has 69 articles and 860 citations in WEB of Science, with an H index of 18. His main focus is quality management in medical laboratories, training of medical laboratory residents, laboratory automation, laboratory information systems, and artificial intelligence in medical laboratories. His publications, projects and other academic activities can be accessed from the official website of Dokuz Eylül University: <http://debis.deu.edu.tr/akademik/index.php?cat=3&akod=19990661>



**Oktay YILDIRIM**, completed his high school study at Adnan Menderes Anadolu High School. Graduated with B.Sc. Degree in Computer Engineering from Dokuz Eylul University and with MSc Degree in Computer Science from Ege University. He is a Computer Engineer with vast experience. He has developed

and contributed many projects as developer, team leader and project manager. In addition, He is also the Co-founder and Project Technical Manager at Labenko Bilisim Inc., Izmir-Turkey. Currently he is pursuing his PhD in Computer Engineering at Dokuz Eylül University.



**Eminullah YAŞAR**, completed his high school at Anadolu High School in 2008. Graduated both with B.Sc. Degree and with MSc Degree in Computer Engineering from Dokuz Eylül University. He is a Computer Engineer with vast entrepreneur experience. Skills and interests include artificial intelligence,

analytical thinking and creative problem solving. He has developed and contributed many projects as developer, team leader and project manager. In addition, He is also the Co-founder, Artificial Intelligence-Robotic System Developer and Robotic Team Leader at Labenko Bilisim Inc., Izmir-Turkey. Currently pursuing his PhD study since 2020 at Izmir Institute of Technology with the motto that "Brains that don't lose their eagerness to learn can achieve great things".

# A Proposed Ensemble Model for The Prediction of Coronavirus Anxiety Scale of Migrant Workers

Emek Guldogan

**Abstract**—This study aimed to evaluate the potential negative effects of the scattered migrant worker population on the anxiety level by estimating the coronavirus anxiety scale (CAS) of the COVID-19 anxiety scale with Gradient Boosting Tree (GBT). In this study, a public data set achieved from a questionnaire [developed using the Coronavirus Anxiety Scale (CAS)] was used to conduct on 1350 people over phone calls. GBT model was constructed for predicting the CAS score of migrant workers based on input variables including demographical data. Hyperparameters of the GBT model were tuned using Optimize Parameters (Evolutionary) operator, which seeks the optimum values of the selected parameters by an evolutionary computation approach. Hyperparameters of the GBT model were 50 for the number of trees, 5 for minimal depth, 0.044 for learning rate, and  $1.0E-5$  for minimum split improvement. A total of 1500 people, 758 (56.1%) male, and 592 (43.9%) female, participated in this study. The experimental findings demonstrated that the GBT yielded a root mean square error of  $3.547 \pm 0.235$ , the absolute error of  $2.943 \pm 0.154$ , relative error lenient of  $31.54\% \pm 0.82\%$ , squared error of  $12.623 \pm 1.691$  and correlation of  $0.577 \pm 0.130$ . Variable importance values for each input were calculated from the model-based results of the GBT model. The largest importance was achieved for income and the lowest was estimated for Covid-19 Infection. The calculated importances can be evaluated the potential impacts on the CAS score. In future works, different algorithms can be built for detailed predictions about COVID-19-related anxiety levels

**Index Terms**— Coronavirus anxiety scale, COVID-19, gradient boosting tree, regression task.

## I. INTRODUCTION

AT THE end of December 2019, a novel coronavirus was identified as the cause of pneumonia cases in Wuhan, China. The disease was later named COVID-19 (coronavirus disease 2019) and the causative agent was designated as SARS-CoV-2 (severe acute respiratory syndrome coronavirus 2). The number of cases significantly increased within a short period and the disease has spread worldwide. COVID-19, which was declared as a global epidemic by WHO on March

11 due to its spread and the severity of the clinic, is the newest infection table caused by coronaviruses in humans [1, 2]. Fever, cough, and fatigue are the most common symptoms at the onset of COVID-19, but other symptoms include headache, hemoptysis, diarrhea, dyspnea, and lymphopenia [3]. The symptom list is expanding day by day. In more severe cases, causes pneumonia, Acute Respiratory Distress Syndrome (ARDS), multiple organ failure, and death [4].

With the COVID-19 pandemic first seen in China and then spread all over the world, humanity has perhaps entered a unique process in history. Education, commercial and social activities have been suspended almost all over the world. Restrictions on transportation, social isolation, quarantine measures and curfews have become a routine of life, and the concept of "new normal" has been introduced. Recent studies on the psychological and social effects of COVID-19 caused by the new coronavirus have also revealed that this disease causes radical changes in the vital conditions of many societies and is associated with negative psychological outcomes. As a result of all these, mental problems have emerged in society, especially anxiety disorders, depression, and post-traumatic stress disorder [5-7].

Methods that enable inference from data stacks and generation of information are included in the data mining discipline. Briefly, data mining is defined as the process of generating information by discovering patterns in data [8]. Data mining includes a combination of techniques from different disciplines such as database technology, statistics, machine learning, pattern recognition, neural networks, data visualization, and spatial data analysis [9].

Machine learning, one of these techniques, is a subfield of artificial intelligence that aims to make predictions about new data when they are exposed to new data by performing data-based learning [10]. Machine learning includes the design and development processes of algorithms that aim to perform data-based learning. The model created with the existing data set and the algorithm used is set up to give the highest performance. For this reason, many machine learning methods have been developed. Some of these approaches are capable of estimation and prediction (regression), some of them are clustering and some of them are capable of classification [11].

This study aimed to evaluate the potential negative effects of the scattered migrant worker population on the anxiety level by estimating the scores of the COVID-19 anxiety scale with the Gradient Boosting Tree (GBT).

EMEK GÜLDOĞAN, is with Department of Biostatistics and Medical Informatics, Faculty of Medicine, İnönü University, Malatya, Turkey, (e-mail: [emek.guldogan@inonu.edu.tr](mailto:emek.guldogan@inonu.edu.tr)).

 <https://orcid.org/0000-0002-5436-8164>

Manuscript received March 9, 2021; accepted April 27, 2021.

DOI: [10.17694/bajece.893672](https://doi.org/10.17694/bajece.893672)

## II. MATERIAL AND METHOD

### A. Public Dataset

The public dataset was received from the related website [12]. The data was constructed with the assistance of a questionnaire developed by employing the Corona Virus Anxiety Scale (CAS). Out of 1350 valid responses elicited through the telephone interview, we have established this knowledge. The data, which is considered to be the peak pandemic period, were collected from June to August 2020. We conclude that the time was critical because it was marked by the unstable environment with badly affected job markets and the government's fear of reintroducing travel restrictions on workers. The knowledge thus provides the interested researchers with insights and guidance to carry out our relevant studies on the mental health of disadvantaged groups such as migrant workers. The data will also encourage researchers and academics to examine the effect on the mental health of vulnerable groups of such pandemics and unpredictable events. This knowledge will allow the investigator to consider the potential adverse effects of the scattered population of migrant workers on the level of anxiety.

Age, gender, marital status, education, income, and Covid-19 infected or not status included in the relevant dataset were predictor variables and the output/target feature was CAS score.

### B. The Coronavirus Anxiety Scale (CAS)

The risk of COVID-19 for migrant workers led to concerns with their mental health. The aim of public data collection, with a focus on migrant workers as the subject of the investigation, is to improve the users' awareness of the data on the effect of the pandemic on the mental health issues of internal migrant workers. Our research explores the psychological problems faced by migrant workers and the stress they encountered during the pandemic using the Corona Virus Anxiety Scale (CAS), which Lee originally developed in 2019. The scale uses four cognitive, mental, behavioral, and psychological aspects [13].

### C. Gradient Boosted Tree (GBT)

GBT is a very effective and accurate machine learning algorithm. In many machine learning tasks, GBT achieves state-of-the-art efficiency, such as multi-class classification, click prediction, and learning to rank [14]. With the advent of big data (in terms of both the number of features and the number of instances) in recent years, GBT faces new challenges, especially in the trade-off between precision and performance. To estimate the information gain of all the possible split points, traditional GBT implementations need to search all data instances for each element. Therefore, both the number of features and the number of instances would be proportional to their computational complexity. When managing big data, this makes these implementations very time-consuming [15].

In the current study, the GBT model was constructed for predicting the CAS score of migrant workers based on input variables described earlier. Hyperparameters of the GBT model were tuned using Optimize Parameters (Evolutionary

operator, which seeks the optimum values of the selected parameters by an evolutionary computation approach [16]. Hyperparameters of the GBT model were 50 for the number of trees, 5 for minimal depth, 0.044 for learning rate, and  $1.0E-5$  for minimum split improvement.

### D. Validation the Model

The GBT model was trained via the validation technique of bootstrapping. After bootstrapping a sample of training data set to estimate the statistical performance of a learning model, the bootstrapping validation operator performs validation and is primarily used to estimate how accurately a model can perform in reality. Performance metrics employed in this study were given below.

### E. Performance Evaluation Criteria

Performance evaluation for the related models was assessed using root mean square error, absolute error, relative error lenient, squared error, and correlation. The elaborate results of the relevant formulas are described in the connected studies [17, 18].

## III. RESULTS

A total of 1500 people, 758 (56.1%) male, and 592 (43.9%) female, participated in this study. The number of those up to the age of 30 was 728 (53.9%), 345 (25.6%) of those aged 31-40, and 277 (20.5%) of those aged 41 and over. Singles are 823 (61.0), partners are 527 (39.0). 786 (58.2%) people did not receive a formal education, 446 (33.0) people dropped out and 118 (8.7%) people finished school. Those with income up to Rs 15000 are 415 (30.7%), those between Rs 15001-20000 are 877 (65.0%), and 58 (4.3%) are more than Rs 20000. The number of those with negative COVID-19 test is 1020 (75.6%), the number of positive ones is 330 (24.4%).

Table 1 summarizes the baseline characteristics of the subjects enrolled in the current study. The highest CAS score among the age categories was 31-40 years old [8.82+4.21 (8.37-9.26)], which was not significantly from the other age classes ( $p=0.145$ ). CAS score for females enrolled in the study was significantly higher than that for males ( $p<0.0001$ ). Similarly, median CAS scores were statistically significant between the categories of marital status and COVID-19 infection, and among the classes of income ( $p<0.05$ ). However, the relevant scores were not significantly different among the education categories ( $p=0.694$ ).

The importance levels of the variables concerning CAS score were presented in Table 2. The largest importance level (0.175) was calculated for income and the lowest level (0.004) was estimated for Covid-19 Infection.

Evaluation metrics for the proposed model were summarized in Table 3. GBT yielded a root mean square error of  $3.547\pm 0.235$ , the absolute error of  $2.943\pm 0.154$ , relative error lenient of  $31.54\%\pm 0.82\%$ , squared error of  $12.623\pm 1.691$  and correlation of  $0.577\pm 0.130$ . The other metrics were presented in the related table.

TABLE I  
BASELINE CHARACTERISTICS OF THE SUBJECTS ENROLLED IN THE CURRENT STUDY

Variable	Variable Categories	n	%	CAS Score [Mean ± S.D. (95% C.I. Median-(Min-Max)]	p
Age	Up to 30 Years old	728	53,9	8.33+4.4 (8.01-8.65)	0.145*
	31-40 Years old	345	25,6	8.82+4.21 (8.37-9.26)	
	41 and Above	277	20,5	8.72+4.04 (8.24-9.2)	
Gender	Male	758	56,1	8.11+4.54 (7.79-8.44)	<0.0001**
	Female	592	43,9	9.08+3.86 (8.76-9.39)	
Marital Status	Single	823	61,0	9.11+4.22 (8.82-9.4)	<0.0001**
	Partnered	527	39,0	7.64+4.23 (7.28-8)	
Education	No formal education	786	58,2	8.54+4.23 (8.24-8.83)	0.694*
	School drop outs	446	33,0	8.61+4.36 (8.2-9.02)	
	School completed	118	8,7	8.23+4.35 (7.44-9.02)	
Income	Up to Rs.15000	415	30,7	7.43+4.22 (7.02-7.84)	<0.0001*
	Rs. 15001-Rs. 20000	877	65,0	8.9+4.24 (8.62-9.18)	
	More than Rs. 20000	58	4,3	10.9+3.45 (9.99-11.8)	
COVID-19 Infection	Yes, tested positive	1020	75,6	12.39+2.6 (12.11-12.67)	<0.0001**
	No, not tested positive	330	24,4	7.29+3.97 (7.04-7.53)	

\*: Mann Whitney U Test, \*\*: Kruskal Wallis H test

TABLE II  
THE IMPORTANCE LEVELS OF THE VARIABLES FOR CAS SCORE

Variable	Importance level
Income	0.175
Marital Status	0.086
Education	0.049
Gender	0.047
Age	0.016
Covid-19 Infection	0.004

TABLE III  
EVALUATION METRICS FOR THE PROPOSED MODEL

Metrics	Value	Micro average
Root mean square error	3.547±0.235	3.553 ± 0.000
Absolute error	2.943±0.154	2.943 ± 1.990
Relative error lenient	31.54%±0.82%	31.55% ± 23.39%
Squared error	12.623±1.691	12.624 ± 14.861
Correlation	0.577±0.130	0.581

#### IV. CONCLUSIONS

The current study aimed to evaluate the potential negative effects of the scattered migrant worker population on the anxiety level by estimating the scores of the COVID-19 anxiety scale with the GBT model. In this context, this paper

has presented a new GBT model for COVID-19 CAS score under the regression task. Moreover, the GBT model is employed for both regression and classification problems during the last years. An experimental analysis was performed to predict CAS score outcome based on the demographic and COVID-19 Infection data. The experimental findings demonstrated that the GBT yielded a root mean square error of  $3.547 \pm 0.235$ , the absolute error of  $2.943 \pm 0.154$ , relative error lenient of  $31.54\% \pm 0.82\%$ , squared error of  $12.623 \pm 1.691$  and correlation of  $0.577 \pm 0.130$ . Therefore, the proposed model may be employed as an appropriate tool to predict classify CAS score concerning the COVID-19 pandemic. Additionally, variable importance values for each input were calculated from the model-based results of the GBT model. The largest importance was achieved for income and the lowest was estimated for COVID-19 Infection. The calculated importances can be evaluated the potential impacts on the CAS score. In future works, different algorithms can be built for detailed predictions about COVID-19-related anxiety levels.

#### REFERENCES

- [1] Ş. Alp and S. Ünal, "Yeni Koronavirüs (SARS-CoV-2) Kaynaklı Pandemi: Gelişmeler ve Güncel Durum," *Flora Dergisi*, vol. 25, 2020.
- [2] M. Hasöksüz, S. Kiliç, and F. Saraç, "Coronaviruses and sars-cov-2," *Turkish journal of medical sciences*, vol. 50, pp. 549-556, 2020.
- [3] W. J. Wiersinga, A. Rhodes, A. C. Cheng, S. J. Peacock, and H. C. Prescott, "Pathophysiology, transmission, diagnosis, and treatment of coronavirus disease 2019 (COVID-19): a review," *Jama*, vol. 324, pp. 782-793, 2020.
- [4] H. A. Rothan and S. N. Byrareddy, "The epidemiology and pathogenesis of coronavirus disease (COVID-19) outbreak," *Journal of autoimmunity*, p. 102433, 2020.
- [5] P. Hyland, M. Shevlin, O. McBride, J. Murphy, T. Karatzias, R. P. Bentall, et al., "Anxiety and depression in the Republic of Ireland during

- the COVID-19 pandemic," *Acta Psychiatrica Scandinavica*, vol. 142, pp. 249-256, 2020.
- [6] N. Salari, A. Hosseinian-Far, R. Jalali, A. Vaisi-Raygani, S. Rasoulpoor, M. Mohammadi, et al., "Prevalence of stress, anxiety, depression among the general population during the COVID-19 pandemic: a systematic review and meta-analysis," *Globalization and health*, vol. 16, pp. 1-11, 2020.
- [7] Y. Erdoğan, F. Koçoğlu, and C. Sevim, "COVID-19 pandemisi sürecinde anksiyete ile umutsuzluk düzeylerinin psikososyal ve demografik değişkenlere göre incelenmesi," *Klinik Psikiyatri Dergisi*, vol. 23, 2020.
- [8] I. H. Witten and E. Frank, "Data mining: practical machine learning tools and techniques with Java implementations," *Acm Sigmod Record*, vol. 31, pp. 76-77, 2002.
- [9] D. J. Hand and N. M. Adams, "Data Mining," *Wiley StatsRef: Statistics Reference Online*, pp. 1-7, 2014.
- [10] R. Polikar, "Ensemble learning," in *Ensemble machine learning*, ed: Springer, 2012, pp. 1-34.
- [11] M. Atalay and E. Çelik, "Büyük Veri Analizinde Yapay Zekâ Ve Makine Öğrenmesi Uygulamaları-Artificial Intelligence and Machine Learning Applications in Big Data Analysis," *Mehmet Akif Ersoy Üniversitesi Sosyal Bilimler Enstitüsü Dergisi*, vol. 9, pp. 155-172, 2017.
- [12] S. K. G. Naveen; Jothi, M., "Data set on Impact of COVID-19 on Mental Health of Internal Migrant Workers in India: Corona Virus Anxiety Scale (CAS) Approach," V2 ed: Mendeley Data, 2021.
- [13] R. Choudhari, "COVID 19 pandemic: mental health challenges of internal migrant workers of India," *Asian journal of psychiatry*, vol. 54, p. 102254, 2020.
- [14] G. Ke, Q. Meng, T. Finley, T. Wang, W. Chen, W. Ma, et al., "Lightgbm: A highly efficient gradient boosting decision tree," *Advances in neural information processing systems*, vol. 30, pp. 3146-3154, 2017.
- [15] C. Krauss, X. A. Do, and N. Huck, "Deep neural networks, gradient-boosted trees, random forests: Statistical arbitrage on the S&P 500," *European Journal of Operational Research*, vol. 259, pp. 689-702, 2017.
- [16] R. Studio, "Visual workflow designer for the entire analytics team," ed, 2019.
- [17] A. Niknafs, B. Sun, M. Richter, and G. Ruhe, "Predictions in Time Series with Repeated Patterns, Using Piecewise Linear Regression," *Technical Report SEDS-TR-094/2011*, University of Calgary 2011.
- [18] J. H. Chan, M. Joshi, R. Tang, and C. Yang, "Trinomial or binomial: Accelerating American put option price on trees," *Journal of Futures Markets*, vol. 29, pp. 826-839, 2009.

### BIOGRAPHIES



EMEK GÜLDOĞAN obtained his BSc. degree in Computer Engineering from Middle East Technical University in 2001. He received MSc. degree in biostatistics and medical informatics from the Inonu University in 2005, and Ph.D. degrees in biostatistics and medical informatics from the Inonu University in 2017. He is currently

working as an assistant professor of the Department of Biostatistics and Medical Informatics at Inonu University and as the information processing manager at Turgut Özal Medical Center. His research interests are cognitive systems, data mining, machine learning, deep learning.

# Light Pollution and Smart Outdoor Lighting

Zehra Karagoz Kucuk and Nazmi Ekren

**Abstract**—With the developing technology and increasing urbanization, many problems have started to arise in the use of energy resources and nature. In addition to environmental effects, energy-saving considerations constitute the main purpose of any proposed smart system. In outdoor lighting, along with the use of energy-efficient bulbs, the lighting should be done with the right method and the right way. In addition to these, an intelligent system integrated with an automatic control mechanism is needed. Incorrect outdoor lighting causes unnecessary energy consumption as well as light pollution and CO<sub>2</sub> emission. These situations have negative consequences on both mental and physical health of the human, as well as on other living creatures and nature. Therefore, smart outdoor lighting systems offer an essential solution in preventing negative consequences that may occur with incorrect outdoor lighting. In this study, outdoor lighting requirements, light pollution and smart cities are examined in detail and the smart outdoor lighting systems within the scope of the smart cities are emphasized. As a result, the importance and necessity of the smart outdoor lighting system which provides energy-efficient and environmentally friendly structures by enabling street lamps to work smartly and efficiently are outlined.

**Index Terms**—Smart cities, lighting pollution, outdoor lighting, smart outdoor lighting, energy saving, dark sky

## I. INTRODUCTION

CITIES ARE unquestionably not only the cause but also the answer to society's sustainability problems. Urbanization is the interaction between the physical growth and socio-economic development of a city that consumes a significant amount of energy and resources. The driving forces underlying urban expansion can be listed as: population, economy, demands and needs, etc. Knowing these forces facilitates academic research as well as guides in policy drafting and practical city management. Researchers need some data to map urbanization and examine driving socio-economic variables in cities. To address this need, they have to make use of innovative remotely sensed datasets such as nighttime lights data (NTL) [1]. To understand urbanization,

that is, the ongoing movement of people into urban environments; It is critical to obtain essential, reliable and consistent data. After the 1970s, data such as remote sensing satellite images, data received via sensors, etc. have become alternative data sources for monitoring urbanization in a more repeatable and broad manner. These data sources are more affluent sources of information than traditional measurement data [2]. In this context, reliable data sources are needed to determine the extent of urbanization and to meet demands and provide appropriate solutions.

Lighting has become an essential factor in making cities suitable for livable spaces to live in all comfort conditions [3]. Proper lighting is crucial in economic, environmental and social aspects. In European Union countries, lighting requirements for frequently used outdoor work areas are regulated according to the standards. However, since the lighting of natural and architectural objects is not standardized, recommendations have been made in technical reports such as the Commission Internationale de l'Eclairage (CIE) report [4]. Excessive or improper lighting causes adverse effects on the environment and the living conditions. This situation has brought light pollution, which is defined as an unwanted skylight, into question due to population growth and increasing outdoor lighting per person. Astronomers and researchers in this century have had to struggle with light pollution [5].

The smart city concept has brought up many technological and scientific problems, including light pollution. Light pollution, which occurs as a direct result of incorrect external lighting, has various negative effects on the economy, ecology and health [6]. Light pollution has a large number of negative effects on individuals, ecosystems, astronomy and energy consumption, just as it is caused by sound, garbage and chemical products. All this occurs as a result of human activities. Some examples of these negative effects are; hormonal disruption, sleep disturbance, cancer, unsafe driving, etc. Also, light pollution has negative effects on some plants and animals [7, 8, 9]. Dealing with such problems is also included within the scope of smart cities.

In 2017, a report called 'CITYkeys' was prepared within the scope of EU projects, which includes determining factors for smart cities. With this report, smart city and smart city projects were defined and Key Performance Indicators were selected for the goals of transforming into smart cities. The main themes of the indicators are as follows; propagation, planet, governance, prosperity and people. And these are determined in line with the needs of smart cities. CITYkeys ultimate goal is to support the acceleration of large-scale deployment of smart city solutions and services to impact the significant societal challenges of urbanization [10]. Key

**ZEHRA KARAGOZ KUCUK**, is with Department of Electrical, Vocational School, University of Dogus, Istanbul, Turkey, (e-mail: [zkaragoz@dogus.edu.tr](mailto:zkaragoz@dogus.edu.tr)).  <https://orcid.org/0000-0002-7578-153X>

**NAZMI EKREN**, is with Department of Electrical and Electronics Engineering, University of Marmara, Istanbul, Turkey, (e-mail: [nazmiEkren@marmara.edu.tr](mailto:nazmiEkren@marmara.edu.tr)).  <https://orcid.org/0000-0003-3530-9262>

Manuscript received February 4, 2021; accepted April 27, 2021.  
DOI: [10.17694/bajece.874343](https://doi.org/10.17694/bajece.874343)

indicators in this report and the report itself are important guides in the process of transformation into smart cities.

New generations will have significant losses that we have yet to anticipate in a world that is rapidly losing its darkness. Some of these losses have been scientifically revealed and the threat can now be seen more clearly [11]. It is seen that the most logical solution in the effective struggle against light pollution, in meeting the data requirements needed with the increase of urbanization and in data management, is to design smart cities. As a result; It has become crucial and necessary to design smart systems and transform them into smart cities by benefiting from the blessings of developing science and technology to meet the demand of the increasing urban population, to contribute to the environment and economy, to facilitate research and studies in many specific areas (such as providing the dark skies needed by astronomers).

#### A. Smart Cities

The word "smart" refers to an automated mechanism adopted to perform the desired activity in space [12]. For example, in the smart kitchen of a smart home, the materials in the kitchen can be controlled remotely/closely accessed, intervention in unusual situations occurring in the kitchen, and comfort can be increased in line with human needs with smart systems, and energy, time savings can be achieved [13]. Similarly, smart cities should meet daily, environmental, security, economic, commercial, social, health needs. It must be able to respond to their needs intelligently. Cities play an important role socially and economically around the world and have a significant impact on the environment. The concept of a smart city has become very popular in international politics and scientific literature in the last 25 years [14]. The concept of "smart city" that emerged in the late 90s includes the integration of all information and communication technologies to manage the urban system effectively [15]. "Smart city" is defined by IBM as "using information and communication technology to perceive, analyze and integrate basic information of basic systems in working cities" [16, 17]. The smart city can also be defined as a city ecosystem that uses connected technologies to improve daily city activities and to make near-real-time smart decisions [18].

The concept of a smart city has many definitions and interpretations in the literature. The definitions made by some researchers in their studies are as follows: The smart city is defined by the capacity to combine people, technological innovations and data to develop a flexible, sustainable and robust infrastructure that provides first-class governance to its residents. Transforming an urban city into a smart city requires community-focused efforts among administration, industry, experts, citizens and researchers [19].; Smart city platforms are ecosystems where governments can provide their services using the transformative power of technologies, but at the same time enable citizens to participate in a democratic dialogue and co-creation of values [20]. The smart city is a paradigm for managing the challenge of urban life, increasing spending, reducing expenses and enhancing the value of the daily life of its residents. It has become extremely critical to discover innovative solutions present to make cities smarter and more efficient. In this context, countries all over

the world adapt to smart cities [21].; The smart city emphasizes the local management's ability to cooperate with other organizations (IT companies, local communities, local business environment) to improve and adapt better policies that are to maximize the benefits of a strategic partnership [22].; It can be said that a smart city is an effective integration of smart planning ideas, smart management methods and smart development approach [17].; According to Zlámál, in recent years, there has been increased attention on the quality of life in connection with the concept of "smart city", which has become the subject of worldwide debate. The concept of "smart city" uses modern technology to streamline governance, innovate local sustainable development approaches, and more. It offers a wide range of individual freedom of application while paying attention to the environment [23].

According to the United Nations, 55% of people worldwide today live in cities, and this increase is estimated to be 68% by 2050 [24]. In this case, it is anticipated that many problems will arise in the management of these cities and in providing a reasonable quality of life for their citizens. A suitable solution for these challenges; to transform traditional cities into smart cities [25, 26]. Also, the international data company (IDC) estimates that spending on smart cities globally will rise to \$ 158 billion by 2022 (doubling from \$ 80 billion in 2018) [27]. Therefore, it is important to take into account economic possibilities when implementing smart city strategies [28]. The transition to smart systems is significant in economic, social and environmental aspects in today's world, which is globalizing and living in the "industry 4.0" era. Sustainable development has become increasingly dependent on the best management of urban growth as urbanization continues (mostly in low and middle-income countries where urbanization is expected to be the fastest) [29]. Due to such rapid urban population growth worldwide, the concept of smart cities needs to be understood more deeply to provide livable conditions [25]. Increasing urbanization impairs the ability of cities to create a livable environment for their citizens. In addition to the population growth of cities, daily commutes to and from workplaces are also increasing. This increases the pressure on the existing infrastructure and causes both discomfort and economic losses [30].

Many smart city attempts are currently underway around the world, and this tendency is expected to increase in the coming years. Such attempts should be tailored to the needs and circumstances of each government to expand or create public value for stakeholders [31]. When designing smart cities, whether technologies make the city smart; whether the city is energy efficient, automatic and environmentally friendly; It is important to ask questions about whether citizens can access justice, safety, jobs, education and culture [28]. The basic idea is to transform every asset of a traditional city into an autonomous object that automatically carries out its activity using modern technologies, without significant outside assistance. The basic assets of a smart city; smart infrastructure, smart management, smart policies, smart health services, smart transportation, smart agriculture, smart education, smart economy, smart environment, smart industry, smart energy, smart security, smart communication, smart

outdoor lighting etc.[12]. The smart economy focuses mostly on competitiveness, the ability to adapt to changes, and flexibility. Smart mobility refers to sustainable, safe and innovative transport systems. Smart people focus on human capital and citizens' participation in public life. The smart environment preserves natural resources. Smart living often contributes to improving the quality of life in the city, from housing to culture. Smart governance is mostly linked to transparency [32].

The integration of the city and its citizens' systems is considered at the centre of the essence of smart cities. Smart cities often try to digitally connect and integrate services in a city to provide efficient services by better anticipating demand and reducing waste and pollution. All of these aim to make smart cities sustainable while improving the functions of cities through digitalization [33]. It is crucial to look at critical factors such as sustainability, ecosystems and digital citizens to achieve the main goals of improving the quality of life of smart cities, providing efficient and optimum services, and thus making the operation of the city smart through digitalization [34]. Technological interventions in daily processes have led to the rise of manageable and accessible smart ecosystems. These ecosystems; governance, transport, agriculture, logistics, maintenance, training and all aspects of everyday life such as health services and automated ways with the help of smart devices to ensure that they can be controlled remotely. Sensors and trainers embedded in smart appliances that sense the environment to facilitate proper decision making are located at the basis of the smart cities [12]. Minimal energy-consuming sensors, wifi networks, digital supervision, automatic data stream processing and utility management systems are just a few examples of digitization and opportunities for smart cities [22]. The smart city is mainly focused on applying next-generation information technologies, sensors and equipment to all walks of life, such as power grids, bridges, buildings, tunnels, hospitals, railways, roads, water systems, oil, dams and gas pipelines and other objects around the world [17]. The smart city includes several electronic objects that interact and communicate through wired and wireless networks, as well as deploying smart platforms and running related services efficiently [35]. A wide variety of electronic sensors are used to efficiently manage assets and resources and collect data. Smart cities have different approaches for analyzing, making decisions, collecting data from devices, citizens and entities used to control transportation systems, power plants, traffic, water supply networks, law enforcement, information systems and others [36, 37]. Subjects such as augmented and virtual reality, big data analysis and discovery, broadband, cognitive/artificial intelligence, internet of things (IoT), real-time, cloud, mobile are topics adopted by cities in the journey of creating smart digital reality [38].

A smart city is a smart and interconnected city that aims to improve the quality of life of its people using information and communication technology (ICT). However, internal linkages make it highly vulnerable to security attacks [39]. Cybersecurity threats are a major obstacle to the realization of the benefits of smart city applications. Because many smart city applications are networked implementations, they can be

attacked to potential cyberattacks same as other network applications [26]. Effective analysis is required to identify these attacks and prevent them all together quickly, or at least reduce the associated risks and impacts. Therefore, it is essential to build a solid architecture that not only provides smart city services but also addresses security issues [39].

Another point of view for smart cities is the concept of slow and smart cities called 'Cittaslow' (slow city). Cittaslow is a non-profit association founded in Orvieto (Italy) on 15 October 1999 bringing the mayors of small and medium-sized towns together. Since then, it has become a worldwide city network. The idea of Cittaslow first arose in the late nineties by adopting the original idea of Paolo Saturnini, then mayor of Greve in Chianti in Italy, focusing on the positive side of slowness, sustainability and social justice. Inputting this idea forward, Paolo Saturnini was inspired by Carlo Petrini, founder of the international slow food movement, and his slow food experiences. The main purpose of the Cittaslow movement is to preserve the spirit of the community and at the same time pass knowledge to new generations to make them aware of their cultural heritage. In addition to this, it is to ensure sustainable development by considering social and environmental interests. Their motto is "There's no Smart without Slow", so if there is no slowness, there is no cleverness. To become a Cittaslow settlement or city, that location must go through a specific certification process. Certification of the settlement is associated with 72 quality requirements divided into 7 macro areas. These 7 macro areas are:

- Energy and environmental policies
- Infrastructure policies
- Quality of urban life policies
- Agriculture, tourism and tradesman policies
- Policies for hospitality, awareness and education
- Social solidarity
- Partnerships

Some of these requirements are mandatory and some are optional criteria. The 10th sub-heading of energy and environmental policies is the "reduction of public light pollution" criterion and is one of the mandatory criteria [40]. Bosch P. et al. prepared a report called 'CITYkeys' within the scope of the EU project to evaluate smart city projects in 2017. This report describes the choice of indicators for evaluating smart city projects and the matching indicators at the city level. Thanks to the report, the non-project situation can be compared with the situation after the application of the project, and the difference created by the project can be identified, thus enabling the comparison of projects with each other. Starting with the definition of smart city and smart city projects, indicators that can function as Key Performance Indicators to monitor the progress towards city and project goals have been selected. The indicators are focused on tracking a city's evolution towards a smarter city. Indicators, taking into account the wishes of the cities and citizens; It is organized within an extended sustainability framework that includes the themes of people, planet, favour, governance and diffusion. The ultimate goal of CITYkeys is to support the acceleration of large-scale deployment of smart city solutions and services to impact the major societal challenges

surrounding the continuous growth and concentration of cities. At the same time, it contributes to the realization of the 20/20/20 energy and climate targets of the European Union. (20/20/20: Energy-related targets determined by the European Union for the years 2020, 2030 and 2050). For this reason, CITYkeys aims to facilitate the exchange of information between stakeholders in projects or cities through a common

integrated performance measurement framework, to build trust in solutions, and to accelerate the transition to low-carbon and sustainable smart cities by making it easier to track progress. Table 1 shows the frame and subtitles of CITY keys indicators [10, 41].

TABLE I  
CITYkeys INDICATORS FRAMEWORK [41].

People	Planet	Prosperity	Governance	Propagation
Health	Energy and mitigation	Employment	Multi-level governance	Scalability
Safety	Materials, water and land	Equity	Organization	Replicability
Access to (other) services	Climate resilience	Green economy	Community involvement	
Education	Pollution and waste	Economic performance		
Diversity and social cohesion	Ecosystem	Attractiveness and competitiveness		
Quality of housing and the built environment		Innovation		

### B. Light Pollution

We illuminate our surroundings at night to see better, to be in a better environment, to work more easily, to feel safer, to improve visibility on roads and intersections, to make historical buildings or places that are desired to attract attention. In the trade or tourism sector, we also make lighting to make more attractive advertising and gain customers by increasing visibility. [42]. Lighting has become a necessity for meeting aesthetic needs and physiological comfort in human life [43]. Lighting is the process of providing visibility by sending light from a specific light source to an object or environment. The basis of the lighting concept is considered to be light; however, the aim of lighting is to visualize the illuminated environment with a light source [44]. Urban lighting affects both the comfort of lighting and the health of living creatures (human, animal and plants) in many dimensions [3]. The wrong selection and misdirection of the fixtures and lamps used to cause light trespass, glare, vertical light and excessive light in outdoor lighting [42].

Today, both very poor lighting applications in Turkey as well as all over the world are available and these wrong practices are becoming more common. As a result, a new type of pollution called "Light Pollution" occurs [45, 46, 47, 48]. Light pollution is the use of light in the wrong place, wrong amount, wrong direction and at the wrong time. Although it is not toxic like air pollution and water pollution, using excessive and in the wrong places means ineffective lighting; As a result, a significant portion of the energy spent to produce light is wasted [42]. Light pollution; is also expressed as the misuse of light in a way that causes energy waste, prevents astronomical observations and creates effects that spoil natural life [49]. The relationship between spatial light intensity and vision quality can be controlled with luminaires for lighting situations that are made in the wrong place, wrong amount, wrong direction and wrong time. The design of the luminaires can be intervened. Artificial lighting used outdoors

is the primary source of light pollution. Lighting should be done in the right place, in the right direction, at the right amount and at the right time. The problem is not in the lighting, but in the incorrect lighting [46]. The right lighting is the most crucial factor that will prevent light pollution and energy consumption [49].

In cases where visual health and comfort are ignored, illumination may cause discomfort, contrary to facilitation. The problem of light pollution may occur in cases such as the application of incorrect lighting fixtures in outdoor areas, incorrect adjustment of the intensity, direction and colour of the light. Systems like unnecessary store lighting, inefficient or low-intensity street lighting fixtures, illuminated billboards that abruptly change intensity and colour to attract people, etc. that do not allow homogeneous light distribution are a part of light pollution and create visual pollution both in terms of visual health and comfort and aesthetics [3, 50]. In general, sources of light pollution can be listed as follows:

- Street lighting such as roads, streets, highways, intersections, toll stations,
- Park, square and garden lightings,
- The lighting of parking lots and sports areas,
- Illumination of touristic facilities,
- Airports, ports and train stations lightings,
- Exterior lighting of buildings,
- Advertising boards,
- Lights overflowing from houses and buildings,
- Security lighting etc.

An important part of the studies on light pollution is to measure how heterogeneous spatial light distribution is related to the lighting system. Light pollution is mainly studied for the characterization of sky glow and the identification of street lamps. This process is done in fields such as astronomy using digital cameras, solar cells, Sky Quality Measurement (SQM) sensors or other remote sensing sensors. Satellite images, the visual equivalent of information perceived by a sensor, can be

used to provide information about artificial nighttime radiation. Due to artificial night radiation, the impact area of atmospheric pollution increases [51, 52, 6]. Urban studies should include a strong foundation of analysis that allows for an interdisciplinary diagnosis to describe the various conditions of urban settlements [53].

One of the fastest-growing types of environmental degradation is light pollution. Pollution levels above natural nighttime lighting levels provided by moonlight and starlight are increasing exponentially. Several effective practices have been identified to limit this pollution: The use of shields on the luminaire to prevent direct upward light, especially at low angles above the horizon; avoiding excessive lighting, that is, excessive lighting; limiting the lighting to the required space and time, etc. However, even if it provides optimal control of light distribution and the appropriate amount of light is used, some light emission remains upward due to reflections and atmospheric scattering from luminous surfaces. At this point, the effect of "residual light pollution" on the environment is undeniable and must be limited [7]. The degree and type of light pollution can be understood depending on the actions of active individuals in society and the characteristics that transform the society into an urban system. The emission function of the pollutant source is determined by the change of these factors [51]. Dust, water vapour, and other particles scatter and reflect light emitted into the atmosphere. This results in the glow over urban areas in the sky sometimes referred to as atmospheric or astronomical light pollution [49]. Understanding night sky brightness is an important and challenging problem to solve. Light transforms atmospheric optics in a blurry environment and converts emissions. Light pollution is directly linked to optical processes in a constantly changing atmospheric environment. The emission function is qualified by the characteristics of public lighting systems that change irregularly [1].

There should be a benchmark and a standard in lighting [3]. Today, many countries are making legal regulations to limit light pollution. For this purpose, the Canary Islands, where large observatories are located, and the states of Arizona, Maine and Texas in the USA are protected by special laws. Related laws and regulations are prepared in more than sixty local governments in the USA and countries such as Canada, Belgium, Germany, France, England, New Zealand and Japan [54]. The United Nations Space Convention has defined space as "the common space of all humanity". A decision was taken at the Conference on the Use of Space for Peaceful Purposes held in Vienna in July 1999. With this decision, the member states of the United Nations are required to control the pollution of the sky by light and other reasons, both for the benefit of science, energy-saving, natural environment, night safety and comfort, and for the benefit of the national economy. In the General Assembly of the International Astronomical Union (IAU) held in Brazil in August 2009, the importance of protecting access to the uncontaminated sky for all humanity was emphasized in terms of education and culture. Also, each country was asked to preserve the astronomical quality of the areas suitable for scientific observation of the universe [55].

The photos in Figure 1 were taken by Jeff Dai in a settlement in Kaihua, China, in 2019. The change in the sky is visible when the public turns off most of the lights. While only Sirius and Betelgeuse stars are visible when the lights are on (before photo), when most of the lights are turned off (after photo) thousands of stars with the curved belt of our Milky Way galaxy are visible [56].



Fig. 1 The difference seen in the sky when the lights are on and off in the city of Kaihua [56].

In Figure 2, 6 different sky views taken from various locations throughout Slovakia are combined. The photographs were taken with the same equipment, at the same time of the night, and were subjected to the same digital post-processing. The sky is entirely dark in the dark sky (far right, in the countryside), while the stars are not visible in the city sky (far left) [57].

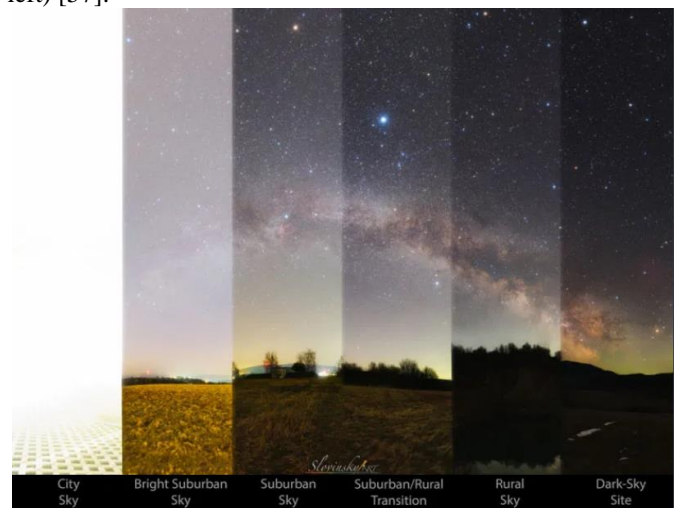


Fig. 2 Sky view in different settlements in Slovakia [57].

Figure 3 shows photographs taken in a lakeside town in the city of Monte Patria, Chile. All the lighting fixtures in the upper photo have been renewed using less few of luminaires and lower intensity. In this way, light pollution is prevented without sacrificing safety, tourism and visual comfort [58]. Few examples of light pollution are seen here, with a significant difference observed in just a small settlement. Based on this, the extent of pollution is better understood globally. As a result, what should be done to prevent light pollution?

- Informing society about light pollution,
- Developing standards for outdoor lighting and fixtures by examining the recommendations of the International Dark-Sky Association (IDA) and the International Lighting Commission (CIE) in other countries,

- Ensuring that technical specifications and regulations are adapted to developing technology [11],
- Preferring dark sky-friendly lighting,
- Building smart cities.

In this way, energy and natural resources will be saved, lighting costs will be reduced, night security will be improved, living life and nature will be protected from a negative light, and the beauty of the sky will be preserved for the next generations [11].



Fig. 3 Dark sky created by changing fixtures in Monte Patria, Chile [58].

### C. Outdoor Lighting

Outdoor lighting is done at night to meet various human needs and perform many functions. The primary classification of outdoor lighting depends on the task required, the type of outdoor area and the activities performed. In European Union countries, lighting requirements for frequently used outdoor work areas are regulated according to the standards. However, since the lighting of natural and architectural objects is not standardized, recommendations have been made in technical reports such as the International Commission on Lighting (Commission Internationale de l'Eclairage: CIE) report [4]. The primary purpose of an outdoor lighting application at night is the need for security. Lighting realization means fulfilling the lighting conditions in which visual functions can be carried out comfortably and effectively. Generally, outdoor lighting: Business and general activities; drivers and pedestrians; decoration and colouring; provided for sports activities. Requirements other than these four basic requirements are: Lighting criteria and parameters; Electrical installation requirements and their energy consumptions, control systems and safety; Simulation and verification methods; It is connected with lighting equipment and maintenance systems [59].

Outdoor lighting applications have changed significantly in recent years as functional lighting increasingly leads to a better quality of light vision. The traditional role of security lighting has evolved towards the use of lighting for urban refinement. This is now an important issue for new lighting

strategies. In this context, other development paths have been followed in lighting design. With the emergence of a more theatrical diffusion of light in contemporary culture, the use of new types of lighting to enhance the urban night experience has become increasingly common. This situation has led to a severe change in the scale, scope and policies of urban lighting strategies. Thus, it has caused an increase in the field of intervention and application in urban lighting. As a result, an increasing number of local governments have begun to see urban lighting as a potential urban development tool. Local governments are under the pressure of several different factors, such as budget cuts, technological advances and demands to mitigate climate change. Accordingly, they turn towards changes in lighting strategies to reduce their energy consumption and financial burden [60].

Today, energy efficiency plays a vital role in the design of indoor and outdoor lighting systems [61]. Nowadays, where the importance of sustainable development is progressively understood, the importance of energy efficiency studies is increasing. Worldwide, grid-based electrical lighting consumes 19% of total global electricity generation, with slightly more than is used by the Organization for European Economic Cooperation and Development (OECD) countries for all purposes [62]. The lighting of streets and buildings, on the other hand, accounts for 75% of the lighting demand for electricity. Intelligence and efficiency play an important role in making a big difference in power consumption, especially in outdoor lighting systems where a large amount of energy is wasted using traditional light bulbs. For these reasons, energy-saving is significant in street lighting systems. Now the primary trend of developing lighting products is to ensure products are energy efficient and environment friendly, and to improve the performance of manufactured products [63, 61].

One of the central focus areas for enhancing the efficiency of complicated street lighting systems is the application of automatic control systems. Everything in the world becomes smarter by being connected and can work on its own without any human interface. IoT has often been used to do this, making everything smart. Outdoor lighting systems can also save more energy than using the IoT if they are made smart enough to operate without human interaction. Modern automatic outdoor lighting systems allow the operator to manage the complete lighting system and each luminaire individually from a central console. Outdoor luminaires should be equipped with advanced electronic control equipment systems to control and handle the operation of luminaires [63, 61]. The lighting systems to be applied should be able to optimize the energy consumption of street lamps and operate the street lamps smartly and effectively to increase efficiency [61]. However, street lighting control systems do not require time-based control as with traditional feedback loops. Control algorithms in such installations are based on a schedule, taking into account information about operating parameter changes (light intensity, usage, number of working lights) provided by specific sensors [64].

Recently, there has been a growing awareness in research and policy that artificial light is not entirely harmless [60]. Accordingly, the increase in light pollution has triggered a large number of research groups to research the impact of

artificial light and especially Light Emitting Diode (LED) and colour-rich sources on sky glare [65]. Also, the emphasis has been placed not only on the quality of illumination but also on the subjective interpretation of light impressions and the adjustment of light to the human circadian rhythm [66]. In this context, human-oriented lighting applications aiming to balance the visual, emotional and biological benefits of humans have gained importance [67]. Also; CO<sub>2</sub> emissions related to global lighting (from grid-based electrical lighting, fuel-based lighting, and vehicle lighting) account for up to 70% of global emissions from passenger cars (1900Mt). Considering all these effects, it is seen once again that an intelligent outdoor lighting system is needed that is energy efficient and can minimize the disadvantages caused by available outdoor lighting control systems [62].

Limitation of light pollution and disturbing lighting can usually be evaluated at the project stage using special lighting computation software and applying varied implementation guidelines. Failure to make field measurements during the commissioning of a lighting installation or during its lifetime increases the negative effects such as excessive illumination, the possibility of light pollution and CO<sub>2</sub> emission. New technology in lighting controls and smart lighting fixtures helps guide adaptive lighting. Several studies also show that outdoor adaptive systems have the potential to reduce the effects of light pollution [65]. Luminaires, which can be dimmed depending on the movement or the ambient light level, and can dim when necessary, are one of the critical parts of smart outdoor lighting.

Light pollution is directly linked to the energy waste of an outdoor lighting installation. This situation creates the need to redefine the energy efficiency problem. It also makes sense to combine outdoor lighting problems with a sustainable development approach. Looking at the analyzed problem with a conscious approach, it is possible to reduce the negative effects of light pollution significantly. This means that thanks to these solutions, it is possible to create dark sky protection areas in selected locations around the world. Thus, artificial light has many significant effects on the environment at night. An outdoor lighting installation should be analyzed in a sophisticated way, taking into account all of the crucial factors such as spectral power distribution of luminaires or light sources. Also, other factors such as safety, environmentalism, economy and aesthetics should be considered. Therefore, there seems to be a need to implement a multi-criteria procedure based on the evaluation of the luminous environment, energy efficiency and light pollution for any outdoor lighting installation [59].

The light pollution component of outdoor lighting is produced directly by the base component. That is, it is the luminous flux that radiates directly into the upper hemisphere and does not interact with any surface. Additionally, the reflected component is the sum of the reflection of the light on the illuminated surfaces and the reflection of the light from the surfaces not intended to be illuminated [65]. To reduce the effect of this situation, it is essential to choose the right luminaire and use the right lighting method. As can be understood from the definitions of light pollution, the most important of all is to make the right lighting. Outdoor lighting

has two essential elements: light source and luminaire. Choosing the right lamp and luminaire has a vital place in combating the negative effects of outdoor lighting on humans and nature (light pollution, CO<sub>2</sub> emission, energy consumption, etc.). In addition, the lighting method that is directed only to the area or object to be illuminated and does not create negative effects such as reflection or glare, regardless of the purpose of use, is of great importance. In summary, in outdoor lighting:

- Selection of suitable elements for the purpose,
- Using the right lighting method,
- Using lamps that consume less energy while serving the same purpose,
- By using smart control and monitoring systems [62],

a useful illumination will be provided in every respect, that is, the main goal will be achieved.

## II. PREVENTION OF LIGHT POLLUTION IN SMART CITIES

Street lights used today are automatically switched on and off according to the day/night sensor or the timer. Recently, LED lamps with a variety of advantages have begun to be replaced by conventional light sources. In addition to this solution that comes to mind first, using a smart outdoor lighting system provides benefits such as reducing energy consumption due to better control of light usage, providing contextual lighting to improve public safety in critical situations or areas of interest, reducing maintenance and asset management costs thanks to data from street light sensors etc. [68].

The benefits of the smart lighting system can be listed as follows:

- To reduce energy costs,
- Save time and energy (helping the maintenance team in the field solve problems quickly),
- To reduce maintenance costs,
- To provide efficient business,
- Remote monitoring of electrical parameters,
- To eliminate the negative psychological effect of incorrect lighting,
- To reduce light pollution caused by incorrect lighting,
- Providing safe lighting,
- Lamp on-off, dimming etc. remote control of operations, remote management of fixtures,
- Fault detection can be made remotely and the fault location can be determined instantly and intervened immediately,
- To be able to monitor the lighting load on the network etc. [68, 69].

Smart outdoor lighting systems considered within the scope of smart cities in the literature generally draw attention to energy saving. However, the issue of light pollution, which is getting more serious day by day, is an issue that should be taken into consideration. One of the most important advantages of smart cities in terms of environment and ecology is to reduce light pollution and thus prevent the negative consequences of light pollution.

### III. CONCLUSION

In today's world, energy consumption is gradually increasing due to urbanization in developed and developing cities. The increasing demand has to be met, and this may cause problems in existing infrastructures and systems. Besides, some negative impacts arising from human activities cause serious damages to the environment (hence energy resources), human beings, nature and disrupt economic, social and environmental balances. Outdoor lighting, which is one of the requirements of cities, has a significant share in energy consumption. If outdoor lighting is not made correctly, energy consumption increases and the environment is harmed by causing light pollution. Besides, incorrect outdoor lighting affects the health and quality of life of humans and other living creatures.

In changing conditions, it is crucial to use available resources economically and to prevent negative consequences in order not to compromise human comfort and not to affect the environment negatively. When designing a system, it is not right to only consider needs. The needs should be met with the lowest cost and least negative impact, with the highest benefit. Therefore, after considering all the conditions of the system to be designed, it should be designed following the purpose. At this point, smart systems come to mind. Outdoor lighting is one of the basic needs of people in particular and cities in general. Therefore, all conditions should be taken into consideration while meeting this need. In this direction, to prevent negative consequences while making outdoor lighting, there is a need for smart systems that will reduce energy consumption and avoid light pollution by ensuring the correct outdoor lighting. A smart outdoor lighting system includes a luminaire and network system with very low energy consumption and uses correct ways that do not cause light pollution. Considering that the share of outdoor lighting in the grid is approximately 14.75%, the savings to be made in this area have a significant contribution to energy production. Besides, when the dark sky deprivation caused by light pollution is eliminated with correct and smart outdoor lighting, people, the environment and scientific studies will be contributed.

In this study, the demands arising from urbanization, outdoor lighting requirements, and light pollution are mentioned and transforming into smart cities is proposed as a solution. Various studies, reports and projects in the literature have shown that smart cities have become a necessity in our age. In fact, smart cities mean that everything necessary to meet human needs is done correctly. Smart cities mean that doing everything right to meet human needs. Developing technology has made smart systems very useful, accessible and sustainable. Therefore, smart cities have the potential to offer a more livable and sustainable world to people and other living creatures by taking advantage of technological opportunities. Thanks to these possibilities, it has become easier to build smart outdoor lighting systems within the scope of smart cities in residential areas (especially in places where urbanization is high). Considering the long-term benefits of smart outdoor lighting, the necessity of these systems is an undeniable fact. Smart outdoor lighting ensures that the necessary things to meet the requirements are done correctly and negative effects (unnecessary energy consumption, light

pollution, security negligence, etc.) are eliminated. As a result; in a world where energy resources are diminishing, the sky is losing its brightness and the balance of living life is gradually deteriorating, something needs to be done to prevent negative conditions. It is a fact that human makes his living conditions difficult with his hand, but also harms nature seriously. While taking the advantage of the natural and artificial possibilities in the world, humans have to look out for the lowest damage with the highest benefit. In this context, we can say that it is both logical and very necessary to design a smart outdoor lighting system for outdoor lighting requirements.

### REFERENCES

- [1] Y. Lu and N. C. Coops, "Bright lights, big city: Causal effects of population and GDP on urban brightness.", *PLoS ONE*, 13(7). <https://doi.org/10.1371/journal.pone.0199545>, 2018.
- [2] A. Schneider, M. A. Friedl and D. Potere, "A new map of global urban extent from MODIS satellite data.", *Environmental Research Letters*, 4(4). <https://doi.org/10.1088/1748-9326/4/4/044003>, 2009.
- [3] E. Korkmazer, Y. Bektas, M. Aykanat, S. Jevdazade, and Y. Caymaz, G. F., "Study of Light Pollution in Urban Lighting in Nisantasi Example.", *Journal of Contemporary Urban Affairs*, 3(2), 8-15. <https://doi.org/10.25034/ijcua.2018.4696>, 2019.
- [4] Technical Report of Commission Internationale de l'Eclairage CIE 094 Guide for Floodlighting; CIE: Vienna, Austria, 1993.
- [5] K. W. Riegel, "Light Pollution: Outdoor lighting is a growing threat to astronomy.", *Science (New York, N.Y.)*, 179(4080), 1285-1291. <https://doi.org/10.1126/science.179.4080.1285>, 1973.
- [6] D. Ziou and F. Kerouh, "Estimation of light source colours for light pollution assessment.", *Environmental Pollution*, 236, 844-849. doi:10.1016/j.envpol.2018.02.022, 2018.
- [7] F. Falchi, P. Cinzano, C.D. Elvidge, D.M. Keith, A. Haim, "Limiting the impact of light pollution on human health, environment and stellar visibility.", *Journal of Environmental Management*. 2011;92(10):2714-2722. doi:10.1016/j.jenvman.2011.06.029, 2011.
- [8] E. Uygun and S. Görgülü. "Investigation of Home Type Heliostat Systems Daylighting Performance With Lighting Simulation Method." *European Journal of Technique (EJT)* 11.1: 7-12.
- [9] International Dark Sky Association, 2010. Visibility, Environmental, and Astronomical Issues Associated with Blue Rich White Outdoor Lighting. Technical Report.
- [10] P. Bosch, S. Jongeneel, V. Rovers, H. M. Neumann, M. Airaksinen and A. Huovila, "CITYkeys indicators for smart city projects and smart cities." Technical Report, DOI: 10.13140/RG.2.2.17148.23686, 2017.
- [11] M. S. Taner, "Işık kirliliği ölçümü için okullarda yapılabilecek deneysel bir etkinlik önerisi", *Anadolu Öğretmen Dergisi*, 3(1), 74-84. DOI: 10.35346/aod.566401, 2019.
- [12] M. A. Ahad, S. Paiva, G. Tripathi and N. Feroz, "Enabling Technologies and Sustainable Smart Cities", *Sustainable Cities and Society*, 61. <https://doi.org/10.1016/j.scs.2020.102301>, 2020.
- [13] Z. Karagöz Küçük and N. Ekren, "Akıllı Mutfak İçin Tasarlanmış Sistemler Üzerine Bir Derleme", *International Periodical of Recent Technologies in Applied Engineering*, 2 (1), 25-34. Retrieved from <https://dergipark.org.tr/en/pub/porta/issue/56304/721927>, 2020.
- [14] V. Albino, U. Berardi and R. M. Dangelico, "Smart Cities: Definitions, Dimensions, Performance, and Initiatives", *Journal of Urban Technology*, 22:1, 3-21, DOI: 10.1080/10630732.2014.942092, 2015.
- [15] D. S. Chirov and Y. A. Kochetkov, "Optimization of the Placement Topology of Spatially Distributed Receiving and Transmitting Posts for the Detection of Small UAVs in the Conditions of a "Smart City."" 2020 Systems of Signal Synchronization, Generating and Processing in Telecommunications (SYNCHROINFO). doi:10.1109/synchroinfo49631.2020.9166037, 2020.
- [16] M. A. Özçelik and M. Yılmaz. "Gün Işığı Alan Mekanda Önerilen Bölgesel Kontrollü Akıllı LED Sistem ile Flüoresan ve Normal LED Aydınlatmanın Karşılaştırılması." *El-Cezeri Journal of Science and Engineering* 6.2: 270-281.

- [17] K. Su, J. Li, and H. Fu, "Smart city and the applications", 2011 International Conference on Electronics, Communications and Control (ICECC), 2011.
- [18] South African Local Government Association (SALGA), "SMART CITIES" in.KNOW .vation, Produced by Corporate Strategy & Research office of the CEO, <http://www.cpsLco.zalwpcontentuploads/2015/05/IFINALSALGAPUBLICATIONLOWRES.pdf>, 2015.
- [19] N. Villanueva-Rosales, R. L. Cheu, A. Gates, N. Rivera, O. Mondragon, S. C. C. Ferregut, C. Carrasco, S. Nazarian, H. Taboada, V. M. Larios, L. Barbosa-Santillan, D. Prochazkova, M. Svitek, O. Pribyl and T. Horak, "A collaborative, interdisciplinary initiative for a smart cities innovation network." 2015 IEEE 1st International Smart Cities Conference, ISC2 2015. <https://doi.org/10.1109/ISC2.2015.7366179>, 2015.
- [20] B. Veselinović Savković, A. Schweigkofler, O. Savković, M. Riedl and D. T. Matt, "Validation Methodology for a Citizen-centric Smart-City Platform." Proceedings of ISPIEM Conferences, 1–12., 2020.
- [21] K. K. Nair, M. M. Pillai, S. Lefophane and H. D. Nair, "Adaptation of Smart Cities in the South African Internet of Things Context", 2020 International Conference on Artificial Intelligence, Big Data, Computing and Data Communication Systems (IcABCD), 2020 International Conference On, 1–6. <https://doi.org/10.1109/icABCD49160.2020.9183832>, 2020.
- [22] G. Suciu and A.-M. Tudor, "Promoting a Business through Events in a Smart City." *E-Learning & Software for Education*, 3, 150–155. <https://doi.org/10.12753/2066-026X-20-189>, 2020.
- [23] L. Zlámal, "Smart City and Smart Region Concept in Zlín and Trenčín Regions." *Social & Economic Revue*, 17(4), 61–70., 2019.
- [24] M. Yılmaz "Real measure of a transmission line data with load fore-cast model for the future." *Balkan Journal of Electrical and Computer Engineering* 6.2 (2018): 141-145.
- [25] H. Chourabi, T. Nam, S. Walker, J. R. Gil-Garcia, S. Mellouli, K. Nahon, H. J. Scholl, "Understanding Smart Cities: An Integrative Framework." 2012 45th Hawaii International Conference on System Sciences. doi:10.1109/hicss.2012.615, 2012.
- [26] N. Mohamed, J. Al-Jaroodi and I. Jawhar, "Opportunities and Challenges of Data-Driven Cybersecurity for Smart Cities." 2020 IEEE Systems Security Symposium (SSS). doi:10.1109/sss47320.2020.9174388, 2020.
- [27] [Online] Available: <https://www.idc.com/getdoc.jsp?containerId=prUS44159418>, Accessed on 31 January 2020.
- [28] J. McClellan, Jimenez, and G. Koutitas (Eds.), "Smart Cities: Applications", Technologies, Standards, and Driving Factors (pp. 209-233). Springer International Publishing. <https://doi.org/10.1007/978-3-319-59381-4-13>, 2018.
- [29] C. Rotuna, A. Gheorghită, A. Zamfiroiu, D. Smada Anagrama, "Smart city ecosystem using blockchain technology", *Inform. Econ*, 23, 41–50, 2019.
- [30] K. Baculáková "Selected Aspects of Smart City Concepts: Position of Bratislava." *Theoretical and Empirical Researches in Urban Management*, 15(3), 68., 2020.
- [31] J. B. Porto and M. Oliveira, "The smart cities methodology based on public value: The first evaluation cycle.", *BAR - Brazilian Administration Review*, 17(1). <https://doi.org/10.1590/1807-7692bar2020190048>, 2020.
- [32] R. Giffinger, C. Fertner, H. Kramar, R. Kalasek, N. Pichler-Milanović, E. Meijers, "Smart cities" Ranking of European medium-sized cities, [http://www.smartcities.eu/download/smart\\_cities\\_final\\_report.pdf](http://www.smartcities.eu/download/smart_cities_final_report.pdf), 2007.
- [33] K. Hernandez, "Achieving Complex Development Goals along China's Digital Silk Road", K4D Emerging Issues Report, Brighton: Institute of Development Studies, 2019.
- [34] B. Krishnan, S. Arumugam and K. Maddulety, "Critical success factors for the digitalization of smart cities.", *International Journal of Technology Management & Sustainable Development*, 19(1), 69–86. [https://doi.org/10.1386/tmsd\\_00016\\_1](https://doi.org/10.1386/tmsd_00016_1), 2020.
- [35] A. AlDairi and L. Tawalbeh, "Cyber Security Attacks on Smart Cities and Associated Mobile Technologies.", *Procedia Computer Science*, 109, 1086–1091. <https://doi.org/10.1016/j.procs.2017.05.391>, 2017.
- [36] T.J.H. Gracia and A. C. García, "Sustainable Smart Cities. Creating Spaces for Technological", *Social and Business Development. Boletín Científico de Las Ciencias Económico Administrativas Del ICEA*, 6(12), 2018.
- [37] A. M. Rashid, A.A. Yassin, A.A. Alkadhawee and A.J. Yassin, "Smart city security: Face-based image retrieval model using gray level co-occurrence matrix.", *Journal of Information and Communication Technology*, 19(3), 437–458., 2020.
- [38] M. Visan and C. Ciurea, "Smart City: Concepts and two Relevant Components.", *International Journal Of Computers Communications & Control*, 15(2). doi:10.15837/ijccc.2020.2.3867, 2020.
- [39] T. Qamar and N. Z. Bawany, "A Cyber Security Ontology for Smart City.", *International Journal on Information Technologies & Security*, 12(3), 63–74., 2020.
- [40] [Online] <https://www.cittaslow.org>
- [41] [online] <http://www.citykeys-project.eu>
- [42] [Online] [https://tug.tubitak.gov.tr/sites/images/tug/isik\\_kirliligi.html](https://tug.tubitak.gov.tr/sites/images/tug/isik_kirliligi.html)
- [43] P. Boyce, "Human factors in lighting.", *Lighting Research Center* (2nd ed.). London: Taylor & Francis. <https://www.crcpress.com/Human-Factors-in-Lighting/Boyce/p/book/9781439874882>, 2013.
- [44] Ş. Sirel, "Aydınlatma ve Mimarlık [Lighting and Architecture]", *Tasarım [Design]*, 110: 98-105. <http://www.yfu.com/yazilar/TasDer110-AydveMim.pdf>, 2001.
- [45] Z. Aslan, "Işık kirliliği", *TÜBİTAK Bilim ve Teknik Dergisi*, Vol.362 pp.66-69, 1998.
- [46] Z. Aslan, "Işık Kirliliği" konferanslar: Öğretmenlere yönelik sunumlar, *Astronomi Öğretmen Seminerleri Serisi (AÖS-3(Antalya), AÖS-5(ODTÜ-Ankara) ve AÖS-13 (ODTÜ-Ankara)* <http://www.astrobilgi.org/category/etkinlik/>, 2015.
- [47] Z. Aslan and Z. Tunca, "Işık Kirliliği", *Sunum.*,17. Ulusal Gökyüzü Gözlem Şenliği 31 Temmuz-3 Ağustos, Saklıkent Antalya, 2014.
- [48] D. Çetegen and A. Batman, "Işık kirliliği.", *İstanbul Teknik Üniversitesi Elektrik Elektronik Fakültesi Yayınları. Yayın No:9*, 2005.
- [49] H. Dokuzcan, "Işık Kirliliği Açısından Kent Aydınlatması ve Taksim Meydanı Örneği", *Yüksek Lisans Tezi, Bahçeşehir Üniversitesi, Fen Bilimleri Enstitüsü, Mimarlık Anabilim Dalı, İstanbul*, 2006.
- [50] J. Meier, U.Hasenöhr, K. Krause and M. Potttharst, "Urban lighting, lightpollution, and society", *New York : Routledge, Taylor & Francis Group*, 2015.
- [51] J.A. Pichardo-Corpus, H. A. Solano Lamphar, R. Lopez-Farias and O. Delgado Ruiz, "Spatio-temporal networks of light pollution.", *Journal of Quantitative Spectroscopy and Radiative Transfer*, 253. <https://doi.org/10.1016/j.jqsrt.2020.107068>, 2020.
- [52] Héctor Antonio Solano Lamphar, and Miroslav Kocifaj, "Light pollution in ultraviolet and visible spectrum: effect on different visual perceptions.", *PLoS ONE*, 8(2), e56563. <https://doi.org/10.1371/journal.pone.0056563>, 2013.
- [53] J. Marull, J. Pino, J. M. Mallarach and M. J. Cordobilla, "A Land Suitability Index for Strategic Environmental Assessment in metropolitan areas.", *Landscape and Urban Planning*, 81(3), 200–212. <https://doi.org/10.1016/j.landurbplan.2006.11.005>, 2007
- [54] C.S. Aksay, O. Ketenoglu and L. Kurt, "Light Pollution.", *Afyon Kocatepe Üniversitesi Fen ve Mühendislik Bilimleri Dergisi Volume: 7, Issue: 2* 231-236, 2007.
- [55] Z. Aslan, O. Gölbaşı, D. Koçer, Z. Tunca, E. Işık, A. Yelkenci, D. Bağdaş, A. Devlen, T. Özdemir, K. Yelkenci, T. Demirciler, U. İkizler, A. Karamahmutoglu, M. Koçer, M. Mutlu, Ü. Özyar and H. İpek, "Türkiye'de gece gökyüzü parlaklığının ölçülmesi", 8. Ulusal Aydınlatma Kongresi, 14-15 Nisan Bildiri Kitabı s:69.4, 2011.
- [56] [Online] <https://astro.org.sv/imagendeldia/mayo-16-2019-cielos-oscuros-enciendan-la-noche-mayo-16-2019-cielos-oscuros-enciendan-la-noche/>
- [57] [online] <https://astro.org.sv/imagendeldia/abril-8-2020-cielo-rural-versus-cielo-ciudadino/>
- [58] [online] <https://www.darksky.org>
- [59] P. Pracki and K. Skarzyński, "A multi-criteria assessment procedure for outdoor lighting at the design stage.", *Sustainability (Switzerland)*, 12(4). <https://doi.org/10.3390/su12041330>, 2020.
- [60] E. Giordano, "Outdoor lighting design as a tool for tourist development: the case of Valladolid.", *European Planning Studies*, 26(1), 55–74. <https://doi.org/10.1080/09654313.2017.1368457>, 2018.
- [61] G.T. Aditya and N. K. Prakash, "Smart and Efficient Outdoor Lighting System.", 2018 Second International Conference on Intelligent Computing and Control Systems (ICICCS), Intelligent Computing and

- Control Systems (ICICCS), 2018 Second International Conference On, 1598–1602. <https://doi.org/10.1109/ICCONS.2018.8663140>, 2018.
- [62] S. Atis and N. Ekren, “Development of an outdoor lighting control system using expert system.”, *Energy & Buildings*, 130, 773–786. <https://doi.org/10.1016/j.enbuild.2016.08.066>, 2016.
- [63] A.A. Filimonova, T. A. Barbasova and D. A. Shnayder, “Outdoor Lighting System Upgrading Based on Smart Grid Concept.”, *Energy Procedia*, 111, pp.678–688. <https://doi.org/10.1016/j.egypro.2017.03.230>, 2017.
- [64] A. Ozadowicz and J. Grela, “The street lighting control system application and case study.”, *Proceedings of 1st International Conference on Event-Based Control, Communication and Signal Processing, EBCCSP 2015*. <https://doi.org/10.1109/EBCCSP.2015.7300701>, 2015.
- [65] C. A. Bouroussis and F. V. Topalis, “Assessment of outdoor lighting installations and their impact on light pollution using unmanned aircraft systems - The concept of the drone-gonio-photometer.”, *Journal of Quantitative Spectroscopy and Radiative Transfer*, 253. <https://doi.org/10.1016/j.jqsrt.2020.107155>, 2020.
- [66] J. Maziarka, L. Bena and H. Wachta, “Meaning of Scotopic/Photopic Ratio of Light Sources in Lighting of Outdoor Spaces.”, 2018 VII. Lighting Conference of the Visegrad Countries (Lumen V4), Lighting Conference of the Visegrad Countries (Lumen V4), 2018 VII, 1–4. <https://doi.org/10.1109/LUMENV.2018.8521093>, 2018
- [67] Ö. Memiş, “İnsan Odaklı Aydınlatma.” *International Periodical of Recent Technologies in Applied Engineering*, 1 (1), 30-35. Retrieved from <https://dergipark.org.tr/tr/pub/porta/issue/44896/542862>, 2019.
- [68] N. T. Tung, L. M. Phuong, N. M. Huy, N. Hoai Phong, T. L. Dinh Huy and N. Dinh Tuyen, “Development and Implementation of Smart Street Lighting System based on Lora Technology.” 2019 International Symposium on Electrical and Electronics Engineering (ISEE), Electrical and Electronics Engineering (ISEE), 2019 International Symposium On, 328–333. <https://doi.org/10.1109/ISEE2.2019.8921028>, 2019.
- [69] F.G. Carloto, M. A. D. Costa, C. H. Barriquello, D. P. Bernardon, N. Silva Spode, L. da, Maziero, W. D. Vizzotto and F. G. Reck, “The Role of a Smart Street Lighting into a Smart Grid Environment.”, 2019 IEEE PES Innovative Smart Grid Technologies Conference - Latin America (ISGT Latin America), 2019 IEEE PES, 1–6. <https://doi.org/10.1109/ISGT-LA.2019.8895267>, 2019.

### BIOGRAPHIES



**ZEHRA KARAGÖZ KÜÇÜK**, she received the B.S. degree from the Electrical Engineering Department, Istanbul University, Istanbul, Turkey, in 2015, and the M.S. degrees from the Erzincan University, Erzincan, Turkey, in 2018. She is continuing PhD education in Marmara University Electrical and Electronics Engineering Department, Istanbul, Turkey. She is currently a lecturer at Dogus University, Vocational School Electrical Department. Her research interests include electric, lighting.



**NAZMİ EKREN**, received the B.S. degree from the Electrical Engineering Department, Yildiz Technical University (YTU), Istanbul, Turkey, in 1987, and the M.S. degrees from the Marmara University in 1989 and PhD degrees from the Istanbul University in 1996. He is currently an associate professor at the Marmara University. His research interests PV systems, fabrication at Nano level and lighting. He works on tissue engineering applications, 3D-bioprinting, electrospinning.

# The Topologies of Multi-Input Single-Output Non-Isolated DC-DC Converter for Distributed Power Generation

Cihat Şeker, M. Tahir Güneşer and Şakir Kuzey

**Abstract**—Today it is an obvious fact that energy consumption tends to increase due to technological developments, population growth, and increasing living standards. In last two decades, renewable energy sources are considered to be the most convenient way to produce clean energy, as it has infinite energy potential. However, most of these alternative systems are not considered sufficient to supply the whole demand alone. But hybrid systems with some alternative energy sources, such as solar, wind, and biomass appear to be a solution to supply the energy needs in the future. In hybrid systems, the DC-DC converter structure is the main device when converting energy for the proper loads. Single/multiple inputs, single/multiple output DC-DC converter topologies vary in design according to the energy demand of the load. Particularly, as the power flow direction differs depending on the energy need and efficiency in energy systems, the usage areas of topologies with bidirectional power flow and fewer circuit elements that reduce system cost and complexity are expanding. In this study, the simulation of multi-input single-output (MISO) DC-DC converter topologies were performed in Matlab / Simulink software. Inductor current and voltage, output current and voltage, as well as output power used in the determining topologies were analyzed. The mathematical equations given in the topologies were confirmed by simulation studies.

**Index Terms**—MIC topologies, hybrid systems, Matlab / Simulink, two-input converters, V-I characteristics

## I. INTRODUCTION

IN THE process from generation to the consumption of electrical energy, the most important reason for using

**CİHAT ŞEKER**, is with Department of Electrical-Electronics Engineering University of Karabuk, Karabuk, Turkey, (e-mail: cihatseker@karabuk.edu.tr).

 <https://orcid.org/0000-0002-9680-4622>

**M. TAHİR GÜNEŞER**, is with Department of Electrical-Electronics Engineering University of Karabuk, Karabuk, Turkey, (e-mail: mtguneser@karabuk.edu.tr).

 <https://orcid.org/0000-0003-3502-2034>

**ŞAKİR KUZEY**, is with Department of Electricity and Energy University of Giresun, Giresun, Turkey, (e-mail: sakir.kuzey@giresun.edu.tr).

 <https://orcid.org/0000-0003-3680-0862>

Manuscript received January 6, 2021; accepted February 17, 2021.

DOI: [10.17694/bajece.855262](https://doi.org/10.17694/bajece.855262)

alternating current (AC) is that the input voltage can be easily converted to different voltage levels with the help of low frequency transformers (LFT). In electrical power systems, LFTs also perform electrical insulation functions besides voltage transformations. However, LFTs constitute the biggest part of the power systems in terms of volume, weight and cost due to the weight of the bulky iron core and copper coils in their structure. The dimensions and weights of transformers vary depending on the ferromagnetic properties of the cores used in their structures and the temperature of the cores and windings.

In power transformers, while the temperature of the transformer is controlled with the help of various cooling devices placed on the transformer, a reduction in weight and volume can be achieved by using materials with high magnetic permeability in the core structure. On the other hand, since the transformer sizes change inversely with frequency, increasing the frequency can reduce the transformer dimensions. However, since increasing the frequency will increase the losses caused by hysteresis and eddy current, there is a need for cores with high magnetic permeability instead of conventional magnetic cores. With advances in material science, cores with high power and high magnetic permeability can be developed at medium voltage levels [1-3].

Today, using the only transformer is insufficient in meeting the needs of loads with different profiles and in connect of renewable energy sources such as solar and wind to the grid. Additional mechanisms are needed to overcome power quality problems such as voltage rise and fall, ripple, or harmonics [4]. With the advances in semiconductor technology, power electronics has emerged as a promising solution to dealing with the problems of complex power systems. High-power and controllable solid-state switches triggered the development of various power electronic converters that find application in both transmission and distribution systems. Power electronic circuits and mechanisms (such as fuses, switches, protection equipment, etc.), initially created with the help of transistors, were primarily used in the industry. This process, which started with motor control units, went beyond the industry thanks to the developing semiconductor technologies and went to electric vehicles [5,6], microgrids [7,8], renewable energy sources [9,10], home, office, agriculture, and animal husbandry [11, 12] has found use in many places. Power electronic circuits, whose production and consumption increased with the increasing demand, made it necessary to

minimize the effect of load effect on the source and peripheral devices and to be compatible with each other. Besides, the quality and uninterrupted energy demands of the users [13] made it necessary to provide power quality, efficiency, safety, and insulation features. It is necessary to prevent wide-ranging power outages that occur in case of malfunctions, to dampen disturbing effects, and to keep the power factor level that creates a load on the grid at the optimum level.

Power converters that result from the combination of conventional transformers and semiconductor converters are defined as power electronics transformers (PET). PET's were first patented by Murray in 1970 [14]. Using conventional transformers in PETs provides easy conversion between different voltage levels as well as electrical insulation. However, transformers used in the network frequency (50Hz / 60Hz) have disadvantages such as very large weight and dimensions depending on the power. Brooks suggested in 1980 that by increasing the frequency of the insulation barrier, the size of the system could be reduced and more power could be transferred with a smaller transformer [15]. Thus, together with transformers that can be operated within the frequency application limits, the way for very high energy conversions from very small dimensions has been opened. It has started to widespread the use of PET instead of LFT, especially at low and medium voltage levels. Safe and efficient power control is provided in a wide range by properly controlling the power electronic elements in the PET's structure. Compared to conventional transformers, PETs are characterized by high power density, small volume, and weight, controlled power factor, controlled voltage reduction, etc. It appears to have good features such as [16,17]. On the other hand, as a result of increasing the operating frequency, the size of the filter elements is reduced, allowing high energy conversions from low volumes [18]. In the light of advances in materials science, PETs have developed in parallel with semiconductor circuit elements.

In this study, the studies on multi-input converters (MICs) are examined and MIC topologies, which are widely included in the literature, are summarized. MIC topologies are grouped under four subtitles as AC / AC, AC / DC, DC / AC, and DC / DC. Topology structures are generally examined and detailed with a sample application. The developed MIC was simulated in Matlab / Simulink environment. The findings obtained from the design criteria and simulation are presented in the third section of the study.

## II. MULTI-INPUT DC/DC SYSTEM

A simulation study of the MISO DC-DC converter system given in [19, 20] has been done. In such multi-input (MI) systems, a separate DC-DC converter is used for each source. The output of the transformers of the sources was connected in series and a single DC output voltage was generated. In such systems feeding a single load, using a separate converter for each source stands out as a disadvantage. According to the given topology, a two-input single-output circuit model was formed in the simulation environment in Matlab / Simulink program. The circuit model is given in Fig. 1. Aleo Solar

S16.185 PV module in Matlab / Simulink software library was used.

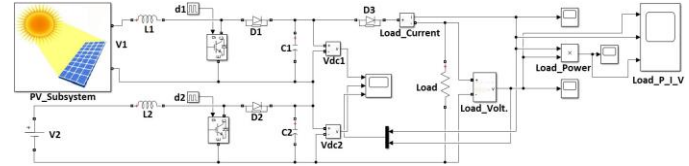


Fig. 1. Two-input single output DC-DC system

The use of boost converters separately for two DC sources is given in Fig. 1.  $V_1$ ,  $V_2$  the source is chosen as  $24 V_{DC}$ . There is a unidirectional flow of power from the sources to the load. The load voltage ( $V_0$ ) can be found by equation 1.

$$\begin{aligned} V_0 &= V_{DC1} + V_{DC2} \\ &= \frac{V_1}{1-d_1} + \frac{V_2}{1-d_2} \end{aligned} \quad (1)$$

Equation 1 is determined according to the two-input DC-DC system. Depending on the number of entries, the equation can be expanded.  $V_{DC1}$ ,  $V_{DC2}$  are the output voltage of the boost converters,  $d_1$  and  $d_2$  are the duty cycle values of the first and second switches, respectively. If the input values ( $V_p = V_1 = V_2$ ) and duty cycle ( $d_p = d_1 = d_2$ ) values for each switch are equal, the output voltage  $V_0$  can be generalized with equation 2 according to the number of sources ( $n$ ).

$$V_0 = \frac{nV_p}{1-d_p} \quad (2)$$

Capacitance value ( $C$ ) is found by Equation 3.

$$C = \frac{n^2 d_p}{1-d_p} \frac{V_p}{R \cdot f \cdot \Delta V_p} \quad (3)$$

where  $R$  is load,  $f$  is the switching frequency, and  $\Delta V_p$  is the fluctuation in voltage. Switching frequencies in topology are fixed. Inductor value ( $L$ ) is given by Equation 4.

$$L = \frac{(1-d_p)^2 d_p \cdot R}{2 \cdot n \cdot f} \quad (4)$$

The parameters and values used in the simulation environment are given in Table I. For a two-input system, the duty cycle ratio is taken as 0.4 in both switches. Input voltage source values are equal and voltage ripple value is taken as  $2 V$ .

TABLE I  
CIRCUIT PARAMETERS

Parameter	Value
$V_1$ (mpp)	$24 V_{DC}$
$V_2$	$24 V_{DC}$
$d_1$	40 %
$d_2$	40 %
$L$	$18 \mu H$
$C$	$160 \mu F$
$R$	$10 \Omega$
$f$	$20 kHz$
$\Delta V_p$	$2 V$

Fig. 2 shows the output DC voltage and current graph for the load in each converter. The output voltage is measured at 48.5V. The output current has been measured as 4.95A.

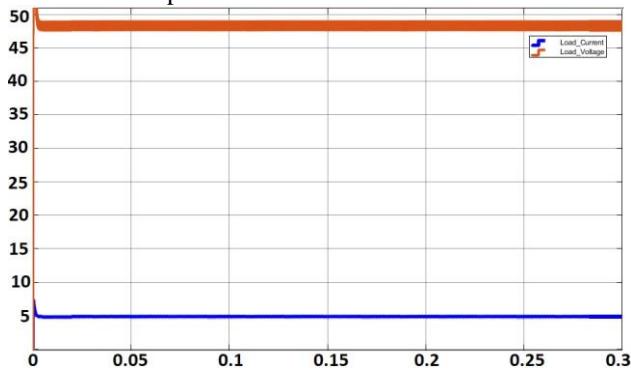


Fig. 2.  $I_0$  and  $V_0$  graph

The output power graph is given in Fig. 3 and it has been calculated as approximately 240 W.

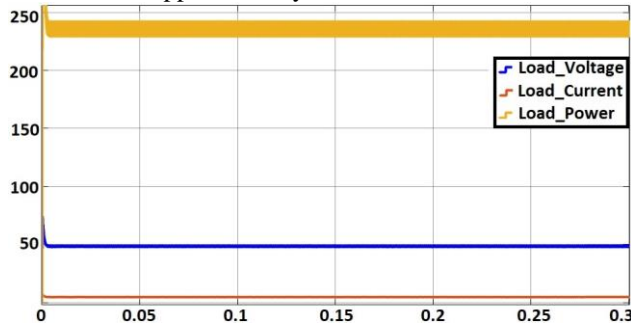


Fig. 3.  $P_0$ ,  $V_0$  and  $I_0$  graph

### III. MISO DC/DC CONVERTER TOPOLOGIES

There are many MI DC-DC converter topologies in the literature. In such systems, power transfer with a common circuit using more than one source and a single inductor was performed either in unidirectional or bidirectional. Meeting the energy needs increases its importance day by day. In this case, the hybrid use of renewable energy sources of different voltage levels is seen as a solution. For this reason, the use of two different voltage levels was preferred in the study, and the number of voltage sources with different profiles can be increased according to the energy need.

MISO DC-DC converter topology is given in [21, 22]. The pulsating voltage source cell (PVSC) structure formed by the parallel connection of diodes to the sources forms the basis of the system. In the topology, the power flow is provided unidirectional with a converter with a single output filter and a single control system. The circuit model is given in Fig. 4.  $V_1$  and  $V_2$  DC power supplies can supply power to the load both separately and simultaneously. By applying PWM signal switching, four different operating modes are formed at the fixed switching frequency. Mode 1; It is the time interval when the switch  $S_1$  is on and the switch  $S_2$  is in an off position. In this time interval, the energy from the  $V_1$  source feeds the load through the inductor. Mode 2; It is the time interval when the switch  $S_1$  is off and the switch  $S_2$  is on. During this time, the  $V_2$  source charges the inductor. The

output capacitor supplies power to the load. Mode 3; It is the interval when both switches are off. In this time interval, it provides its load power from the energy stored in the inductor and the capacitor. Mode 4; It is the time interval when both switches are on. During this time, both sources work at the same time. The sources charge the inductor and the power of the load is provided by the capacitor. Since it has four different operating modes, the PWM signal applied to the switches must be applied in a way that creates these modes. Switches are operated at the same frequency. The output voltage  $V_0$  of the system can be found by Equation 5.

$$V_0 = \frac{d_1 V_1 + d_2 V_2}{1 - d_2} \quad (5)$$

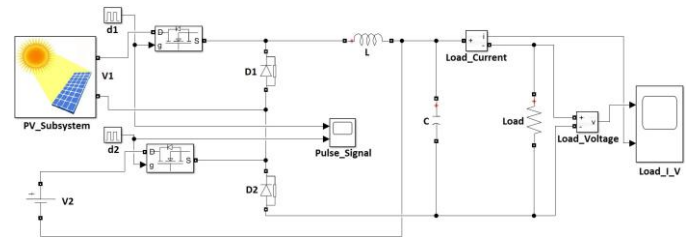


Fig. 4. Two-input single-output buck / buck-boost converter circuit

If the source with high voltage value is defined as  $V_H$  and the source with low voltage value as  $V_L$  there is a relationship between input voltages and output voltage as  $V_H > V_0 > V_L$ . The parameters used in the simulation environment are given in Table II.

TABLE II  
CIRCUIT PARAMETERS

Parameter	Value
$V_1$ (mpp)	24 $V_{DC}$
$V_2$	12 $V_{DC}$
$d_1$	40 %
$d_2$	28 %
$L$	82 $\mu H$
$C$	160 $\mu F$
$R$	10 $\Omega$
$f$	20 kHz

The signals used in the simulation study of two input DC-DC converter topologies are given in Fig. 5.

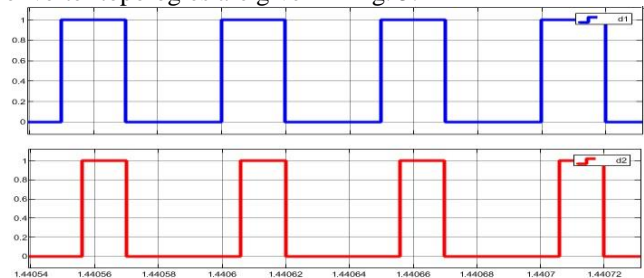


Fig. 5.  $d_1$  and  $d_2$  duty cycle graph

When the power control relationship of the circuit is examined, it is seen that three different situations occur. The  $V_1$  or  $V_2$  source will be the main source that provides the power needed by the load, and the remaining power will be

supplied from another source. The third case is that both sources will provide power to the load and always provide the highest power to the output by controlling the input currents. Fig. 6 shows the output current and output voltage graph.

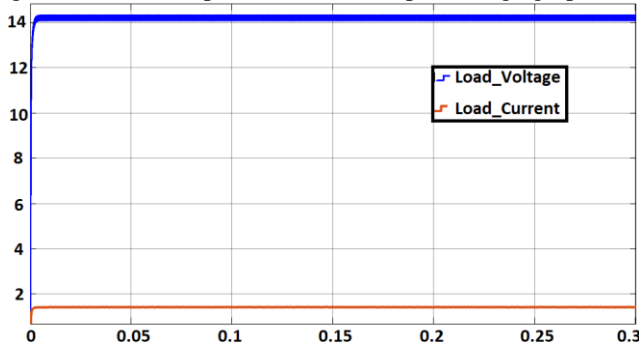


Fig. 6.  $V_0$  vs  $I_0$  graph

The circuit structure with a common converter structure utilizing a single inductor that provides bidirectional power flow analysis is given in Fig. 7. Contrary to the topologies given in the previous sections, it provides bidirectional power flow. This is particularly desirable for electric vehicle applications. For example, the power to be generated during regenerative braking in electric vehicles (EVs) is desired to be recovered. This situation points out that there should be a converter that can provide bidirectional power in EV systems. In the literature, many studies have been done for different modes of this topology [23-27].

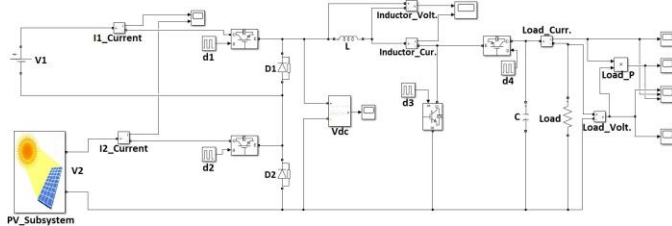


Fig. 7. MISO DC-DC converter topology

$S_1$  and  $S_2$  switches determine which source will provide power,  $S_3$  switch to determine whether the converter will operate in buck, boost, or buck-boost modes, and the power flow way with the  $S_4$  switch. Unidirectional power flow is preferred in buck-boost converter mode for the system to be analyzed. There are four operating modes since there are two voltage sources and whether these sources are in transmission or not. Since the switching modes and PWM signal strategies to be applied to the switches are explained in detail in the mentioned sources, there is no need for explanation in this study. A fixed frequency is applied to the keys. The output voltage  $V_0$  to be obtained when the MIC works in buck-boost mode is given in Equation 6.

$$V_0 = \frac{d_1 V_1 + d_2 V_2}{1 - d_1 - d_2 + d_{12}} \quad (6)$$

The  $d_{12}$  used in Equation 6 indicates the time depending on the period in which both switches  $S_1$  and  $S_2$  are on. Assuming a lossless system, the output current  $I_0$  from the input and output power equations is given in Equation 7.

$$I_0 = \frac{V_1 I_1 + V_2 I_2}{V_0} \quad (7)$$

The  $I_1$  and  $I_2$  currents given in Equation 7 represent the currents drawn from the first and second sources, respectively.  $I_1$  and  $I_2$  currents are found by multiplying the duty cycle ratios of switches  $S_1$  and  $S_2$ , respectively, by the inductor current. Inductor and capacitor values of MIC can be found from the inductor current reference ripple value and the output voltage reference ripple value with Equation 8 and Equation 9, respectively.

$$\Delta_i = \frac{V_0 [1 - (d_1 + d_2 - d_{12})]}{L \cdot f} \quad (8)$$

$$\Delta_c = \frac{V_0 (d_1 + d_2 - d_{12})}{R \cdot C \cdot f} \quad (9)$$

The parameters used in the simulation environment are given in Table III. The switching frequency is set at 20 kHz and the load at 5  $\Omega$ .

TABLE III  
MIC CIRCUIT PARAMETERS

Parameter	Value
$V_1$	48 $V_{DC}$
$V_2$ (mpp)	24 $V_{DC}$
$d_1$	40 %
$d_2$	40 %
$d_3$	60 %
$d_{12}$	20 %
$L$	28 mH
$C$	4.32 mF
$R$	5 $\Omega$
$f$	20 kHz
$\Delta_i$	5 %
$\Delta_c$	10 %

The output voltage, current, and power graph obtained in the simulation environment are given in Fig. 8. When the graphs are examined, it is seen that there are small differences according to the mathematical equations. The reason is that the circuit elements used in Simulink software are not ideal and have internal resistances.

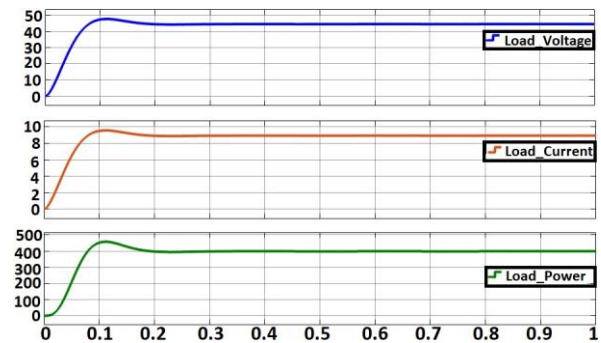


Fig. 8. The output voltage, current, and power graph

Inductor voltage and inductor current graph are given in Fig. 9. When the inductor voltage graph is investigated, it is seen that it is proper for the PWM switching strategy used. A medium synchronous switching strategy is used in this study.

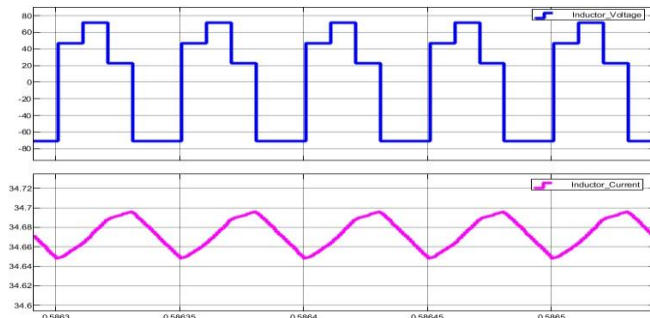


Fig. 9. Inductor voltage and current graph.

#### IV. COMPARISON OF TOPOLOGIES

Three different approaches have been chosen from MISO converter topologies. In the Matlab / Simulink simulation environment, small tolerance, accurate and stationary results were obtained according to the topology of each system. In the first topology, a separate converter circuit was used for each source, and this situation increased the number of circuit elements. In the second topology, the model with a single inductor common converter circuit is handled. The advantage of this topology is that it has a single inductor and a common converter circuit. However, unidirectional power flow is provided in both topologies. This situation can be considered as the disadvantage of topologies. In the third topology, bidirectional power flow is provided with the  $S_4$  switch. In terms of this feature, the last topology is different from other topologies. All topologies are operated at a fixed frequency. The PWM signal strategy required for the switching of each topology is simple. Although a constant DC source has been selected as the input source in the simulation studies for all three topologies, in practice these sources are photovoltaic, wind, etc. it is important in that sources with different characteristics provide power to the load.

TABLE IV  
TOPOLOGY COMPARISON

Parameter	Topology-1	Topology-2	Topology-3
Source values	same	different	different
Converter type	boost	buck/buck-boost	buck/boost
Power flow direction	unidirectional	unidirectional	bidirectional
Common inductance	no	yes	yes

#### V. CONCLUSIONS

Three different MIC topologies were analyzed and circuit models were installed in the simulation environment. When the topologies are compared, the two-input single-output

buck-boost converter topology, which is the last used topology, came to the forefront especially in terms of providing bidirectional power. Considering that the use of renewable energy sources will increase to meet the energy needs in the future, it is predicted that new topologies will be needed to be created with DC-DC converter combinations with MIs or multiple outputs. Thus, it will be useful to work on the power flow control of MISO DC-DC converter systems using photovoltaic energy sources in future studies.

#### REFERENCES

- [1] Siemens® Databook, "Ferrites and Accessories", www.epcos.com.
- [2] Ferroxcube® Databook, "Soft Ferrites and Accessories", www.ferroxcube.com.
- [3] Magnetics® Databook, 2004 Magnetics Catalog, www.mag-inc.com.
- [4] D. Dujic, F. Kieferndorf, and F. Canales, "Power electronic transformer technology for traction applications-An overview," *Electronics*. 2012.
- [5] Y. J. Lee, A. Khaligh, and A. Emadi, "Advanced integrated bidirectional AC/DC and DC/DC converter for plug-in hybrid electric vehicles," *IEEE Trans. Veh. Technol.*, 2009.
- [6] Y. Du, S. Lukic, B. Jacobson, and A. Huang, "Review of high power isolated bi-directional DC-DC converters for PHEV/EV DC charging infrastructure," 2011.
- [7] J. Rocabert, A. Luna, F. Blaabjerg, and P. Rodriguez, "Control of power converters in AC microgrids," *IEEE Trans. Power Electron.*, 2012.
- [8] F. Wang, J. L. Duarte, and M. A. M. Hendrix, "Grid-interfacing converter systems with enhanced voltage quality for microgrid application concept and implementation," *IEEE Trans. Power Electron.*, 2011.
- [9] Z. Zhao, M. Xu, Q. Chen, J. S. J. Lai, and Y. Cho, "Derivation, analysis, and implementation of a boost-buck converter-based high-efficiency PV inverter," *IEEE Trans. Power Electron.*, 2012.
- [10] B. Sri Revathi and M. Prabhakar, "Non-isolated high gain DC-DC converter topologies for PV applications – A comprehensive review," *Renewable and Sustainable Energy Reviews*. 2016.
- [11] D. Burmester, R. Rayudu, W. Seah, and D. Akinyele, "A review of nanogrid topologies and technologies," *Renewable and Sustainable Energy Reviews*. 2017.
- [12] Buning, E. A. (2010). Electric drives in agricultural machinery-approach from the tractor side. *Journal of Agricultural Engineering*, 47(3), 30-35.
- [13] Hemetsberger F. A. (2003). An Investigation Of Power Quality Problems In A Remote Mine Site, M.S. Thesis, The University of Queensland.
- [14] McMurray, W. (1970). U.S. Patent No. 3,517,300. Washington, DC: U.S. Patent and Trademark Office.
- [15] J. L. Brooks, "Solid State Transformer Concept Development," 1980.
- [16] E. R. Ronan, S. D. Sudhoff, S. F. Glover, and D. L. Galloway, "Application of power electronics to the distribution transformer," 2000.
- [17] L. Yang, T. Zhao, J. Wang, and A. Q. Huang, "Design and analysis of a 270kW five-level DC/DC converter for solid-state transformer using 10kV SiC power devices," 2007.
- [18] A. W. Lotfi and M. A. Wilkowski, "Issues and Advances in High-Frequency Magnetics for Switching Power Supplies," *Proc. IEEE*, 2001.
- [19] M. Davari, S. M. Ale-Emran, H. Yazdanpanahi, and G. B. Gharehpetian, "Modeling the combination of UPQC and photovoltaic arrays with multi-input single-output DC-DC converter," 2009.
- [20] R. Noroozian, M. Abedi, G. B. Gharehpetian, and A. Bayat, "On-grid and off-grid operation of multi-input single-output DC/DC converter based fuel cell generation system," 2010.
- [21] Yalamanchili K. P., Ferdowsi M., Lu S., Xiao P., and Corzine K., "Derivation of Double-input DC-DC Power Electronic Converters", *Electric Power Components and Systems*, vol.39, no.5, 478-490, 2011.
- [22] Archana N. and Anupamma K. I., "Multi-input Inverter for Hybrid Wind-Photovoltaic Standalone System", *Second International Conference on Computing Methodologies and Communication*, ICCMC 2018.

- [23] L. Kumar and S. Jain, "A novel multiple-input DC-DC converter for electric vehicular applications," 2012.
- [24] L. Kumar and S. Jain, "A multiple-input DC-DC converter for interfacing of battery/ultracapacitor in EVs/HEVs/FCVs," 2012.
- [25] F. Akar, Y. Tavlasoglu, E. Ugur, B. Vural, and I. Aksoy, "A Bidirectional Nonisolated Multi-Input DC-DC Converter for Hybrid Energy Storage Systems in Electric Vehicles," IEEE Trans. Veh. Technol., 2016.
- [26] Shetty S. N. and Raheman Md. A., "Design and Simulation of Dual Input DC/DC Converter", International Journal of Innovative Research in Electrical, Electronics, Instrumentation, and Control Engineering (IJIREEICE), National Conference on Advances in Electrical Engineering NCAEE, 2017.
- [27] Shetty S. N. and Raheman Md. A., "Modelling of Dual Input DC/DC Converter for Hybrid Energy System", 2th IEEE International Conference on Recent Trends in Electronics Information & Communication Technology RTEICT, 2017.

### BIOGRAPHIES



**Cihat Şeker** He was born in Sivas, Turkey, in 1989. He received the B.S. in Electronics and Communication Engineering from the Suleyman Demirel University, Isparta, Turkey, in 2012 and the M.S. degree in Electrical-Electronics Engineering from Karabuk University, Karabuk, Turkey, in 2016. He graduated Ph.D. Degree from Karabuk University Electrical and Electronics Engineering Department in 2020. His research interest includes wireless communication technologies, solar energy and design and fabrication of compact microstrip antenna.



**M. Tahir Güneşer** He was born in Turkey in 1975. He graduated Istanbul Technical University Electronics and Telecommunication Engineering Department in 1999 and Ph.D. Degree from Karabuk University Electrical and Electronics Engineering Department in 2015. His research interests are Communication on sub-THz Frequencies, Optimization and Control systems, Solar Energy, Energy Management.



**Şakir Kuzey** He was born in Turkey in 1985. He graduated from Gazi University Electrical Education Teaching Department in 2008 and Atatürk University Electrical and Electronics Engineering Department in 2018. He is continuing his doctorate education in Karabuk University Electrical and Electronics Engineering Department. His areas of interest are Solar Energy, Energy Management, Optimization and Control systems, Electrical Machines, Power Electronics, Renewable Energy Systems.

# An Infodemiological Study to Estimate Risk Factors of Urinary Incontinence Using Elastic Net Regression

Adem Doganer

**Abstract**— Urinary incontinence is a health problem of having a higher prevalence in the society which is observed widely and affecting the life quality negatively. In this study, it is hereby aimed to determine the risk factors which lead to urinary incontinence and to assess the seasonality of it. This study was a cross-sectional research. In the study, infodemiologic procedures were used. Persons' nationwide, relative search volume for the words relevant with urinary incontinence and risk factors were obtained from the internet search engines during 2016-2021. Relative search volume values were received from Google Trends. Urinary incontinence reasonability was determined through seasonal decomposition. Risk factors' effect on urinary incontinence was evaluated through Elastic.net regression procedure. Search volume of the words relevant to urinary incontinence in internet search engines displays seasonality. Search volume of urinary incontinence in internet search engines between November and February is hereby determined to be higher than other months. Risk factors on urinary incontinence are; prostate, diabetes, kidney pain, constipation and menopause. In the study, infodemiologic procedures were being applied and it was determined that urinary incontinence is showing seasonality. Risk factors of urinary incontinence were estimated successfully. Relative search volumes obtained from Google Trends are able to be used for the estimation of the epidemiologic parameters of urinary incontinence in the society successfully. In researches, enabling to include more countries and more variables to the models may provide a contribution for the generalization of the results.

**Index Terms**— Google Trends, Infodemiologic analysis, Seasonality, Urinary Incontinence.

## I. INTRODUCTION

URINARY INCONTINENCE is one of the disorders which is widely seen in the society. Urinary incontinence means an involuntary evacuation of urinary or excessive loss of urinary. There are different types of urinary incontinence such as; urge urinary incontinence, stress urinary incontinence and

ADEM DOGANER, Department of Biostatistics and Medical Informatics, Faculty of Medicine, Kahramanmaraş Sutcu Imam University, Kahramanmaraş, Turkey, (e-mail: adem\_doganer@hotmail.com).

 <https://orcid.org/0000-0002-0270-9350>

Manuscript received March 16, 2021; accepted April 30, 2021.  
DOI: [10.17694/bajece.897802](https://doi.org/10.17694/bajece.897802)

mixed urinary incontinence [1-4]. Urinary incontinence is a widely experienced disorder in the society. In Turkey, the prevalence of urinary incontinence between women of 17-80 age is hereby determined as 46, 3% averagely [5]. In terms of both genders, stress sourced urinary incontinence prevalence is found as %11, 1 approximately. Urinary incontinence particularly is observed more frequently in women over 60 [6].

People suffering from urinary incontinence problem tend to conceal the disorder because of feeling of the embarrassment [7]. People suffering from urinary incontinence do not go to the hospital as they are embarrassed and abstain from being treated [8]. This is a problem for finding the accurate prevalence of this disorder. In different researches, it was determined that urinary incontinence prevalence in women is between 8% - 45% [9]. This prevalence gets higher in pregnant women. In various researches, urinary incontinence prevalence in pregnant women seems to have a wider range [10]. As the patients hide their problem the prevalence in various researches gives different results. Patient hides their urinary incontinence disorder, so no homogeneous data can be obtained from the researches.

One of the methods applicable for the estimation of the prevalence of disorders in the society is infodemiologic researches. Infodemiology has introduced a new approach for obtaining health data in line with the advance of internet and computer technologies. Infodemiology was set forth by Eysenbach (2002). Infodemiology means the researches made on the distribution and dissemination of health-information and inaccurate information in the society [11]. Infodemiology may provide significant information about the contagion of epidemics in the society. Besides, infodemiology may provide important findings about the dissemination of inaccurate information in the society. Infodemiology provides a strong alternative with its advantages in terms of field researches. Infodemiology; besides estimating the contagion of epidemics in the society may be also used for the estimation of the prevalence of seasonal and chronic diseases, estimation of symptoms of the diseases and for the determination of the society's attitudes against diseases.

Infodemiology researches' one of the most important data sources is the internet. Inquiries made for diseases on the internet by the society may provide important information thereof. One of the most popular tools of infodemiology which

is used for the examination of inquiries made in the internet search engines is Google Trends (<https://trends.google.com/trends/?geo=TR>). Google Trends is a free access portal which gives the users' relative search volume according to a specific region or time period belonging to inquiries made online on the internet search engine [12]. Google Trends has provided an important alternative for the researches in which obtaining data seems to be difficult. With Google Trends, important information can be provided in relation to disease prevalence, the contagion of epidemics and society's attitude towards diseases [13]. Google Trends has been applied for the estimation of the contagion of various epidemics in the society. Mavragani and Gkillas (2020), in their studies, utilized Google Trends data in order to estimate the contagion of Covid-19 in United States [14]. Morsy et al. (2018), in their studies, estimated the number of Zika virus cases that were seen in Brazil and Colombia by using Google Trends data [15]. Samaras et al. (2017), in their studies, utilized Google Trends data to model the syndromic surveillance flue cases in Italy and Greece [16]. With Google Trends, various researches have been made for the determination of society's mental health and society's behaviors. Parker et al. (2017), in their studies, for the estimation of deaths based on suicide used Google Trends data as well [17]. Google Trends data is used for model production for the determination of the seasonality of diseases. The prevalence of some diseases may vary seasonally. Google Trends data may be used for the examination of seasonal movements of diseases. Moccia et al. (2016), in their studies, utilized Google Trends data for the modeling of seasonal change of Multiple-Sclerosis disease [18]. Rossignol et al. (2013) utilized Google Trends data for the modeling of the seasonality of urinary tract infections. [19]. Zhang et al. (2018), used Google Trends data to reveal that the occurrence of cellulite changes seasonally [20].

The literature includes very little information about the seasonality of Urinary Incontinence. This study, to the best of our knowledge, is one of the primary studies in the literature in which the seasonality of urinary incontinence is assessed through infodemiologic procedures. In this study, in order to determine the urinary incontinence seasonality, an infodemiologic study has been planned. Besides, for the determination of factors that affect urinary incontinence, Google Trends data on urinary incontinence and risk factors within the last 5 years in Turkey were assessed.

## II. MATERIAL AND METHODS

This study is a cross-sectional study. Infodemiologic research was made in the study. In the study, the relative search volume

## III. RESULTS

In the study, urinary incontinence cases' seasonality was examined. In figure 1, during 2016-2021, a change of RSV values regarding urinary incontinence in internet search engine

of the individuals in Turkey regarding urinary incontinence made on internet search engines was obtained for the period 15 February 2016 - 15 February 2021 in Turkey. Such data were obtained from Google Trends [12]. Google Trends assesses the words' rates of search in internet search engines between 0-100 points. The words' rate of search provided from Google Trends is defined as, Relative Search Volume (RSV). RSV values take place between 0-100 points. In the study, in order to find out the relative search volume of urinary incontinence in internet search volume, inquiries were made in Google Trends. These inquiries were made between 15 February 2016- 15 February 2021 and in Turkish and nationwide. For rates of search volume of urinary incontinence; in Google Trends inquiries, various definitions were searched. For the determination of the risk factors of urinary incontinence; words; "Prostate", "Diabetes", "Renal Pain", "Constipation", "Vaginal infection", "Menopause", "Fistula" and "Cystitis" were searched in Google Trends".

### A. ELASTIC.NET REGRESSION

Elastic.net regression is a resistant regression procedure against the higher correlation among independent variables. In fact, Elastic.net uses the techniques which are applied in Lasso regression and Ridge regression procedure together [21]. In higher dimensional data, successful estimations are achievable. In Lasso regression procedure;  $l_1$  penalty coefficient is being applied, but in Ridge regression procedure  $l_2$  penalty coefficient is applied. In Elastic.net regression calculations,  $l_1$  and  $l_2$  coefficients are used together. The basic purpose of Elastic.net regression is; with  $l_1$  and  $l_2$  coefficients, to obtain the coefficient which minimizes the error sum of squares [22].

### B. STATISTICAL ANALYSIS

The conformity of the variables to normal distribution was examined with the Kolmogorov- Smirnov test. In variables which comply with normal distribution, for the comparison of RSV values in terms of months, Anova test was applied. For the determination of differences in terms of months, Tukey HSD test and Tamhane T2 test was applied. For the determination of seasonality, a seasonal decomposition procedure was applied. The relation between quantitative variables was examined by Pearson correlation test. The effect of risk factors over urinary incontinence values was assessed by Elastic.net regression procedure. Statistical parameters were defined with Mean±Standard Deviation. Statistical significance was accepted;  $p < 0.05$ . For the assessment of data, IBM SPSS Statistics version 22 (IBM SPSS for Windows version 22, IBM Corporation, Armonk, New York, United States) and R 3.3.2 statistical software was utilized.

in Turkey was specified. Urinary incontinence RSV values were observed to increase in winter and decrease in summer. During 5 years period, for every year, in winters, RSV values rose up and declined in summer.

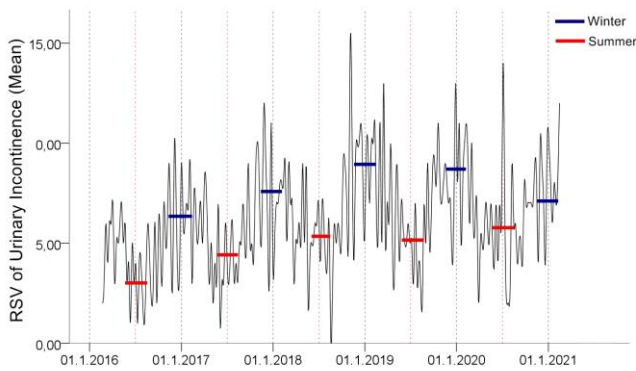


Fig.1. The change of RSV values of urinary incontinence between 2016-2021 in Turkey

For the determination of urinary incontinence seasonality, a seasonal decomposition procedure was applied. Urinary incontinence RSV values' seasonal factors effect was assessed. In winter and autumn, RSV values related to urinary incontinence were observed to increase importantly whereas these values tended to decrease in spring and summer. Findings relevant to urinary incontinence's seasonality are defined in figure 2. Urinary incontinence's RSV values display seasonality.

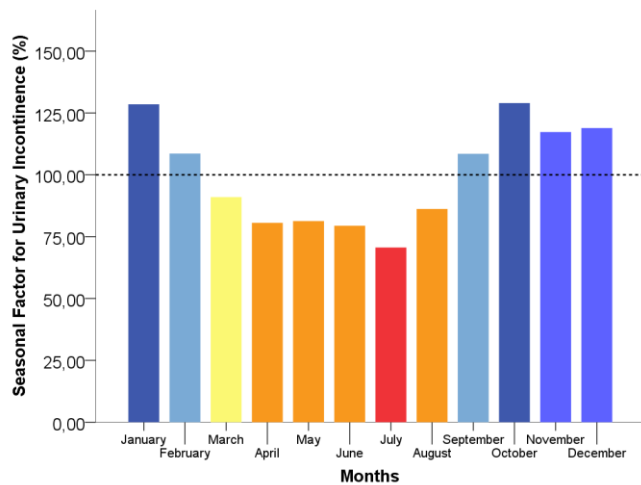


Fig.2. Seasonality of Urinary Incontinence

In the study, risk factors affecting urinary incontinence were evaluated. It is hereby determined that the relation of urinary incontinence RSV values with renal pain, prostates, diabetes, menopause, vaginal infection and fistula RSV values are statistically significance ( $p < 0.05$ ). Findings were determined in Table 1. The effect of risk factors on urinary incontinence RSV values was evaluated. The most important variables which explain the change in urinary incontinence was determined respectively as Prostates, Diabetes and renal pain. Prostates, diabetes and renal pain, menopause and constipation affect urinary incontinence significantly. The most important variables which explain the change in urinary incontinence were defined in figure 3. Effects of independent variables on urinary incontinence were assessed by Elastic.net regression.

In Table 2, the effect of independent variables over urinary incontinence was estimated. Prostates, renal pain, diabetes, constipation and menopause were seen to have affected the urinary incontinence substantially.

TABLE I  
CORRELATION BETWEEN RISK FACTORS AND URINARY INCONTINENCE

	Urinary Incontinence	
	r	p
Constipation	0,058	0,352
Cystitis	0,062	0,321
Renal Pain	0,257	<b>p&lt;0,001*</b>
Prostate	0,348	<b>p&lt;0,001*</b>
Diabetes	0,332	<b>p&lt;0,001*</b>
Menopause	0,173	<b>0,005*</b>
Vaginal Infection	0,130	<b>0,036*</b>
Fistula	0,182	<b>0,003*</b>

Pearson Correlation Test; $\alpha:0.05$ ; \*Correlation is statistically significant

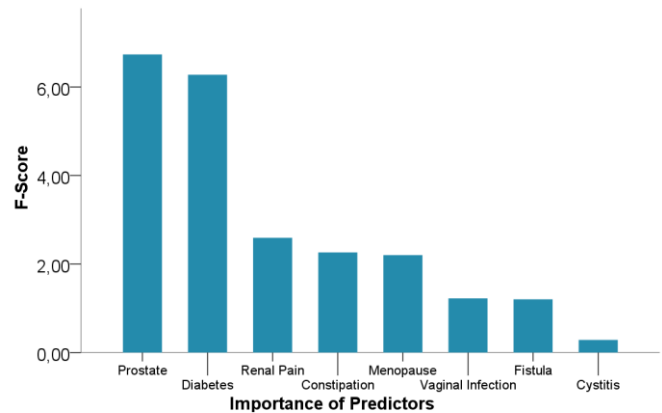


Fig.3. Importance of risk factors in terms of urinary incontinence

TABLE II  
EFFECTS OF RISK FACTORS ON URINARY INCONTINENCE

Predictor Variables	Regression Coefficient
Constant	0.062
Constipation	0.001
Renal Pain	0.073
Prostate	0.065
Diabetes	0.051
Menopause	0.026

Elastic net regression:Dependent variables: Urinary Incontinence; MAE:1.823;RMSE:2.316; R<sup>2</sup>:0174

The difference between the RSV values of urinary incontinence and risk factors in terms of months are defined in table 3. The difference were determined among urinary incontinence, Prostate, cystitis, constipation, diabetes, renal pain and fistula RSV values in terms of months ( $p < 0.05$ ). RSV values of urinary incontinence, renal pain, diabetes and prostate are higher in November compared to other months. The change in RSV values of renal pain, diabetes and prostate in terms of months show similarity with the change in urinary incontinence.

TABLE III  
COMPARISON OF RSV VALUES OF RISK FACTORS AND URINARY INCONTINENCE BY MONTHS

	Urinary Incontinence Mean±SD	Constipation Mean±SD	Cystitis Mean±SD	Renal Pain Mean±SD	Prostate Mean±SD	Diabetes Mean±SD	Menopause Mean±SD	Vaginal Infection Mean±SD	Fistula Mean±SD
<b>December</b>	7,39±2,90	49,43±7,58	10,65±2,44	17,04±4,94	44,38±8,74	36,52±6,72 <sup>1</sup>	22,04±4,82	2,09±1,35	7,61±2,74
<b>January</b>	7,61±1,64	53,00±4,70	11,22±1,59	16,91±4,32	46,48±6,89	32,13±5,30 <sup>1</sup>	<b>23,00±5,57</b>	2,17±1,15	7,70±2,12
<b>February</b>	7,58±2,85	51,74±6,12	11,05±3,92	16,11±4,51	47,74±10,81	33,84±6,79 <sup>1</sup>	22,89±4,33	2,21±1,40	7,84±2,93
<b>March</b>	6,50±2,50	49,68±7,37	10,32±2,97 <sup>1</sup>	16,09±4,00	45,00±14,85	35,32±5,95 <sup>1</sup>	21,23±5,65	2,45±1,34	7,23±2,69
<b>April</b>	5,68±1,84	51,82±10,93	10,91±2,99	16,00±4,92	38,27±8,68	33,18±5,40 <sup>1</sup>	19,64±3,99	1,91±1,11	7,09±2,31
<b>May</b>	5,32±1,96 <sup>k</sup>	<b>53,14±16,68</b>	10,82±2,54	14,68±3,12	40,73±7,09	31,73±6,66 <sup>1</sup>	20,45±4,91	1,91±1,11	6,18±1,97
<b>June</b>	4,71±1,71 <sup>1</sup>	46,14±6,92	12,38±2,96	13,67±3,40 <sup>1</sup>	38,24±8,80	26,57±3,92 <sup>1</sup>	21,00±4,99	2,05±0,97	7,14±2,31
<b>July</b>	4,61±2,68 <sup>1</sup>	44,65±7,28 <sup>f</sup>	12,74±2,80	13,61±3,16 <sup>1</sup>	40,78±12,95	24,30±5,38 <sup>1</sup>	19,30±3,95	1,96±1,36	6,74±2,36
<b>August</b>	4,24±2,05 <sup>1</sup>	46,67±6,58	<b>12,81±3,08</b>	15,24±3,33	37,24±7,55 <sup>1b</sup>	24,57±4,74 <sup>1</sup>	21,19±4,15	2,43±1,21	5,81±2,46 <sup>k</sup>
<b>September</b>	5,55±1,97 <sup>1</sup>	42,00±4,82 <sup>f</sup>	11,91±2,22	15,23±3,32	40,91±6,60	25,23±4,98 <sup>1</sup>	22,05±3,67	2,59±1,44	6,14±1,98
<b>October</b>	6,91±2,02	44,91±6,02 <sup>f</sup>	12,23±2,93	16,05±3,48	43,00±7,80	30,55±5,49 <sup>1</sup>	21,32±5,48	<b>2,68±1,67</b>	<b>8,18±2,67</b>
<b>November</b>	<b>7,86±2,87</b>	43,90±4,39 <sup>f</sup>	11,33±2,37	<b>18,62±4,44</b>	<b>47,96±8,51</b>	<b>54,43±22,12</b>	20,00±4,57	2,29±1,27	7,24±3,10
P	p<0.001*	p<0.001*	0.023*	0.002*	p<0.001*	p<0.001*	0.179	0.526	0.042*

Anova ; $\alpha$ :0.05; Post-hoc: Tukey HSD test; Tamhane T2 test;\*Statistical significance; <sup>a</sup>Significant difference with December values; <sup>b</sup>Significant difference with January values; <sup>c</sup> Significant difference with February values; <sup>d</sup> Significant difference with March values; <sup>e</sup> Significant difference with April values; <sup>f</sup> Significant difference with May values; <sup>g</sup> Significant difference with June values; <sup>h</sup> Significant difference with July values; <sup>i</sup>Significant difference with August values; <sup>j</sup> Significant difference with September values; <sup>k</sup>Significant difference with October values; <sup>l</sup> Significant difference with November values

#### IV. DISCUSSIONS

Urinary incontinence is an important health problem affecting the individuals' life quality negatively [23]. For the treatment of urinary incontinence, the factors causing this situation should be determined correctly. There are various factors causing urinary incontinence. Age, gender, sociologic and psychologic factors, physical factors, comorbid diseases may be listed. People generally do not prefer to go to the hospital due to the sense of embarrassment or being blamed [24]. Alternatively, in order to get information about urinary incontinence, people are getting informed by using internet search engines and try to find the reasons and treatment methods thereof. In this study, the seasonality of urinary incontinence and factors causing it were researched through infodemiologic procedures. In the study, relative search values for urinary incontinence in internet search engine were assessed. RSV values of the terms relevant to urinary incontinence were reached by Google Trends.

Some diseases may show seasonality depending on environmental and physiological properties. Most of the contagious diseases may show seasonality [25]. Rotavirus shows seasonality in tropical climates and more rotavirus cases are seen in cold air [26]. Watad et al.(2017) in their studies, stated that autoimmune diseases may be affected by environmental factors, Type 1 Diabetes Mellitus and Multiple Sclerosis diseases. Autoimmune diseases change seasonally and are observed more in spring. [27]. Rosello et al. (2018), in their studies, stated that urinary tract infections show seasonality. Urinary tract values infection is mostly observed in September-November period [28]. In our study, urinary incontinence's seasonality was evaluated by infodemiologic researches. The research was made nationwide in Turkey. Weather is generally hot in spring (March-April-May) and summer (June-July-August) whereas the weather is cold in autumn (September-October-November) and winter (December-January-February). In our study, it is determined that urinary incontinence reveals seasonality. In the study,

November was found to have the highest urinary incontinence values. RSV values relevant to urinary incontinence were observed to reach at the highest level between November-February periods.

Different risk factors lead to urinary incontinence to occur. Urinary incontinence may be observed more by some factors such as; physical disorders, higher age, obesity and gender [29]. Urinary incontinence is observed more in women. Urinary tract infection, intestinal obstruction, vaginal birth, menopause, hormonal disorders are defined as important risk factors for urinary incontinence for women [30-31]. Diabetes, body mass index is the most important risk factor for women; whereas advanced age, prostate, cystitis and urinary tract infection is the most important risk factor for urinary incontinence for men [32]. In this study, for the determination of risk factors relevant with urinary incontinence, an infodemiologic research was made. Besides the 5 years RSV values of urinary incontinence, 5 years- RSV values of the words; prostate, constipation, renal pain, vaginal infection cystitis, menopause, diabetes and fistula were also researched. Prostate, diabetes, menopause, constipation and renal pain were observed to be the factors affecting urinary incontinence. Our findings provided various results which are compliant with the literature.

The study involves some constraints. In the study, Relative Search Volumes of the words relevant to urinary incontinence which are searched by the people in internet search engines were evaluated. Apart from the risk factors specified in the study, despite different risk factors affecting urinary incontinence, these factors were not included into the study as they have not been searched on internet search engines. Urinary incontinence and risk factors are searched under different names in the society. Therefore in Google Trends inquiries, the most used terms thereof have been researched. The study was conducted in Turkey only. As the genders, ages and comorbid diseases of the searchers are not known, the data in the study were not assessed according to age, gender and comorbid diseases. In literature, as there is not a known research made for urinary incontinence's infodemiologic

researches, the findings of the study were not compared with the literature.

## V. CONCLUSION

In this study, an infodemiologic research was made for the determination of the seasonality of urinary incontinence and the risk factors affecting it. In the study, RSV values in Google Trends regarding urinary incontinence and risk factors were evaluated in Turkey for the period 2016 – 2021. According to the findings, urinary incontinence reveals seasonality. The highest rate of urinary incontinence case is observed between November-February. Risk factors affecting this disease were determined. Prostate, diabetes, renal pain, constipation and menopause affect urinary incontinence. With RSV values obtained from Google Trends, successful estimations have been made for the determination of seasonality relevant to urinary incontinence and for the evaluation of risk factors thereof. By including more risk factors in the study, the research's estimation achievement may be increased. Including different countries into the study may provide a contribution to the generality of the findings. For the researches in which various difficulties are encountered for the determination of prevalence, infodemiologic researches may be an important alternative to field researches.

## ACKNOWLEDGMENT

The author declares that they have no conflict of interest. There is no funding for this study. We did not evaluate any human participants or animals in this study. Data that anyone can access were evaluated. Therefore, there was no need for approval of the ethics committee for this study.

## REFERENCES

- [1] Y. Ahn and Y. Jun, "Measurement of pain-like response to various NICU stimulants for high-risk infants," *Early Hum. Dev.*, vol. 83, no. 4, pp. 255–262, 2007.
- [2] B. T. Haylen et al., "An international urogynecological association (IUGA)/international continence society (ICS) joint report on the terminology for female pelvic floor dysfunction," *Neurourology and Urodynamics*, vol. 29, no. 1, pp. 4–20, 2010.
- [3] S. Hunnskaar, K. Burgio, A. Diokno, A. R. Herzog, K. Hjälmås, and M. C. Lapitan, "Epidemiology and natural history of urinary incontinence in women," in *Urology*, 2003, vol. 62, no. 4 SUPPL. 1, pp. 16–23.
- [4] DeMaagd, G.A. and Davenport, T.C., "Management of urinary incontinence", *Pharmacy and Therapeutics*, vol.37, no.6, pp.345, 2012.
- [5] R. Onur, S. E. Deveci, S. Rahman, F. Sevindik, and Y. Acik, "Prevalence and risk factors of female urinary incontinence in eastern Turkey," *Int. J. Urol.*, vol. 16, no. 6, pp. 566–569, 2009.
- [6] I. Maral, H. Özkardeş, L. Peşkirioğlu, and M. Ali Bumin, "Prevalence of stress urinary incontinence in both sexes at or after age 15 years: A cross-sectional study," *J. Urol.*, vol. 165, no. 2, pp. 408–412, 2001.
- [7] J. Edgley, "The psychosocial impact of incontinence on older people: a review," *Nursing older people*, vol. 14, no. 1, pp. 17–19, 2002.
- [8] F. Güngör Uğurlucan, C. Comba, Ş. Emegil, and Ö. Yalçın, "thoughts and attitudes toward urinary incontinence in Turkey," *Journal of Istanbul Faculty of Medicine*, vol. 79, no. 4, pp. 141–141, 2016.
- [9] B. K. Agarwal and N. Agarwal, "Urinary incontinence: prevalence, risk factors, impact on quality of life and treatment seeking behaviour among middle aged women," *Int. Surg. J.*, vol. 4, no. 6, p. 1953, 2017.
- [10] A. Dinç, "Prevalence of Urinary Incontinence During Pregnancy and Associated Risk Factors," *LUTS Low. Urin. Tract Symptoms*, vol. 10, no. 3, pp. 303–307, 2018.
- [11] G. Eysenbach, "Infodemiology: The epidemiology of (mis)information," *American Journal of Medicine*, vol. 113, no. 9, pp. 763–765, 2002.
- [12] Google Trends. URL: <https://trends.google.com/trends/?geo=TR>. (visited on Feb 24-26, 2021).
- [13] A. Mavragani and G. Ochoa, "Google Trends in Infodemiology and Infoveillance: Methodology Framework," *JMIR Public Heal. Surveill.*, vol. 5, no. 2, p. e13439, 2019.
- [14] A. Mavragani and K. Gkillas, "COVID-19 predictability in the United States using Google Trends time series," *Sci. Rep.*, vol. 10, no. 1, 2020.
- [15] S. Morsy et al., "Prediction of Zika-confirmed cases in Brazil and Colombia using Google Trends," *Epidemiol. Infect.*, vol. 146, no. 13, pp. 1625–1627, 2018.
- [16] L. Samaras, E. Garcia-Barriocanal, and M.-A. Sicilia, "Syndromic Surveillance Models Using Web Data: The Case of Influenza in Greece and Italy Using Google Trends," *JMIR Public Heal. Surveill.*, vol. 3, no. 4, p. e90, 2017.
- [17] J. Parker, C. Cuthbertson, S. Loveridge, M. Skidmore, and W. Dyar, "Forecasting state-level premature deaths from alcohol, drugs, and suicides using Google Trends data," *J. Affect. Disord.*, vol. 213, pp. 9–15, 2017.
- [18] M. Moccia, R. Palladino, A. Falco, F. Saccà, R. Lanzillo, and V. Brescia Morra, "Google Trends: New evidence for seasonality of multiple sclerosis," *Journal of Neurology, Neurosurgery and Psychiatry*, vol. 87, no. 9, pp. 1028–1029, 2016.
- [19] L. Rossignol, C. Pelat, B. Lambert, A. Flahault, E. Chartier-Kastler, and T. Hanslik, "A Method to Assess Seasonality of Urinary Tract Infections Based on Medication Sales and Google Trends," *PLoS One*, vol. 8, no. 10, 2013.
- [20] X. Zhang et al., "Seasonality of cellulitis: Evidence from Google Trends," *Infect. Drug Resist.*, vol. 11, pp. 689–693, 2018.
- [21] J. Friedman, T. Hastie, and R. Tibshirani, "Regularization paths for generalized linear models via coordinate descent," *J. Stat. Softw.*, vol. 33, no. 1, pp. 1–22, 2010.
- [22] H. Zou and T. Hastie, "Regularization and variable selection via the elastic net," *J. R. Stat. Soc. Ser. B Stat. Methodol.*, vol. 67, no. 2, pp. 301–320, 2005.
- [23] V. A. Minassian, H. P. Drutz, and A. Al-Badr, "Urinary incontinence as a worldwide problem," *Int. J. Gynecol. Obstet.*, vol. 82, no. 3, pp. 327–338, 2003.
- [24] S. Horrocks, M. Somerset, H. Stoddart, and T. J. Peters, "What prevents older people from seeking treatment for urinary incontinence? A qualitative exploration of barriers to the use of community continence services," *Fam. Pract.*, vol. 21, no. 6, pp. 689–696, 2004.
- [25] D. Fisman, "Seasonality of viral infections: Mechanisms and unknowns," *Clinical Microbiology and Infection*, vol. 18, no. 10, pp. 946–954, 2012.
- [26] K. Levy, A. E. Hubbard, and J. N. S. Eisenberg, "Seasonality of rotavirus disease in the tropics: A systematic review and meta-analysis," *International Journal of Epidemiology*, vol. 38, no. 6, pp. 1487–1496, 2008.
- [27] A. Watad et al., "Seasonality and autoimmune diseases: The contribution of the four seasons to the mosaic of autoimmunity," *Journal of Autoimmunity*, vol. 82, pp. 13–30, 2017.
- [28] A. Rosello et al., "Seasonality of urinary tract infections in the United Kingdom in different age groups: Longitudinal analysis of The Health Improvement Network (THIN)," *Epidemiol. Infect.*, vol. 146, no. 1, pp. 37–45, 2018.
- [29] Y. Aoki, H. W. Brown, L. Brubaker, J. N. Cornu, J. O. Daly, and R. Cartwright, "Urinary incontinence in women," *Nat. Rev. Dis. Prim.*, vol. 3, 2017.
- [30] P. Norton and L. Brubaker, "Urinary incontinence in women," in *Lancet*, 2006, vol. 367, no. 9504, pp. 57–67.
- [31] L. A. Möller, G. Lose, and T. Jørgensen, "The prevalence and bothersomeness of lower urinary tract symptoms in women 40-60 years of age," *Acta Obstet. Gynecol. Scand.*, vol. 79, no. 4, pp. 298–305, 2000.
- [32] B. S. Buckley and M. C. M. Lapitan, "Prevalence of urinary incontinence in men, women, and children-current evidence: Findings of the fourth international consultation on incontinence," *Urology*, vol. 76, no. 2, pp. 265–270, 2010.

## BIOGRAPHIES



**ADEM DOGANER** obtained his BSc. degree in Statistics from Mugla University in 2008. He received MSc. degree in Statistical Information Systems from the Fırat University in 2011, and Ph.D. degrees in Statistical Information Systems from the Fırat University in 2015. Adem Doganer has a second Ph.D degree on Biostatistics and Medical Informatics from the Inonu University in 2020. He is currently working as an assistant professor the Department of Biostatistics and Medical Informatics in Kahramanmaraş Sutcu Imam University His research interests are, Statistical analysis, information systems, cognitive systems, bionformatics, data mining, Modeling and simulation, machine learning, artificial intelligence.

# Reconstruction with In-Line Digital Holography Quantitative Phase Imaging for Tissue- Mimicking Phantom Samples

Tugba Ozge Onur and Gulhan Ustabas Kaya

**Abstract**—Optical imaging has attracted recent attention as a non-invasive medical imaging method in biomedical and clinical applications. In optical imaging, a light beam is transmitted through an under-test tissue by using an optical source. The beams which are gone through the tissue and/or reflected from the tissue surfaces are received by an array sensor. Based on the light intensity of these received beams on the sensor, sub-tissue maps are generated to scan large tissue areas so that any further biopsy is not required. Although the large tissue areas in pathological images can be scanned by using various methods, nonlinear deformations occur. To overcome this problem, the reconstruction process is frequently used.

In this study, we propose an application of biomedical imaging based on performing the reconstruction of a phantom image via an in-line digital holography technique. Hence, many different sub-tissues can be imaged at the same time without the storage problem of the reconstructed image. To neglect the biopsy process required in medical imaging, the phantom image is obtained by using a linear array transducer for this study. We present the performance evaluation of the simulation results for the proposed technique by calculating the error metrics such as mean squared error (MSE), mean absolute error (MAE) and peak signal-to-noise ratio (PSNR). The obtained results reveal that the reconstructed images are well-matched to the original images, which are desired to be displayed by the holography technique.

**Index Terms**—In-line digital holography, image reconstruction, optical imaging, phantom image.

## I. INTRODUCTION

IMAGING TECHNOLOGY is conventionally used both for the detection and localization of disease and mapping the anatomy of the human body. Hence, new medical imaging

TUĞBA ÖZGE ONUR, is with Department of Electrical Engineering University of Zonguldak Bülent Ecevit University, Zonguldak, Turkey, (e-mail: [ozdincozge@gmail.com](mailto:ozdincozge@gmail.com)).

 <https://orcid.org/0000-0002-8736-2615>

GÜLHAN USTABAŞ KAYA, is with Department of Electrical Engineering University of Zonguldak Bülent Ecevit University, Zonguldak, Turkey, (Corresponding Author e-mail: [gulhan.ustabas@beun.edu.tr](mailto:gulhan.ustabas@beun.edu.tr)).

 <https://orcid.org/0000-0002-5643-0531>

Manuscript received November 23, 2020; accepted April 27, 2021.  
DOI: [10.17694/bajece.829857](https://doi.org/10.17694/bajece.829857)

technologies that provide insight into the function, physiology, and metabolism of an organ have constantly been developed. These technologies are so crucial because the accurate diagnosis of diseases with advanced visuals are obtained by medical images and therefore, effective personal treatment options can be provided for all diseases. There are several commonly used types of medical imaging such as computed tomography (CT), mammography, positron emission tomography (PET), single photon emission computerized tomography (SPECT), magnetic resonance imaging (MRI) and etc. [1-3].

Differently from other medical imaging techniques such as x-rays, since visible light and photons are used in optical imaging, it is possible to achieve more detailed image versions of the body region of interest [4]. It also enables smaller structures such as cells and molecules to be visualized. For instance, biomedical optical imaging (BOI) methods are based on transferring a light beam through the tissue and collecting photons that escape from the tissue surface. In the BOI methods, the light beam is transferred through the tissue and the reflected beams are received by photo-detectors or cameras where the light intensity is measured by forming algorithms. The photons sent to the living tissue continue their travel between the organelles within the tissue cells (the largest of which is the nucleus organ) with diffraction through the cell membranes and absorption in the micro-molecules inside the cell, and the routes are determined as a result of these travels [4].

The obtained images with optical imaging can be used for the diagnosis and treatment of diseases by clinicians. In addition to imaging advantages, optical imaging also has several advantages in other respects [5]. One of them, and perhaps most importantly, is that the optical imaging decimates the harmful radiation to which the patient is exposed. Another one is that, unlike other imaging techniques, in optical imaging, many different features of an organ or a tissue can be seen and measured at the same time by using various light colors. All these advantages make optical imaging popular today. Thus, the studies in this area have increased tremendously for the last few years [6-13].

On the other hand, physical phantoms are used for clinical verification of current and newly developed medical imaging methods under different conditions. The validity of the imaging method is tested by performing various tests on the used phantoms such as geometric accuracy, dose algorithm

accuracy, image quality, machine and patient quality assurance, irradiation techniques [1, 14-16]. Therefore, the structure of the used phantom and the quality of the obtained medical image are important criteria to evaluate the performance of the imaging system. The solution to overcome these problems can be applying the image reconstruction process to the medical images via optical imaging. In addition, to obtain the three dimensional (3D) medical images, the reconstruction process is required where the series of images are sliced from a target sub-tissue [17-19].

#### A. Related Works and Motivation

In the literature, the sub-tissue images obtained by image reconstruction include the images of the sub-tissue microstructures although they cannot be seen directly with the human eye. [18, 19]. The sub-tissue maps are created with the light intensity values measured from the surfaces. On the other hand, the unnatural deformations of the anatomical structures are occurred resulting from the matching of the adjacent images. To remove the nonlinear deformation of the pathological images, the three dimensional (3D) reconstruction process is frequently used in the literature [17]. Kugler et al. proposed a non-rigid image registration method to reconstruct the 3D image of the microstructures in the tissue. They consider the smoothness of each constituent and the spatial continuity of the tissue [20]. Adler et al. reconstructed the post mortem MR images [21].

Digital holography is one of the methods to reconstruct the image in 3D [8]. In this context, Depeursinge et al. developed a method to observe the deformations and very small movements in excitable cells and tissue by using digital holography. This method allows determining the cells and morphology of the tissue [10]. However, in the mentioned studies of literature, the reconstructed images cannot be stored efficiently. To overcome this problem, holography technique can be used to reconstruct the image [8].

In the holography, the accurate three-dimensional (3D) imaging can be achieved by using the correct depth markings, without the necessity of specific imaging devices and strain of the eye [22, 23]. The 3D image which is recorded holographically can be reconstructed for visualization purposes. In addition to this, recording holographically have advantages in terms of storage since the obtained 3D information can be stored efficiently and encryptedly in holograms. Unfortunately, a long-time processing for the recording and a powerful laser source are needed for the traditional optical holographic recording process. This problem has been resolved in digital holography (DH) by using a digital camera for recording the media [8]. Because, after the phase and amplitude information of the object is recorded as digital in the CCD or CMOS cameras (recorded as a hologram), the object itself can be retrieved as digital by using reconstruction methods. On the other hand, instead of the photochemical procedures in traditional holography, the digital methods make the DH attractive in a wide variety of fields for science and technology.

One of the main features of the DH is that to be a full-field with high-resolution technique which records amplitude and phase information of the sample to be displayed. On the other

hand, the optical field consisting of amplitude and phase information is measured in holography and interferometry while only the amplitude information is measured in conventional bright field imaging [24]. The cells and the tissues that are intended to be viewed medically have a transparent appearance when they are in the visible light zone. The phase information becomes beyond only a feature since there will be no good contrast in amplitude information when the samples are transparent. Because the transparent samples create a phase delay for the hologram records in the DH. In other words, when an optical wave passes through a transparent object with a thickness and refractive index, it experiences a phase delay which has detailed structural information about the sample [25]. Therefore, the phase information created by these phase delays is used in the DH while the images are reconstructed [26, 27].

The DH has enabled non-contact measurement of the cells and the tissues and their pathophysiological differentness [28]. Therefore, there have been various researches in literature related to the DH applications in the field of biomedical imaging, recently. Kim [29] has provided a review of the DH by examining its applications in the biomedical imaging. Furthermore, researchers have applied the DH to image various cell types such as red blood cells [30], fibroblast cells [31], diatom skeletons [32] and cancer cells [33].

#### B. Contribution

The main contributions of this paper is to apply the in-line digital holography technique for biomedical image reconstruction with different phantoms. Hence, the storage problem of the reconstructed image can be neglected by using digital holographic reconstruction process. Another one is that, many different sub-tissues can be detected at the same time. On the other hand, any further biopsy is not required when the created phantom image is used.

We present an application of biomedical imaging based on performing the reconstruction of a phantom image by using the in-line DH technique, which has been carried out with simulations by evaluating the image quality measurement. To this end, the hologram of the images obtained with a linear array transducer has been created with computer simulations by using the hologram recording and reconstruction senses in the DH. Thereafter, the phase information has been extracted from these holograms and the samples have been reconstructed in 3D. Based on the simulation results, the difference between the created phantom image and the reconstructed images are quite low. In this context, we reveal that using the DH reconstruction process with simulation and the phantom image is superior to conventional reconstruction techniques in terms of storage of reconstructed image and human health.

The rest of this paper is organized as follows: A summary of the formation of the used phantom image and the basic principles of in-line DH technique have been introduced in Section II. The Section III presents the obtained results and the superiority of the proposed technique has been revealed. Finally, the Section IV discusses the results and concludes the paper.

## II. SIMULATION PROCESS

### A. Image Formation

The data used in this study has been obtained by using a linear array transducer consisting of various transducers. By sampling with 128 beam lines at 40 MHz, the data has been collected in the sample where the sound velocity is 1540 m/s. Beam lines are 15 mm apart. One of the used phantom was formed by randomly inserting 5-43  $\mu\text{m}$  glass beads scatters into the agar gel. Phantom images presented in Fig. 4a and 5a are created with simulation by applying logarithmic compression and histogram equalization methods in MATLAB program [34]. In addition, for the other one, a cylindrical phantom with two cylindrical fields that have similar sound velocities and a three-wire filament was used. The value of related parameters such as radius (r), speed of sound (c), density ( $\rho$ ) and attenuation ( $\mu$ ) for the phantom is detailed in Fig.1. Thereafter, with the help of this known model data, the phantom image given in Fig. 6a is created by using MATLAB program [35].

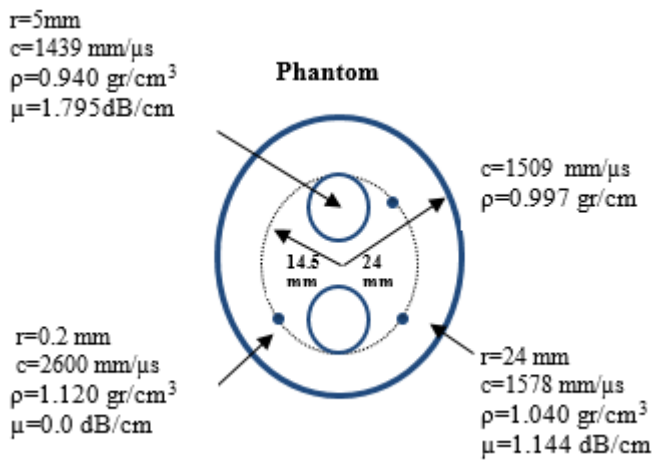


Fig.1. Phantom model used for created phantom [35]

### B. Creation of the Hologram with Simulation

To create a hologram by simulation, the events that are the bases of the hologram recording should be expressed mathematically. Therefore, at this part of the study, the mathematical expressions used to create the hologram in in-line holography are provided. In this context, the methods of simulating holograms created with plane waves are described in Fig. 2. Thereafter, the original images of the samples are reconstructed from the created hologram [36].

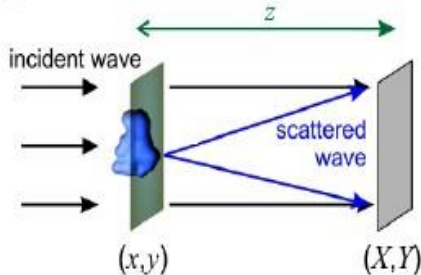


Fig.2. The scheme of in-line holography realized by using a plane wave [36]

Before describing the in-line holography, the description of the plane wave should be given. The plane wave defined by a distribution with complex-valued ( $\exp(i(k_x x + k_y y + k_z z))$ ) has a constant phase value on all planes perpendicular to the wave propagation direction at time  $t$ . In an arbitrary timescale,  $t=0$  can be accepted to define the spatial distribution of the wave. In 3D space,  $k = k_x, k_y, k_z$  is defined as the wave vector, and  $k_x, k_y, k_z$  are the vector components of this wave. Here,  $k$  is defined as the number of the waves ( $k = \frac{2\pi}{\lambda}$ ).  $\lambda$  is the wavelength of the light [37].

Two plane waves called reference and object waves are used to create a hologram in in-line holography. The object to be recorded on the hologram and the beam which comes from the light source are in the same plane. While the wave that the beam generates by reflecting from the object is called the object wave ( $O_{exit\_wave}(x, y)$ ), the reference wave ( $R_{incident}(x, y)$ ) never touches the object along the plane. With the superposition of these waves, two light waves constitute an interference.

In this context, when the object position is set to  $z=0$  by selecting the origin of the  $z$  axis, the incident wave is given as

$$R_{incident}(x, y) = R_0 \exp(i(\phi_1(x, y))) = 1 \quad (1)$$

This incident wave is called the reference wave ( $R_{incident}$ ). Here, we can select the optical axis along the propagation of this plane wave to achieve  $k_x = k_y = 0$  [36, 37]. In Eq. (1),  $(x, y)$  is identified as the coordinates of the plane.

On the other hand, the wave, whose information that will be recorded on the hologram and reflected from the object constitutes the object wave. This wave propagation is expressed mathematically with a transmission function (See Eq. (2)) as

$$\begin{aligned} O_{exit\_wave}(x, y) &= t(x, y) \\ &= \exp(-a(x, y)) \exp(i\phi_2(x, y)) \end{aligned} \quad (2)$$

where the absorption is defined as  $a(x, y)$  and the phase distribution is given as  $\phi(x, y)$ .

As mentioned above, the interference pattern created by the object and reference waves in the recording plane ( $X, Y$ ) is given by the Fresnel-Kirchhoff diffraction formula given in Eq. (3). It expresses the propagated wave, which is spread from the object plane ( $x, y$ ) toward the recording-CCD/CMOS camera plane ( $X, Y$ ) [36].

$$U_{\text{detector}}(X, Y) = \frac{i}{\lambda} \iint R_{\text{incident}}(x, y) t(x, y) \frac{\exp(ik|\vec{r} - \vec{R}|)}{|\vec{r} - \vec{R}|} d_x d_y \quad (3)$$

where the distance of the object plane  $(x, y)$  to the recording detector plane is given as  $|\vec{r} - \vec{R}| = \sqrt{(x - X)^2 + (y - Y)^2 + z^2}$ .

In this expression, the constant phase is neglected.

Hologram simulations based on the creating hologram with mathematical expressions consist of the following steps:

1. Firstly, the object to be created hologram should be imread.
2. Secondly, the coordinate axes should be determined and the imread object should be placed on the coordinate axes.
3. Thirdly, once the reference coordinates are also determined, the created hologram should be placed on the coordinate axes.
4. Finally, by using the Eq. (3), the interference pattern should be calculated.

In order to reconstruct the sample object from the hologram created by simulation and to extract the phase information, Fourier transform algorithm (FTA) is used in this study [36, 38, 39]. Therefore, to find the phase information and to reconstruct the object, the following processes should be implemented.

a) Fourier transforms of the holograms are taken line by line.

b) An appropriate filtering is done to separate the real and virtual images. This filtering is applied by spatially in the Fourier domain.

c) With this process, the maximum frequency point where the phase is collected can be found. Hence, it will be filtered since it is the virtual region after the half of the amplitude and phase sequences.

d) Finally, the phase of the hologram is obtained by taking the inverse Fast Fourier transform (IFFT) line by line.

### III. SIMULATION RESULTS

In this study, the used phantom image, created by randomly inserting glass beads scatters, has been obtained by using a linear array transducer. Thereafter, the holograms of the acquired images have been produced by simulations and the real phantom images have been extracted from the phase information of these images with the reconstruction process.

As a first step, instead of the obtained phantom images, the hologram of the words "phantom created with glass bead", written in paint program, has been created by simulation. The phase information has been extracted from these holograms to retrieve the original text. The original, the reconstructed and the hologram images for the used text "phantom created with glass bead" are presented in Fig. 3, respectively.

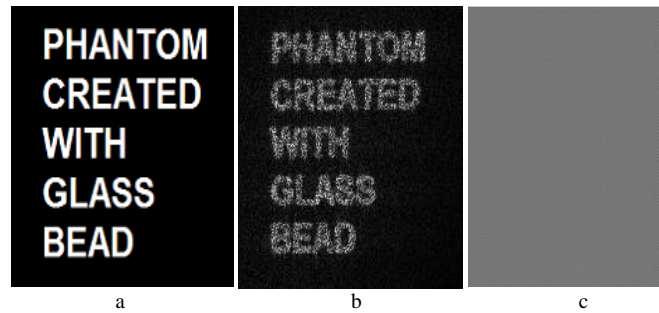


Fig. 3. Simulation results; a) Original text created in paint program; b) Reconstruction of the original text; c) Hologram of the original text structure

For the second stage of the study, a hologram has been created from the images of the phantom which is formed by randomly inserting glass beads scatters into agar gel and viewed by a linear array transducer. Then, the phase information has been extracted from these holograms to reconstruct the original phantom image as stated in the first step. The obtained results for three different phantom images are presented in Fig. 4, Fig. 5 and Fig. 6, respectively.

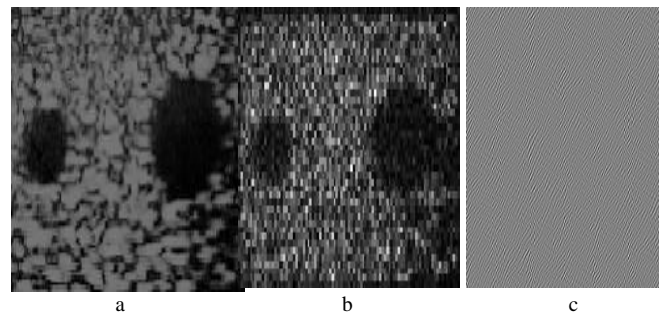


Fig. 4. Simulation results; a) First image of the used phantom b) Reconstruction of the first image c) Hologram of the first image

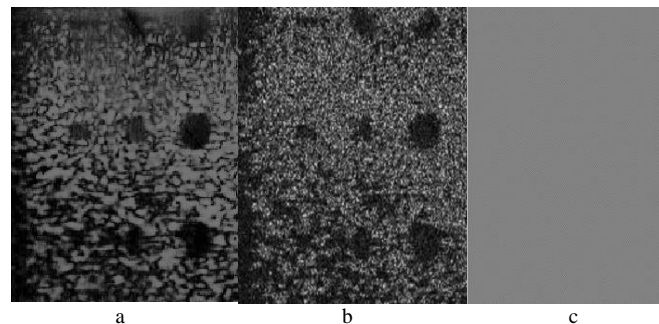


Fig. 5. Simulation results; a) Second image of the used phantom b) Reconstruction of the second image c) Hologram of the second image

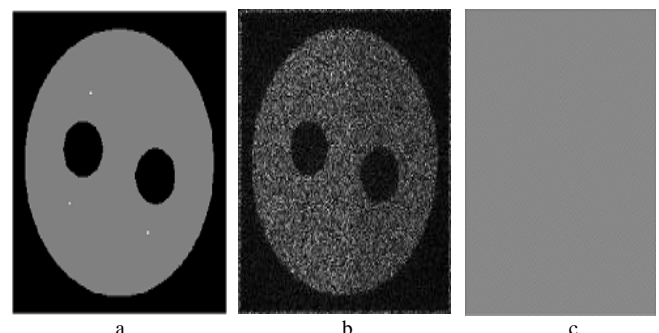


Fig. 6. Simulation results; a) Third image of the used phantom [35] b) Reconstruction of the third image c) Hologram of the third image

Finally, the differences between the used original images whose holograms to be created and the reconstructed images by using the phase information of the hologram have been revealed by the mean squared error (MSE), mean absolute error (MAE) and peak signal-to-noise ratio (PSNR) which are the most common predictors of image quality measurement and calculated by using the equations given in Eqs. (4-6) respectively [40-42].

$$MSE = \frac{1}{mn} \sum_{i=0}^{m-1} \sum_{j=0}^{n-1} (I(i, j) - K(i, j))^2 \quad (4)$$

$$MAE = \frac{1}{mn} \sum_{i=1}^m \sum_{j=1}^n |I(i, j) - K(i, j)| \quad (5)$$

$$PSNR = 10 \log_{10} \frac{(2^n - 1)^2}{\sqrt{MSE}} \quad (6)$$

where  $m$  and  $n$  are the numbers of the rows and columns of the images (size of the images),  $i$  and  $j$  are the indices of the pixel values which are investigated in the images.  $I$  and  $K$  are the original and the reconstructed images, respectively. The comparison of MSE, MAE and PSNR quality measurements values for the used original images are given in Table I [40], and the calculation of these metrics between the used images to create the holograms and the reconstructed ones are presented in Table II.

TABLE I  
MSE, MAE AND PSNR VALUES FOR ORIGINAL IMAGES [40]

Original Image Values		
No	The Parameter of Quality Measurement	Quality Value
1	MSE	0
2	MAE	0
3	PSNR	$\infty$

TABLE II  
MSE, MAE AND PSNR VALUES OF THE USED AND RECONSTRUCTED IMAGES

Used Image	MSE	MAE	PSNR
Original text created in paint program	0.0226	0.0511	116.1410
First image of the used phantom	0.0400	0.0925	92.0757
Second image of the used phantom	0.0307	0.0803	103.6434
Third image of the used phantom	0.0181	0.0587	126.5263

It can be seen from Table II, consistent results are found for all used images in terms of MSE and MAE since the closer to zero values are achieved which are the better performance in

terms of MSE and MAE reference metric [40,41]. Moreover, the indication of the higher quality for the reconstruction is generally a higher PSNR value. The results obtained for all used phantom images are in the desired levels in terms of PSNR values.

#### IV. CONCLUSION AND DISCUSSIONS

The BOI has become a developing imaging technique with the DH imaging. In other medical imaging techniques, small lesions, masses, or the structure of existing masses in the investigated tissue or organ are often undetectable. This situation causes delays in diagnosis and treatment phases. Also, in these methods, it is mostly sent to pathology at the detection stage and either by passing through a set of biochemical agents which is called staining or after cutting the tissue directly, it is cut into slices and displayed under a microscope. Cells are examined histopathologically by staining with biochemical agents.

The reason for the examining under microscopy is to understand what tissue cells look like and if the carcinogen ones are malignant or benign to understand its kind and diagnose accordingly and to initiate treatments. Since both phase and amplitude information can be recorded and the object itself can be retrieved without any loss of information from these in digital holography, the presence of these cells can be diagnosed in tissues and similar cells without the need for pathological examination and the treatment process can be accelerated. In addition, the ability to obtain detailed images without exposure to excessive radiation makes the imaging technique superior to other similar methods.

Tissue mimicking phantoms have a wide range of biomedical applications in the field of various techniques such as, Raman spectroscopy, digital holography, acoustic waves imaging, photoacoustic imaging, holographic tomography microscope (HTM) and etc. (Table III). Most of the mentioned applications are used to analyze the characterization of the phantoms whereas some of them are used to investigate the reconstruction process of many different tissue types. A comparison of this work with existing studies in the literature are given in Table III.

For instance, Chaiken et al. evaluate the system for the detection of glucose in blood by using tissue modulated Raman spectroscopy [43]. Hydrogel is used for tissue model. They also discuss the variations between the spectra human blood in vitro and their noninvasively measuring spectra. Raman spectroscopy is also used by Vardaki et al. to review the biomedical applications for the types of tissue phantoms that are created as liquid phantoms [44]. Shiguang et al. produce the homogeneous and two-layer soft-tissue phantoms to map the elasticity inside soft tissues. They perform their study by using digital holography and surface acoustic waves imaging [45]. Karaböce et al. detect the positions of objects inside the phantom that created with agar gel. The Sonix Touch Q "+" ultrasonic device and different types of probes are used to verify the image processing and measurement in this study [46]. Maneas et al. introduce the gel wax-based tissue-mimicking phantom for imaging with photoacoustic. The acoustic and optical characterizations are investigated on homogeneous phantoms [47].

TABLE III  
RELEVANT STUDIES DEALING WITH BIOMEDICAL APPLICATIONS  
FOR THE TYPES OF TISSUE PHANTOMS

Authors	Simulated tissue/ purpose of the study	Used method	Phantom type
Chaiken et al (2001)[43]	To evaluate the system for the detection of glucose in blood	Raman spectroscopy	Hydrogel
Shiguang et al. (2011)[45]	To map the elasticity inside soft tissues	Digital holography and surface acoustic waves imaging	Homogeneous and two-layer soft-tissue phantoms
Karaböce et al. (2017) [46]	To verify the measurement results of different objects in tissue-mimicking phantom	Sonix Touch Q "+" ultrasonic device and different types of probes	Agargel
Maneas et al. (2018) [47]	To introduce the gel wax based tissue-mimicking phantom	Multispectral photoacoustic imaging	Gel wax
Pichat et al. (2018)[18]	To review the 3D histology reconstruction methods for many different types of tissue	3D histology reconstruction methods	Liquid phantoms
Ziemczonok et al. (2019) [48]	To characterize the performance of a limited-angle HTM by using phantom	Holographic tomography microscope (HTM) and tomographic reconstruction analysis	Manufactured by 3D laser photolithography
Kugler et al. (2019) [17]	To propose a reconstruction method for pancreatic cancer tumors obtained from histopathological images	Non-rigid 3D reconstruction method	-
Vardaki et al. (2020)[44]	To review the biomedical applications for the types of tissue phantoms	Raman spectroscopy	Liquid phantoms

In these studies mentioned above, the reconstruction process is not evaluated. However, in order to eliminate the storage problem when the investigated images take the big space, the reconstruction process can be required. In this context, Pichat et al. performed a survey about 3D histology reconstruction for many different types of tissue that are created as liquid phantoms [18]. They first summarise the digitised process from a tissue specimen, and then to overcome the storage problem, they describe the 3D histology reconstruction process where the 3D medical imaging is used or not. On the other hand, Ziemczonok et al. characterized the performance of a limited-angle holographic tomography microscope by using phantom manufactured by 3D laser photolithography. A full reference image quality assessment metric which is given

such as the universal quality index  $Q$ , is applied to the tomographic reconstruction process [48]. In addition, to reconstruct the 3D image of the microstructures in the tissue, Kugler et al. used a method of non-rigid image registration. They remove the nonlinear deformation of the pathological images and investigate the smoothness of each spatial continuity of the tissue [17].

To the best of authors' knowledge, the reconstruction of tissue mimicking phantoms imaging with digital holography is very limited in the literature. In addition, there has been no work which considers reconstruction process performed by using in-line digital holography and evaluated in terms of image quality measurement [40] for reconstructed phantom images, yet. In this context, biomedical image reconstruction is performed with in-line digital holography in order to eliminate the storage problem for many different types of tissue in 3D medical imaging. Moreover, the obtained reconstructed images are evaluated in terms of image quality measurement to validate the study as a strong work.

As mentioned in Section II, hologram recording has been performed with a simulation study based on in-line digital holography for a text created in paint (paintbrush) as the first stage and for phantoms formed by randomly inserting 5-43  $\mu\text{m}$  glass beads scatters into the agar gel and scanned by a linear array transducer as the second stage. The reconstructed process is performed by using FTA.

In order to examine the validity of the study, the difference between the original image recorded with the hologram and the image reconstructed with this technique has been obtained by calculating the error metrics. Because, the assessment of image quality is closely related to the assessment of the image similarity. Sasi Varnan et al. defined the quality measurement parameter and their corresponded value [40]. For this context, MSE, MAE and PSNR values are calculated for each obtained results and evaluated based on [40]. These results are presented in Table II.

As it can be clearly seen in Fig. 3-6, the reconstructed images provide consistent results with the original images that are desired to be displayed by holography technique. The MSE values for the images of original text created in paint program, first image of the used phantom, second image of the used phantom and third image of the used phantom are obtained as 0.0226, 0.0400, 0.0307 and 0.0181, respectively. These results are closer to zero, which are expected values based on [40]. This means that the similarity between the original and the reconstructed image has maximum value. On the other hand, the MAE values obtained for the images given in Fig. 3-6 are calculated as 0.0511, 0.0925, 0.0803 and 0.0578, respectively. According to the results, the differences between the original and reconstructed images are quite low like as MSE values. As for the PSNR values, it is expected that these values are closer to  $\infty$  and quite high. In this study the PSNR values are obtained as 116.1410, 92.0757, 103.6434 and 126.5263 for the investigated images, respectively. These results supply the expectations (Table I).

In the light of the results obtained in this study, it can be concluded that the neglectation of the storage problem for the reconstructed images and making possible to image many different sub-tissues at the same time can be provided by in-

line digital holography. Because, the reconstructed images are obtained with high image quality. Moreover, the use of a phantom image eliminates the necessity of the biopsy process in medical imaging.

#### REFERENCES

- [1] D. Welch, A.D. Harken, G. Randers?Pehrson, D.J. Brenner. "Construction of mouse phantoms from segmented CT scan data for radiation dosimetry studies." *Phys Med Biol.* vol. 60, 1, 2015, pp 3589-3598.
- [2] F. Zito, E. De Bernardi, C. Soffientini, C. Canzi, R. Casati, P. Gerundini, G. Baselli. "The use of zeolites to generate PET phantoms for the validation of quantification strategies in oncology." *Med Phys.* Vol. 39, 9, 2012, pp 5353-5361.
- [3] A. Hellerbach, V. Schuster, A. Jansen, J. Sommer. "MRI phantoms - are there alternatives to Agar?" *PLoS ONE*, vol. 8, 8, 2013, pp e70343.
- [4] A.P. Gibson, J.C. Hebden, S.R. Arridge. "Recent advances in diffuse optical imaging." *Phys. Med. Biol.* Vol 50, 4, 2005, pp R1-R43
- [5] G.D. Liew, R.M. Trimboli, T. Sella, F. Sardaneli. "Optical imaging of the breast: basic principles and clinical applications." *American Journal of Roentgenology*, vol. 290, 1, 2017, pp 230-238.
- [6] A. Anand, I. Moon, B. Javidi. "Automated disease identification with 3-D optical imaging: a medical diagnostic tool." *Proc. IEEE*, vol. 105, 5, 2017, pp 924-946.
- [7] F. Maes, D. Loeckx, D. Vandermeulen, P. Suetens, Image registration using mutual information. In: *Handbook of biomedical imaging*, Springer US, 2015, p. 295-308.
- [8] U. Schnars, W. Jueptner, *Digital Holography: Digital Hologram Recording, Numerical Reconstruction, and Related Techniques*, Springer-Verlag Berlin Heidelberg, 2005, p. 164.
- [9] A. Doblas, E. Roche, F. Ampudia-Blasco, M. Martinez-Corral, G. Saavedra, and J. Garcia-Sucerquia. "Diabetes screening by telecentric digital holographic microscopy." *J. Microsc.* Vol. 261, 3, 2016, pp 285-290.
- [10] C. D. Depeursinge, E. Cuhe, T. Colomb, P. Dahlgren, A. M. Marian, F. Monfort, P. Marquet, P. J. Magistretti, "Cells and tissue imaging with digital holographic microscopy." *Novel Optical Instrumentation for Biomedical Applications*, 14 October 2003, SPIE vol. 5143.
- [11] N.F. Boyd, H. Guo, L.J. Martin. "Mammographic density and the risk and detection of breast cancer." *N. Engl. J. Med.* vol. 356, 3, 2007 pp 227-236.
- [12] C.K. Kuhl. "Current status of breast MR imaging. Part 2: clinical applications." *Radiology*, vol. 244, 3, 2007, pp 672-691.
- [13] N.H. Peters, R. Borel, N.P. Zuihoff, W.P. Mali, K.G. Moons, P.H. Peeters. "Meta-analysis of MR imaging in the diagnosis of breast lesions." *Radiology*, vol. 246,1, 2008, pp 116-124.
- [14] C. C. Chen, Y.L. Wan, Y.Y., Wai, H.L. Liu. "Quality assurance of clinical MRI scanners using ACR MRI phantom: preliminary results." *J Digit Imaging* vol. 17, 2004, pp 279-284.
- [15] M. Freed, J. A. de Zwart, J. T. Loud, R. H. El Khouli, K. J. Myers, M. H. Greene, J. H. Duyn, A. Badano. "An anthropomorphic phantom for quantitative evaluation of breast MRI." *Med Phys.* Vol. 38, 2, 2011, pp 43-753.
- [16] K. Hattori, Y. Ikemoto, W. Takao, T. Harimoto, S. Kanazawa, M. Oita, K. Shibuya, M. Kuroda, H. Kato. "Development of MRI phantom equivalent to human tissues for 3.0T MRI." *Med Phys.* Vol. 40, 3, 2013, pp 032303?1-032303?11.
- [17] M. Kugler, Y. Goto, Y. Tamura, N. Kawamura, H. Kobayashi, T. Yokota, C. Iwamoto, K. Ohuchida, M. Hashizume, A. Shimizu, H. Hontani. "Robust 3D image reconstruction of pancreatic cancer tumors from histopathological images with different stains and its quantitative performance evaluation." *International Journal of Computer Assisted Radiology and Surgery*, vol. 14, 1, 2019, pp 2047-2055.
- [18] J. Pichat, J.E. Iglesias, T. Yousry, S. Ourselin, M. Modat. "A survey of methods for 3D histology reconstruction." *Medical Image Analysis*, vol. 46, 1, 2018, pp 73-105.
- [19] Y. Song, D. Treanor, A. J. Bulpitt, D. R. Magee. "3D reconstruction of multiple stained histology images." *J Pathol Inform.* Vol. 4, 2, 2013, pp S7.
- [20] M. Kugler, Y. Goto, N. Kawamura, H. Kobayashi, T. Yokota, C. Iwamoto, K. Ohuchida, M. Hashizume, H. Hontani, Accurate 3D reconstruction of a whole pancreatic cancer tumor from pathology images with different stains. In: *Computational pathology and ophthalmic medical image analysis*, Springer International Publishing, 2018, p. 35-43.
- [21] D. H. Adler, L. Pluta, S. Kadivar, C. Craige, J. C Gee, B. B. Avants, P. A. Yushkevich. "Histology-derived volumetric annotation of the human hippocampal subfields in postmortem MRI." *Neuroimage*, vol. 84, 1, 2014, pp 505-523.
- [22] P. Hariharan, *Optical holography: principles, techniques and applications*, Cambridge University Press, 2nd Edition, September 1996, p. 428.
- [23] C.B. Burckhardt, R.J. Collier, L. H. Lin, *Optical holography*, Academic Press, New York, NY, USA, 1971, p. 605.
- [24] J. Di, Y. Li, M. Xie, J. Zhang, C. Ma, T. Xi, E. Li, J. Zhao. "Dual-wavelength common-path digital holographic microscopy for quantitative phase imaging based on lateral shearing interferometry." *Applied Optics*, vol. 55, 26, 2016, pp 7287-7293.
- [25] P. Ledwig, F. E. Robles "Epi-mode tomographic quantitative phase imaging in thick scattering samples." *Biomedical Optics Express*, vol. 10, 7, 2019, pp 3605-362.
- [26] K. Lee, K. Kim, J. Jung, J. Heo, S. Cho, S. Lee, G. Chang, Y. J. Jo, H. Park, Y. K. Park. "Quantitative phase imaging techniques for the study of cell pathophysiology: from principles to applications." *Sensors (Basel)*, vol. 13, 4, 2013, pp 4170?4191.
- [27] Y. K. Park, C. Depeursinge, G. Popescu, "Quantitative phase imaging in biomedicine." *Nature Photonics*, vol. 12, 1, 2018, pp 578-589.
- [28] Y. S. Kim, S. Lee, J. Jung, S. Shin, H. G. Choi, G. H. Cha, W. Park, S. Lee, Y. Park. "Combining three-dimensional quantitative phase imaging and fluorescence microscopy for the study of Cell pathophysiology." *Yale Journal of Biology and Medicine*, vol. 91, 3, 2018, pp 267-277.
- [29] M. K. Kim. "Applications of digital holography in biomedical microscopy." *Journal of the Optical Society of Korea*, vol. 14, 2, 2010, pp 77-89.
- [30] F. Yi, I. Moon, B. Javidi. "Automated red blood cells extraction from holographic images using fully convolutional neural networks." *Biomedical Optics Express*, vol. 8, 10, 2017, pp 4466?4479.
- [31] A. Calabuig, M. Mugnano, L. Miccio, S. Grilli, P. Ferraro. "Investigating fibroblast cells under "safe" and "injurious" blue-light exposure by holographic microscopy." *Journal of Biophotonics*, vol. 10, 6-7, 2017, pp 919-927.
- [32] E. M. Zetsche, A. El Mallahi, F. J. R. Meysman. "Digital holographic microscopy: a novel tool to study themorphology, physiology and ecology of diatoms." *Diatom Research*, vol. 31, 1, 2016, pp 1-16.
- [33] Z. El-Schich, A. L. Mölder, A. G. Wingren. "Quantitative phase imaging for label-free analysis of cancer cells-focus on digital holographic microscopy." *Applied Sciences*, vol. 8, 7, 2018, pp 1027.
- [34] T. Ö. Onur, R. Hacıoğlu, "Image enhancement in ultrasound imaging." *SIU 2016-Signal Processing and Communication Application Conference*, Zonguldak, Turkey, 16-19 May 2016.
- [35] T. Ö. Onur, "Reducing Speckle in Ultrasound Images with Image Compounding." *SIU 2020-Signal Processing and Communication Application Conference*, Gaziantep, Turkey, 05-07 October 2020.
- [36] T. Latychevskaia, H. W. Fink. "Practical algorithms for simulation and reconstruction of digital in-line holograms." *Applied Optics*, vol. 54, 9, 2015, pp 2424-2434.
- [37] T. Kreis, *Handbook of holographic interferometry, optical and digital methods*, Wiley?VCH Verlag GmbH & Co. KGaA, Weinheim, Germany, 1st edition, 2005, p. 554.
- [38] E. Cuhe, P. Marquet, C. Depeursinge. "Spatial filtering for zero-order and twin-image elimination in digital off-axis holography." *Applied Optics*, vol. 39, 23, 2000, pp 4070-4075.
- [39] G. Ustabas Kaya, Z. Saraç, D. Önal Tayyar, "Image reconstruction from phase hologram obtained by using single phase information." *SIU 2014-Signal Processing and Communication Application Conference*, Trabzon, Turkey, 23-25 April 2014.
- [40] C. Sasi Varman, A. Jagan, J. Kaur, D. Jyoti, Dr. D. S. Rao. "Image quality assessment techniques *pn* spatial domain." *International Journal of Computer Science and Technology IJCSST*, vol. 2, 3, 2011, pp 177-184.
- [41] U. Sara, M. Akter, M. S. Uddin. "Image quality assessment through FSIM, SSIM, MSE and PSNR-A comparative study." *Journal of Computer and Communications*, vol. 7, 3, 2019, pp 8-18.
- [42] D. Asamoah, E. O. Oppong, S. O. Oppong, J. Danso. "Measuring the performance of image contrast enhancement technique." *Int. J. Comput. Appl.* vol.181, 22, 2018, pp. 6-13.

- [43] J. Chaiken, W. F. Finney, Knudson PE, et al. "Noninvasive blood analysis by tissue modulated NIR Raman spectroscopy." Proc SPIE. vol. 4368, 2001, pp. 134-145.
- [44] M. Z Vardaki, N. Kourkoumelis, "Tissue phantoms for biomedical applications in Raman spectroscopy: A review." Biomedical Engineering and Computational Biology, Vol.11, 1, 2020, pp. 1-15.
- [45] S. Li, K. D. Mohan, W. W. Sanders, A. L. Oldenburg, "Toward soft-tissue elastography using digital holography to monitor surface acoustic waves." Journal of Biomedical Optics, vol. 16, 11, 2011, pp. 116005 (1-7).
- [46] B. Karaböce, E. Çetin, C. M. Özdingiş, H.O. Durmuş, "Image measurement verification studies of different objects in tissue-mimicking fantom." In Proc. TIPTEKNO, 2017, pp. 1-4.
- [47] E. Maneas, W. Xia, O. Ogunlade, M. Fonseca, D.I. Nikitichev, A.I. David, S.J. West, S. Ourselin, J.C. Hebden, T. Vercauteren, A.E. Desjardins, "Gel wax-based tissue-mimicking phantoms for multispectral photoacoustic imaging." Biomedical Optics Express, vol.9,3, 2018, pp. 1151-1163.
- [48] M. Ziemczonok, A. Kus, P. Wasylczyk, M. Kujawińska, "3D-printed biological cell phantom for testing 3D quantitative phase imaging systems." Scientific Report, vol. 9, 1, 2019, pp. 1-9.

### BIOGRAPHIES



**TUĞBA ÖZGE ONUR** is an Assistant Professor in the department of Electrical Electronics Engineering at Zonguldak Bülent Ecevit University. She received her MSc and PhD degrees, with highest honors, in Electrical-Electronics Engineering from Zonguldak Bülent Ecevit University in 2008 and 2016, respectively. Her doctoral thesis study

was partly carried out at Luleå University of Technology (Luleå, Sweden) and University of Wisconsin-Madison (Madison, Wisconsin, USA). Her research interests include signal and image processing, ultrasound signal processing, system identification and nonlinear systems. She has published papers in the field of signal processing applications.



**GÜLHAN USTABAŞ KAYA** is a Research Assistant Dr. in the Department of Electrical-Electronics Engineering at Zonguldak Bülent Ecevit University. She received her MSc and PhD degrees in Electrical-Electronics Engineering from Zonguldak Bülent Ecevit University in 2013 and 2019, respectively. Her interest fields are in the development of novel techniques and applications in digital holography,

interferometry, microscopy, photonics, signal and image processing, data mining and machine learning. She has published papers in the field of optics, signal processing and machine learning applications. She is also an OSA member.

# Publication Ethics

The journal publishes original papers in the extensive field of Electrical-electronics and Computer engineering. To that end, it is essential that all who participate in producing the journal conduct themselves as authors, reviewers, editors, and publishers in accord with the highest level of professional ethics and standards. Plagiarism or self-plagiarism constitutes unethical scientific behavior and is never acceptable.

By submitting a manuscript to this journal, each author explicitly confirms that the manuscript meets the highest ethical standards for authors and coauthors

**The undersigned hereby assign(s) to *Balkan Journal of Electrical & Computer Engineering* (BAJECE) copyright ownership in the above Paper, effective if and when the Paper is accepted for publication by BAJECE and to the extent transferable under applicable national law. This assignment gives BAJECE the right to register copyright to the Paper in its name as claimant and to publish the Paper in any print or electronic medium.**

Authors, or their employers in the case of works made for hire, retain the following rights:

1. All proprietary rights other than copyright, including patent rights.
2. The right to make and distribute copies of the Paper for internal purposes.
3. The right to use the material for lecture or classroom purposes.
4. The right to prepare derivative publications based on the Paper, including books or book chapters, journal papers, and magazine articles, provided that publication of a derivative work occurs subsequent to the official date of publication by BAJECE.
5. The right to post an author-prepared version or an official version ( preferred version) of the published paper on an internal or external server controlled exclusively by the author/employer, provided that (a) such posting is noncommercial in nature and the paper is made available to users without charge; (b) a copyright notice and full citation appear with the paper, and (c) a link to BAJECE's official online version of the abstract is provided using the DOI (Document Object Identifier) link.



ISSN: 2147- 284X  
Year: April 2021  
Volume: 9  
Issue: 2

## CONTENTS

- M. Abdeh, F. Abut, F. Akay;** Autonomous Navigation in Search and Rescue Simulated Environment using Deep Reinforcement Learning, .....92 - 98
- T. Özmen, N. Onat;** The Effects of Magnetic Circuit Geometry and Material Properties on Surface Mounted Permanent Magnet Synchronous Generator Performance,..... 99 - 105
- H. Sucu, T. Göktaş, M. Arkan;** Design, Simulation and Application of Buck Converter with Digital PI Controller,.....106 - 113
- R. Çelikel, A. Gündoğdu;** Comparison of PO and INC MPPT Methods Using FPGA In-The-Loop Under Different Radiation Conditions,.....114 - 122
- A. Gencer;** Comparison of T-Type Converter and NPC for the Wind Turbine Based on Doubly-Fed Induction Generator,.....123 - 128
- S. Yazar;** Reconstruction of the Taguchi Orthogonal Arrays with the Support Vector Machines Method,.....129 - 137
- B. K. Engiz, Y. A. Rajab;** Spectrum Occupancy Measurements in Cellular Frequency Band in Samsun,.....138 - 143
- I. Aksakalli, S. Kaçdioğlu, Y. S. Hanay;** Kidney X-ray Images Classification using Machine Learning and Deep Learning Methods,.....144 - 151
- E. Demir, A. Öztekin;** Automatic Positioning of Mobile Users via GSM Signal Measurements,.....152 - 160
- H. Eroğlu, Y. Oğuz;** Energy Efficient Driving Optimization of Electrical Vehicles Considering the Road Characteristics,.....161 - 170
- A. Çiçek, B. Uluğ;** First-Principles Study of Graphene-6H SiC Surface Interactions,.....171 - 177
- M. A. Yimer, S. Sevinç, A. R. Şişman, Ö. Aktaş, O. Yildirim, E. Yaşar;** Monitoring the Treatments and Interventions to Intensive Care Patients: A Study for Multidimensional Evaluation of Changes in Patient Test Results with Principal Component Analysis,.....178 - 186
- E. Gündoğan;** A Proposed Ensemble Model for The Prediction of Coronavirus Anxiety Scale of Migrant Workers,.....187 - 190
- Z. K. Küçük, N. Ekren;** Light Pollution and Smart Outdoor Lighting,.....191 - 200
- C. Şeker, M. T. Guneser, Ş. Kuzey;** The Topologies of Multi-Input Single-Output Isolation-Free DC-DC Converter for Hybrid Power Plants,.....201 - 206
- A. Doğaner;** An Infodemiological Study to Estimate Risk Factors of Urinary Incontinence Using Elastic Net Regression,.....207-211
- G. U. Kaya, T. Ö. Onur;** Reconstruction with In-Line Digital Holography Quantitative Phase Imaging for Tissue-Mimicking Phantom Samples,.....213-220

## BALKAN JOURNAL OF ELECTRICAL & COMPUTER ENGINEERING

(An International Peer Reviewed, Indexed and Open Access Journal)

### Contact

Batman University  
Department of Electrical-Electronics Engineering  
Bati Raman Campus Batman-Turkey

Web: <http://dergipark.gov.tr/bajece>  
<http://www.bajece.com>  
e-mail: [bajece@hotmail.com](mailto:bajece@hotmail.com)

